2022

THEORETICAL INVESTIGATION ON OPTICAL PROPERTIES OF 2D MATERIALS AND MECHANICAL PROPERTIES OF POLYMER COMPOSITES AT MOLECULAR LEVEL

Geeta Sachdeva
Michigan Technological University, gsachdev@mtu.edu

THEORETICAL INVESTIGATION ON OPTICAL PROPERTIES OF 2D MATERIALS AND MECHANICAL PROPERTIES OF POLYMER COMPOSITES AT MOLECULAR LEVEL

By

Geeta Sachdeva

A DISSERTATION

Submitted in partial fulfillment of the requirements for the degree of

DOCTOR OF PHILOSOPHY

In Applied Physics

MICHIGAN TECHNOLOGICAL UNIVERSITY

2022

This dissertation has been approved in partial fulfillment of the requirements for the Degree of DOCTOR OF PHILOSOPHY in Applied Physics.

Department of Physics

Dissertation Advisor: *Dr. Ravindra Pandey*

Committee Member: *Dr. Max Seel*

Committee Member: *Dr. Ranjit Pati*

Committee Member: *Dr. Gregory M. Odegard*

Department Chair: *Dr. Ravindra Pandey*

Contents

List of Figures

List of Tables

Preface

This dissertation is an original intellectual product of the author, Geeta Sachdeva. Two topics have been studied including optical properties of 2D materials studied with density functional theory method and interfacial properties of polymer composites studied with density functional theory and molecular dynamics method.

Chapter 3 of this thesis is a combined work published in Applied Physics Letter (Applied Physics Letters 116 (26), 263102) and Computation (Computation 9 (9), 101). Dr. Ashok Kumar, Dr. Suman deep Kaur and myself conducted the calculations, data collection, and analysis under the supervision of Prof. Ravindra Pandey. Dr. Sumandeep Kaur, Prof. Ashok Kumar, Prof. Ravindra Pandey, and Prof. Shashi P. Karna were involved in the analysis of the results and contributed to the manuscript edits.

Chapter 4 is reproduced from the published paper in ACS Applied Polymer Materials (ACS Applied Polymer Materials 3 (2), 1052-1059). Chapter 5 uses similar study as Chapter 4 but for cyanate ester monomers. I conducted the calculations, data collection, and analysis under the supervision of Prof. Ravindra Pandey. Dr. Alvaro Lobato Fernandez, Prof. Gregory M. Odegard and Prof. Ravindra Pandey were involved in the analysis of the results and contributed to the manuscript edits.

Chapter 6 is accepted in Journal of Materials Research. I conducted the calculations, data collection, and analysis under the supervision of Prof. Ravindra Pandey. Sagar U. Patil,

William A. Pisani, Prathamesh P. Deshpande, Swapnil S. Bamane, Prof. Gregory M. Odegard and Prof. Ravindra Pandey, were involved in the analysis of the results and contributed to the manuscript edits.

Acknowledgements

In the first place, I am grateful to my advisor, Prof. Ravindra Pandey, for his constant guidance, trust, and inspiration. “In addition to being a phenomenal mentor, you have provided a steady voice of reason that has been and will remain a guiding light in my professional life”. I feel very fortunate to have had the freedom to explore many projects, from 2D structures to polymer composites. Prof. Pandey has always believed in and encouraged me. I am deeply grateful for the time and energy he has invested in me over the past five years. His support and encouragement have allowed me to achieve my academic goals. Working with him has been an honor and a privilege.

Many thanks to Prof. Odegard. I am fortunate to work with him on the ‘Computational Development of Materials for Space Application **(**USCOMP)’ project, which has helped me better understand the scope of the current research. I would like to thank my collaborators at Georgia Tech, Penn State, and Colorado University. My research career has been enhanced by working with them. I am deeply indebted to Prof. Ashok for believing in me during my master's program and through whom I was able to collaborate with Prof. Pandey at Michigan Tech.

I wish my gratitude to my committee members. I would like to thank Prof. Ranjit Pati; he has been a great instructor who taught me how to solve quantum physics problems

correctly. I want to thank Prof. Max Seel, whose curios questions and positive suggestions helped me imagine beyond my imagination level. My sincere thanks to each of you for your time and effort in my Ph.D. progress. All of your suggestions have been helpful in improving my dissertation.

It is my pleasure to thank Dr. Shashi P Karna from the Army Research Laboratory. Your thoughtful comments and careful revision of our published paper are greatly appreciated. Thanks to my mentors; Dr. Ping Yang, Dr. Enrique R Batista, and Dr. Goaxue Wang for the exciting and insightful discussion, during my internship at Los Alamos National Laboratory. Thank you for your patient support and the opportunities I was given to carry out my research.

I would like to thank Cameron Shock for being my great friend and officemate who has offered much help since my first day. I am grateful for the help I have received from Dr. Lokanath Patra, Dr. Qing Guo, Dr. Kevin Waters, Dr. Gemechis D. Degaga and Dr. Nabanita Saikia during my beginning years of PhD. It would have been much harder to get through graduate school without my team. I am thankful for our seemingly random discussions that led to many new research ideas. I am grateful to the physics department at MTU, especially for the invaluable lessons I have learned from the faculties and for the support I have received from the staff.

I want to thank both of my family who I owe so much for being in a foreign country and to whom I dedicate this thesis. I want to thank my mom first, and it is all her hard work, love, and support through all these years that encourage me to always keep improving myself and to come to the US to work on a Ph.D. My Dad, who is my good friend and who always supported my decisions. I would like to thank my brother, sister, and school and college friends as well.

Many thanks to my husband Nihar for making me a better person, always expanding my mind, and showing me how to be an open and accepting individual. You are a constant source of love and imagination and have brightened my days by being one of the most influential individuals in my life. Thank you for sharing my ups and downs in these years.

I acknowledge the sources of funding that have supported the research that is featured in this dissertation, including the ARL, NASA, and the MTU finishing fellowship in my final year. Helpful support from Dr. S. Gowtham is gratefully acknowledged in using Superior, high-performance computing clusters at MTU. Inevitably, I might leave someone deserving of my appreciation for helping me complete this thesis. Therefore, I am thankful to all of those who have contributed in some way to my success.

"Anything is possible when you have the right people to support you"

List of Abbreviations

2D	Two-Dimensional
CVD	Chemical Vapor Deposition
DFT	Density Functional Theory
DOS	Density of States
SEOS	Spinodal Equation of State
GGA	Generalized Gradient Approximation
BN	Boron Nitride
HF	Hartree-Fock
KS	Kohn-Sham
LCAO	Linear Combination of Atomic Orbitals
LDA	Local Density Approximation
MD	Molecular Dynamics
PAW	Projector Augmented Wave
PBC	Periodic Boundary Condition
DOS	Density of States
SCF	Self-Consistent Field

VASP	Vienna Ab initio Simulation Package
vdW	van der Waals
XC	Exchange-Correlation

Abstract

The field of two-dimensional (2D) layered materials provides a new platform for studying diverse physical phenomena that are scientifically interesting and relevant for technological applications. Theoretical predictions from atomically resolved computational simulations of 2D materials play a pivotal role in designing and advancing these developments. The focus of this thesis is 2D materials especially graphene and BN studied using density functional theory (DFT) and molecular dynamics (MD) simulations. In the first half of the thesis, the electronic structure and optical properties are discussed for graphene, antimonene, and borophene. It is found that the absorbance in (atomically flat) multilayer antimonene (group V) is comparable to or greater than that for multilayer borophene (group III) and graphene (group IV). The number of layers has a substantial impact on the electrical and optical properties of graphene, antimonene, and borophene. Unlike graphene and antimonene, however, multilayer δ_6-borophene exhibits extremely anisotropic electrical and optical characteristics. Overall, our findings imply that multilayer graphene and antimonene are good optical absorbers, particularly in the infrared region of the spectrum, and could be employed as a coating to protect against mid-IR tunable lasers. However, borophene because of its high optical transparency and good metallicity, could be a promising choice for transparent conductive 2D materials with applications in photovoltaics, performance-controlled optoelectronic devices, and touch displays.

Molecular-level simulations for monomers with graphene/BN were undertaken to relate the interfacial features with the corresponding mechanical response in terms of strain and stiffness. The results show that the nature of bonding at the interface determines the interaction strength between resin (or hardener) and graphene and that the mechanical response follows the hierarchical order of the interaction strength at the interface. In addition, the change in polarity from graphene to BN monolayer also leads to improved interfacial strength as well as increased transverse stiffness at the molecular level for both resins and hardeners. We have also studied the effect of BN reinforcement with representative cases of cyanate esters, epoxy, and bismaleimide (BMI) resins using molecular dynamics to characterize the bulk level properties of reinforcement/polymer interface. Calculations simulating pull-apart transverse tension experiments find that the non-fluorinated ester interface exhibits higher stiffness and toughness than the fluorinated interface. On the other hand, the epoxy/BN interface is predicted to have significantly lower toughness (or resistance to fracture) than the BMI/BN interface. BMI, thus, appears to be the polymer matrix of choice when considering the BN nanomaterials as reinforcement compared to either cyanate ester or epoxy polymers for structural applications. These results based on molecular simulations emphasize the need to use computational modeling to efficiently and accurately determine molecular-level polymer/surface combinations that yield optimal composite material mechanical performance. This is especially true when designing and developing high-performance composites with nanoscale reinforcement.

1 Introduction

Two-dimensional (2D) materials are fascinating new materials that have attracted the attention of many scientists. Their goal is to discover its unique, distinct properties from its 3D counterparts. These 2D materials are crystalline materials with a thickness ranging from a few layers to many layers and contained either inorganic or organic substituents that have a two-dimensional arrangement. Limiting a material's leading dimensions can directly affect its properties[1]. As a result of electron confinement and lack of interlayer interactions, not only optical and electronic properties are affected, but also mechanical and chemical properties. In general, the interlayer interactions are very weak and greatly influence the band structure. This is typically due to geometrical effects, as well as the very high, and sometimes infinite, surface-to-bulk ratio of thin materials. As a result of their use in nano- and atomic-scale devices, these materials can have a variety of electrical, optical, and mechanical properties [2-4]. They are considered the new generation of nanomaterials with many applications, including field-effect transistors (FETs), photovoltaic solar cells, optical devices, spintronics, and valley electronics [4-8, 9-11]With the boom of graphene, two-dimensional (2D) materials, such as graphene, BN, silicene, germanene, phosphorene, transition metal dichalcogenides, arsenene, borophene, and antimonene have attracted dramatically increasing interest in the past decade [1, 2, 7, 12, 13, 14].

Due to the two-dimensional nature of these materials, electrons are constrained in the out-of-plane direction, leading to some very interesting quantum physics. Therefore, they may be easily stacked on top of each other to form vertical heterostructures. Since different layered materials act as metals, insulators, semiconductors, or superconductors in their monolayer limit, different heterostructures of different materials can run the full spectrum of imaginable device architectures[11]. "What could we do with layered structures with just the right layers?", Richard P. Feynman asked in his famous lecture entitled There's Plenty of Room at the Bottom in 1959. "What would the properties of materials be if we could arrange the atoms the way we want them?".[15] The idea of designing materials at the atomic/molecular level is very appealing, but almost 60 years after Feynman's talk, its implementation remains a major goal of materials science[16]. Understanding the structure-property and dynamic response of these multilayer materials at the atomic level will provide guiding principles for predicting bulk properties and assisting in the development of novel materials[17]. This key technology has helped to develop many important optoelectronic and structural applications which have affected the future material design strategy positively[18]. In this work, we have studied 2D materials like graphene and its analogous materials for different applications, such as optoelectronic devices, and use them in structural designs. Because graphene and BN are physically similar yet have different electrical properties, we investigated the properties of BN in polymer composites.

1.1 Graphene

Graphene is a two-dimensional allotrope of graphite containing sp^2 bonded carbon atoms that are arranged in a honeycomb structure[19, 20]. Materials based on graphene have shown excellent electronic, chemical, and mechanical properties, as well as a unique combination of high thermal conductivity, electrical conductivity, and optical transparency[9, 19, 21, 22-24]. Due to the lack of an energy difference between the valence and conduction bands (i.e., bandgap) (Figure 1[25]), graphene electrically acts like a metal, prompting a surge in research into field-effect transistors (FETs), optoelectronic devices, biomedical devices, chemical sensors, and conductive polymer composites[26]. In this study, optical properties including absorption coefficient, transmittance, and reflectance, as a function of wavelength and incident energy, are studied and compared with other 2D materials like antimonene and borophene. A key optical property in the infrared region, absorption is studied as a function of wavelength for multilayered graphene.

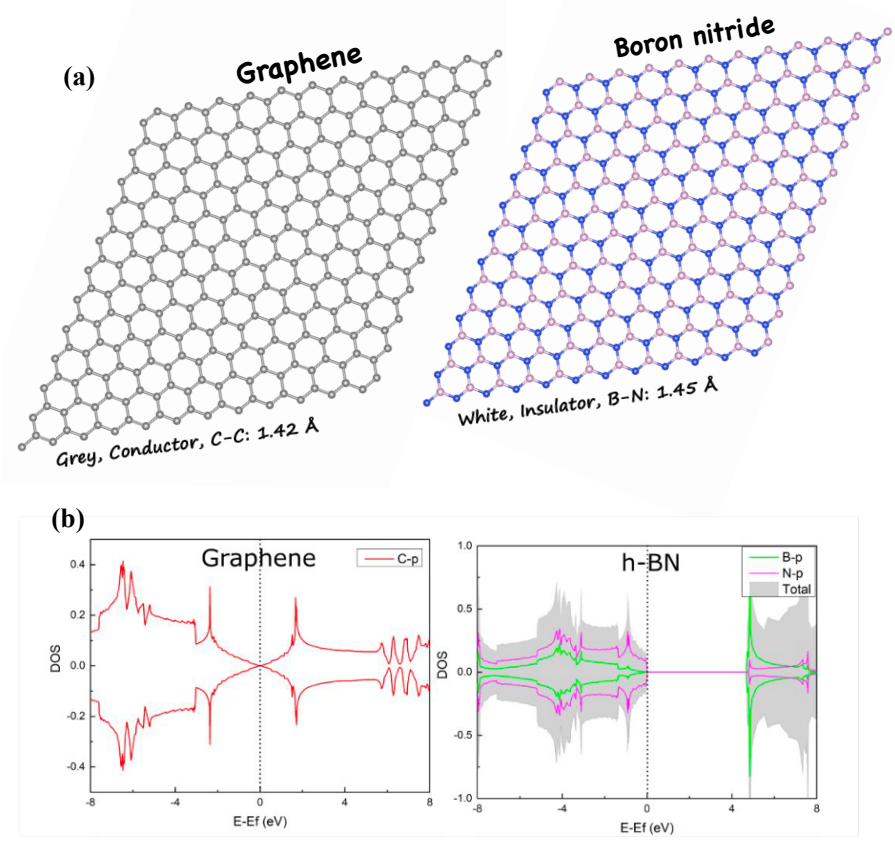

Figure 1: (a) Graphene and BN ball and stick model. (b) Electron density of states for graphene and BN monolayer. Color codes: C- grey, N-Blue, B- Pink

Graphene has emerged as a material of scientific interest due to its exceptional mechanical and thermal properties. Contrasting properties of graphene as reinforcement in polymers are interfacial interactions as the load will be transferred from the matrix to the reinforcement will improve mechanical properties. Individual layers of Graphene, under external loadings and thermal stresses, undergo out-of-the-plane wrapping, rippling, folding, scrolling, and crumpling making graphene suitable to enhance the toughness of polymers[27-29]. Most commonly used Polymers include epoxy, BMI,

polycarbonate, polyester, polymethylmethacrylate (PMMA), polyethylene, polystyrene (PS), nylon and Teflon, etc. as reinforcement among TiO_2, SiO, $Al2O_3$, clay, SiO_2, CNT's, Fullerene the Graphene has more publications and popular filler material[30]. Graphene is found to have a very high elastic modulus and intrinsic strength[28]. The reliability of polymer/graphene composites on end-use applications depends on understanding the effect of the structure-property relationship of the composite. Therefore, we simulated pull-out tests on graphene polymer complexes to study the mechanical properties of polymer composites.

1.2 Hexagonal boron nitride (h-BN)

The h-BN is an insulator material with two different atoms B (Boron) and N (Nitrogen) arranged in different sublattices of the hexagonal lattice. Despite the structural similarity between graphene and h-BN, their electronic property exhibits wide variation (Figure 1). It has a direct bandgap of about 4.5 eV while the graphene is highly conductive as a semimetal[24, 31]. Furthermore, due to its insulator properties h-BN is an excellent substrate for supporting and encapsulating some materials such as graphene, black phosphorus, etc[24]. Polymer/BN composites are one of the important classes of materials with a wide range of applications spanning from automotive, aerospace, healthcare and medicine, energy storage, to electronic engineering. While many efforts have been devoted to graphene incorporation into polymer materials, polymer -BN composites are less explored. BN nanomaterials have superior fracture strength (165 GPa), high Young's

modulus (0.8 TPa), and high thermal stability (up to 800 °C in the air)[32, 33]. Although both BN and graphene nanomaterials show vdW force and π–π interactions with polymers, the partial ionic electronic structure of B-N bonding can be advantageous in terms of molecular interactions with polymer materials as shown in Figure 2. Therefore, to benchmark our results obtained from graphene as reinforcement we also studied polymer/BN complexes.

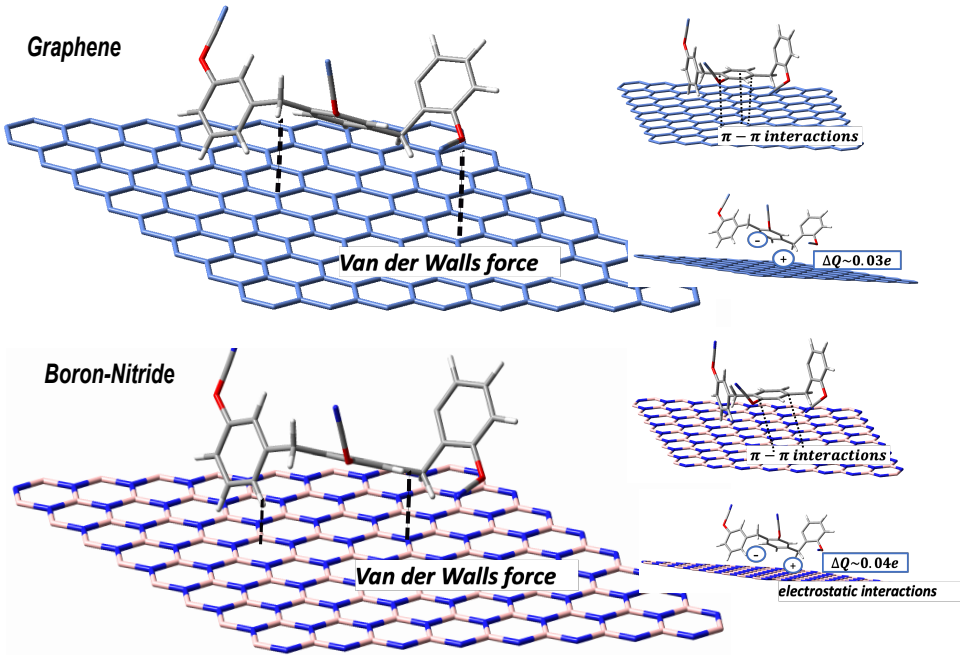

Figure 2: Graphene and BN both shows van der Waals (vdW) force and π–π interactions with monomers whereas there are electrostatic interactions in case of BN due to partial ionic electronic structure of B-N bonding. Color codes: C- Light blue (graphene) and grey (monomer), N-Blue, B- Pink, O- Red, H-White

1.3 Polymer Composites

Composite properties are determined by the properties of components, composition, structure, and interfacial interactions. For example, properties of graphene-based composite are investigated by modeling the graphene at an atomic scale and considering hybrid interphase between graphene and a monomer. The interaction between graphene and polymer composites can be covalently and non-covalently. Generally, in non-covalently bonded graphene-polymer composites, the interfacial interactions consist of Van der Waals forces that are weaker than covalent bonds[34]. The interfacial adhesion characteristic plays an important role in determining the improvements in mechanical properties of graphene and its derivatives-based polymer composites. The interface between polymers and graphene has been investigated at multiple scales from coarse-grained methods to quantum mechanical methods such as DFT. In this study, we investigated the interface properties of resins and hardener monomers of BMI, Epoxy, and Cyanate ester polymer with graphene and then compared it with BN monolayer. Studying from the isolated monomers gives us an understanding of the relative effect of each monomer with respect to the reinforcement. Later, we investigated these interfaces with similar types of polymers using the molecular dynamics to study polymerized complexes with thousands of atoms.

1.4 Outline of the Thesis

The focus of much of this research has been on the structural, electronic, and optical properties of a few 2D materials and investigation on mechanical properties of polymer composites at the molecular level. Chapter 1 presents an introduction to 2D materials specially graphene and BN and a brief overview to the use of graphene and BN in composites. Chapter 2 provides an overview of the basic fundamentals of the computational models for material simulations. This section highlights the methods applied in this study, first molecular simulations based on DFT and secondly, MD. The chapter 3 describes application of DFT in obtaining the optical properties of few-layered graphene, antimonene and borophene. We have compared our results with the previous theoretical and experimental work.

Chapters 4 and 5, described the studies on interfacial properties of Epoxy, BMI and cyanate esters monomers with graphene or BN monolayer using DFT. To obtain the mechanical properties at interface we mimic the pull apart tests on the monomer graphene (or BN) complex. In the discussed the results of a large-scale simulation performed using MD method to investigate the mechanical response of the polymer composite. In next chapter we have investigated the mechanical response of the cyanate esters, BMI and Epoxy polymer interface with BN reinforcement using MD method. Using the pull apart test we have found interesting mechanical properties based on the structures of the considered polymers. We expect that the work included in chapter 4, 5 and 6 will add to

the understanding of next generation polymer composites for aerospace and structural applications. Lastly, in Chapter 7 we have provided the summary and possible future work.

2 Methodology

Understanding the properties of materials and predicting their behavior is a fascinating branch of science. The quest for a theoretical framework to explain and predict the properties of materials represents a significant fraction of theoretical condensed matter physics. Computer simulation plays an advantageous role in physics. In which the computer program simulates the physical system. Simulation studies are performed not on the real-world system, but on a model of the system created to study certain system dynamics and characteristics. One of the goals of computer simulation is to mimic experiments to light up the invisible microscopic details and thus explain the results. In parallel, simulations can be a useful tool for predicting experimental results. Molecular systems can be simulated using two common methods, DFT, and MD simulation, which we have applied in my dissertation work.

2.1 Theoretical Background

The theory of systems ranging from atoms and molecules to complex materials (many-electron systems) is one of the most complicated and fundamental problems in quantum mechanics. It has been attracting considerable interest from theoreticians for more than half a century. One of the main problems is that in many phenomena, only a single electron is of real interest. However, the many-electron interactions prevent describing

the electron in the conventional terms of eigenfunctions, eigenvalues, ionization energy, excitation energy [35], etc.

Since electrons are governed by the laws of quantum mechanics, all these systems are fully described by the Schrodinger equation (*Eq. 2.1*). In its time-independent format, the equation is typically presented as:

$$H\psi = E\psi \qquad \textit{Eq. 2.1}$$

Where the Hamiltonian is given by:

$$H = -\frac{h^2}{2m_e}\sum_i \nabla_i^2 - \frac{h^2}{2M_I}\sum_i \nabla_I^2 - \frac{1}{2}\sum_{ij}\frac{Z_I e^2}{|r_i - R_i|} + \frac{1}{2}\sum_{i\neq j}\frac{e^2}{|r_i - r_j|} + \frac{1}{2}\sum_{I\neq J}\frac{Z_I Z_J e^2}{|R_I - R_J|} \qquad \textit{Eq. 2.2}$$

$$or\ H = \hat{T}_e(r) + \hat{T}_N(R) + \hat{V}_{eN}(r,R) + \hat{V}_{ee}(r) + \hat{V}_{NN}(R)$$

Here, r and R are radii of the electrons and nuclei, and all other notations are chosen to be represented by lower and upper-case subscripts, respectively. The first and second terms in *Eq. 2.2* are the kinetic energies of the electrons and nuclei, respectively. The third term describes the electron-nuclear interaction. The fourth and fifth terms represent the electron-electron and nucleus-nucleus Coulomb repulsion, respectively.

All the information about a given system is contained, in principle, in the quantum mechanical wavefunction. For the case of a simple system like 2D square potential or a hydrogen atom, we can solve the Schrodinger equation to get the wave function of the system. We can then determine the allowed energy states of the system. Unfortunately, it is very difficult to solve the Schrodinger equation for an N-body system. Hence, we must include some approximations to make the N body system solvable.

Then the basic approximation that has been employed is the Born-Oppenheimer or adiabatic approximation[36]. According to this, the motion of the electron and the nuclei can be decoupled as the electrons move way faster than the nuclei due to their lighter mass. Hence Schrodinger equation can be written as[37]:

$$H = -\frac{h^2}{2m_e}\sum_i \nabla_i^2 - \frac{1}{2}\sum_{ij}\frac{Z_I e^2}{|r_i - R_i|} + \frac{1}{2}\sum_{i\neq j}\frac{e^2}{|r_i - r_j|} \qquad \textit{Eq. 2.3}$$

$$H = -\frac{h^2}{2M_I}\sum_I \nabla_I^2 + U(R) \qquad \textit{Eq. 2.4}$$

Equation 2.4 and 2.5 represents the individual equations for electron and nuclear Hamiltonian. The wave function can be written as a product of the electronic and nuclear wave functions:

$$\psi(r,R) = \psi_e(r,R)\psi_N(R) \qquad \textit{Eq. 2.5}$$

The term U(R), called as the nuclear potential in the nuclear Hamiltonian can be represented as:

$$U(R) = \frac{1}{2}\sum_{I\neq J}\frac{Z_I Z_J e^2}{|R_I - R_J|} + E(R) \qquad \textit{Eq. 2.6}$$

where E(R) is the total electronic energy within a set of nuclear coordinates R.

Even after the application of the Born-Oppenheimer approximation, the number of terms in the electronic Hamiltonian is quite large. To further simplify the Hamiltonian the Hartree approximation is employed in which each electron is an independent particle, and it interacts with other electrons in an averaged way (*Eq. 2.8*)[38]. Hence total energy can be written as the sum of n numbers of one-electron energies because every electron behaves as an independent entity [39]:

$$E = E_1 + E_2 + \ldots\ldots E_n \qquad \textit{Eq. 2.7}$$

And similarly, wavefunction can be written as the product of n numbers of the independent one-electron wavefunction:

$$\psi\,(r_1, r_2, ..., r_n) = \psi_1(r_1)\,\psi_2\,(r_2)\,....\,\psi_n\,(r_n) \qquad \textit{Eq. 2.8}$$

However, the biggest drawback of the Hartree method is that it does not satisfy two basic principles of quantum mechanics which must be followed by electrons which come in the category of fermions, the first one being Pauli's exclusion principle i.e., antisymmetric behavior of the wave function. Secondly, It does not include the exchange and correlation energies that are due to the spin effect of the electrons[39]. Therefore, the main problem with this approximation is that it does not include the spin effect of the electrons. Hence, comes the Hartree-Fock approximation which overcomes the drawbacks of the Hartree approximation. It contains the spin effect of the electrons which is the main achievement of this approximation.

It can be viewed as a variational method where the full many-body wave function is replaced by a single Slater determinant. The elements of the determinant are one-electron orbitals with the orbital and spin part[40]. In Hartree-Fock approximation, the wave function is taken in the form of a determinant called the slater determinant given by:

$$\Psi_{HF} = \frac{1}{\sqrt{N!}}\begin{vmatrix} \psi_1(x_1,\sigma_1) & \psi_1(x_2,\sigma_2) & \psi_1(x_3,\sigma_3) & \dots & \dots & \psi_1(x_N,\sigma_N) \\ \psi_2(x_1,\sigma_1) & \psi_2(x_2,\sigma_2) & \psi_2(x_3,\sigma_3) & \dots & \dots & \psi_2(x_N,\sigma_N) \\ \vdots & \vdots & \vdots & \dots & \dots & . \\ \vdots & \vdots & \vdots & \ddots & \ddots & . \\ \psi_N(x_1,\sigma_1) & \psi_N(x_2,\sigma_2) & \psi_N(x_3,\sigma_3) & \dots & \dots & \psi_N(x_N,\sigma_N) \end{vmatrix} \qquad \textit{Eq.2.9}$$

The energy expectation value using this wave function can be given by[41]:

$$E = \langle \psi_{HF} | H | \psi_{HF} \rangle$$
$$= \sum_i \int \psi_i^*(\vec{r}) \left[-\frac{h^2}{2m_e} \nabla_i^2 + v(\vec{r}) \right] \psi_i(\vec{r}) d^3r$$
$$+ \frac{1}{2} \sum_{i \neq j} \iint \frac{e^2}{|\vec{r} - \vec{r}'|} |\psi_i(\vec{r})|^2 |\psi_j(\vec{r})|^2 d^3r \, d^3r'$$
$$- \frac{1}{2} \sum_{i \neq j} \iint \frac{e^2}{|\vec{r} - \vec{r}'|} \psi_i^*(\vec{r}) \psi_i^*(\vec{r}') \psi_i(\vec{r}') \psi_j(\vec{r}) d^3r \, d^3r'$$

Eq. 2.10

An exchange of particles is equivalent to an exchange of columns, which produces a change of sign due to a known property of determinants. It is important to note that if two rows are equal, the determinant is zero and, therefore all ϕ_i 's must be different. This illustrates that two (or more) identical fermions cannot occupy the same state, which proves Pauli's exclusion principle. This method employs the Hartree potential but also forces the exchange interactions by forcing the antisymmetric of the electronic wavefunction. As a result, electrons with parallel spins stay apart, lowering the total binding energy of atoms. The downside to the theory is that it neglects correlations in the motion between two electrons with anti-parallel spins [40, 42].

2.2 Density Functional Theory

DFT attempts to address both the inaccuracy of HF and the Thomas Fermi model by replacing the many-body electronic wavefunction with the electronic density and including the exchange-correlation part. Whereas, instead of the N electron system which is dependent on 3N variables, the density is a function of only three variables and is a simpler quantity to deal with both conceptually and practically, while electron correlation is included indirectly from the outset[43]. This was the beginning to solve the many-body theory by making use of the first principal technique. In 1964, Hohenberg and Kohn published a paper and thus provided the DFT formulation[44]. The main aim behind this study is to find out an equation that is easier and solvable and hence to remove the complicated many-body wavefunction and its equations which contains 3N variables i.e., three degrees of freedoms, with the functional (functional is the function of another function, which map a number to a function) of electron density, which contains only 3 variables. So in the new system, there is no need to worry about the huge amount of 3N variables, instead, we only have to solve with 3 variables, which is very easy to solve[45]. Hohenberg and Kohn proved two theorems in 1964. These theorems can be stated as follows:

> *For any system of interacting particles in an external potential $V_{ext}(r)$, the ground state particle density uniquely determines the external potential $V_{ext}(r)$, except for a constant.*

A universal functional for the energy E can be defined in terms of density. The exact ground state is the global minimum value of this functional[46, 47].

The total energy functional can be written as:

$$E[n] = F[n] + \int v_{ext}(r)n(r)dr \qquad \textit{Eq. 2.11}$$

where the first term is the unknown functional and the second term describes the interaction of electron with nuclei and other field. According to this the minimum of the energy E_0 is exactly equivalent to the true ground state energy given i.e.,

$$E_o = minE[n(r)] = E[n_o(r)] \qquad \textit{Eq. 2.12}$$

The minimum energy can be calculated by the use of the variational principle which gives an upper bound for the ground state energy. The power of this principle lies in the fact that choosing any approximate wave function will give energy higher than the true energy of the system and therefore, we can look for energy that makes the Hamiltonian stationery. Hence the ground state wave functions can be found using this principle. The electron density can uniquely determine the external potential, therefore the many-electron wavefunction could be obtained using the Schrödinger equation. Therefore, in

principle, the Hamiltonian operator can be uniquely determined given the charge density. The Hohenberg-Kohn theorem asserts that the density of any system determines all ground-state properties of the system. Since the total ground state energy of a many-electron system is a functional of the density, if we know the electron density functional, we know the total energy of our system. By focusing on the electron density it is possible to derive an effective one-electron type Schrödinger equation[47].

2.3 Kohn-Sham Formalism

The Kohn-Sham approach to DFT allows an exact description of the interacting many-particle systems in terms of an effective non-interacting particle system. The effective potential in this noninteracting particle system (the Kohn-Sham system) can be shown to be completely determined by the electron density of the interacting system and is for this reason called a density functional. In particular, the ground state energy of the system is density functional. Due to the complicated nature of the many-body problem, it is difficult to determine the exact expression for the functional.

The unknown functional F[n] can be written in the form:

$$F[n] = T[n] + \int \frac{n(r)n(r')}{|r-r'|} drdr' + E_{XC}[n] \qquad \textit{Eq. 2.13}$$

where the non-interacting kinetic energy T[n] is given by:

$$T[n] = \frac{h^2}{2m}\sum_i \int \psi_i^*(r)\nabla^2\psi_i(r)dr \qquad \textit{Eq. 2.14}$$

The Kohn-Sham energy functional becomes:

$$E[n] = T[n] + \int \frac{n(r)n(r')}{|r-r'|}drdr' + E_{XC}[n] + v_{ext}(r)n(r)dr \qquad \textit{Eq. 2.15}$$

Minimizing this energy functional gives

$$\left[-\frac{1}{2}\nabla^2 + V_{eff}(r)\right]\psi_i(r) = \varepsilon_i\psi_i(r) \qquad \textit{Eq. 2.16}$$

$$\mathrm{V_{eff}}\,(\mathrm{r}) = \mathrm{V_{ext}}(\mathrm{r}) + \mathrm{V_H}[\mathrm{n}] + [\mathrm{n}]\,\mathrm{V_{XC}}\,[\mathrm{n}]. \qquad \textit{Eq. 2.17}$$

$$V_{ext}(r) = -\sum_I \frac{Z_I}{|r-R_z|}, \qquad \textit{Eq. 2.18}$$

$$V_H[n] = \frac{\partial E_{Hartree}}{\partial n(r)}, \qquad \textit{Eq. 2.19}$$

$$V_{XC}(r) = \frac{\partial E_{XC}[n(r)]}{\partial n(r)} \qquad \textit{Eq. 2.20}$$

V_{ext} (r) is the potential due to the nuclear and other external fields, V_H(r) accounts for the classical Coulomb interaction electron density. These two terms can be easily calculated hence the only unknown term in the Kohn-Sham equations is the exchange-correlation functional E_{XC}(r). Therefore, if this term is known the exact ground state energy and density can be obtained for any real system.

The local density approximation (LDA) is a simple functional that describes exchange-correlation energy. In LDA, the core idea is that if you divide space into small pieces, then the electron density $n(\mathbf{r})$ in each piece is constant and the same as that for a homogeneous electron gas. The symbolic expression of this functional is derived from a simple homogeneous electron gas model [47, 48]:

$$E_{XC}[n] = \int n(r)\varepsilon_{XC}[n(r)]dr \qquad \textit{Eq.2.21}$$

Where ε_{XC} [n(r)] is the energy per electron at point r that depends only upon the density of electrons at the same point. The exchange and correlation energy in LDA is given by:

$$E_X = -\frac{3}{4}\left(\frac{3}{\pi}\right)^{\frac{1}{3}} n^{\frac{4}{3}}V \qquad \textit{Eq.2.22}$$

$$E_C = nV.\begin{cases} 0.0311\, lnr_s - 0.0480 + 0.002 r_s lnr_s - 0.0116 r_s & if \quad r_s < 1, \\ \dfrac{-0.1423}{1 + 1.0529\sqrt{r_s} + 0.3334 r_s} & if \quad r_s \geq 1 \end{cases} \qquad Eq.2.23$$

The above *Eq. 2.21* calculates the exchange energy, and the negative sign indicates that it is attractive thereby implying a reduction in total energy. However, it sometimes underestimates atomic ground state energies and ionization energies, while overestimating binding energies for systems like semiconductors where density varies rapidly. The reason is that the energy density does not depend on density at the same point only but on density far from that point. So to overcome this another approximation is used called generalized gradient approximation[49].

LDAs assume the same density throughout the system. Because of this, the LDA tends to overestimate the exchange-correlation energy. This inaccuracy can be improved by considering the gradient of the electron density, called Generalized Gradient Approximation (GGA) Symbolically, GGA functional can be written as:

$$E_{xc}[n, \nabla n, \nabla^2 n] \qquad Eq.2.24$$

In general, GGA is more accurate than LDA when it comes to predicting bond lengths and binding energies of molecules, crystal lattice constants, etc., especially in cases where the charge density is rapidly changing. While there is only one LDA there are several

different parameterizations of the GGA[50]. A commonly used functional is the PW91 functional.

2.3.1 Hybrid Functionals

There were however still known shortcomings of the GGA functional, it lacked the correct longed-ranged behavior that a theory like Hartree-Fock had. This leads to the underestimation of the bandgap, incorrect description of reaction barriers and van der Waals interactions, and other properties due to the local nature of the functionals[51]. These functionals came about in the 90s and they were called hybrid functionals. Hybrid functionals are another approximation used to find exchange-correlation energy in DFT that incorporates an exact exchange from Hartree-Fock theory with the rest of the exchange-correlation energy from other approximation methods. They include fractions of exact Hartree-Fock exchange energy, calculated as a functional of the Kohn-Sham molecular orbitals.

$$E_X^{HF}[\{\psi_i\}] = -\sum_{i=1}^{\frac{N_{el}}{2}}\sum_{j=1}^{\frac{N_{el}}{2}}\iint \frac{\psi_j{}^*(r)\psi_j(r)\psi_j{}^*(r')\psi_i(r')}{|r-r'|}drdr' \qquad Eq.2.25$$

These have the following general form:

$$E_{XC} = (1-a)E_{XC}^{DFT} + aE_X^{HF} \qquad Eq.2.26$$

The most commonly used hybrid functional is B3LYP, which stands for Becke, 3-parameter, Lee-Yang-Parr[52].

2.3.2 Pseudopotential

In the Schrödinger equations with many electrons, dividing electrons into two groups: valence electrons and inner core electrons can greatly simplify the equations. Since electrons in the inner shells are tightly bound, they are not responsible for chemical bonding between atoms; they also partially screen the nucleus, resulting in an almost inert core[53]. The binding properties in most materials are due to valence electrons, especially in metals and semiconductors. This separation suggests that only valence electrons can be used for a large number of cases and inner electrons can be ignored, thereby reducing the number of interactions. Fermi and Hellmann were the first to propose the use of effective interaction, a pseudopotential, to approximate the potential felt by valence electrons. We need pseudopotential to use DFT for practical calculations. To reduce the numerical cost, in many DFT implementations, the external potential is replaced by the pseudopotential.

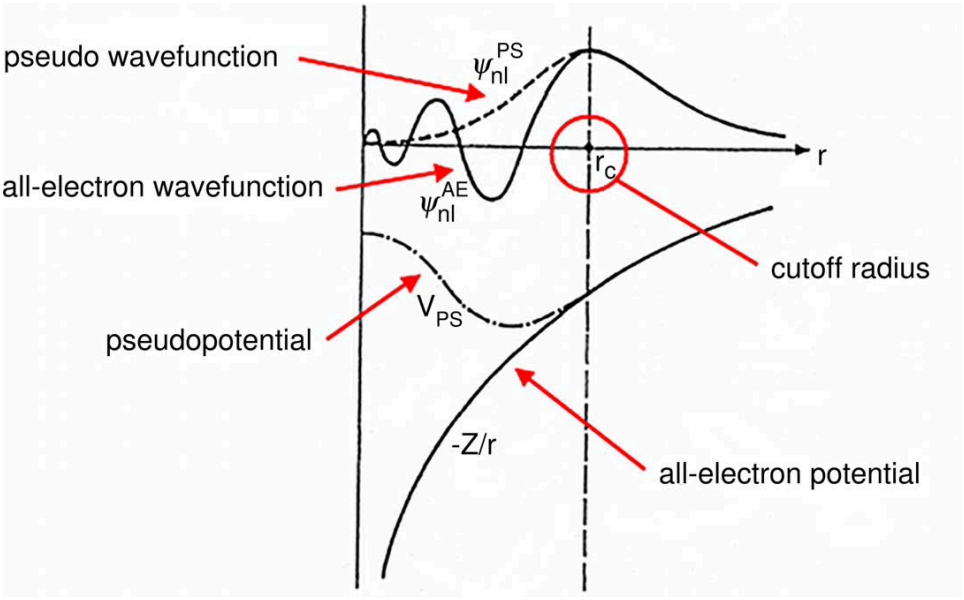

Figure 3: Wave-function in the presence of all-electron potential and pseudopotential. r_c is the cutoff radius beyond which the real and pseudopotential match

2.3.3 Brillouin Zone and k-point Sampling

Almost all of the solids that we deal are characterized by periodicity in their structures. As a result of this periodicity, our system can be reduced as small as possible for computational treatment. The solid is first reduced to a super cell composed of a large number of unit cells in this reduction procedure. The super cell can be extended to infinity using periodic boundary conditions. After this, the supercell is contained within the first Brillouin zone in reciprocal space. Using reciprocal lattice vectors G and k, all electronic wave functions are effectively mapped in the first Brillouin zone, and all properties are

represented by Bloch equations. As a result of the rotation and inversion symmetry operations, the first Brillouin zone is reduced to the irreducible Brillouin zone (IBZ) without losing any information. All of the necessary quantities are achieved by integrating the k-points which are used to map the IBZ. Because of the periodicity of the solid, we only have to deal with a bit of the k-points in the IBZ. Each point in an IBZ can represent a k-point, therefore, there are an infinite number of discrete k-vectors which can be considered to be wave-functions. Wavefunctions and other properties can now be evaluated only over the IBZ by sampling only a limited number of k-points. Monkhorst Pack method is the most commonly used method for sampling the Brillouin zone using k-points. Using this method, a rectangular grid of k-points is formed that is evenly spaced throughout the IBZ, with the columns and rows parallel to the reciprocal lattice vectors that span the BZ. For a larger supercell, a lesser or even a single point may be sufficient to depict the properties in the IBZ. The point at k=0 is the Γ point, which is having the highest weight factor and where the real and the reciprocal coordinates coincides and at this point the wave function would be real so the we don't have to consider the complex numbers. Since the computational efficiency also increases by the use of this point hence it is favorable choice for the massive calculations.

2.3.4 Basis Sets

Basis sets are sets of functions used to create the molecular orbital, which is expanded as linear combinations with coefficients to be determined. These functions are usually centered on atoms, but they have also been centered on bonds or lone pairs.

$$\psi(x) = \sum c_i \, \varphi_i(x) \qquad \textit{Eq.2.27}$$

The function Ψ is then stored as several coefficients:c_1, c_2, c_3, and so on. Unfortunately, we can only solve the Schrödinger equation to obtain nice formulae for ψ when we have a hydrogenic atom (H, He+, Li2+, Be3+). If we desire to solve the Schrodinger equation for any system with more than two particles (a nucleus and an electron) then we are forced to make guesses as to what is Ψ. The first guess would be to use functions that are similar to the formulae obtained already. We might therefore describe basis sets, very loosely, as sets of functions like s, p, d, f, etc. that describe the behavior of electrons in all systems, regardless of whether they are hydrogenic or not. The bigger and better the basis set the closer we get to ψ and hence E.

There are two types of atomic orbital functions used i.e. Slater-type orbitals and another is Gaussian type orbitals[54]. Nowadays almost everyone utilizes Gaussian functions in

basis sets. Each AO in the molecule of interest is represented by one or more Gaussian-type functions. A Gaussian type orbital can be written as follows:

$$\psi(r) = \sum_i c_i \, exp[-\alpha_i (r - R_i)^2] \qquad \textit{Eq.2.28}$$

There are thus three ingredients an exponent, α controls the width of the Gaussian, a center R controls the location, a coefficient c_i varied to minimize the energy[55]. Furthermore, basis sets consisting of sets of plane waves are often used, especially in calculations involving periodic boundary conditions. The Slater-type orbitals are closely related to the true eigenfunctions for single-electron ions, and as such have been created by chemical or physical intuition. Also, the Gaussian is well localized to specific atoms, although the potential for they are eigenfunctions is less relevant in electronic structure calculations for molecules and solids. A completely different approach was used called plane waves as basis functions (*Eq 2.29*). These are completely delocalized and can therefore not attribute to individual atoms.

$$\chi(\mathbf{r}) = e^{i\mathbf{k}.r} \qquad \textit{Eq.2.29}$$

2.3.5 Computational Implementation of DFT

The question now is how to solve Kohn-Sham equations and once it is solved then how to calculate total energy. However, to determine the eigenfunctions and eigenvalues, we first need to find the total potential in *Eq. 2.17*. The nuclear and Hartree potentials, V_{ext} and V_H come from *Eq. 2.89* and *2.19* respectively. The complication here is that V_{xc} depend on the density, n, and the density depends on the unknown eigenfunctions, through *Eq. 2.20*. In other words, we can say that all the solutions are linked to each other in KS equations. This implies that we need a step-by-step procedure to do calculations to find out total energy self-consistently.

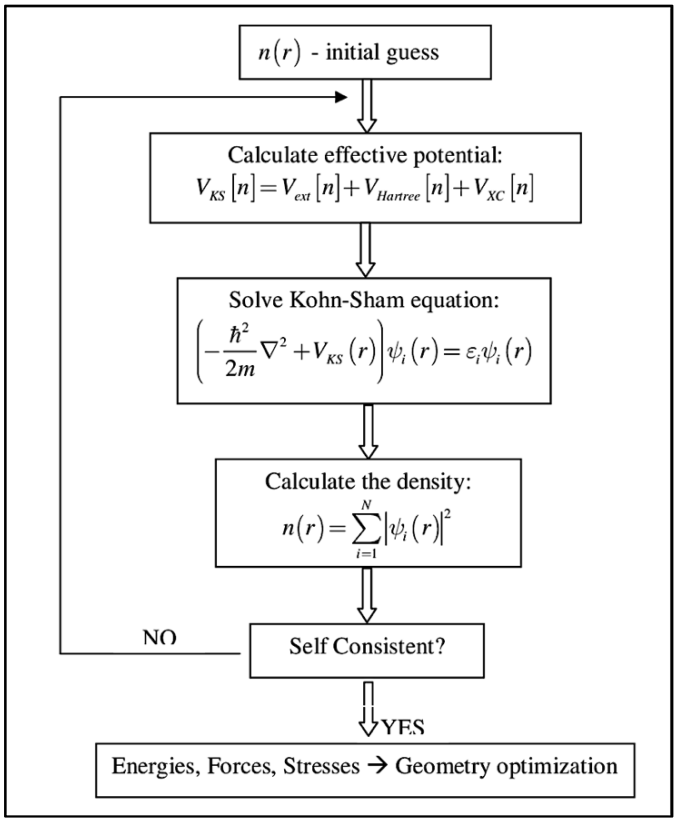

Figure 4: Schematic flow chart for finding self-consistent solutions of the Kohn-Sham equations

Electrons experience a Coulomb potential due to the nuclei. This has a known and simple form:

$$V_n = -\frac{Z}{r} \qquad \textit{Eq.2.30}$$

But this leads to computational problems. So, we use Pseudopotential which is fixed for every element of the periodic table. As we know core orbitals do not change much during

chemical interactions, valence orbitals feel the electrostatic potential of the nuclei and the core electrons so we can construct a Pseudopotential to replace the electrostatic potential of the nuclei and the core electrons. It reduces the size of the basis set needed to represent the atom (but introduces additional approximations). Moving to the first step of the figure shown we have to guess a density for which we have to use a basis set as discussed earlier. Having density, we can find out wavefunction as:

$$n(r) = \sum_i f_i \, |\psi_i(r)|^2 \qquad \textit{Eq.2.31}$$

so, we can find out density by using the trial wave function. Now the second step is to find out Hartree potential and exchange potential, which can find out using Hartree energy and LDA/ GGA approximations respectively[56].

By calculating Hartree potential and exchange potential and using Pseudopotential one can get effective potential so-called Kohn-Sham potential. $V_{xc} = dE_{xc}/dn$ contains all the many-body information. Now step by step calculations leads to a Hamiltonian with which new density and hence new wave function can be calculated and Iterations n of the self-consistent cycle will exist. In DFT, instead of using wave function, the total energy is expressed in terms of the total one-electron density. The total electron density is approximated using an approximate Hamiltonian and an approximate Hamiltonian expression. DFT methods can be very accurate for the little computational cost[45].

2.3.6 DFT and Structural Properties

The most basic type of DFT calculation is the computation of the structural properties of the given system. One can begin with electron density, then use the trial density to define the effective potential. The Kohn-sham equations with effective potential are solved self consistently till a self-consistent solution for electron density is obtained as stated earlier. The electron density so obtained has been used to calculate the ground state energy for a given system. Various methods can be used for structure optimization. The conjugate gradient is one such structure optimization method. In these calculations, one can allow the position of atoms to change keeping the shape of the supercell constant, or can allow both atoms and supercell to change. The structure corresponding to minimum energy tells us about the structural parameters (for example lattice type, lattice constant, bond length, bond angle, etc.) [39, 50].

2.3.7 DFT and Electronic Properties

The electronic density of states (DOS) is a primary measure of a material's electronic state:

ρ(E)dE= number of electronic states with energies in the interval (E; E+dE)

Once the DFT calculations have been performed, the electronic DOS can be determined by integrating the resulting electron density in k-space. There is another very important electronic property known as band structure, that can also be estimated using DFT. The

DFT does not gives us an exact band structure but gives us the Kohn-Sham band structure. The Kohn-Sham band structure is generally a one-electron band structure, which is the dispersion of the energy levels n as a function of k in the Brillouin zone. For the electron in the solid, Kohn-Sham Eigenvalues and Eigenstate do not correspond to one-electron energy states. Despite this, it is common to interpret the solutions of Kohn-Sham equations as one-electron states: the result is often a good representation, especially when it comes to band dispersion.

The main problem with the band structure is the underestimation of the bandgap. Bandgap error is not due to LDA but can be attributed to the discontinuity in the exact V_{xc}. DFT is, in principle, an exact theory that reproduces and predicts ground state properties like the total energy, the atomic structure, etc. However, Kohn-Sham-based DFT cannot investigate excited-state properties, such as a solid's band plot. Therefore, it can be said that it is not suitable for calculating band and band- plots [45, 48]. Using time-dependent DFT, the true band structure can be determined, although it can be challenging in practice. Quantum ballistic conductance of nanowires can be determined by the number of conducting band lines crossing the Fermi Energy. For each line crossing the E_f, the ballistic conductance is G_o which results in total conductance of nG_o for n numbers of bands crossing E_f. These lines arise from the atomic orbital having a significant contribution to the bands above E_f [56, 57].

2.4 Atomistic Method: Molecular Dynamics Method

In molecular dynamics (MD) simulations, the equations of motion are derived based on the force between atoms in an initial configuration to obtain the new configuration. MD calculates the movement of atoms in light of the changes in position, velocity, and orientation with respect to time. As a result, MD generates a series of configurations based on the initial configuration and velocity. MD simulates the dynamics of molecular systems by using Newton's equations of motion. The quantum behavior of each particle in the system is ignored in this method, which assumes each particle behaves as a Newtonian particle. This implies that electronic motions are ignored and that electrons stay in their ground state and adjust automatically in response to changes in atomic positions (the Born-Oppenheimer approximation)[58]. The motion of the particles can only be described using classical mechanics. This means that the equation of motion F = ma applies to particles where F denotes force, m represents mass, and a denotes acceleration. Knowing the positions and velocities of all the atoms enables predictions of system state and calculation of new positions and velocities. A trajectory of atomic motions can be obtained by repeating the procedure over and over[59]. Several numerical integration algorithms are available for calculating Newton's equations of motion.

Newton’s equations of motion are used to calculate the position and velocity of the atoms at each time step. There are four main ways of controlling the pressure, volume, temperature, energy, and enthalpy of the simulation box. The first is the NVT ensemble

which keeps the number of moles (N), the volume (V), and the temperature (T) constant. A thermostat is used to exchange energy between the system and a heat bath in order to keep the temperature constant. The second is the NPT ensemble which keeps the number of moles (N), the pressure (P), and the temperature (T) constant while the volume is allowed to fluctuate. Both a thermostat and a barostat are necessary for this ensemble. The third is the NVE ensemble which keeps the number of moles (N), the volume (V), and the total energy (E) constant. This is an adiabatic process (no heat exchange). The fourth is the NPH ensemble which keeps the number of moles (N), the pressure (P), and the enthalpy (H) constant [60].

2.4.1 The Verlet Algorithm

The Verlet Algorithm is a method for integrating Newton's equations of motion. It was originally conceived by Delambre and later rediscovered by Loup Verlet[61]. It has a simple derivation and is preferable to most other integration methods. This is because the computational cost is low (only a single calculation per time-step) and it is better at energy conservation for Lennard-Jones (LJ) type potentials than higher-order methods. The verlet algorithm uses positions and accelerations at time t and the positions from time (t-Δt) to calculate new positions at a time (t + Δt). The Verlet algorithm uses no explicit velocities. This algorithm is a two-step method because it estimates x (t + Δt) from the current position x(t) and the previous position x (t - Δt). Therefore, it is not self-starting:

initial positions x (0) and velocities v (0) are not sufficient to begin a calculation, and a backward Euler method must be done at t = 0 to get x (-Δt).

$$x\,(t+\Delta t) = \frac{1}{2}a(t)\Delta t^2 + V(t)\Delta t + x(t) \qquad \textit{Eq.2.32}$$

$$x\,(t-\Delta t) = \frac{1}{2}a(t)\Delta t^2 - V(t)\Delta t + x(t) \qquad \textit{Eq.2.33}$$

$$x\,(t+\Delta t) = a(t)\Delta t^2 - x\,(t-\Delta t)\Delta t + 2x(t) \qquad \textit{Eq.2.34}$$

This shows that velocity is not required for this calculation. Since we need the current and last positions to predict the next position this method is not self-starting. Also, the current velocity must be calculated separately. There is a form of the Verlet algorithm known as the Velocity Verlet that solves both of those issues. Velocity verlet algorithm is the complete form of verlet algorithm[62]. In this algorithm both the atomic positions and velocities are calculated at the same time. Positions and velocities at time t are used to integrate the equations of motion. In other words, positions, velocities, and accelerations at time t + Δt are obtained from the same quantities at time t.

$$x\,(t+\Delta t) = \frac{\Delta t^2}{2m}F(t) + V(t)\Delta t + x(t) \qquad \textit{Eq.2.35}$$

$$v\,(t+\Delta t) = \frac{\Delta t}{2m}[F(t) + F(t+\Delta t) + v(t) \qquad \textit{Eq.2.36}$$

2.4.2 Leap-frog Algorithm

The leap-frog algorithm is also based on two steps, like the verlet algorithm. For this algorithm, the first step is to calculate the velocities at a time (t+ Δt). Calculating the position of x at a time (x + t) requires that we use this velocity as the initial velocity. As a result, velocity leaps over positions, and then positions leap over velocity[63].

$$x(t+\Delta t) = v\left(t+\frac{1}{2}\Delta t\right)\Delta t + x(t) \qquad \textit{Eq.2.37}$$

$$v\left(t+\frac{1}{2}\Delta t\right) = v\left(t-\frac{1}{2}\Delta t\right) + a(t)\,\Delta t \qquad \textit{Eq.2.38}$$

$$v(t) = \frac{1}{2}\left[v\left(t-\frac{1}{2}\Delta t\right) + v\left(t+\frac{1}{2}\Delta t\right)\right. \qquad \textit{Eq.2.39}$$

2.4.3 Interaction Potentials

With equation 2.36, we can find the next position of a particle, but we need to know the F(t) of the particle. An important step in molecular dynamics simulation is describing the atomic interactions among molecules, called force fields. In order to model the important degrees of freedom, the force field must cover all relevant molecular interactions. It is important to evaluate the forces first before building an atomistic model. Based on the potential energy V gradient at time t, the force F_i is determined at time t. It is the force

exerted on the particle by the interactions in the system. Various potentials are used to model these interactions.

In MD simulation, Lennard-Jones potential is one of the most commonly used potentials. The Coulomb potential, ion-dipole interactions, beads-and-spring potentials, etc., are a few other potentials that can be used. The potentials can also be created based on empirical evidence or through quantum calculations. Systems are very sensitive to the interactions and can be largely determined by the potentials chosen[64]. For a given potential, the force can be calculated by:

$$\mathrm{F} = -\nabla \mathrm{U} \qquad \textit{Eq.2.40}$$

The potential energy V can be calculated as the sum of bonded and non-bonded interactions:

$$E(R) = \sum_{bonded} E_i\,(R) + \sum_{non-bonded} E_i\,(R) \qquad \textit{Eq.2.41}$$

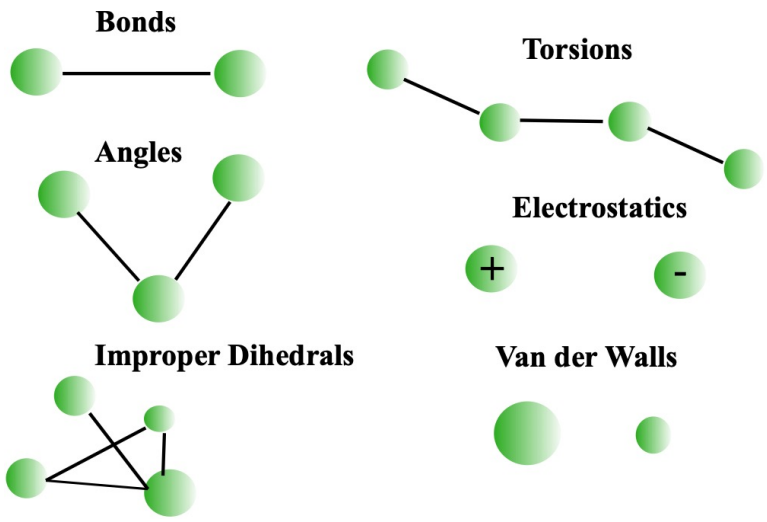

Figure 5: Force Field described in terms of Bonds, Torsions, Angles, Electrostatics, Improper Dihedrals and Van der Walls

2.4.4 Non-bonded Interactions

Non-bonded atoms have two potential functions to consider: Lennard-Jones interactions and Coulombic interactions between electrostatic charges, reflecting the van der Waals interaction between atoms. With van der Waals interactions, even atoms with no net electrostatic charge are still likely to be attracted at short distances or to repel when too close together. This potential is defined as:

$$E_{vdw} = \sum_{\substack{nonbonded \\ pairs}} \left(\frac{A_{ik}}{r_{ik}^{12}} - \frac{C_{ik}}{r_{ik}^{6}} \right) \qquad Eq.2.42$$

Where A and C are determined by experimental data and depend on the types of atoms. Electrostatic interactions involve the interaction of atom charges. Atoms with opposite charges attract each other, while atoms with like charges repel each other. There is an inverse relationship between the force of attraction and the square of the distance in this potential:

$$F = \frac{q_1 q_2}{4\pi\varepsilon_o r^2} \qquad Eq.2.43$$

2.4.5 Bonded Interactions

The interactions of bonded atoms include stretching along with the bond (E_{str}), bending between bonds (E_b), distortion along with the bond ($E_{improper}$), and torsion (E_t). E_{str} includes the energy needed to compress or stretch a covalent bond. Hooke's law for an ideal spring can approximate the energy required to stretch or compress a bond as follows:

$$E_{str} = \frac{1}{2} k_{s,ij} \left(r_{ij} - r_o\right)^2 \qquad Eq.2.44$$

The bending energy E_{bend} is the energy required to bend a bond from its equilibrium angle, θ_o. In addition to spring, you can model bending as given by Hooke's law in terms of angle

$$E_{bend} = \frac{1}{2} k_{b,ijk}\left(q_{ijk} - q_o\right)^2 \qquad \textit{Eq.2.45}$$

$E_{improper}$ is the amount of energy required to deform a planar group of atoms from its equilibrium angle, ω_o, which is normally equal to zero. Another way to model this system is by using a spring, and the energy can be calculated using Hooke's law when considering the planar angle:

$$E_{improper} = \frac{1}{2} k_{o,ijkl}\left(\omega_{ijkl} - \omega_o\right)^2 \qquad \textit{Eq.2.46}$$

E_{tor} is the energy required to rotate around the bonds. Potential that is used to model torsional interactions are:

$$E_{tor} = \sum_{1:4\ pairs} K_\phi \left(1 - \cos(n\phi)\right)^2 \qquad \textit{Eq.2.47}$$

The parameters of the force field are derived from experimental data on small molecules as well as from theoretical calculations. Crystallographic data for small molecules are generally used to determine bond lengths and angle references. Also, spectroscopic measurements of small molecules provide bonds, angles, and improper dihedral forces that describe molecular vibrations. The dihedral parameters are usually determined by quantum chemical calculations. We can also predict partial atomic charges through quantum chemical calculations. In molecular dynamics simulations, parameters for the Lennard-Jones function are typically derived from the knowledge of viscosity, diffusion,

viscosity, and heat of vaporization of small molecules which is further refined by molecular dynamics simulations[65]. For large systems in thermal simulations or elastic simulations, the OPLS (Optimized Potentials for Liquid Simulations) force field is a good choice. With OPLS, thousands of atoms can be handled relatively easily[66]. However, ReaxFF (reactive force field) is an extremely complex force field that has been proven to be effective in simulations of small elastic-plastic and reactive systems[67]. An OPLS simulations run much faster than ReaxFF simulations with the same number of atoms.

3 Optical Absorbance in Multilayer Two-Dimensional Materials: Borophene, Graphene and Antimonene

3.1 Introduction

The remarkable physical and chemical characteristics of 2D Materials have inspired considerable attention. These materials have strong in-plane chemical bonding between constituent atoms and weak interlayer interactions. Encouraged by the discovery of graphene, which is a group IV atomically thin monolayer of covalently connected sp^2 hybridized carbons[20], a large number of 2D materials have been found. Materials based on graphene have shown excellent electronic, chemical, and mechanical properties, as well as a unique combination of high thermal conductivity, electrical conductivity, and optical transparency[9, 19, 21, 22-24]. However, due to the lack of an energy difference between the valence and conduction bands (i.e., bandgap), graphene electrically acts like a metal, prompting a surge in research into field-effect transistors (FETs), optoelectronic devices, biomedical devices, chemical sensors, and conductive polymer composites[26]. Recently, new types of 2D materials have been successfully synthesized and quickly attracted widespread attention. The 2D materials that have been reported so far are mainly distributed in the main groups III (B, Al, Ga, and In), IV (Si, Ge, Sn, and Pd), V (P, As, Sb, and Bi) and VI (Se and Te) of the periodic table. In this chapter, we focus on 2D materials based on elemental Carbon (group IV), antimony (group V), and Boron (group

III) for their optical properties. Figure 6 shows the structure and schematic electron configuration of considered materials.

Antimonene, a single layer of antimony that is a member of group V in the periodic table member presents outstanding stability under ambient conditions. In a recent study, Ares et. al. reported both micromechanical exfoliation of antimony down to the single-layer regime and experimental evidence of its stability[68]. They demonstrated that single/few-layer antimony flakes are highly stable in ambient conditions showing mechanical stability upon origami nanomanipulation and no degradation over month periods. DFT simulations mimicking ambient conditions confirm the geometrical experimental findings and predict a bandgap of 1.2-1.3 eV within the range of optoelectronics applications[13, 69, 70]. They have used optical microscopy used to study the optical properties of few-layer antimonene flakes and quantitatively estimate their thickness in a fast and non-destructive way. Antimonene has been recently isolated by the liquid-phase exfoliation, which has been successfully applied to generate single- or few-layer (FL) samples of several 2D materials on a large scale[71]. The theoretical calculations [72, 73] have predicted 2D antimonene to be a narrow bandgap semiconductor with two configurations of monolayer antimonene, α-Sb, which has a puckered structure with two atomic sublayers with an indirect bandgap of ~ 0.28 eV and β-Sb, with buckled hexagonal lattice and a slightly higher indirect bandgap of ~0.76 eV. Note that β–Sb can be synthesized by various physical or chemical methods such as molecular-beam epitaxy, epitaxy growth, etc [68, 69, 74, 75].

Moreover, unlike phosphorene, atomically-flat antimonene can be grown on a lattice-matched Ag (111) substrate with hexagonal symmetry[73, 76]. It, therefore, appears that sp^2 hybridized Sb atoms form a planar graphene-like antimonene in which the lone-pair electrons on adjacent sites likely form out-of-plane nonbonding orbitals (Figure 6). However, the optical properties of multilayer antimonene have not been explored yet, so in this chapter, we will discuss the optical properties of multilayer antimonene using DFT.

The atomically thin 2D structure of the group III element boron, known as **borophene**, has an evident anisotropic crystal structure, allowing considerable optical and electronic anisotropy to be observed, as well as strong optical transparency and electrical conductivity in the direction, have been predicted[77, 78]. In its 2D lattice, several structural configurations were predicted composed of fused boron clusters forming either a stripped anisotropic structure (i.e., δ_6-borophene) [77] or an atomically flat honeycomb structure with hollow hexagons [79]. It has also been noted that boron sheets grown on Ag (111) surface are characterized as metallic β_{12} and χ_3 sheets, with β_{12} being gapless with Dirac cones [78, 80]. Both β_{12} and χ_3 sheets are atomically flat in a triangular lattice having atomic vacancies. Following the theoretical predictions of the stability of the borophene [81], its synthesis on metallic substrates including Ag, Au, and Cu [31, 82] has now extended the possibility of the realization of the boron nanostructure-based devices [83]. It is worth mentioning that, while borophene has been synthesized on metallic substrates, it has not

yet been isolated. Thus, most of the understanding of its properties arises from simulation studies based on DFT method.

The successful fabrications of borophene have inspired many follow-ups works, especially for the δ_6-borophene. This δ_6-borophene, due to its anisotropic structure, possesses the highest young's modulus of all other polymorphs whose value along one of the directions is higher than that of graphene and depicts a negative Poisson's ratio resulting from the out of plane buckling [77, 84]. The dynamic and thermodynamic instability in its free-standing form arises from its high stiffness originating from the directional bonding [85]. Owing to its anisotropic structure, however, the δ_6-borophene shows highly anisotropic metallic properties [77, 78, 86], very different from the semi-metallic graphene [19] and semiconducting transition metal dichalcogenides (TMDCs) [14]. Furthermore, the monolayer of δ_6-borophene is predicted to have high optical transparency and electrical conductivity along the un-corrugated direction, which may rival those of graphene [87]. Relative to its group-IV counterpart graphene, borophene exhibits anisotropic dependence of its electronic and magnetic properties due to its structural configuration, which can be exploited for orientation-dependent applications [86].

The unique properties of 2D materials relative to that of the bulk, in general, motivate the exploration of their layered configurations for future device fabrication[5]. Recently synthesized graphene, silicene, boron-nitride nanosheets, transition-metal dichalcogenides (TMDs), and black phosphorus possess novel properties that differ from

or exceed their bulk counterparts [5, 7, 8, 23, 88]. For example, in some of the layered metal dichalcogenides (e.g., MoS_2), the transition from an indirect semiconductor in bulk to a direct semiconductor in a monolayer[89, 90] inspires investigation into their optoelectronic properties[74]. However, scientific literature still lacks investigation of their multi-layered structures. Therefore, in this chapter, we investigate and compare the layer dependence on the optical properties of graphene, antimonene, and borophene. Since directional bonding between Sb atoms in the planar antimonene and B atoms in δ_6-borophene appears to be analogous to C-C bonds in graphene, it is of interest to examine the optical properties of multilayer borophene and antimonene vis-à-vis multilayer graphene. As it lacks one valence electron, boron has features that are similar to carbon, such as a small covalent radius and the ability to adopt sp^2 hybridization, which favors the creation of 2D boron allotropes.

In this chapter optical properties including absorption coefficient, transmittance, and reflectance, as a function of wavelength and incident energy, are studied. A key optical property in the infrared region, absorption is studied as a function of wavelength for multilayered borophene, antimonene, and graphene. Both layer- and topology dependence on the absorption spectra are investigated via a detailed analysis of the band structure. Figure 6 shows the schematic electronic configuration of the 2D graphene and its analog borophene (group-III) and antimonene (group V).

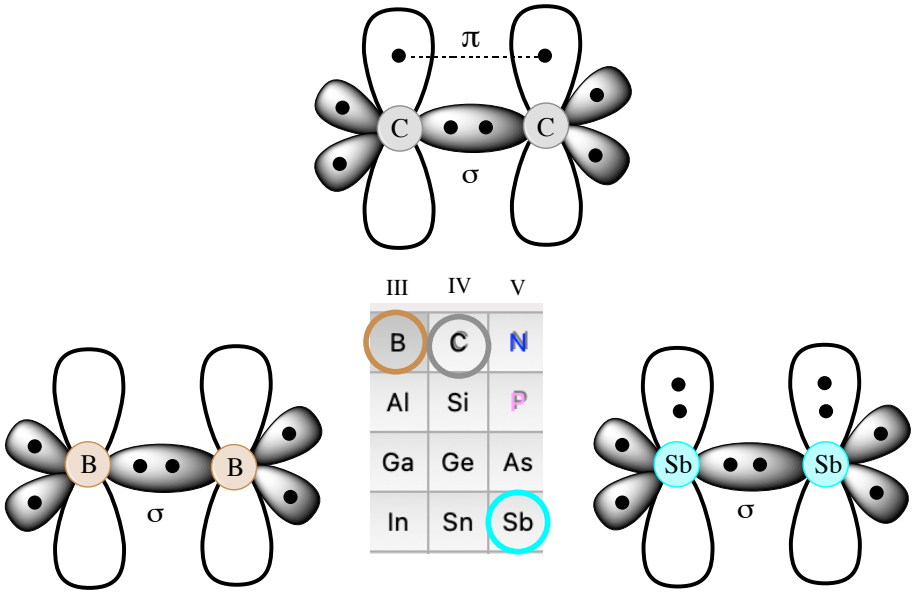

Figure 6: Schematic diagram of molecular orbitals in graphene, antimonene, and borophene. The presence of lone pair electrons forms out-of-plane nonbonding orbitals in antimonene

3.2 Computational Method

Calculations were performed by the DFT approach using the projector augmented wave (PAW) potentials as implemented in the *Vienna ab-initio simulation package* (VASP). The exchange and correlation functional were treated within the framework of generalized gradient approximation (GGA) given by the Perdew-Burke-Ernzerhof (PBE) functional [91]. Contributions from the van der Waals interactions were incorporated by using Grimme's semi-empirical dispersive D2 term [92].

A plane-wave basis set with a kinetic energy cutoff of 500 eV was used. The structural configurations were fully relaxed using the standard conjugate gradient method, with residual forces smaller than 0.001 eV/Å on each atom. The energy convergence value between two consecutive steps was chosen to be 10^{-8} eV. The Monkhorst-Pack scheme for the k-point sampling of the Brillouin zone integration was adopted with a (32×32×1) grid for the structural relaxation of graphene and antimonene multilayer systems. To eliminate the interaction with replica images in the 2D system, a periodic supercell geometry with a vacuum of about ~15 Å perpendicular to the surface was used. For the borophene, the Monkhorst-Pack scheme with a (25×40×1) grid for the k-point sampling was used as also reported previously [93].

Additional calculations for borophene have been performed using the 2×2 and 3×3 periodic supercells to assess two-atom periodic unit cell reliability and accuracy. The calculated bond lengths, band structure, and density of states nearly remain the same suggesting a periodic unit cell containing two atoms for monolayer borophene sufficient for further calculations.

Low-energy optical absorption can be measured via absorption spectroscopy [94, 95, 96-98] and calculated using the imaginary part of the dielectric function [9, 99]. Here the frequency-dependent dielectric matrix ($\epsilon_2(\omega)$) was calculated by the 'sum-over-states' (SOS) method [100].

The imaginary part of the dielectric function can be expressed as:

$$\epsilon_2(\omega) = \frac{4\pi^2 e^2}{\Omega} \lim_{q \to 0} \frac{1}{q^2} \sum_{k,v,c}^{\infty} 2\omega_k \delta\left(\epsilon_{c,k} - \epsilon_{v,k} - \omega\right) < u_{c,k+q} | u_{v,k} >< u_{v,k} | u_{c,k+q} > \qquad \textit{Eq.3.1}$$

Here, c and v refer to conduction and valence band states, respectively, k is the wave vector, $u_{v(c),k}$ represents the wave function with a periodicity of the lattice, and Ω is the volume of the supercell. To calculate the optical absorbance, the fraction of photon energy ($E=\hbar\omega$) absorbed by a multilayer system is given as:

$$A(\omega) = \frac{\omega}{c} \epsilon_2(\omega) L_z \qquad \textit{Eq.3.2}$$

where L_z is the length of a supercell in the z-direction and c is the speed of light.

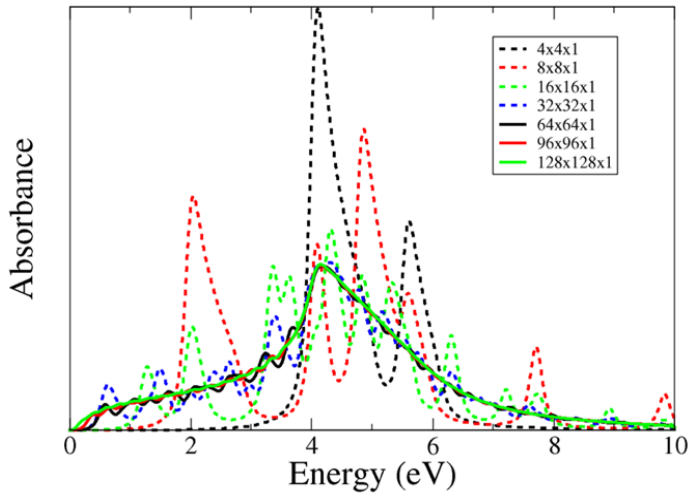

Figure 7: Absorbance vs. k-point grid for graphene

In this way, the calculated absorbance is independent of the size of the vacuum in the z-direction of the periodic supercell (Figure 8(a)) and is equivalent to the absorbance calculated using the expression $\frac{4\pi\omega}{c}\alpha_2(\omega)$ withα_2 being the imaginary part of the polarizability per unit area. For a multilayer system, the thickness is equivalent to L_z and is defined as a sum of the vacuum distance and the interlayer distance.

To accurately describe the optical spectra, k-point sampling was increased to (128x128x1) as guided by the convergence test performed on graphene (Figure 7). The convergence calculations find ≈64 states associated with the conduction band regime to be sufficient to describe low-energy optical spectra in the present study. The dependence of absorbance an $\epsilon_2(\omega)$ the vacuum distance considered in calculations is displayed in

Figure 8(b) since dielectric functions are inversely proportional to the volume of the cell in a periodic supercell method (*Eq. 3.2*).

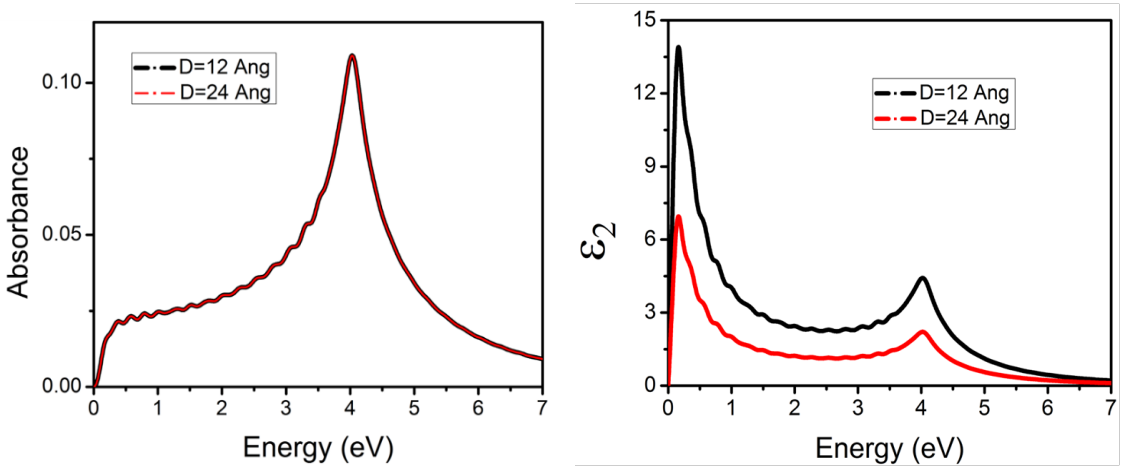

Figure 8: (a) Absorbance calculated at two different vacuum distances (D) perpendicular to the surface in the periodic supercell method employed for graphene (b) The imaginary part of the dielectric function calculated at two different vacuum distances (D) perpendicular to the surface in the periodic supercell method for graphene

3.3 Results and Discussions

3.3.1 Graphene

DFT calculations were first performed on multilayer graphene for which the experimental low-energy absorption spectrum is known in the literature [73, 101]. In our work, we find the energetically preferred configurations to be AB-stacked for bilayer (2L), ABA-stacked for trilayer (3L), and ABAB-stacked for a quad-layer (4L) at the DFT (PBE)+D2 level of theory (Table 1). It is worth noting that multilayer graphene exhibits distinct optical conductivity for Bernal (ABA) and rhombohedral (ABC) stacking in infrared absorption spectroscopy measurements [98]. Further, trilayer graphene also exhibits distinct electronic structures for different stacking (AAA, ABA, ABC) as measured with NanoARPES [102] and calculated using the tight-binding method [103].

The calculated optical absorbance properties of multilayer graphene in terms of absorbance and % Transmittance (i.e. %T=antilog(2-absorbance)) are shown in Figure 9(a). Here 1L is monolayer, 2L is AB-stacked bilayer, 3L is ABA-stacked trilayer and 4L is ABAB-stacked graphene. In the IR region, the absorbance of monolayer graphene is nearly constant (~2.3%), which agrees well with experiments [73, 101] and the calculated results obtained using the imaginary part of polarizability per unit area [22].

Table 1: Multilayer graphene: Total energy, interlayer distance, and interlayer binding energy values calculated at PBE+D2 level of theory. The interlayer binding energy is calculated as (E_n - $nE_{monolayer}$).

Planar configurations	Total energy (eV)	Interlayer distance (Å)	Interlayer binding energy (eV)
Monolayer	-18.56	---	---
Bilayer - AA	-37.19	3.51	0.07
Bilayer - AB	-37.22	3.24	0.1
Trilayer - AAA	-55.83	3.51	0.15
Trilayer -ABA	-55.89	3.24	0.21
Trilayer -ABC	-55.88	3.24	0.20

For graphene, the out-of-plane polarization component of the electromagnetic field for absorbance is nearly zero in the visible spectrum, suggesting that it is optically transparent (Figure 10). On the other hand, the in-plane polarization component of the electromagnetic field for absorbance is large and is mainly attributable to the atomic thickness of monolayer graphene. The most prominent absorption band appears at ~4 eV (≈310 nm) (Figure 10), which is consistent with the results of previous studies [96]. The increase in the intensity of the ~4eV band with the number of layers is likely due to the availability of a larger number of bands associated with the inter-band transition at the M point (Figure 11). In the 1.77-3.1 eV (i.e., 700-400 nm) region, a relatively small increase in transmittance is predicted (Figure 9(b)) and is consistent with experiments [94, 102, 104].

As thickness increases, the nonlinear behavior of transmittance can be seen in multilayer graphene. For λ = 300 nm and 800 nm (Figures 9 (c) and (d)), a linear decrease in transmittance in going from monolayer to bilayer is noticed. Beyond n=2, the transmittance shows a small nonlinearity which is relatively pronounced for 300 nm.

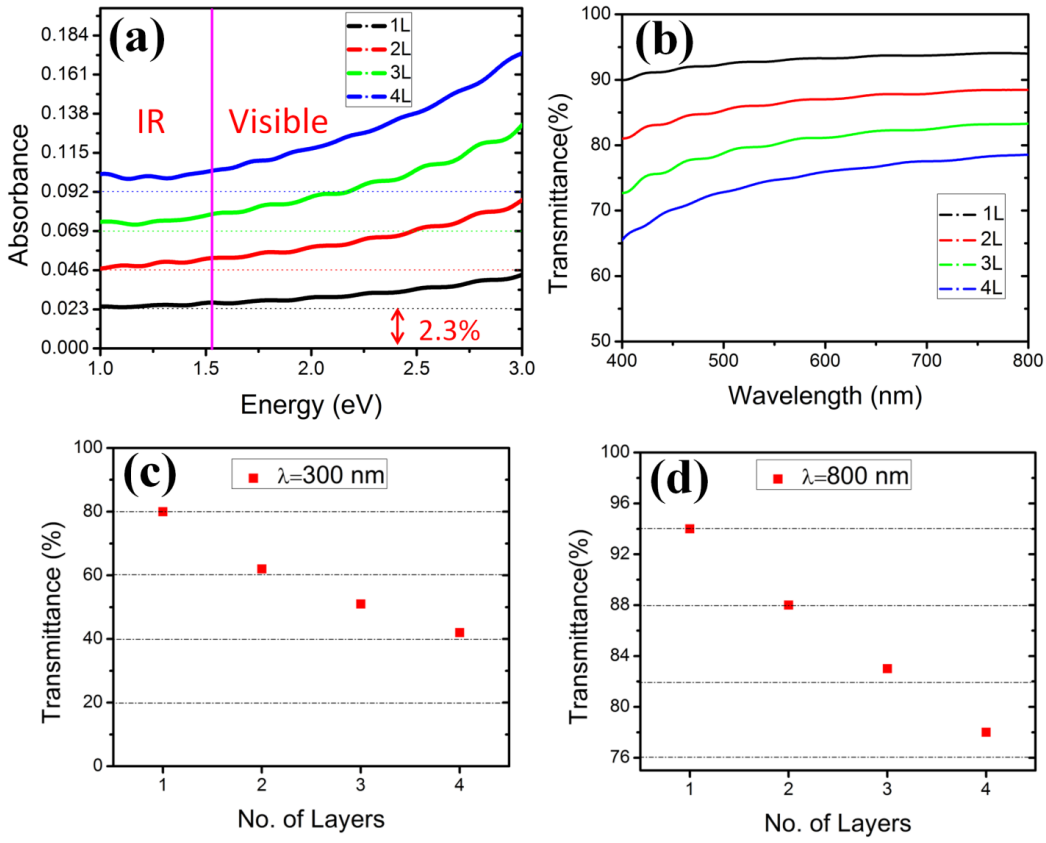

Figure 9: Multilayer graphene (1L-monolayer, 2L-AB-stacked bilayer, 3L-ABA-stacked trilayer, and 4L- ABAB-stacked): **(a)** Absorbance as a function of the number of layers. **(b)** % Transmittance as a function of the number of layers. The calculated % Transmittance at **(c)** 300 nm and **(d)** 800 nm, as a function of the number of layers

The calculated results affirm the observation of the nonlinear behavior of transmittance of white light for 5-layer graphene [94]. Overall, the transmission was reduced to ≈79% for 800 nm, ≈74% for 532, and ≈40% for 300 nm in ABAB-stacked 4L relative to that of the monolayer. Next, we calculate the frequency-dependent refractive index given by the expression, $n(\omega) = \frac{1}{\sqrt{2}}\left[\epsilon_1 + \sqrt{\epsilon_1^2 + \epsilon_2^2}\right]^{\frac{1}{2}}$. The real part of the dielectric function (ε_1) is obtained from the imaginary part of the dielectric function (ε_2) using the Kramers-Kronig relations [105]. n(ω) exhibits a large increase in going from single to the bilayer, then shows reduced increases upon successive addition of layers (Figure 12).

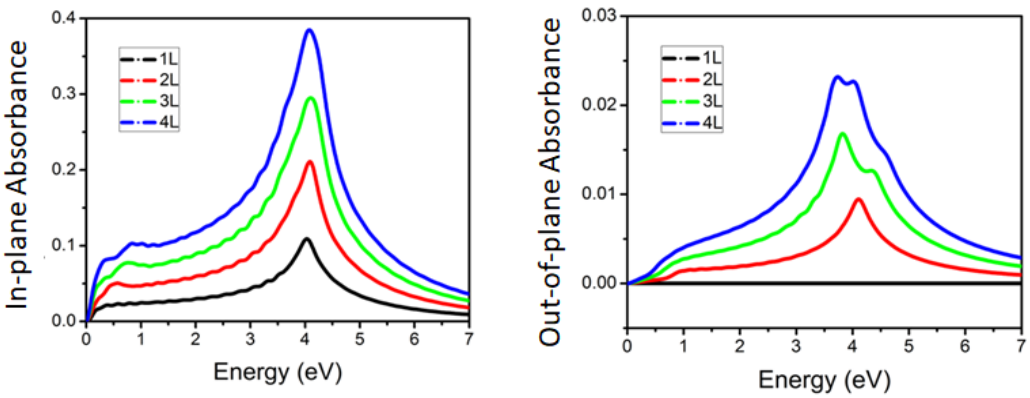

Figure 10: In-plane and out-of-plane polarization components of the electromagnetic field for absorbance of multilayer graphene. 1L is monolayer, 2L is AB-stacked bilayer, 3L is ABA-stacked trilayer and 4L is ABAB-stacked graphene

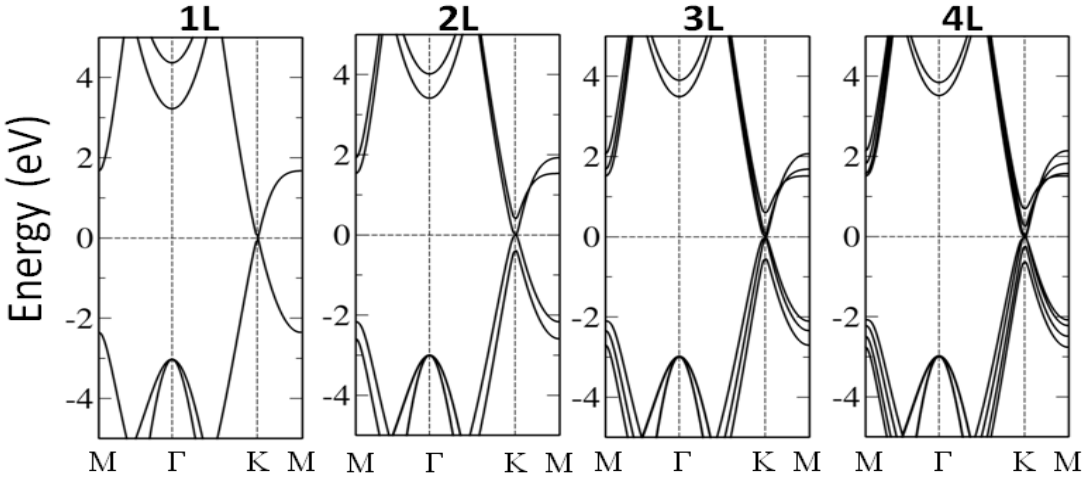

Figure 11: Calculated band structure of monolayer (1L), bilayer (2L, AB-stacked), trilayer (3L, ABA-stacked), and quad-layer (4L, ABAB-stacked) of graphene

In multilayer graphene, a weak interlayer interaction allows a variety of stacking patterns to be formed; bilayer graphene can be arranged in either AB (Bernal) or AA (hexagonal) stacking configurations, whereas trilayer graphene may exist in ABA (Bernal), ABC (rhombohedral), or AAA (hexagonal) stacking configurations [106]. ABA-stacked trilayer graphene is predicted to be energetically stable as compared to ABC and AAA stacked trilayers. The energy difference (ΔE) is ≈4 meV and ≈51 meV for ABC- and AAA-stacked trilayers, respectively. Despite a rather small ΔE among the three stacking configurations, noticeable differences are seen in their IR absorbance, which suggests that the optical response can be influenced by topology (Figure 13). For example, the ABC-stacked trilayer shows a prominent absorption band at 0.45 eV (≈2.75 μm) with absorbance significantly higher than that of the AAA-stacked trilayer (Figure 13-inset).

It should be noted that thermal effects, which were not included in the present study, can be a factor in modifying absorbance below 0.1 eV (≈12 μm).

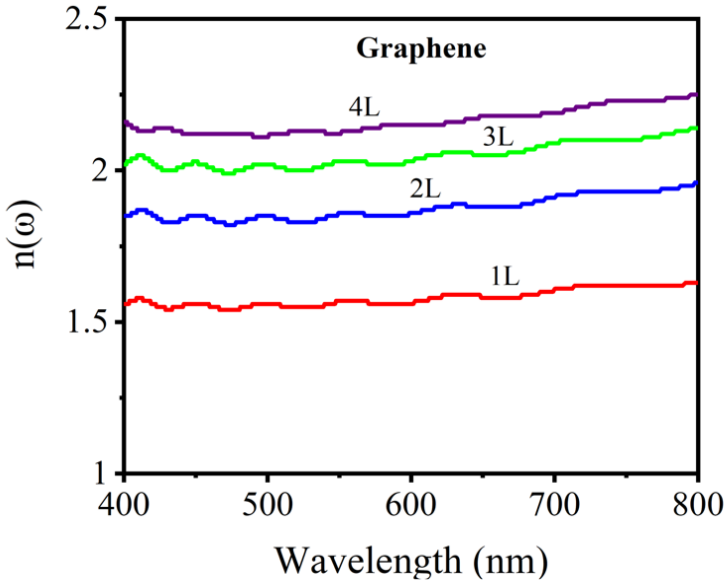

Figure 12: The refractive index as a function of layers calculated for multilayer graphene. (1L-monolayer, 2L-AB-stacked bilayer, 3L-ABA-stacked trilayer, and 4L- ABAB-stacked)

To obtain further insight into the stacking-dependent absorption, we also calculated the low-energy electronic band structure around the K-point (Figure 14). Here, the AAA-stacked trilayer shows a distinctly different electronic structure than ABA or ABC stacked trilayer. The band structure of AAA-stacked graphene can be seen as a superposition of bands associated with individual layers, showing three Dirac cones near the Fermi level (Figure 14(c)). Due to a highly symmetric stacking pattern, the middle

layer of graphene interacts equally with the top and the bottom layer, which results in a delocalized charge distribution associated with the middle layer. These results are in agreement with those reported in previous theoretical studies [96-98, 107].

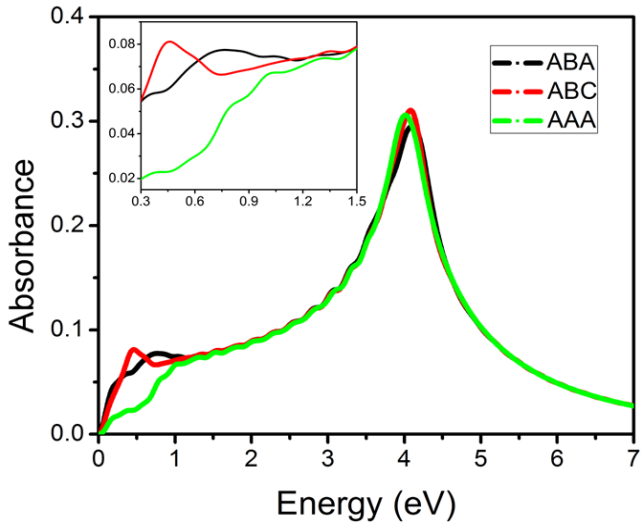

Figure 13: Absorbance with inset focusing on the mid-IR spectral region of trilayer graphene

There exist two pairs of energy bands associated with VBM and CBM near the Fermi level for ABA stacking, and only one pair for ABC stacking. The other pair of bands associated with VBM and CBM moves away from the Fermi level which may lead to the prominent absorption at 0.45 eV as seen in Figure 14(b). These stacking-dependent features may likely be associated with the number of uncoordinated atomic sites in adjacent layers; ABA stacking has two equidistant layers (top and bottom layers). This is reflected in the calculated charge density difference, $\Delta\rho = \rho_T - \left(\rho_{\frac{AB}{AA}} + \rho_{\frac{A}{C}}\right)$ where ρ_T is

total charge density of trilayer system, $\rho_{AB/AA}$ is charge density (Figure 15). A weak interlayer coupling between layers is seen in the charge density difference profile of AB or AA bilayer and $\rho_{A/C}$ is the charge density of the top A or C layer of trilayer graphene.

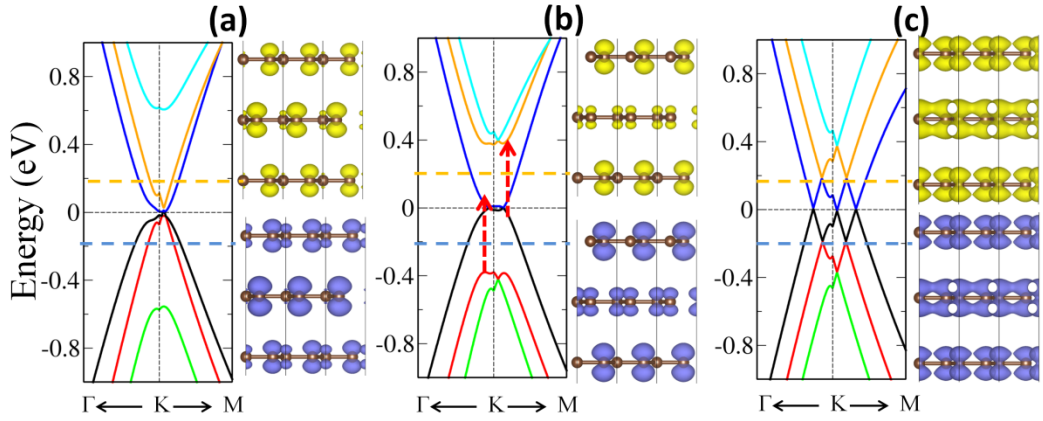

Figure 14: Calculated band structure and charge density associated with VBM and CBM for (a) ABA- (b) ABC- and (c) AAA- stacked graphene. Horizontal dashed lines represent charge density contributions in the vicinity of K, and vertical arrows show interband transit

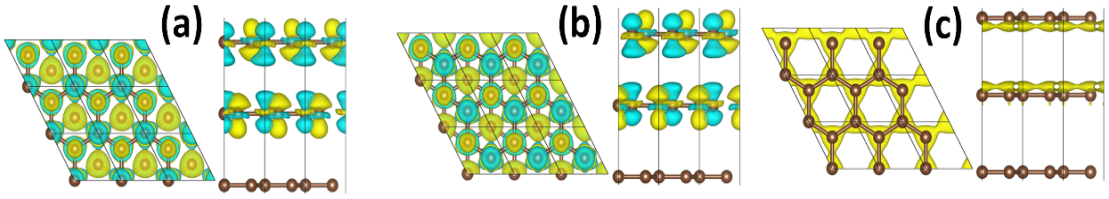

Figure 15: The charge density difference plots for (a) ABA- (b) ABC- and (c) AAA-stacked graphene obtained by using the expression $\Delta\rho = \rho_{Trilayer} - \left(\rho_{\frac{AB}{AA}} + \rho_{\frac{A}{C}}\right)$, The charge density profiles are obtained at the isosurface of 10^{-4} e/Å^3

3.3.2 Antimonene

The planar antimonene is semi-metallic [108] and, unlike graphene, its absorption spectrum shows a relatively larger increase in absorbance in going from near-IR to the visible region (Figure 16). Absorption increases linearly with photon energy, though a small absorption band appears at 1.2 eV (≈ 1 μm) with an absorbance of nearly 4%. This band is attributed to the interband electronic transition from the valance band maximum (VBM) to the conduction band minimum (CBM) along the M-K-Γ direction. Note that the buckled antimonene shows negligible absorption in the visible region [109], whereas relatively small visible light absorption is predicted for multilayer buckled antimonene [110]. For (atomically-flat) multilayer antimonene, Table 2 shows the stacking configurations to degenerate with $\Delta E \leq 13$ meV, although AA-stacked bilayer and AAA-stacked trilayer can be considered as the energetically preferred configurations. Previously, the buckled multilayer antimonene was predicted to prefer ABC-stacking, though decreasing its interlayer separation, leads to either AAA- or ABA-stacking configurations with the energy difference of 113 meV/atom [111].

Table 2: Multilayer antimonene in planar configurations: Total energy, interlayer distance, and interlayer binding energy values calculated at the PBE+D2 level of theory

Planar configurations	Total energy (eV)	Interlayer distance (Å)	Interlayer binding energy (eV)
Monolayer	-7.23	---	-----
Bilayer - AA	-15.69	3.0	-1.24
Bilayer - AB	-15.56	2.9	-1.11
Trilayer - AAA	-23.54	3.51	-1.86
Trilayer -ABA	-23.45	3.37	-1.77
Trilayer -ABC	-23.41	3.40	-1.73

We find that the calculated transmittance decreases as thickness increases in going from monolayer to trilayer (Figure 17(a)). The decrease in transmission in trilayer relative to monolayer is about ≈25% for 400 nm and about ≈10% for 800 nm. The calculated refractive index of the planar antimonene varies with the thickness (Figure 17(b)) in contrast to the results obtained for multilayer graphene. At 400 nm, the calculated refractive index is 2.12 for monolayer and 2.2 for bilayer/trilayer antimonene. Note that the refractive index of the buckled β-antimonene is reported to be 2.0 for the UV spectral region [13].

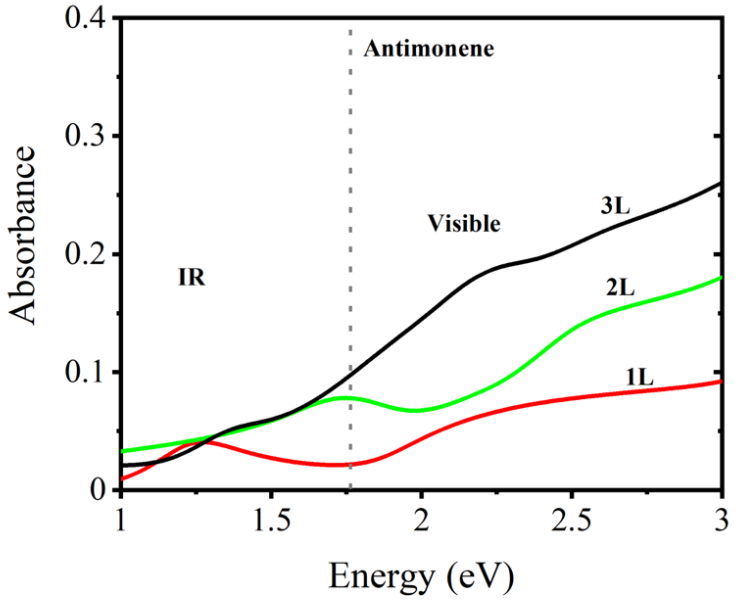

Figure 16: Antimonene: absorbance as a function of the number of layers

The topological dependence of the optical absorption calculated for trilayer antimonene is shown in Figure 18. The absorption band in the visible region is at about 2.2 eV (≈ 0.56 μm) in AAA, 2.3 eV (≈ 0.54 μm) in ABA and 2.0 eV (≈ 0.62 μm) in ABC stacked configuration, while a noticeable IR absorption at ~0.5 eV (≈2.5 μm) appears only for ABA-stacked antimonene. To understand these features, we examine the low-energy electronic band structure along the Γ-K-M direction together with the partial density of states Figure 19. The ≈2.5 μm bands are likely associated with the interband transition along the K-M direction for ABA-stacked antimonene. Analysis of the partial density of states suggests this transition be associated with electric dipole allowed s → p transition in ABA-stacked antimonene. Note that a significant increase in the number of bands

available for transition in trilayer antimonene leads to higher absorption compared to that calculated for the bilayer antimonene.

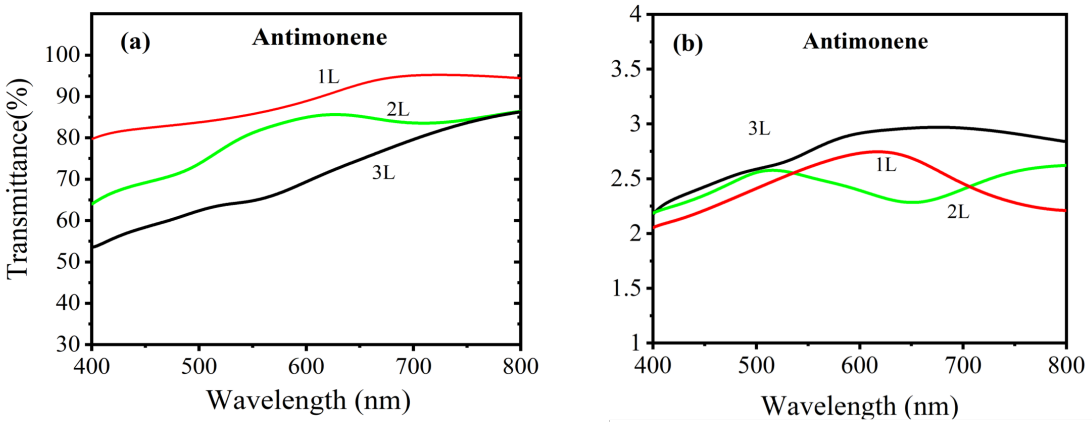

Figure 17: (a) The calculated % transmittance in the visible region as a function of the number of layers for multilayer antimonene. (1L-monolayer, 2L-AB-stacked bilayer, 3L-ABA-stacked trilayer, and 4L- ABAB-stacked) (b) The refractive index as a function of layers calculated for multilayer antimonene

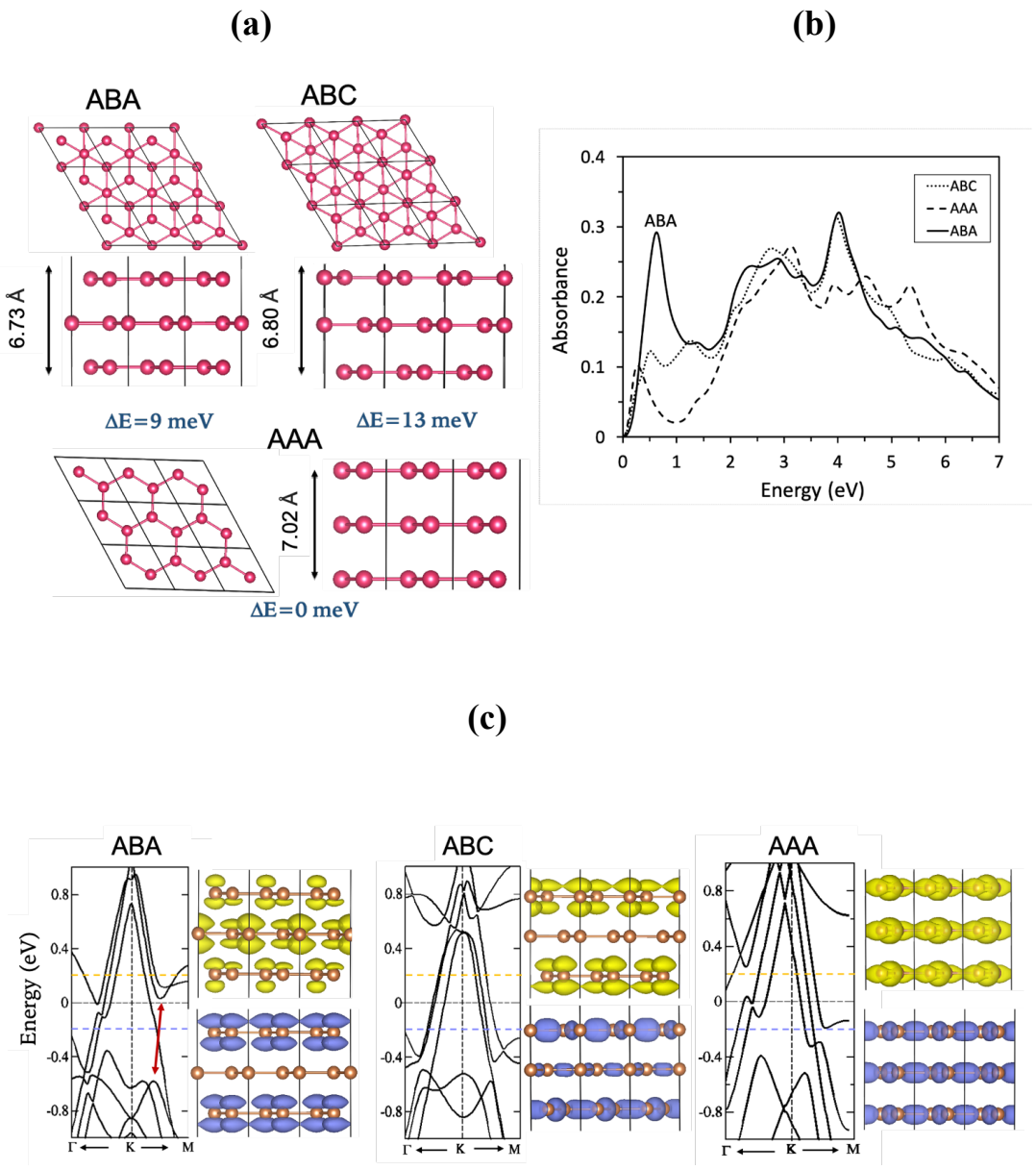

Figure 18: Trilayer antimonene: (a) Top and side views of stacking configurations (b) absorbance (c) Horizontal dashed lines represent charge density contributions in the vicinity of K, and vertical arrow show possible interband transitions in the trilayer

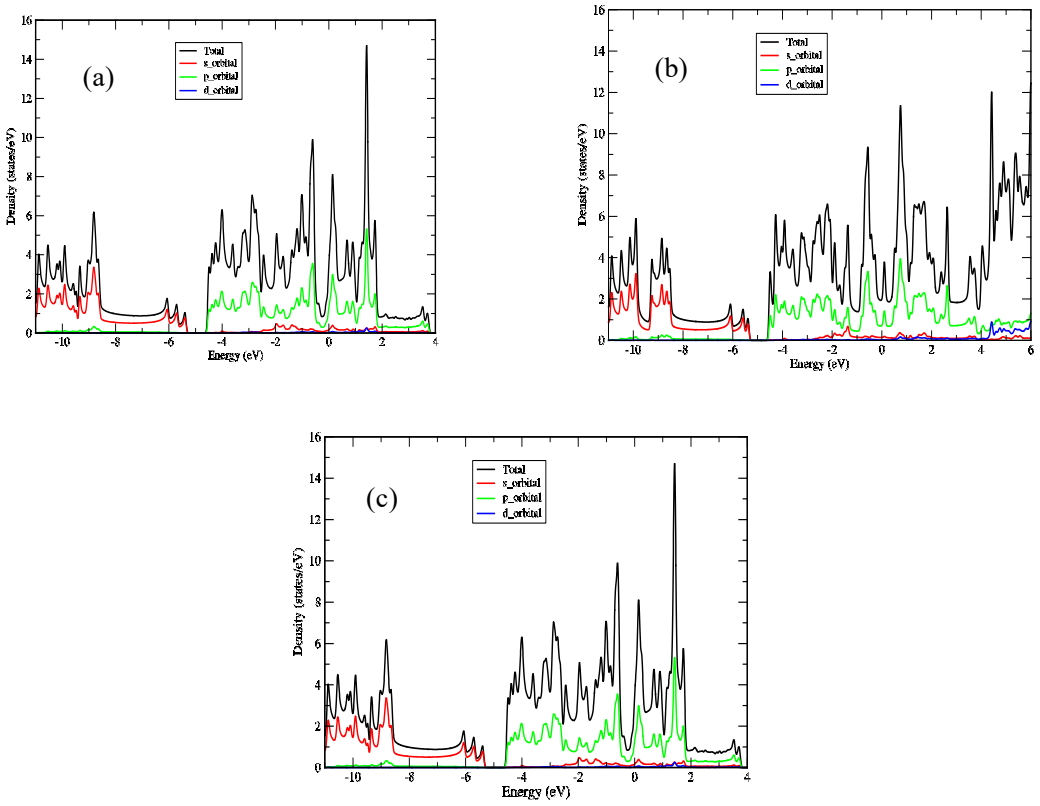

Figure 19: (a) Calculated projected density of states for (a) ABA- (b) ABC- (c) AAA-stacked trilayer antimonene. Zero is taken to be Fermi energy

3.3.3 Borophene

Figure 20 (a) shows the ball and stick representation of the multilayer δ_6-borophene. Unlike the planar hexagonal configuration of graphene, δ_6-borophene adopts a buckled triangular structure. Its space group is *Pmmn* with two B atoms per unit cell [77]. As is shown, the parallel linear chains of B–B bonds exist along its armchair direction while buckling occurs along its zigzag path. In the equilibrium configuration of a monolayer,

the calculated lattice constants, $a = 2.87$ Å, and $b = 1.61$ Å, agree with previously reported theory and experiment [77, 112] values. The bond length along the b direction (i.e., B_1–B_1 or B_2–B_2) is 1.61 Å, and B_1–B_2 is 1.87 Å.

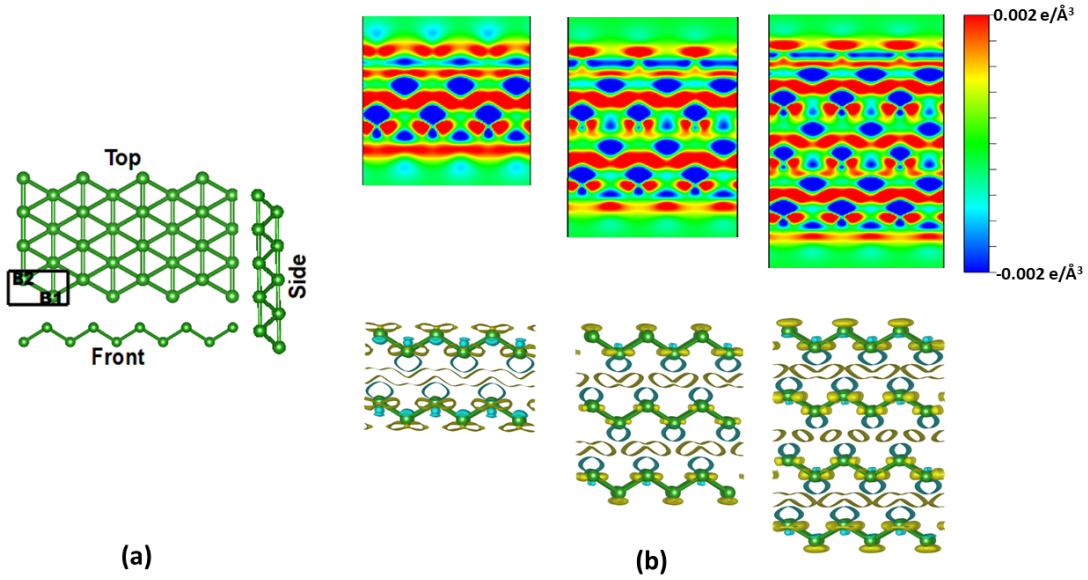

Figure 20: (a) The top, side, and front views of monolayer borophene. The atoms occupying the B1 and B2 sites are on different planes. A rectangular box represents the unit cell. (b) The 2D cross-sectional display of the charge density difference plot along the xz direction for the bilayer, trilayer, and quad-layer of borophene. The iso-value for the electron density is 0.002 e/Å^3. The yellow (cyan) represents charge accumulation (depletion)

Table 3: Multilayer borophene: The interlayer distance ($R_{interlayer}$) and the interlayer binding energy ($BE_{interlayer}$) are calculated at the PBE+D2 level of theory. $BE_{interlayer} = E_n - nE_{monolayer}$ with n=2,3,4

Borophene	**$R_{interlayer}$ (Å)**	**$BE_{interlayer}$ / atom (eV)**
Monolayer	---	---
Bilayer - AA	2.58	0.05
Trilayer - AAA	2.63	0.09
Quad-AAAA	2.60	0.10

We follow the previously obtained DFT results [113] for the bilayer configuration, which reported the AA stacking sequence as the energetically preferred configuration. Subsequently, we consider the stacking sequence of AAA and AAAA for trilayer and quad-layer borophene. Table 3 lists the interlayer binding energy and interlayer distances obtained after performing constraint-free optimization of multilayer borophene.

The charge density difference plots for the bilayer, trilayer, and quad-layer show a noticeable change between the layers indicating the presence of the interlayer interaction (Fig. 20 (b)). The calculated interlayer separation is 2.58, 2.63, and 2.60 Å for bilayer, trilayer, and quad-layer borophene. This separation is comparatively smaller than that of the other 2D materials, e.g., ~3.1 Å for bilayer phosphorene [6] as well as bilayer MoS_2 [114]. Therefore, the results find that the interlayer interaction in layered borophene is slightly higher than in the other 2D layers.

Figure 21 shows the band structure of multilayer borophene computed within the DFT approximation. For the monolayer, two bands cross the Fermi energy at distinct locations in the Brillouin zone, suggesting this to be metallic in agreement with previous calculation [96], with a noticeably wide energy gap of 4.3 eV in the band structure at Γ (Γ-Y direction). More bands cross the Fermi level for the multilayer cases because of the band splitting due to interlayer interactions retaining the metallic nature with increasing thickness. We note that the local energy gaps resulting from the buckling at Γ and S still exist. The energy gap at the Γ point (Γ-Y direction) decreases from 4.32 eV (monolayer) to 2.12 eV (quad layer) as a result of the increasing band splitting with the increasing thickness. Since no splitting exists at the S point, the energy gap at this high symmetry point barely changes from monolayer to quad-layer. One, therefore, expects the multilayer borophene to exhibit highly anisotropic electronic properties, including confinement of electrical conductivity along the un-corrugated direction. The band splitting around Γ along the Y-Γ direction near Fermi can estimate the strength of the interlayer interaction in multilayer borophene relative to other 2D layered materials, such as MoS_2 and black phosphorous. Our calculated band splitting for borophene is ~4eV, higher than ~ 1 eV in bilayers of MoS_2 and black phosphorus [115], suggesting that the interlayer interaction in the former is more substantial than those in the other 2D materials.

The partial density of states (PDOS), representing the relative contribution of each orbital to the total DOS, also reflects the changes that occurred in going from monolayer to quad-

layer (Figure 21). For example, a shift in the peak positions in the valance band is accompanied by an increase in the number of bands in the band structure of multilayer borophene.

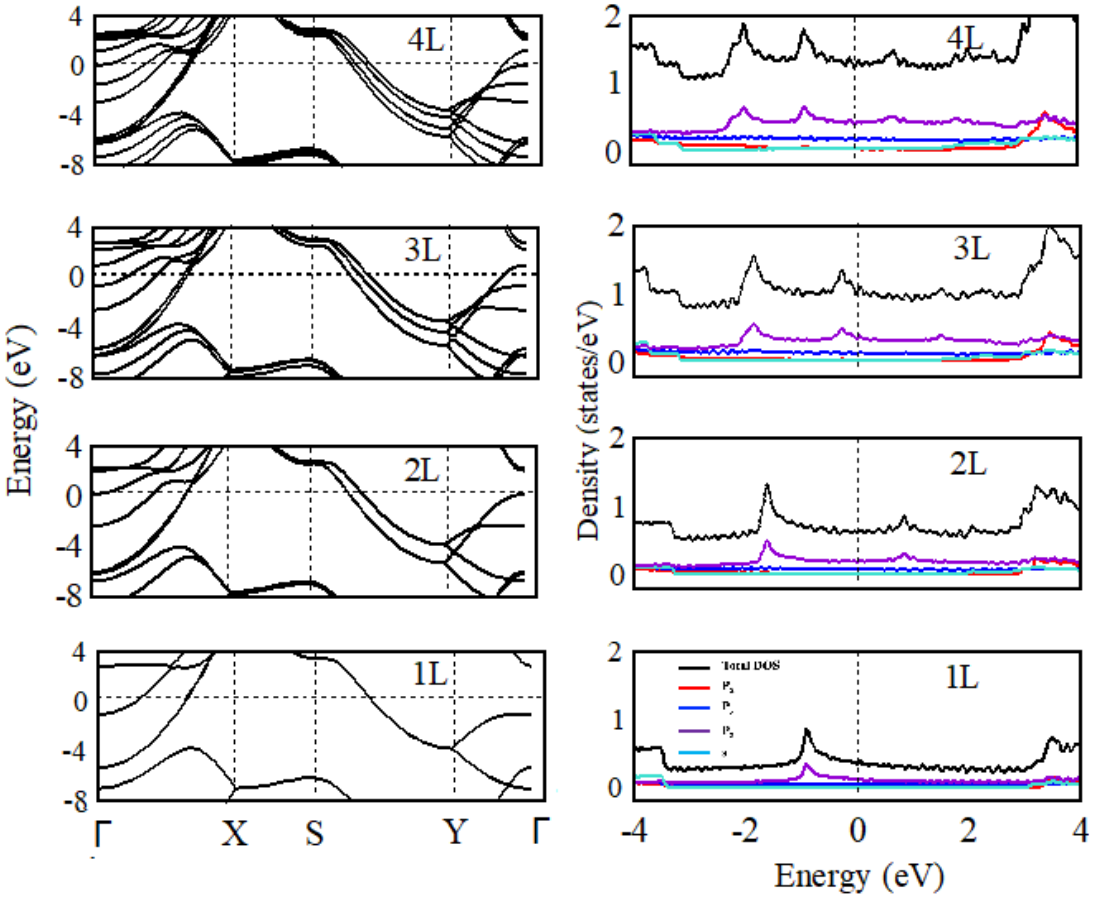

Figure 21: The calculated band structures and partial density of states for monolayer, bilayer, trilayer, and quad-layer (bottom to top) borophene, respectively. Zero of the energy is taken to be the Fermi energy of the system

Considering the enhanced stability and the modifications in the electronic properties of borophene with an increasing number of layers, it is worthwhile to examine their effects

on the optical properties, specifically the optical absorbance, shown in figure 22. It is clear from the figure that the in-plane absorbance (for X and Y polarized light) shows broad transparency in the visible region between ~1.8-3.1 eV with less than 0.2% absorbance. For monolayer borophene, the results agree with the previously published results [93] and the results obtained using the imaginary part of polarizability per unit area [22, 90].

With an increase in the number of layers, a broad shoulder appears at about ~2.6 eV in the X direction, specifically for tri- and quad-layer structures, which is likely associated with an intra-band transition between the partially occupied bands along the Γ−X direction (Figure 21). Furthermore, the anisotropic structure is reflected in the calculated absorbance with the X-component, which though still remarkably low, shows a significant layer dependence in the UV region.

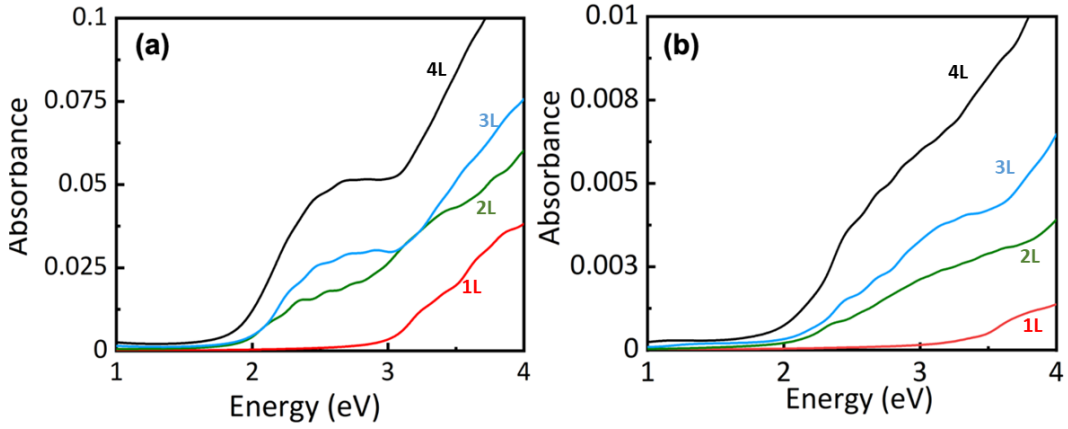

Figure 22: Multilayer borophene: (a) X and (b) Y (in-plane polarization) component of the electromagnetic field for absorbance as a function of the number of layers (1L-monolayer, 2L-AA bilayer, 3L-AAA trilayer, and 4L-AAAA quad layer).

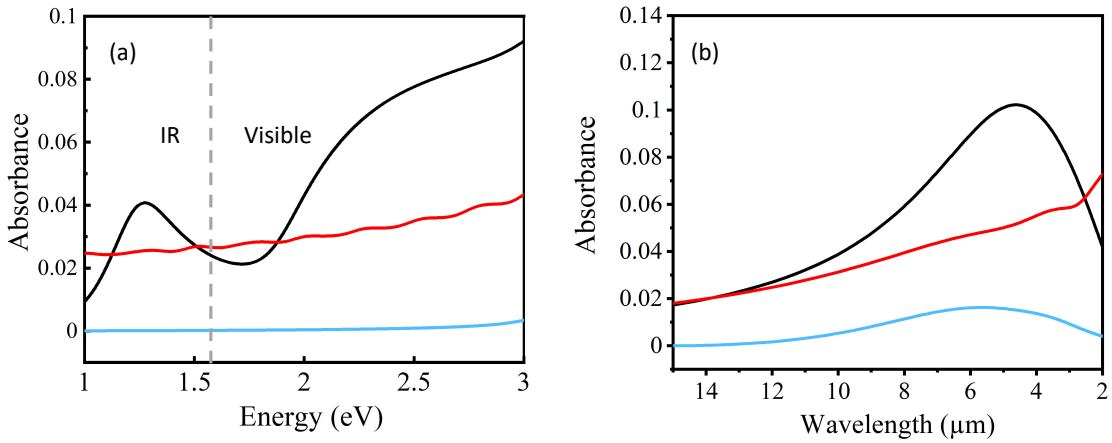

Figure 23: (a) Absorbance of monolayer graphene, (atomically-flat) antimonene, and δ_6-borophene (b) IR absorbance of trilayer graphene, (atomically-flat) antimonene, and δ_6-borophene. Color code: graphene in red, antimonene in black, and borophene in blue.

The low-energy absorbance calculated for graphene, antimonene, and borophene is compared in figure 23. Although graphene and antimonene both are semi-metallic, and borophene is metallic, a significant difference in their optical absorption is expected since the electronic configurations of C: [He] $2s^2 2p^2$, Sb: [Kr] $4d^{10} 5s^2 5p^3$ and B: [He] $2s^2$ $2p^1$ differ significantly. In graphene, each C atom forms a covalent (σ) bond with each of its neighbors together with a π-bond oriented out-of-plane. On the other hand, in the case of antimonene, the out-of-plane component is the lone-pair electron on Sb atoms (Figure 6), which may interact weakly with neighboring atoms as compared to the π-orbital interaction in the case of graphene, leading to the calculated difference in the absorption spectra of graphene and antimonene. However, borophene forms a covalent bond with its neighbor and does not have extra out-of-plane electrons which affect the absorbance, and hence it shows transparent behavior.

The difference in the electronic configurations of C, Sb, and B is reflected in absorption in the visible spectral region where antimonene absorbs significantly higher than graphene and borophene; at 3 eV, absorbance is 3%, 9%, and 1% for graphene, antimonene, and borophene respectively. The difference is further enhanced in the IR spectral region where a prominent, broadband appears at ≈ 4 μm for trilayer antimonene. This is not the case with trilayer graphene and borophene for which a nearly linear decrease in absorption is predicted ranging from 2 μm to 15 μm. This suggests that multilayer antimonene could be a good candidate as a Mid-IR tunable laser absorber.

3.4 Conclusion

In conclusion, absorbance in (atomically flat) multilayer antimonene (group V), and borophene (group III) is calculated to be comparable to or greater than that for multilayer graphene (group IV). The electrical and optical properties of graphene, antimonene, and borophene are found to be significantly dependent on the number of layers. Specifically, the IR absorption in antimonene is significantly higher than that in graphene, with a prominent band at about 4 μm associated with the dipole-allowed interband transitions in trilayer (atomically flat) antimonene. However, in contrast to graphene and antimonene, multilayer δ_6-borophene shows highly anisotropic electronic and optical properties. Due to the anisotropic structure, absorption for multilayer borophene is found to be higher in the X-direction relative to the Y direction, enabling the fabrication of performance-controlled optoelectronic devices. Optical transparency (nearly 100% transmission) in borophene is predicted up to roughly 3 eV in the visible region. Moreover, a large splitting of ~1.7 eV at Γ directs toward significant interlayer interactions in multilayer borophene relative to the other multilayer 2D materials. Overall, our study suggests multilayer graphene and antimonene be good optical absorbers, especially in the IR region of the spectrum, and can be potentially used as a coating for protection against mid-IR tunable lasers. Furthermore, the fabrication of antimonene/semiconductor heterostructures may open up the possibility of nanoscale applications for energy storage applications. Combining the good metallicity with such high optical transparency could make borophene a good candidate as a transparent conductive 2D material with possible

applications in photovoltaics and touch screens. Our study indicates that borophene can function as a transparent electrode and will complement graphene in the library of possible two-dimensional materials for optoelectronic devices.

In summary, our results suggest that multi-layered 2D materials such as graphene, antimonene, and borophene are promising for integrating optoelectronics into high-performance devices.

4 Mechanical Response of Polymer Epoxy/BMI Composites with Graphene and Boron Nitride Monolayer from First Principles

4.1 Introduction

In a fiber-polymer composite system, the fibers play an important role as load-bearing components and the polymer matrix provides support to the fibers by maintaining their orientation in the composite. In recent years, the use of carbon nanotubes (CNT) as a fiber element has helped to make significant advances in transport technology due to its low weight to stiffness ratio, resistance to environmental impact, and processability [116-118]. The C-C covalent bond in the carbon rings, which is regarded as the most stable chemical bond in nature, endows graphitic surfaces with excellent mechanical properties [119], thereby making them promising candidates for the next generation of high-performance composites. For example, Young's modulus of CNTs with a density of 1.33g/cm^3 can be as high as 1 TPa [120]. Therefore, focused scientific efforts have been invested in engineering CNT-based composites that exploit the outstanding mechanical properties of individual CNTs. However, the stiffness and strength of individual CNTs have generally not transferred well to large-scale assemblages.

To address the above-mentioned challenge, both experimental [121, 122] and theoretical [123] methods have investigated the interface formed by a CNT fiber with the polymer matrix to gain insight into its role in determining the mechanical response of the composite. For example, it has been shown that sliding occurs within the fractured fibers of long CNTs leading to poor load transfer [124], and multi-walled CNTs are often deformed and twisted which increases their flexibility [125]. One weakness of CNT assemblages is the inadequate non-covalent interaction between adjacent circular CNTs, which leads to the slippage of CNTs during deformation [124]. Hence, it was recently proposed to fabricate self-assembled stacks of large-diameter (~10 nm) CNTs, referred to as flattened CNTs (flCNTs), which maximizes the contact area between CNTs, and thus the non-covalent type of bonding [126]. Therefore, it appears possible that the mechanical properties of the flCNT-composite may be further enhanced by carefully engineering its interface.

Also, flattened CNTs, which are referred to as a 'dog-bone'-type collapse in the scientific literature, have been linked to improved mechanical performance because of their similarity to graphitic carbon [127]. They can be considered as stacked layers of graphene which is a two-dimensional hexagonal monolayer with sp^2 hybridized covalent bonds [28]. The van der Waals (vdW) interaction terms between the graphene planes provide the stability to flattened CNTs which possess reactive edges, the curvature of which can be used to control not just chemical and mechanical properties, but thermal and electronic properties as well [128].

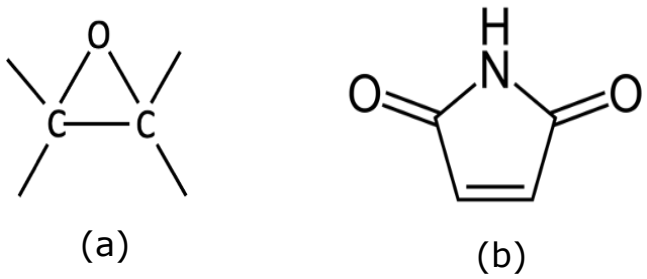

Figure 24: (a) Epoxide group containing reactive C atoms and an O atom, and (b) maleimide group consisted of a –NH group

Among polymers, epoxies containing epoxide groups and bis-maleimides (BMI) containing maleimide groups (Figure 24) are the most commonly used thermosetting resins [129] for making high-performance composites because they provide a unique balance of thermal and mechanical properties combined with extreme processing versatility [130, 131]. It is worth mentioning that diglycidyl ether of bisphenol A (DGEBA) and, 4′-bismaleimidodiphenylmethane (BMPM) are some of the most widely used high-performance Epoxy and BMI resins in the aerospace industry. For example, the fifth-generation combat aircraft F-35 Lightning II developed by Lockheed Martin is stated to consist of about 35% carbon fiber composites out of the entire structural weight, and the primary structural composites used in the aircraft are composed of either Epoxy or BMI matrices. Although other matrices like polyethylene and polystyrene facilitate a mechanical response at room temperature that satisfies property requirements for some applications, there exist challenges in using such matrices in more rigorous applications as it does not perform well at elevated temperatures [132]. This is not the case with either

epoxy (DGEBA) or BMI (BMPM) which are stable at elevated temperatures [133]. Note that the DGEBA and BMPM monomers are often crosslinked with diethyl toluene diamine (DETDA) and o, o′-diallyl bisphenol A (DABPA) monomers, respectively. DETDA is an aromatic amine curing agent, and DABPA is allylphenol which is found to offer excellent toughness to the BMPM [134].

In general, a detailed understanding of the interaction between the graphene and the resin (hardener) matrix at the molecular level is crucial for improving the composite's mechanical response. This is because adhesion between resin (hardener) and graphene is related to the chemistry of the interface [117, 135] which has, without doubt, a considerable influence on the fracture/failure behavior of a composite, although it is not yet understood completely. We are aware of only a few theoretical studies based on atomistic modeling which were used to characterize the interfacial bonding in composites [136]. Overall, it has been recognized that the interface plays a significant role in the stress transfer and the consequent improvements in the composite stiffness and strength [137].

In the following, we will present the results related to the resin/graphene (hardener) focusing on the characterization of the interface at the molecular level using a periodical supercell model. The mechanical response in terms of the separation point (or breaking point) and stiffness will be determined. Within this atomic framework, one can directly modify the interface, even with modifications that are extremely difficult or impossible

to control in the experiment, to predict the consequences on the interfacial strength and thereby its mechanical response.

The resin (hardener) monomers, DGEBA (DETDA), and BMPM (DABPA) (Figure 25) interacting with the surface of graphene are considered. Figure 26(a) shows the top and side view of a monomer forming a complex with graphene in a periodic supercell. It should be noted that our focus is not on the cured polymer composites, but rather on individual monomers to provide a fundamental understanding of the structure-property relationship in the graphene-polymer composites. Moreover, we will also consider the cases of these monomers interacting with a BN monolayer to benchmark the results obtained for the monomer/graphene complexes. Both graphene and BN monolayer are structurally similar, but electronically dissimilar materials; the covalently-linked graphene is a zero-gap material whereas the semi-ionic h-BN monolayer, has a nearly identical honeycomb configuration as that of graphene, is semi-conducting [138].

The results show that the interaction strength between resin (or hardener) and graphene is mainly governed by the nature of bonding at the interface, and subsequently, the mechanical response follows the hierarchical order of the interaction strength at the interface; transverse stiffness of BMPM/graphene is higher than that of DGEBA/graphene. Moreover, the change in the polarity of the surface from graphene to BN monolayer adds to both superior interfacial strength and thereby a higher transverse stiffness of both resin and hardener composites at the molecular level. These results

emphasize the need to use computational modeling to efficiently and accurately determine molecular-level polymer/surface combinations that yield optimal composite material mechanical performance. This is especially important in the design and development of high-performance composites with nano-scale reinforcement.

4.2 Computational Method

Electronic structure calculations were performed using the PAW potentials within the framework of DFT, as implemented in the VASP [139]. The exchange and correlation potential were treated using a GGA with the PBE functional form [91]. Contributions from the vdW interactions, which are important for graphitic systems, were incorporated by using Grimme's semi-empirical dispersive D2 term [92]. The energy cut-off and the convergence criterion of the energy were 500 eV and 10^{-5} eV, respectively.

In a supercell, the periodic boundary conditions with a lateral separation along the *c* direction of 20 Å were employed to ensure the negligible interaction between the periodic images. The relaxation process for the equilibrium configuration was carried out by placing monomer on the top of graphene in various orientations and the distances between them were set to the value that was slightly larger (or similar to) the sum of the nearest resin (hardener) atom and carbon atoms covalent radii. The structure was then relaxed using the conjugate gradient algorithm until the maximum forces acting on the atoms became smaller than 0.001 eV/Å.

The mechanical response of the complex consisting of a resin (or hardener) and graphene (or BN monolayer) was investigated in a way that mimics the 'pull-apart' experimental setup commonly used for polymer composites [121, 140]. In our setup, a resin, which is in the equilibrium configuration, is pulled up along the direction perpendicular to the surface of the constrained (frozen) graphene. DFT calculations were performed for each step of the pull-apart process to generate the energy surface describing the interaction of resin (hardener) with graphene.

In the pull-apart setup, we define the tensile strain to be the perpendicular displacement between the resin (hardener) and the surface of the monolayer with respect to the equilibrium separation. In this way, the strain ε can then be defined as $\varepsilon = (l-l_0)/\ l_0$, where l is the displacement of the resin (hardener) with respect to the distance l_0 calculated in the equilibrium configuration of the complex. The mechanical properties can then be calculated from the strain-energy relationship, $Es = E(\varepsilon) - E(0)$; the energy difference between systems under a given strain ε and no strain associated with the equilibrium configuration.

The calculated strain-energy curve is used to obtain the *force vs strain* curve which can be fitted to the spinodal equation of state [141] to determine the critical force and critical strain of a given complex. It is worth mentioning that the spinodal equation of state, in general, applies to the bulk material, but its use has been extended to low-dimensional materials, including graphene and BN monolayer.

It has been shown that the one-dimensional (1D) spinodal equation of state can reproduce stress dependence on the strain energy of a given system [141, 142]. The equation of state can be written as:

$$\sigma = \sigma_{sp}\left(1 - \left(\frac{\epsilon_{sp}-\epsilon}{\epsilon_{sp}}\right)^{\frac{1}{1-\gamma}}\right) \qquad \textit{Eq.4.1}$$

where ϵ and ϵ_{sp} represent strain at a particular point and spinodal strain, respectively. γ is a pseudocritical exponent that varies with the direction of (stretching or compressing) strain. Equation 4.1 can be written in terms of the force by multiplying the stress terms by the effective area as follows:

$$f = f_{sp}\left(1 - \left(\frac{\epsilon_{sp}-\epsilon}{\epsilon_{sp}}\right)^{\frac{1}{1-\gamma}}\right) \qquad \textit{Eq.4.2}$$

An interesting feature of the proposed *force–strain* equation of state is that it can be also expressed analytically in its energy form. Considering the isotherm at 0 K, the force is related to the internal energy *E* and the equilibrium length L employing the relationship of $f = \frac{1}{L}\frac{dE}{d\epsilon}$. Here, f_{sp} accounts for the maximum force at which the system breaks, and therefore represents the elastic limit of the material. It is referred to as the critical force.

The value of strain corresponding to the critical force is called the critical strain. In the following discussion, we designate critical strength to represent (out-of-plane) transverse strength and critical strain to be the (out-of-plane) separation point at which the monomer breaks from the monolayer. E can be understood as the energy needed for the out-of-plane pull-apart (or separation) of the resin (hardener) from the surface and, therefore, to overcome the interatomic forces binding the complex.

4.3 Results and Discussions

4.3.1 Interaction Energy

Initial DFT calculations were performed to determine the equilibrium configurations of resin (DGEBA and BMPM) and hardener (DETDA and DABPA) molecules. Figure 25 displays the structural configurations of these molecules and Table 4 lists the calculated C-C and B-N bond lengths (~1.42 Å) which are found to be in excellent agreement with previous reports [19, 138, 143].

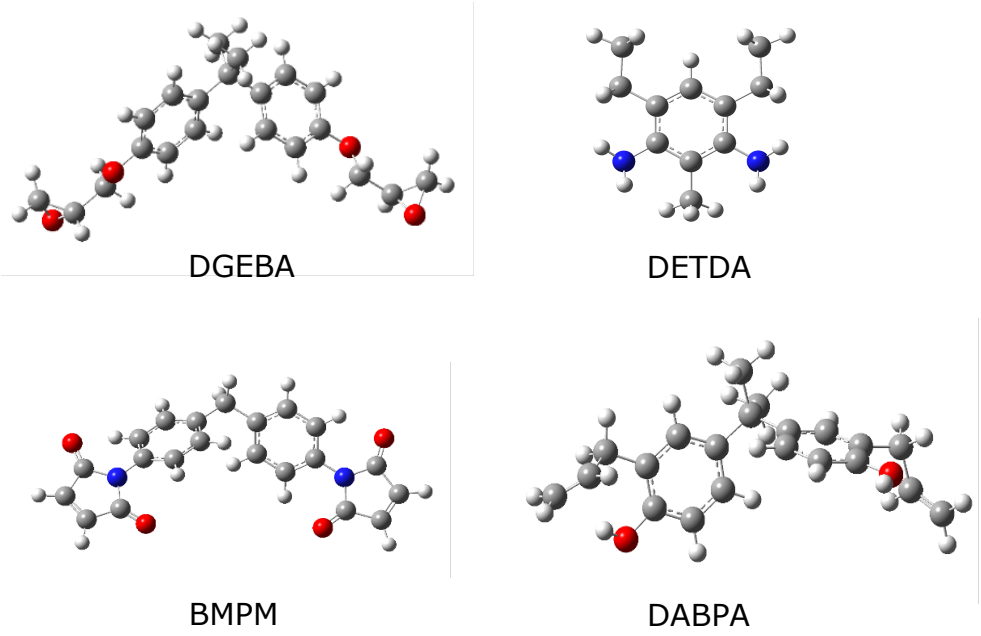

Figure 25: The structural configurations of Epoxy (DGEBA (resin) and DETDA (hardener)) and BMI (BMPM (resin) and DABPA (hardener)) monomers. Color codes- O (red), C (Grey), N (Blue), and H (white)

In calculations of the energy surface describing the interaction of a resin (hardener) with the monolayer, we allow it to approach the surface in the direction perpendicular to the surface with a specific orientation while keeping the monolayer fixed. For example, DGEBA is oriented in such a way that (i) both end groups and hydrogen ends are oriented towards the surface – the *in-plane* orientation (Fig. 26(b)(i)), (ii) both the epoxide end groups are facing the surface and the hydrogen end is away from the surface – the *flip-in* orientation (Fig. 26(b)(ii)), (iii) both the end epoxide groups are aligned away from the surface and the hydrogen end is close to the surface - the *flip-up* orientation (Fig.

26(b)(iii)), and (iv) only one end group is facing the surface – the *vertical* orientation (Fig. 26(b)(iv)). At the minimum energy distance associated with a specific orientation, full optimization of the conjugated system in which all atoms were free to relax was performed.

Table 4: Some of the representative structural parameters of the resin (hardener) considered

	DGEBA (resin)	**BMPM (resin)**	**DABPA (hardener)**	**DETDA (hardener)**
Total Energy, (eV)	-302.54	-284.10	-291.38	-183.80
Bond distance, C-C (Å)	1.46	1.50	1.40	1.39
C-H (Å)	1.09	1.08	1.09	1.08
C-O (Å)	1.42	1.22	1.37	-
C-N (Å)	-	1.41	-	1.41
Bond angle, C-C-C (°) (benzene ring)	121.9	121.8	121.2	117.9

The characteristics of the complexes are determined in terms of the interaction energy, area of contact, the population of atoms, Bader's charge [144], critical force, and critical strain. We define the interaction energy (ΔE) to be as E (complex) - E (resin (hardener)) - E (monolayer), and a negative value of ΔE suggests the stability of the complex. ΔE can also be considered as the adsorption energy of resin (hardener) on the monolayer. The contact area is the area of the resin (hardener) projected on the surface of a monolayer. The population of atoms is defined as the number of resin (hardener) atoms within the

range of 3 Å from the surface. Note that the interplanar distance of ~3 Å can be taken as the characteristic distance of vdW-bound systems including the complexes considered [145].

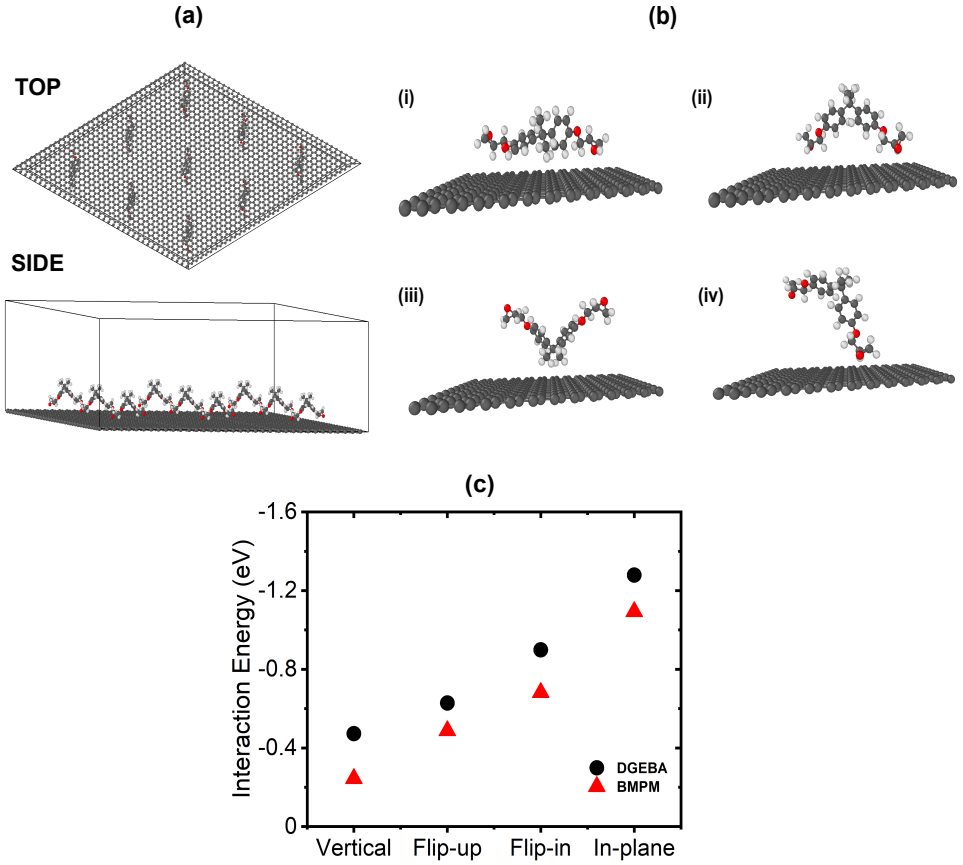

Figure 26: (a) Top and side views of a complex. (b) molecular orientations (i) in-plane (ii) flip-in (iii) flip-up (iv) vertical over graphene. Atomic color codes- O (red), C (Grey), and H (white). (c) The orientation-dependent interaction energy of DGEBA (red) and BMPM (black) interacting with graphene

Figure 26(c) shows the calculated values of the interaction energy consisting of DGEBA and BMPM forming a complex with graphene. The results find the *in-plane* orientation to be energetically preferred and is followed by *flip-in*, *flip-up*, and *vertical* orientations. The interaction energy steadily increases by ~ 0.9 eV in going from *vertical* to *in-plane* orientations, thereby suggesting that graphene prefers the resin to be aligned parallel to the surface. Table 5 lists the interaction energy, the bond distances at the interface, area of contact, and population of atoms of the equilibrium configurations of the above-mentioned cases.

Next, we calculate the effective area of contact by using the estimated length and width of the surface covered by the resin (hardener) using its distance of one end to the other in both x- and y-directions. We find that the calculated area for the '*in-plane*' orientation is significantly higher than the rest of the orientations for both cases (Table 5). This is further corroborated by calculations of the population of atoms by counting the number of atoms that are within the range of ~3 Å above the surface. The results show the *in-plane* population is significantly larger than in the other three orientations, thereby facilitating a larger degree of interaction between the resin atoms and graphene at the interface. Subsequently, the *in-plane* orientation leads to the energetically preferred configuration for DGEBA and BMPM on graphene. We note that our results are in line with the PBE (DFT) results on the DGEBA/CNT complex reporting the preference of the longitudinal orientation over the transverse orientation of DGEBA on a CNT [146].

Both resin and hardener consist of aromatic rings and the side groups containing oxygen or nitrogen atoms. On the other hand, graphene consists of a honeycomb lattice, in which C atoms form in-plane sp^2 hybridized bonds together with out-of-plane π-bonds. The interaction of resin (or hardener) with graphene is, therefore, expected to be governed by π-π noncovalent interactions with a small contribution from the polarizable O and N atoms of the side groups. This is what has been affirmed by analysis of the interface in terms of area of contact and population of atoms; a large effective contact area and population of atoms yield the *in-plane* orientation to be the energetically preferred configuration of a resin (hardener) on graphene.

Figure 27 displays the (in-plane) equilibrium configurations of the complexes and the calculated values of the corresponding interaction energy values are listed in Table 6. For the complexes, the calculated results find the order of the interaction strength to be DGEBA < BMPM for resins and DETDA < DABPA for hardeners. Specifically, the difference between the interaction strength of DGEBA and BMPM is noticeable and can be explained in terms of the population of atoms which is significantly larger for DGEBA (Table 6). Furthermore, the polarizable O atoms (of DGEBA) induce a hybridized state which appears in the valance band region of the density of states, though the H (resin)-C (graphene) hybridized states dominate the valence band in both resin complexes (Fig. 28 (c, d)).

Table 5: The interaction energies (ΔE), bond distances at the interface ($d_{monomer\text{-}graphene}$), Area of contact, and the population of atoms for the resin monomers, DGEBA and BMPM conjugated with graphene. The distance of one end to the other is taken to be the estimated length and width of the molecule for calculations of the area of contact

	Orientation	**ΔE (eV)**	**$d_{monomer\text{-}graphene}$ (Å)**	**Area of contact**	**Population of atoms (%)**
DGEBA/graphene	In-plane	-1.27	2.4	136.5	16
	Flip-in	-0.89	2.7	95.12	12
	Flip-up	-0.62	2.6	94.5	8
	Vertical	-0.47	2.5	78.2	6
BMPM/graphene	In-plane	-1.09	2.3	91.3	10
	Flip-in	-0.68	2.7	85.9	2
	Flip-up	-0.48	2.4	61.7	9
	Vertical	-0.24	2.4	58.4	2

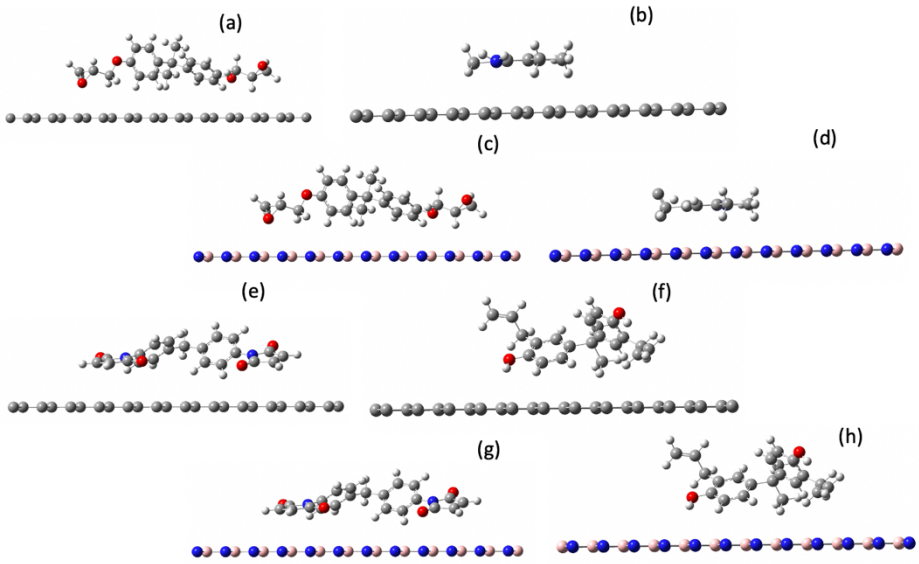

Figure 27: Ball and stick model of the complexes: (a) DGEBA/graphene (b) DETDA/graphene (c) DGEBA/BN (d) DETDA/BN Epoxy/BN (e) BMPM/graphene (f) DABPA/graphene (g) BMPM/BN (h) DABPA/BN complex in in-plane orientation. Color codes: O (red), N(blue), H(white), B(pink) and C (grey)

For the case of the BN monolayer, we expect a small, but noticeable difference in the calculated results as compared to those obtained for graphene. This is because the BN monolayer being semi-ionic may induce a slightly higher degree of electrostatic interaction with resin (hardener) relative to graphene. The calculated values of the interaction energy are higher; $DGEBA_{(graphene)} < DGEBA_{(BN)}$ and $BMPM_{(graphene)} < BMPM_{(BN)}$ for the resin complexes and $DABPA_{(graphene)} < DABPA_{(BN)}$ and $DETDA_{(graphene)} < DETDA_{(BN)}$ for the hardener complexes.

Table 6: The interaction energy (ΔE), the population of atoms, and Bader's charge (Q) calculated for the resin and hardener complexes

	Complex (*in-plane)*	**ΔE (eV)**	**Population of atoms (%)**	**$Q_{graphene}$ (e)**
Resin	DGEBA/graphene	-1.27	16	0.03
	BMPM/graphene	-1.09	10	0.05
	DGEBA/BN	-1.33	16	0.03
	BMPM/BN	-1.30	15	0.06
Hardener	DETDA/graphene	-0.96	20	0.04
	DABPA/graphene	-0.74	11	0.02
	DETDA/BN	-1.24	20	0.02
	DABPA/BN	-0.86	11	0.02

Moreover, the results indicate that curing agents (e.g., DETDA) participate effectively at the interface, which implies that the load transfer of epoxy/graphene composites is governed by both resin and hardener in this case. The interaction energy values for DETDA and DABPA are in line with the expectations arising from their values of the population of atoms (Table 6). It is worth mentioning that the aromatic ring of DETDA is aligned parallel to graphene thereby yielding a higher degree of vdW interaction with monolayers at the interface.

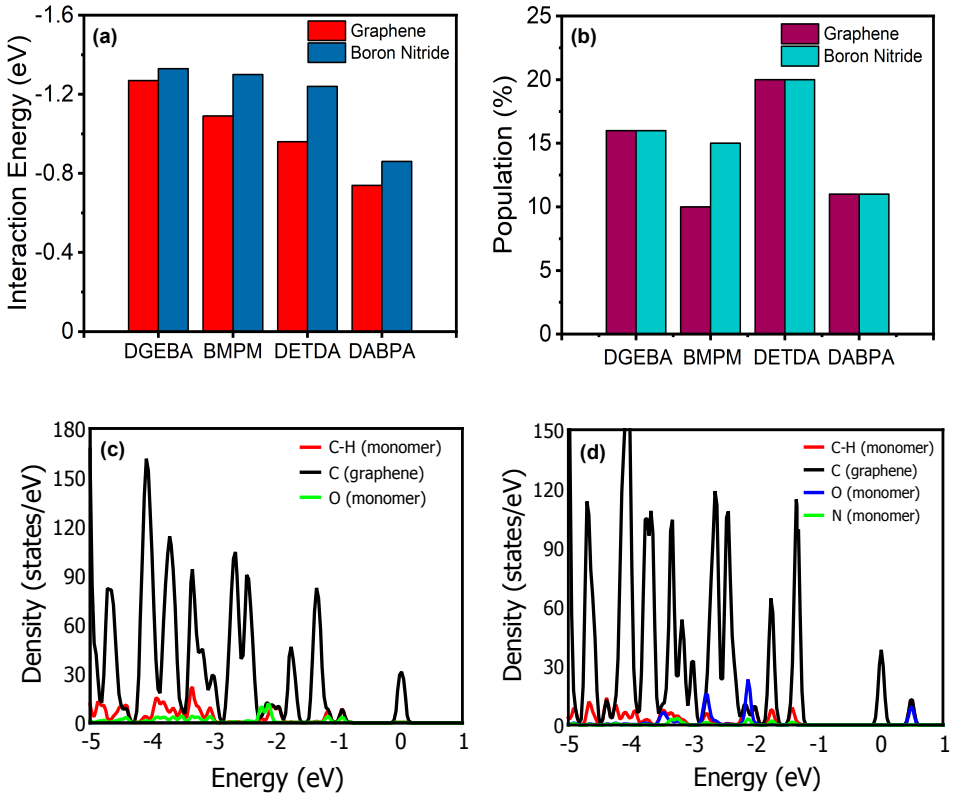

Figure 28: (a) Calculated interaction energy of the resin (DGEBA and BMPM), and hardener (DABPA and DETDA) with graphene (red) and BN monolayer (blue). (b) The calculated population of atoms within the range of 3 Å distance above the monolayer. Atom projected density of states for (c) resin DGEBA with graphene (d) resin BMPM with graphene

Overall, the interaction between resin (or hardener) and graphene (or BN monolayer) is governed by the dispersive force like vdW in the cases considered. This is due to the fact that the analysis of the calculated Bader charge suggests the occurrence of a small charge transfer (<0.1 *e*) from graphene (BN monolayer) to resins (hardeners) (Table 6).

Moreover, the hydrogen-bonding interactions with π electrons of graphene (or B/N atoms of BN monolayer) at the separation of 2.5 Å are expected to be weak [147].

4.3.2 Mechanical Response

The (out-of-plane) mechanical response of the complexes was calculated using the setup by applying the load in only the 'z' direction, which is perpendicular to the surface starting from its equilibrium separation to the separation of ≈3.8 Å with a step-size of 0.02 Å. DFT calculations were performed at each step generating the energy surface of the resin (DGEBA or BMPM) and hardener (DABPA or DETDA) forming complexes with graphene (or BN monolayer) (Fig. 29). The strain (or separation)-energy surfaces were then used to calculate *force vs strain curves* as shown in Fig. 31. Subsequently, the *force vs strain curve* was fitted to the 1D SEOS (Eq. 4.2). We note here that two parameters define the shape of each of these curves, f_c and ε_c, which will be used to characterize the transverse strength and separation point of the conjugated monomers considered (Table 7). $\boldsymbol{\gamma}$ is the 1D correspondence of the pseudocritical exponent β which, in general, takes

a value of 0.85 associated with the volumetric compression of solids [148, 149]. In the present case, γ varies between 0.5-0.8 (Table 7).

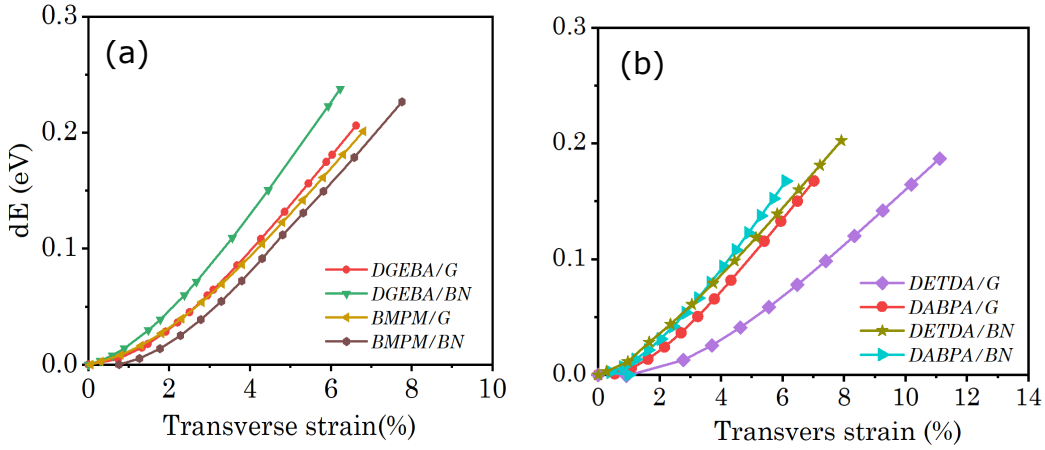

Figure 29: The calculated strain (or separation)-energy relationship of the (a) resin (DGEBA and BMPM) and (b) hardener (DABPA and DETDA) interacting with graphene and BN monolayer. Zero is taken to be the equilibrium configuration and dE is the energy with respect to the total energy of the equilibration configuration

It is worth mentioning that the equation of state (e.g., *Eq 4.1*), in general, is used to investigate the constitutive responses of a bulk-like system. In the present case, we have used the spinodal equation of state to differentiate the (out-of-plane) mechanical response of quasi-3D complexes consisting of resin (hardener) and graphene (BN monolayer). Therefore, in the following discussion, we use "transverse" to describe out-of-the-plane and designate critical strength to represent transverse strength and critical strain to be (out-of-plane) separation point at which the monomer apart from the monolayer (Fig. 30).

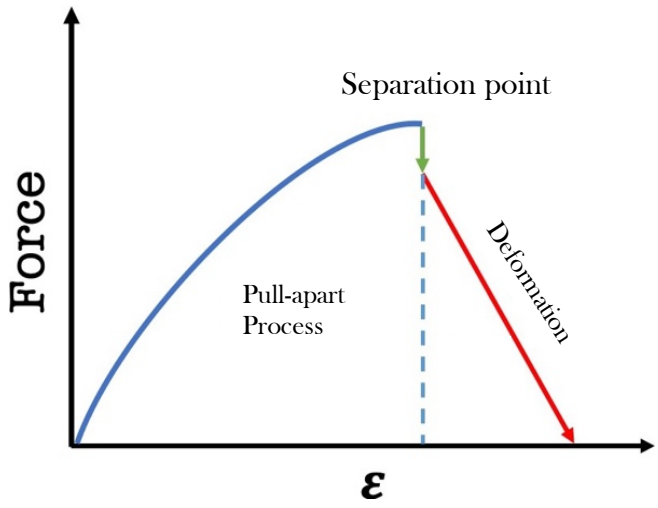

Figure 30: Typical force-strain behavior during pull-apart mechanism, where at the point of maximum force the complex separates into its constituents. The (out-of-plane) separation point can be considered transverse stress

The calculated results show that resin (hardener) forming complexes with the BN monolayer exhibit slightly higher transverse strength than the corresponding complexes with graphene. Among resin, BMPM exhibits a slightly higher transverse strength relative to that of DGEBA. This is not the case with the separation point values for which we find the order to be DGEBA/graphene ≈ DGEBA/BN < BMPM/graphene < BMPM/BN. Interestingly, the hardener DETDA exhibits a relatively high value of separation point suggesting that, as a curing agent, it is likely to improve the interfacial load transfer of the epoxy/graphene composite. It is worth noting that the calculated transverse strength of DGEBA/graphene is comparable to the calculated value of DGEBA/CNT; MD

calculations reported the value of the force to be ~3.8 nN which breaks a DGEBA strand from a CNT [29] whereas we find the value of ~1 nN to break the DGEBA from graphene (Table 7).

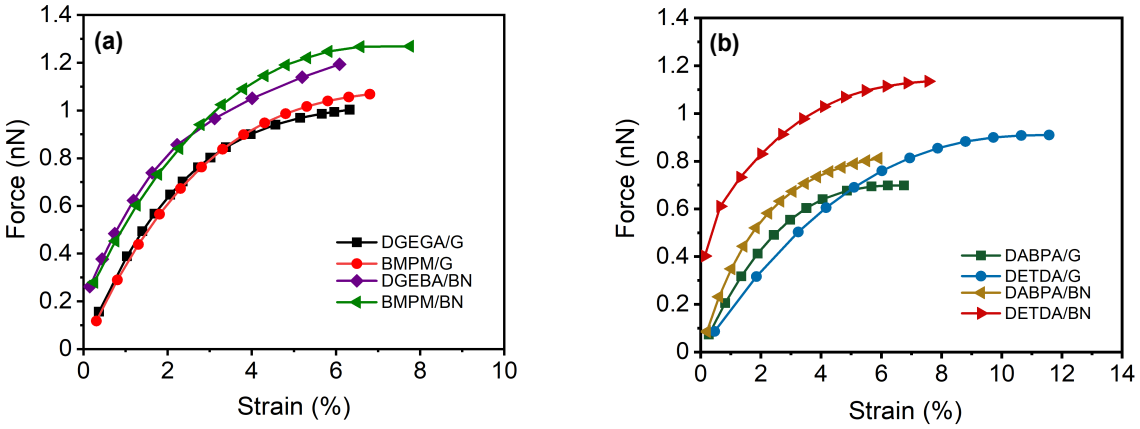

Figure 31: Calculated force vs transverse strain curves for the (a) resin (DGEBA or BMPM), and (b) hardener (DABPA or DETDA) forming complexes with graphene (or BN)

Table 7: Calculated values of transverse strength, (out-of-plane) separation point and Gamma (γ) of the complexes

	Complex	Transverse strength, f_c (nN)	Separation point, ε_c (%)	Gamma, γ
Resin	DGEBA/graphene	1.0	6.3	0.77
	BMPM/graphene	1.1	6.8	0.74
	DGEBA/BN	1.2	6.1	0.69
	BMPM/BN	1.3	7.7	0.78
Hardener	DETDA/graphene	0.9	11.6	0.59
	DABPA/graphene	0.7	6.7	0.56
	DETDA/BN	1.1	7.6	0.67
	DABPA/BN	0.8	5.9	0.72

In general, the (out-of-plane) stiffness can be taken as a measure of the quasi-3D Young's modulus suggesting that a higher value of stiffness leads to a higher Young's modulus which is one of the desired characteristics of an engineered composite. Table 8 lists the values of the transverse stress and the stiffness calculated from the stress-strain curve displayed in figure 32 for which the area is estimated by projecting the length and width of the resin (hardener) over the graphene (or BN monolayer). The results show that BMPM/graphene (or BMPM/BN) is stiffer than the corresponding DGEBA complexes. Among the hardener considered, DETDA having the (graphene-like) planar structure is predicted to have higher stiffness than DABPA in the complexes considered.

Next, we benchmark our stiffness values to the values calculated for bilayer graphene employing a similar pull-apart setup. The elastic stiffness of bilayer graphene is calculated to be 24 GPa, an order of magnitude higher than what is predicted for resin (or hardener) forming complexes with graphene. This is in line with the expectation of the occurrence of a relatively high degree of vdW interactions at the interface with a 100% population of atoms for the case of bilayer graphene.

Finally, figure 32 summarizes the result of the present study displaying the predicted relationship between the interaction strength at the interface and the mechanical response in terms of stiffness obtained at the molecular level for Epoxy and BMI composites. The results show that the mechanical response is directly related to the degree of the interface

adhesion, though it can also be influenced by the nature of the chemical bonds at the interface in the polymer composites.

Table 8: Mechanical properties in terms of separation point, transverse stress, and stiffness for the resin (or hardener) forming complexes with graphene (or BN monolayer)

	Complex	**ΔE/atom (eV)**	**(Out-of-plane) Separation point, εc (%)**	**(Out-of-plane) Transverse stress (GPa)**	**(Out-of-plane) Stiffness (GPa)**
Resin	DGEBA/graphene	-0.026	6.3	0.74	0.19
	BMPM/graphene	-0.027	6.8	0.85	0.22
	DGEBA/BN	-0.027	6.1	0.9	0.23
	BMPM/BN	-0.032	7.7	1.0	0.25
Hardener	DETDA/graphene	-0.03	11.6	1.24	0.21
	DABPA/graphene	-0.015	6.7	0.60	0.17
	DETDA/BN	-0.04	7.6	1.55	0.39
	DABPA/BN	-0.018	5.9	0.74	0.20
Bilayer Graphene			14.6	1.6	
Graphene/BN			13	2	

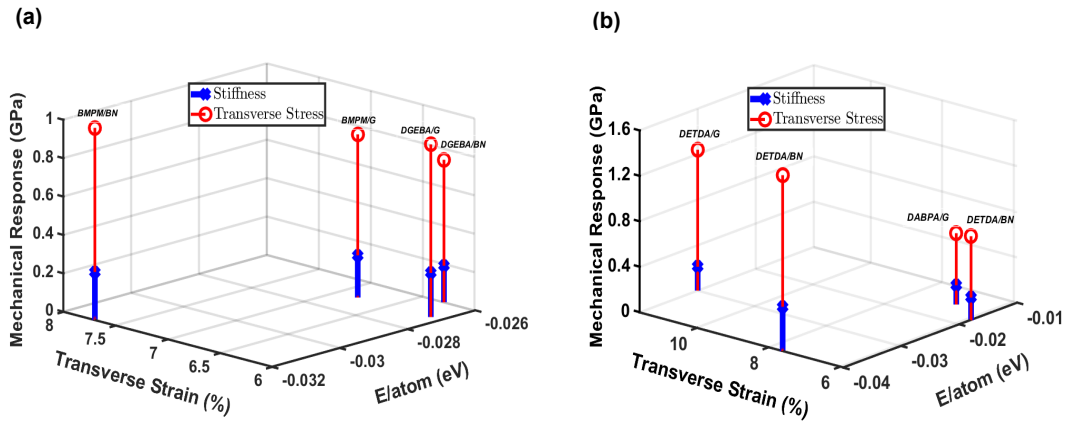

Figure 32: The interaction energy/atom vs. transverse strain and stiffness for the (a) resin (DGEBA or BMPM), and (b) hardener (DABPA or DETDA) forming complexes with graphene (or BN monolayer).

4.4 Conclusion

We have performed an atomistic investigation of the representative polymer composites employing DFT to establish the relationship between the nature of the interface and its mechanical response. Specifically, DGEBA (DETDA) and BMPM (DABPA) are considered to represent resin (hardener) components of epoxy and BMI, respectively. The calculated results indicate that the interfacial adhesion is highly influenced by the orientation of the resin (hardener) on graphene due to van der Waals interactions being dominated at the interface. Next, we used the strain-energy energy relationship to extract the force vs strain curves which are then fitted to the 1D spinodal equation of state to determine the mechanical response of a complex. We find that the mechanical response

in terms of stiffness follows the hierarchical order of interaction strength at the interface; the elastic stiffness of BMPM/graphene is higher than that of DGEBA/graphene. The change in polarity of the surface from graphene to BN monolayer improves the interfacial strength and thereby the elastic stiffness due to the presence of covalent polar bonds at the interface. Furthermore, the presence of aromatic rings in the DETDA hardener yields a significantly higher mechanical response relative to the one exhibited by the DABPA hardener suggesting that DETDA, as a curing agent, is likely to improve the interfacial load transfer of the epoxy/graphene composite. Overall, the results predict a small degree of polarity at the interface dominated by van der Waals interactions can help in improving its mechanical response. In light of the intricate molecular-level simulations based on first-principles methods, predicting the interfacial properties of composites is challenging but can provide an insight to the experimentalists in tailoring composite properties as demanded by aerospace applications.

5 Influence of Interfacial Interactions on Mechanical Properties of Cyanate Ester Monomer and Graphene or BN Monolayer: A DFT Study

5.1 Introduction

Deep space exploration into the solar system requires technology advancements for space vehicles that can sustain a voyage with minimal mass and volume. Polymer matrix composites, particularly those with carbon fiber reinforcement, have become more popular in aerospace applications in recent years as a result of their high stiffness-to-weight ratio, which results in significant weight and fuel savings on commercial and military aircraft [150]. It has been recognized that existing carbon fiber-based composite materials are insufficient for a manned mission to Mars [151]. However, one expects nanomaterials, including graphene and carbon nanotubes (CNTs), can exceed the mechanical properties of carbon fibers used for structural reinforcements in composites [152]. Essentially, composites are engineered materials that consist of at least two materials that are significantly different in terms of their chemical or physical properties.

Because of their excellent mechanical properties, CNTs are a good reinforcement for high-performance polymer matrix composites. The Young's modulus of carbon nanotubes is roughly 1 TPa which makes them effective reinforcements for materials with exceptional stiffness and strength. However, CNTs dispersed in polymer matrix have

lower stiffness and strength than those that are isolated [126]. The problem associated with the dispersion of CNTs arises as a result of insufficient noncovalent bonding between neighboring CNTs, resulting in the deformation-induced movement of CNTs [124]. On the other hand, CNTs with large diameter (~10 nm), also called flattened CNTs (flCNTs), observed in nanocomposites formed with highly aligned thin CNT films and bismaleimide (BMI) (a type of resin) have been found to have remarkably high tensile strength than those of small diameter CNTs because of their large contact area, and hence a higher degree of noncovalent type of bonding among themselves [126]. For example, the mechanically stretched sheets of flCNTs combined with BMI resin were 78% and 283% greater Young's modulus and tensile strength, respectively, than sheets of randomly oriented CNT with BMI resin. These flCNT bundles can thus serve as highly effective reinforcing materials [126].

FCNTs can be viewed as stacked layers of two-dimensional graphene [28] in which van der Waals forces dominate the interlayer interactions. This weak attractive interaction essentially compensates the energy loss from the formation of reactive edges and provides stability to flCNTs [128]. In the present study, we show that graphene representing the graphitic structure of flCNTs can provide excellent interfacial strength in forming polymer composites.

The question now becomes, "Which polymer matrix is most compatible with graphene?" The efficacy of load transfer between composite constituents is determined by the binding

strength (or interaction strength at the interface) between those constituents. Previously, Sachdeva et al. [153] used density functional theory (DFT) to investigate the interaction properties and mechanical characteristics of two different (epoxy and BMI) monomers interacting with graphene. They demonstrated that various functional groups (e.g., R-O-R in epoxy resin) significantly affect the interfacial interaction energy, pull-apart force, and separation point. Although the reported results are essential in determining the behavior of monomer/graphene interfaces, it's unclear how it interacts with other monomer systems that could be employed in graphene-based polymer composites.

In general, it is expected that functional groups containing nitrogen will be most compatible for graphene-based composites due to the interaction between amide/amine and the orbitals of graphitic structures (i.e., NH_2–π interaction) [154]. Accordingly, aromatic cyanate esters, Primaset PT-30 and AroCy F-10, consisting of nitrogen-containing functional groups, can be candidate matrices for such composites. These ester resins have evolved as a distinct and new category of thermosetting resins with excellent performance that are employed in structural applications as matrices [155]. The cyanate ester resins have some basic features, such as low moisture absorption, good electrical qualities, easy processability, good flammability characteristics, high service temperature and toughness, which makes them ideal composite matrices and a competitor for epoxy and bismaleimides resins in structural applications [156, 157].

Cyanate esters are characterized by a phenol backbone with cyanate (-OCN) groups attached at each end of the monomer. AroCy F-10 is a fluorinated cyanate ester (Fig. 1(a)) with a tensile strength of 75 MPa, an elastic modulus of 3.11 GPa, a maximum strain of 2.8 %, and fracture toughness of 140 Jm^{-2} [158]. Primaset PT is a non-fluorinated cyanate ester (Fig. 1(b)) with a tensile strength of 77 MPa, a tensile modulus of 4.0 GPa, a strain-to-break of 2.0%, and flexural strength of 112 MPa [159]. In this work, we consider the complexes consisting of ester monomer and graphene (or BN) monolayer to provide an atomistic description of the interface via interaction energy, density of states, Bader's charge [160] and the population of atoms [153]. Subsequently, the mechanical response of these esters and graphene (or BN monolayer) complexes in terms of separation point, transverse strength, and stiffness are characterized using pull-apart simulations [153]. It is again noteworthy that we intend to focus on the individual monomer interaction at the reinforcement (monolayer) surface rather than the cured polymer composites in the present study.

Since boron nitride (BN) has a graphene-like structure with regularly stacked planar networks of hexagons [138, 161], its interactions with the ester monomers were also investigated. It exhibits a polar bonding character which is likely to have a distinct nature of interaction with various monomers than graphene.

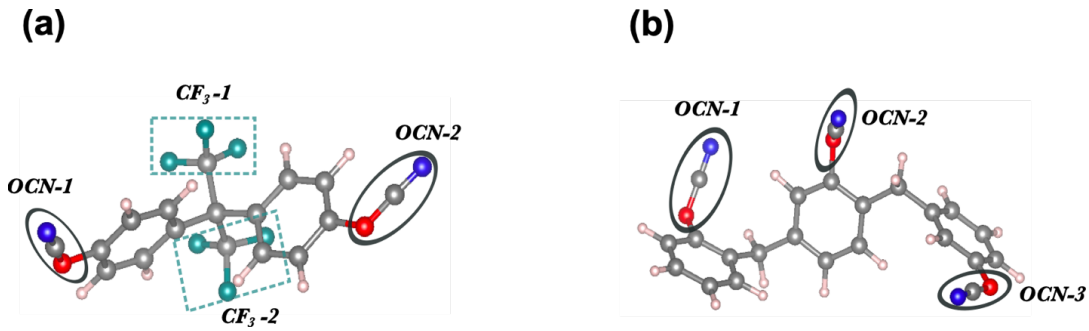

Figure 33: Ball and stick model of (a) AroCy-F10 (fluorinated) and (b) Primaset PT-30 (non-fluorinated) cyanate ester resin monomers. Color codes: C- Grey, O- Red, N- Blue, H- White, F-Green

5.2 Computational Method

The VASP [139] was used to perform DFT calculations utilizing PAW [162] potentials. For the exchange-correlation functional, the PBE parameterization of GGA was employed [91], and van der Waals interactions were incorporated using Grimme's D2 technique [92]. In addition, we used a gamma-centered k-point grid with a plane-wave cutoff of 500 eV, ensuring an energy convergence of 10^{-5} eV. Local energy-minimum structures were fully relaxed with atoms having forces less than 0.001 eV/ Å using the conjugate gradient (CG) algorithm.

We employed a 30×30×20 Å supercell and applied the periodic boundary conditions to mimic the system as a non-polymerized composite system. To ensure that periodic images

do not interfere with each other, a vacuum of 20 Å has been applied along the z-axis. The monomer is placed on top of the monolayer at a distance of ~2.5 Å, i.e. slightly higher than the nearest monomer and monolayer atoms van der Waal radii [147], and then the geometry optimization was performed to find the equilibrium configuration of the ester/graphene (or BN monolayer) complex.

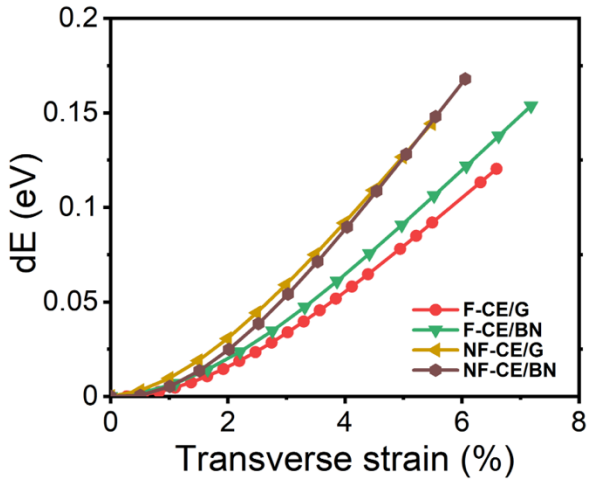

Figure 34: The calculated strain-energy relationship of the fluorinated (F-CE) and non-fluorinated cyanate ester (NF-CE) interacting with graphene (G) and BN monolayer. Zero is taken to be the equilibrium configuration, and dE is the energy with respect to the to be the equilibrium configuration, and dE is the energy with respect to the total energy of the equilibration configuration

A similar "pull-apart" setup discussed in chapter 4 was implemented to determine the mechanical response of the ester complexes [121, 140]. The pull-apart simulation setup schematic to derive the force-strain relationship is shown in Fig. 30. The calculated

variation in energy as a function of each incremental step referred to as (out-of-the-plane) transverse strain is shown in Fig. 34. As previously defined, we designate critical strain to the transverse strain or separation point. Likewise, the transverse strength of the material is referred to as critical strength. An interesting feature of the proposed *force-strain* equation of state is that it can also be expressed analytically in its energy form. Overall, this appears to be a preliminary step to link molecular description of the interface obtained from the first-principles method to the macroscopic mechanical response of the system via the 1D spinodal equation of state for the ester monomers interacting with graphene or BN monolayer.

5.3 Results and Discussions

5.3.1 Interaction energy

Figure 35 illustrates how the molecular-level description of the ester-monolayer complex was obtained. First, the ground-state configurations of fluorinated and non-fluorinated monomers were obtained (Table 9). Next, the monomer in an in-plane configuration was approached perpendicularly to the surface while keeping the monolayer configuration fixed. It is to be noted that in our previous study of epoxy/BMI monomers interacting with graphene (or BN monolayer), a detailed conformational sampling in terms of the orientation of a monomer approaching the surface was investigated [153]. The in-plane orientation was anticipated to be the energetically preferable orientation of the monomer

on a surface out of four representative orientations: flip-up, flip-in, vertical, and in-plane. The results were also confirmed in terms of contact area and population of atoms at the surface. In-plane orientation has the highest population of atoms and interaction energy compared to the flip-up, flip-in, and vertical orientations [153].

Table 9: Some of the representative structural parameters of the fluorinated and non-fluorinated cyanate ester monomers

	AroCy-F10	**Primaset PT-30**
Binding energy/atom (eV)	-4.3	-4.1
Bond distance		
C-C (Å)	1.40	1.40
C-H (Å)	1.09	1.09
C-O (Å)	1.41	1.30
C-N (Å)	1.17	1.17
C-F (Å)	1.35	-
Bond angle, C-C-C (°) (Benzene ring)	121.4	119.6

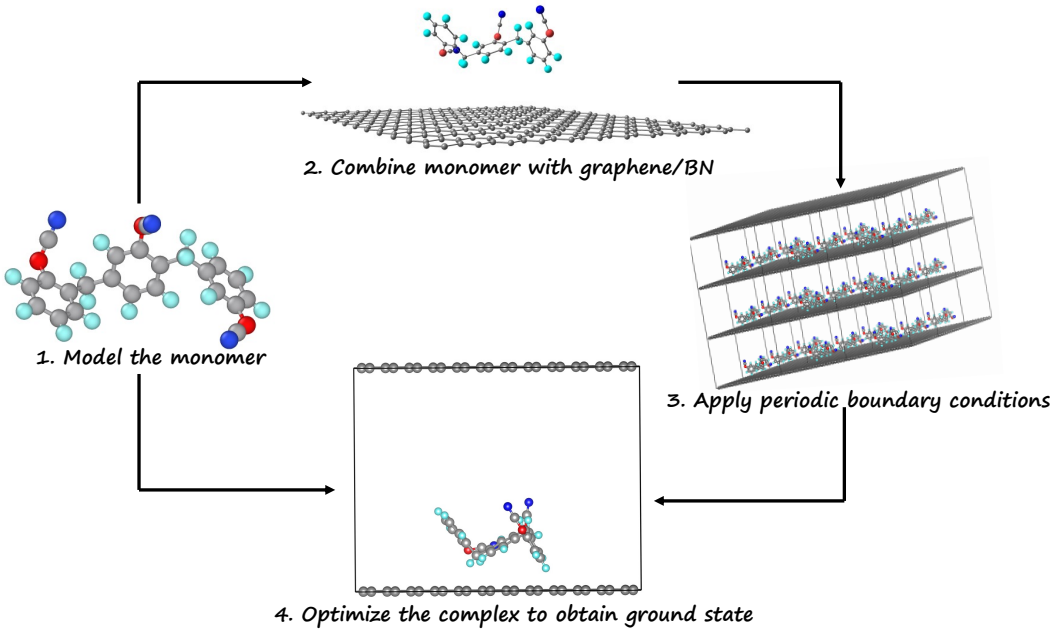

Figure 35: A workflow diagram describing the steps taken to determine the equilibrium configuration of monomer/graphene complex

Next, to validate the case for ester monomer, the interaction energy for the representative orientations of fluorinated ester monomer with graphene monolayer was calculated. Furthermore, a preference of longitudinal configuration of monomer over CNT was obtained over the transverse configuration [145].

Following that, the properties such as interaction energy, effective area of contact, population of atoms, density of states and Bader's charge [144] were calculated to characterize the interface formed by ester monomers with graphene (or BN) monolayer.

The number of monomer atoms within a distance of 3 Å from the surface is defined as the population of atoms. The contact area is the effective area projected by the monomer on the surface of a graphene (or BN) monolayer. By measuring the length and width of the monomer-covered surface, we were able to compute the effective area of contact. It should be noted that the interplanar distance in the vdW complexes, which includes the monomer-monolayer system under consideration, is reported to be ~3 Å [145]. The interaction energy is defined as $\Delta E = E_{complex} - E_{monomer} - E_{monolayer}$, where a negative value of ΔE indicates that the complex is the stable (Figure 36, Table 10).

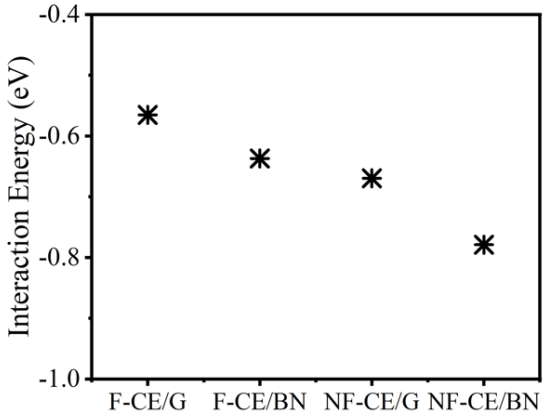

Figure 36: The calculated interaction energy of the ester resins, AroCy-F10 (fluorinated cyanate ester) labeled as F-CE and Primaset PT-30 (non-fluorinated cyanate ester) labeled as NF-CE. G refers to graphene, and BN refers to a boron nitride monolayer

BN/monomer interactions are stronger than those produced with the graphene due to the polar-π interactions between a polar surface of the BN monolayer and the π system of the monomer [163]. In contrast, the interaction strength of graphene/ester monomer complexes

is governed only by the templating effect [164] of the phenyl groups interacting with a graphitic surface. Note that aromatic rings prefer to align themselves parallel to the surface, forming the π-π stacked configurations [165]. DFT calculations also predict relatively high stability for the non-fluorinated monomer than the fluorinated monomer (see Fig. 36). This effect is associated with the larger area of contact of the non-fluorinated ester (≈ 102 $Å^2$) compared to the fluorinated ester (≈ 95 $Å^2$), leading to an increase in the vdW interactions at the interface. The area of contact for a non-fluorinated ester is relatively large due to presence of an additional phenyl ring and cyanate group.

This has been affirmed by the population of atoms as well, which is higher for non-fluorinated ester than fluorinated ester monomers (Table 10). Likewise, the calculated values of the area of contact normalized interaction energy shows that non-fluorinated ester interacting with graphene has higher interaction energy per unit area (-0.007 $eV/Å^2$) than fluorinated ester (-0.006 $eV/Å^2$). Furthermore, the -CF_3 group of the fluorinated ester induces steric hindrance effects, which may restrict the parallel alignment of the monomer on the surface. This effect has been noted in previous studies of the other fluorinated polymers and CNTs functionalized with fluorine atoms [166].

Table 10: The interaction energy (ΔE), the population of atoms, and Bader's charge (Q) calculated for the ester resins, AroCy-F10 (fluorinated cyanate ester), and Primaset PT-30 (non-fluorinated cyanate ester) interacting with graphene (or BN monolayer)

Complex		**ΔE (eV)**	**Population (%)**	**Q (e)**
Graphene	AroCy-F10 (fluorinated)	-0.56	11.4	0.03
Graphene	Primaset PT-30 (non-fluorinated)	-0.67	13.6	0.04
BN monolayer	AroCy-F10 (fluorinated)	-0.64	11.4	0.04
BN monolayer	Primaset PT-30 (non-fluorinated)	-0.78	13.6	0.04

To determine whether charge transfer occurs between the constituents in the complex, we now perform Bader's charge analysis. In both cases, a small charge transfer (<0.1e) occurred from graphene monolayer (or BN) to monomer (Table 10). It then rules out the dominance of the electrostatic interactions at the interface. Furthermore, the electronic density of states (DOS) of the ester complex, shows that the DOS of the ester complex is nearly a superposition of the DOS of the individual components (see Figure 37). Moreover, ester monomers do not modify the behavior of the DOS near the Fermi level suggesting the nature of the interaction at the interface to be dominated by the weak vdW forces. Consequently, the dipole moments of the fluorinated and non-fluorinated ester monomers are predicted as 2.61 Debye and 6.2 Debye, respectively. A relatively high dipole moment of the non-fluorinated monomer, in turn, provides relatively high flexibility in the electronic density, thus facilitating a higher vdW interactions at the

interface. Ultimately, the results predict the interface of the ester complexes to be dominated by the noncovalent interactions. However, because of the semi ionic behavior of the BN, we found a small but remarkable difference in the interaction energies of when compared to graphene complexes; $E_{interaction}$(AroCy F-$10_{(graphene)}$) < $E_{interaction}$(AroCy F-$10_{(BN)}$) and $E_{interaction}$(Primaset PT-$30_{(graphene)}$) < $E_{interaction}$(Primaset PT-30 $_{(BN)}$).

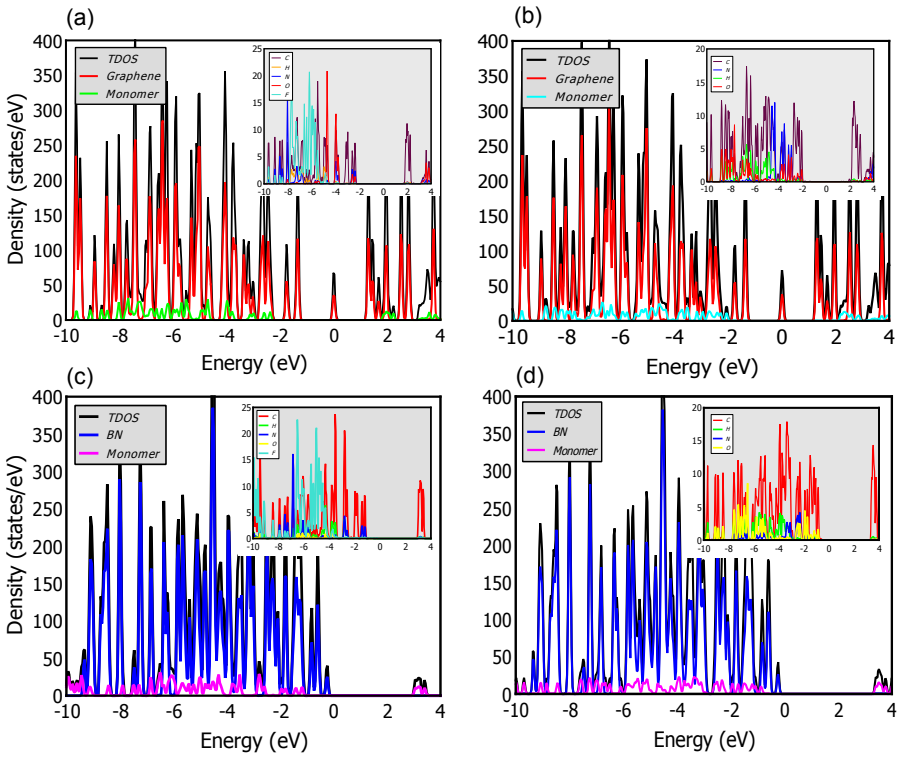

Figure 37: Calculated total density of states and density of states for monomers forming composites with graphene or BN monolayer: (a) fluorinated ester/graphene, (b) non-fluorinated ester/graphene (c) fluorinated ester/BN (d) non-fluorinated ester/BN. The inset shows DOS contributions from the corresponding monomers in the complexes

5.3.2 Mechanical Response

The mechanical properties (out-of-plane) of the ester complexes were predicted in terms of critical force (transverse strength), transverse stress, transverse stiffness, and critical strain using the pull-apart set-up. In the simulation, an ester monomer was displaced in small steps (≈0.02 Å) normal to the graphene (or BN) surface, starting from its optimized state (equilibrium distance) until ≈3.8 Å of separation (Figure 38). We note that H atoms of the ester monomers are the nearest-neighbor atoms for graphene (or BN) monolayer (Figure 39). The critical force calculated during the pull-apart process at various strain points can accurately determine the critical stress and strain.

The point at which the separation occurs is the point of maximum interaction between the monomer and surface and can be called the separation point. Moreover, if a further strain is applied to the complex, then the force will decrease until it vanishes, indicating that the applied external force has overcome the mechanical strength at the interface of the complex.

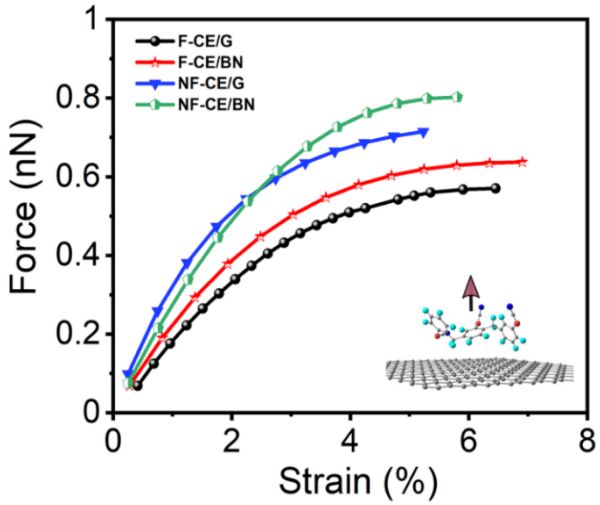

Figure 38: Calculated force vs. transverse strain curve of the ester/monolayer; AroCy-F10 (fluorinated cyanate ester) labeled as F-CE and Primaset PT-30 (non-fluorinated cyanate ester) labeled as NF-CE. G refers to graphene, and BN refers to a BN monolayer

Application of the 1D-SEOS allows us to derive transverse strength and separation point values for the ester complexes based on the associated fitting parameters σ_{sp}, ϵ_{sp} respectively (Table 11). Furthermore, we would like to point out that pseudocritical exponent (i.e., γ) varies between 0.5 and 0.8 (Table 11) for the ester complexes within the stretching region of the spinodal stress-strain equation of state. For a solid under high pressure, γ is reported to be 0.85 [149]. On the other hand, the lower values of γ (~0.5) [141] are attributed to the stretching region of the curve.

Table 11 shows the computed transverse stiffness as well as separation point values, which are used to describe the mechanical behavior of the ester complexes. According to our findings, the non-fluorinated ester has a higher transverse strength than the fluorinated

ester with the hierarchical order being AroCy F-$10_{(graphene)}$ < AroCy F-$10_{(BN)}$ < Primaset PT-$30_{(graphene)}$ < Primaset PT-$30_{(BN)}$. Interestingly, the fluorinated ester is predicted to have a relatively higher separation point than the non-fluorinated ester, enhancing its interfacial load transfer. This fact can be attributed to the influence of flourine atoms which cause steric hindrance as well as interlocking effects in the fluorinated case, and hence it prevents its separation against the surface, as reported previously [166].

Table 11: Predicted transverse strength and (out-of-plane) separation point of the fluorinated and non-fluorinated cyanate ester complexes formed with graphene (or BN) monolayer

Complex		**Transverse strength f_c (nN)**	**(Out-of-plane) Separation point, εc (%)**	**Transverse stress (GPa)**	**Stiffness**	**Gamma, γ**
Graphene	AroCy-F10 (fluorinated)	0.57	0.6	0.18	0.65	5.9
Graphene	Primaset PT-30 (non-fluorinated)	0.71	0.7	0.26	0.76	5.2
BN monolayer	AroCy-F10 (fluorinated)	0.63	0.7	0.20	0.54	6.4
BN monolayer	Primaset PT-30 (non-fluorinated)	0.80	0.8	0.25	0.63	5.8

Figure 40 summarizes the result of the present study displaying the predicted relationship between the interaction strength and the mechanical response in terms of transverse stress and stiffness for cyanate ester complexes. A stress-strain data is given in Figure 40, and Table 11 lists the calculated values for which the effective contact area at the interface was estimated using the projected length and width of the ester monomer over graphene (or BN monolayer).

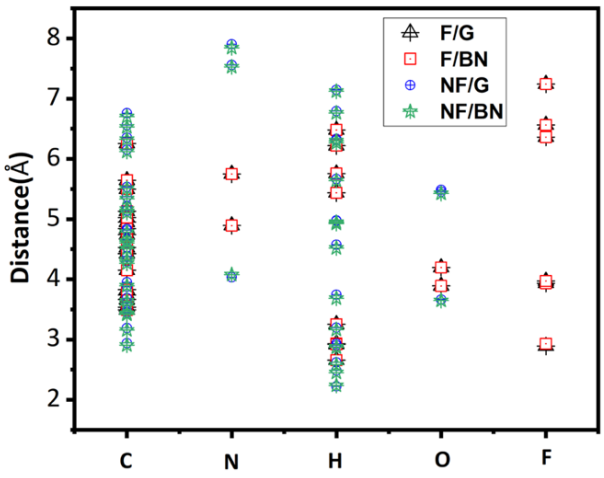

Figure 39: The distances between the atoms of the fluorinated and non-fluorinated ester monomer with nearest C atom of graphene and nearest B or N atom of BN monolayer

The results predict the non-fluorinated ester complexes to be stiffer than the fluorinated ester complexes following the order obtained for the interaction energy values (Table 10). Given that (out-of-plane) stiffness is related to quasi-3D Young's modulus, a relatively high stiffness value results in a higher Young's modulus at the interface, which is one of

the polymer composite's useful features for structural and aerospace applications. It is significant to mention that the calculated separation point values of the cured fluorinated/flCNT and non-fluorinated/flCNT are predicted to be 0.6 and 1.1, respectively, by employing the Polymer Consistent Force Field - Interface Force Field (PCFF-IFF) model in molecular dynamics (MD) computations [167].

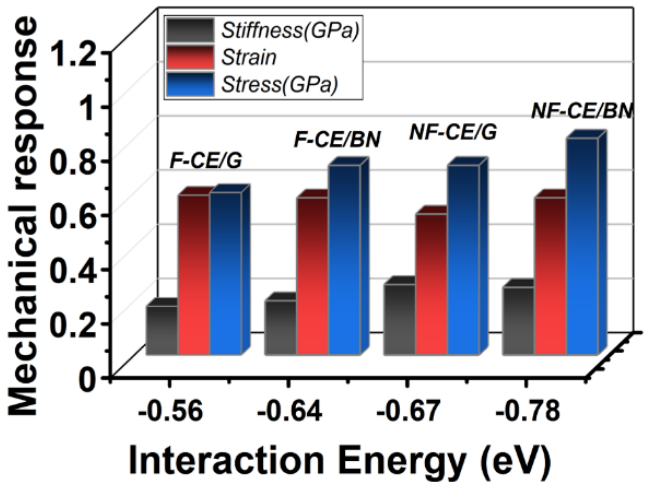

Figure 40: Calculated mechanical response and the interaction energy of the ester complexes; AroCy-F10 (fluorinated cyanate ester) labeled as F-CE and Primaset PT-30 (non-fluorinated cyanate ester) labeled as NF-CE. Also, G refers to graphene, and BN refers to a BN monolayer

5.4 Conclusion

To provide a molecular-level understanding of the interfacial properties of fluorinated and non-fluorinated cyanate esters forming complexes with graphene (or BN) monolayer, state-of-the-art DFT simulations are conducted. We find that the nature of the interface depends on the specific monomer configuration, with the non-fluorinated monomer markedly possessing a higher degree of interaction with graphene (or BN) monolayer than the fluorinated monomer. This leads to a smaller transverse strength but a higher separation point for the fluorinated ester. This may explain the higher steric hindrance associated with fluorine groups at the interface. Despite the limited flexibility of the fluorinated ester which reduces the interaction energy, it seems to provide mechanical interlocking that increases the transverse strain at the interface. Therefore, the present study has enabled us to elucidate the properties at the molecular level that are difficult to determine by experiments. Moreover, we show that the BN-based ester complexes are likely to have a higher mechanical strength than those based on graphene, thus, can be considered as structural materials in aerospace vehicles.

6 Mechanical Response of polymer/BN Composites Investigated by Molecular Dynamics Method

6.1 Introduction

Polymer composite materials are important to many industries, such as the automobile and aerospace industries because of their superior strength to weight ratio[168]. As a reinforcement for polymer composites, carbon nanotubes (CNTs) have received increased attention due to their high aspect ratios and high intrinsic strength of the sp^2–sp^2 covalent bond between carbon atoms. With high tensile strength, high fracture strain, and high elastic modulus, CNTs even show exceptionally high mechanical responses[169].

Numerous techniques have been used in the past to improve the surface activity, roughness, and wettability of fiber/reinforcement materials in order to promote the interfacial adhesion between the reinforcement and matrix for better mechanical performance[170]. Increasing non-covalent bond interaction between fibers and matrix, such as van der Waals forces, hydrogen bond interaction, and electrostatic interaction could also enhance the bond to improve interfacial properties without deteriorating single fiber tensile strength[171]. Even techniques such as oxidation[172], plasma treatment[173], sizing/coating, and vapor deposition helped to improve the wettability[174], chemical bonding, and mechanical interlocking[175] between fiber and matrix and result in an excellent performance to meet the comprehensive requirements of some scientific fields.

This study utilized one of these methods to explore how polar/electrostatic surfaces change the interface interaction.

Soon after the synthesis of CNTs[118], efforts were made to search for noncarbon tubular materials; the stability of boron nitride nanotubes (BNNTs) was predicted by exploring the similarity between hexagonal BN and graphite structures[176] followed by the synthesis of BNNTs[177]. It is noteworthy that BNNTs are expected to be even more thermally efficient than CNTs[178]. BNNTs have superior mechanical properties, including the strength (165 GPa)[179], high Young's modulus (0.8 TPa), and high thermal stability[180]. Subsequently, applications of BNNTs have been suggested in a wide range of industries, including automotive[33, 181], aerospace[182], healthcare and medicine[183], energy storage[184], and electronics[185].

While many efforts have been devoted to incorporating CNT/graphene into polymer materials[27, 186], the BN/polymer composites are less explored. Moreover, the partial ionic electronic structure of B-N bonding can be advantageous in terms of its atomic-level interaction with polymer[187], though the tubular surface of a BNNT is likely to interact via van der Waals (vdW) forces with polymers as the case with carbon-based reinforcements[188].

Another design factor that contributes to polymer composites with excellent mechanical properties is the choice of polymer resin. The features of the polymer/reinforcement

interface have long been known to have a major impact on bulk-level properties, and computational modeling techniques can be utilized to predict these effects[189]. As a result, computational modeling can aid in the selection of polymers for composite systems in order to get the best molecular-level interfacial features and thus bulk-level properties. High-performance polymers used for structural purposes in aerospace vehicles are of particular relevance. The interfacial characteristics of typical nanocomposites, consisting of epoxy resin (DGEBA/DETDA)[190], polystyrene (PS)[191], polyethylene[192], and polythiophene (PT)[191] filled with boron nitride derivatives, were investigated using molecular dynamics simulation[193] to study the strong interaction between BN and polymers; however, cyanate esters, epoxy (TGMDA/DDS), and BMI with BN surfaces are not yet explored.

In this chapter, we investigate four high-performance polymers: fluorinated cyanate ester, non-fluorinated cyanate ester, epoxy, and bismaleimide (BMI). The cyanate esters are characterized by phenol backbones with cyanate groups (-OCN) attached to each end. AroCy F-10 is a fluorinated cyanate ester shown in figure 1(a). Primaset-PT is a non-fluorinated cyanate ester, shown in figure 1(b)[167]. Cyanate esters are thermoset matrices generally used in aerospace and defense industries for high-temperature applications because of their low moisture absorption and low coefficient of thermal expansion, making them exceptionally thermally stable[156, 194].

Epoxy 977-3 is a two-component system, tetragly-cidyl methylene dianiline (TGMDA) and dia-mino-diphenyl sulfone (DDS)[195], shown in figure 41 (c). For a TGMDA/DDS system, the end groups are the epoxy (-C-O-C-) and amine (NH2) groups. Due to their good impregnation and adhesion to fiber reinforcement, epoxy resins are widely used for matrices in high-performance composites[196]. These resins offer excellent mechanical and electrical properties and chemical resistance when cured[197]. Bismaleimide (BMI) resin, on the other hand, is a two-component system- 4′-bismaleimidodiphenylmethane (BMPM) and *o*,*o*′-diallyl bisphenol A (DABPA), where maleimide and allyl are the end groups, respectively[195] (Figure 41(d)). Due to its excellent heat resistance, electrical insulation, radiation resistance, good dimensional stability, and mechanical properties, BMI resin is widely used in aviation, aerospace, and other industrial fields as the resin matrix of advanced composite materials[198]. Each of the polymers simulated in this work is unique in terms of reaction chemistry and molecular topology, and all of them are aerospace-related polymers.

While reinforcement or matrix has superior mechanical properties, this does not ensure that it will reflect directly in composites. However, these properties are strongly influenced by the physics that govern reinforcement–polymer interfaces. Interfacial load transfer is well known as a key factor for the bulk performance of polymer composites. The interface must be strong for the load to transfer efficiently from the reinforcement to the polymer.

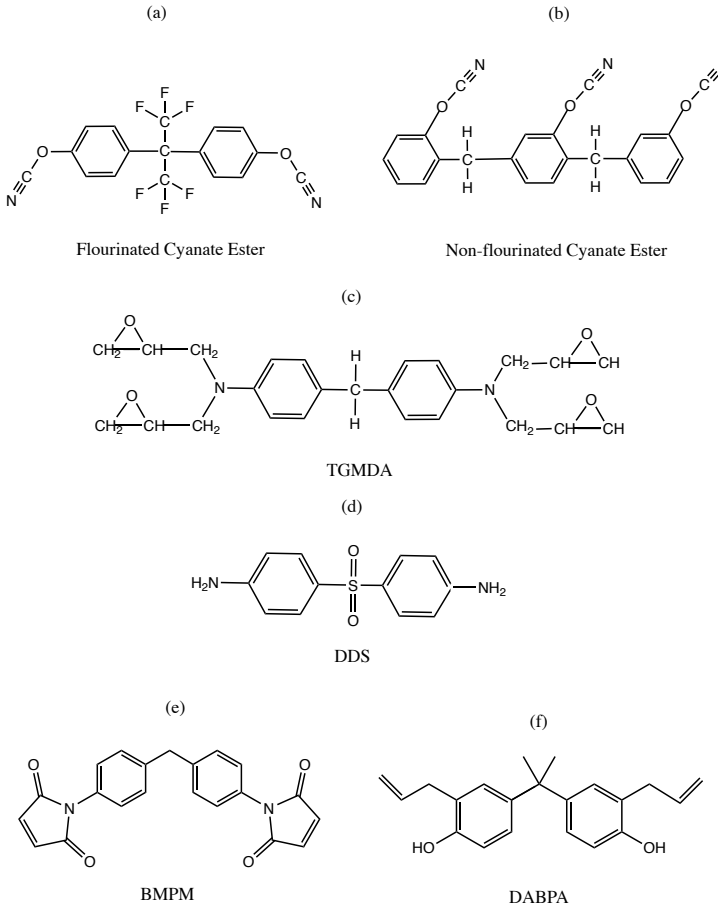

Figure 41: Chemical structures of (a) fluorinated cyanate ester, F10 (b) non-fluorinated cyanate ester, PT-30 (c) epoxy- DDS (hardener), TGMDA (resin) and, (d) BMI- DABPA (hardener), BMPM (resin). One-to-one molar ratios of TGMDA to DDS and BMPM to DABPA constitute the epoxy polymers and BMI, respectively

Pisani et al. used MD simulations to investigate the interfacial compatibility of a fluorinated and a non-fluorinated cyanate ester with flattened carbon nanotubes (flCNT)[26]. The authors found that the fluorinated cyanate ester/flCNT composite would

likely excel in applications with shear-dominated loads (due to the CF_3 groups) while the non-fluorinated cyanate ester would excel in applications with tensile loads normal to the flCNT alignment. Additionally, the authors found that different functional groups affected the interfacial properties differently. A similar study by Deshpande et al. investigated the compatibility of epoxy and BMI with flCNT using MD simulations and compared these two polymer composites with those of Pisani et al. and Patil et al. They predict that BMI has the greatest overall compatibility with flCNTs. However, similar polymer interfaces were not investigated using BN as reinforcement.

Therefore, our focus in this chapter is be to predict the relative differences in the mechanical response of (i) fluorinated and non-fluorinated cyanate esters and (ii) epoxy and BMI polymers forming the composite with a BN bilayer representing a fragment of the tubular surface of a large-diameter double-walled BNNT. Furthermore, the results were be compared with the previously published results for these polymers forming the composites with the large-diameter, flCNTs[195, 167], thereby identifying the advantages of a semi-polarized interface in forming a polymer composite.

6.2 Computational Details

We begin with constructing a periodic supercell (x=100 Å, y=50 Å) simulating a polymer/BN interface in which the interatomic interactions are described by the INTERFACE Force Field (IFF)[199]. It is important to note that IFF can quantify the

dihedral energies between atoms and assign accurate partial charges to molecules[199, 200]. Recently the IFF parameters were parameterized for B, N, and virtual pi electrons demonstrating that IFF can reliably predict interfacial properties such as wettability between polymer resin and BN surface[201].

Figure 42 shows the representative composite model used for all of the polymers investigated. A mass fraction of 0.4 polymers was considered following the guidance from previously published works on the polymer/flCNT composites[167, 195, 202]. The mass fraction can be defined as the ratio of the molecular mass of the monomer or polymer and the total mass of the system. The MD calculations were performed using the LAMMPS[203] software package, and OVITO[204] software was used to construct atomistic visuals.

Figure 43 displays the steps taken to investigate the mechanical response of well-equilibrated, polymerized BN/polymer composites. In step 1, the monomer structures were generated, followed by step 2. A BN monolayer was created using LAMMPS to generate initial atomic positions and a python script to add the required bond, angle, and dihedral information. The surface area of the monolayer is 5000 $Å^2$, with a total of 5760 B and N atoms. The monolayer structure was then replicated in the MD environment to create BN bilayer. Subsequently, the (NVT ensemble) MD run was performed for 50 ps at 300 K to obtain the equilibrated configuration of the bilayer. Note that, to accurately capture the Coulombic interaction with the polymer atoms at the interface, virtual pi atoms were added onto the B and N atoms[201].

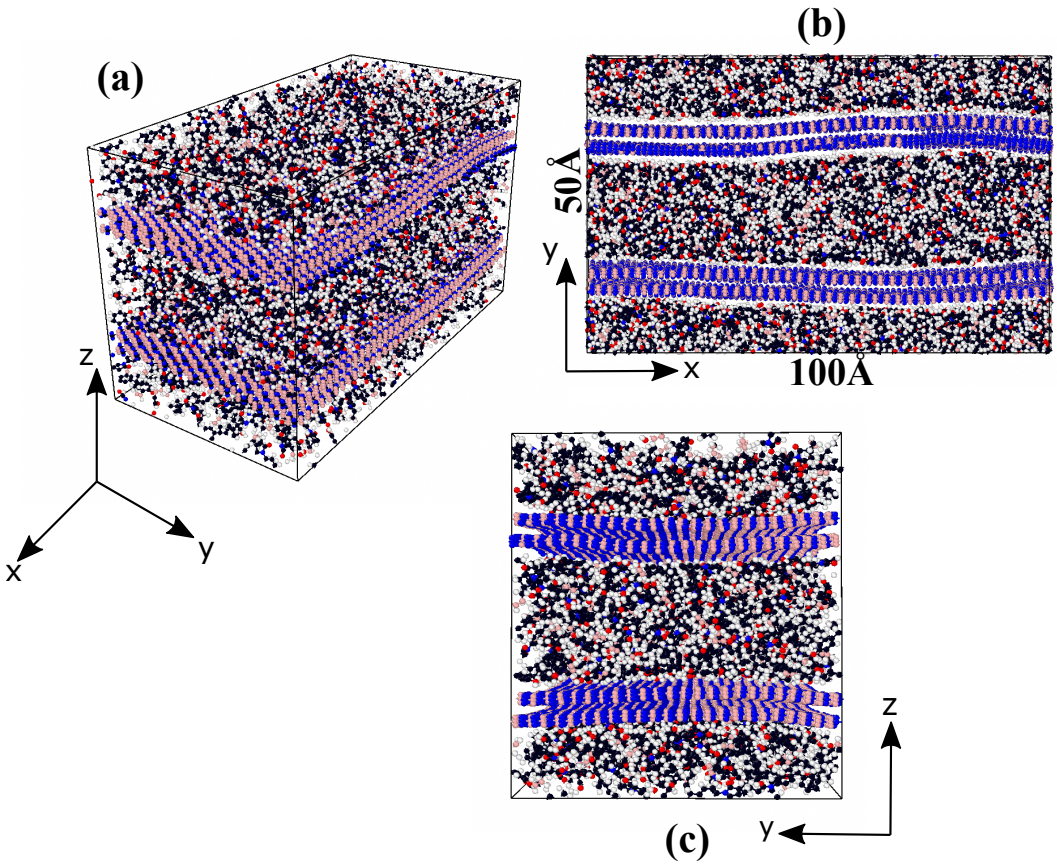

Figure 42: Representative model setup for the BMI/BN composite: (a) isometric view, (b) front view, and (c) side view

In step 3, the model was densified to achieve a mass density of 1.2 g/cm^3. Densification simulations were carried out using LAMMPS, implementing the "fix deform" command to align the x and y dimensions with those of the BN bilayer. The z-axis was reduced gradually with a rate of 10 Å/ns. For all simulations in this study, a timestep of 1.0 fs was chosen. The box boundaries were non-periodic during densification and set up to be

reflective using the "fix wall/reflect" command in LAMMPS such that atoms could not cross the boundary. This prevents any issues when combining the monomer with the BN bilayer in a later step.

Next, the second similar layer of densified monomer was duplicated to create a monomer bilayer. In a periodic simulation box, these two layers were separated by 10 Å in the *z*-direction. We apply the periodic boundary conditions to all three dimensions at this step. Note that the simulation box was kept similar to the dimensions of the BN (100 × 50 Å) in the *XY plane*. Open spaces were filled below and above the BN layers by inserting the monomer (e.g., epoxy) layers (step 4), as shown in figure 43. Energy minimization was carried out once the monomer/BN composite was assembled. The number of atoms in the periodic supercell varied between 39000 to 47000, depending on the monomer type.

Next, the single densified monomer layer was duplicated, creating a second identical layer. In a periodic simulation box, these two layers were separated by 10 Å in the *z*-direction. At this step, periodic boundaries were applied in three directions. Since the simulation box was bounded by the dimensions of the BN (100 × 50 Å) in the *XY plane*, open regions were formed both below and above the layers. The BN layers were inserted into the openings for step 4, as shown in figure 43 (d). This approach placed the monomer and BN layers immediately in close contact to keep the monolayer flat. Upon assembling the layers with a close fit, energy minimization was performed. The number of atoms in the periodic supercell varied between 39000 to 47000, depending on the monomer type.

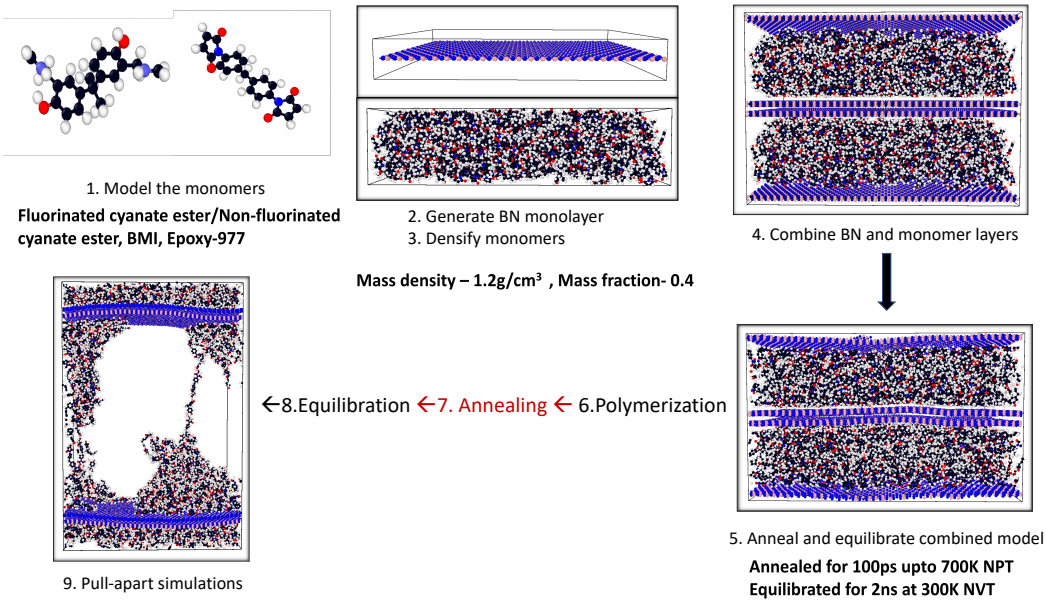

Figure 43: A schematic diagram showing the steps taken to calculate the mechanical response of a polymer/BN interface. Color codes: H-white, N-blue, O-red, C-black, B-pink

In step 5, an annealing simulation was run to bring the monomer configurations to a structural equilibrium. The model was annealed by simulating it at 700 K for 100 ps and then cooling it to 300 K over 5 ns, resulting in an 80 K/ns cooling rate. The maximum annealing temperature was chosen at 700K. It is at least 50 K greater than the glass transition temperature for all polymers, e.g., T_g for fluorinated cyanate ester is 540K and 450K for epoxy[205]. The monomer/BN system was further equilibrated for 2 ns at 300 K and 1 atm.

Next, in step 6, the polymerization simulations were carried out in the NPT ensemble at 300K using the "fix bond/react" command in LAMMPS[206]. The cyanate esters polymerize via cyclotrimerization, whereas BMI and epoxy prefer crosslinking. It is important to note that these polymerization reactions are adaptations to simplify the polymerization process, not actual polymerization reaction mechanisms. A set of pre-and post-reaction templates is employed in this approach to represent the molecular structure before and after a series of chemical reactions. The cyclotrimerization of esters involves three pre- and post-reaction templates, whereas epoxy and BMI polymerization necessitate one and two pre- and post-reaction templates, respectively. In cyclotrimerization, up to three bonds between monomers are generated until the reaction is complete, as shown in figure 44, labeled as I, II, and III, requiring one set of pre-and post-mapping templates for each reaction. The first set of templates forms the first bond between two monomers to form a dimer (Fig. 44, reaction I); the second set forms the bond between the dimer and the third monomer, making a trimer (Fig. 44, reaction II); and the third set forms the final bond to create the final polymerized template (Fig. 44, reaction III). Using three sets of templates with continuous bonding allows for greater flexibility in potential bond sites and network connectivity even if the entire ring is not produced. Every timestep, bonds may be formed between atoms separated by a maximum cutoff distance of 7 atoms. To target completing the cyclotrimer rings, the esters' second and third reaction probabilities were set higher than the first step.

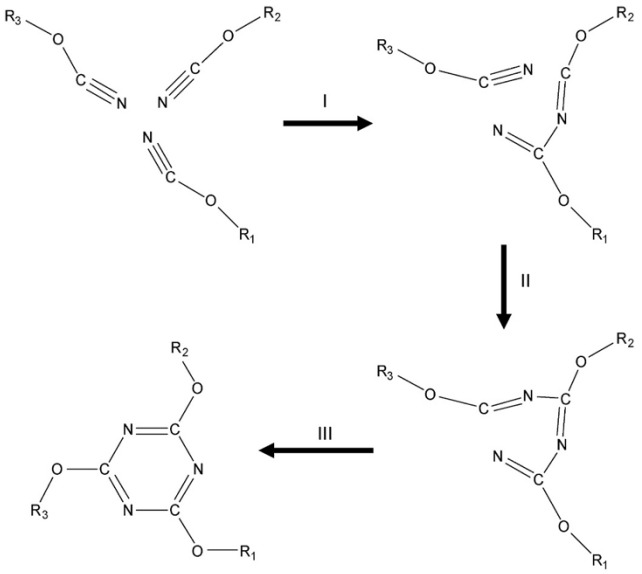

Figure 44: The bonding of three cyanate groups in ester monomers is referred to as cyclotrimerization for both fluorinated and non-fluorinated cyanate esters. The rest of the monomer is represented by "R"

As illustrated in figure 45, the epoxy system was polymerized via self-promoted crosslink processes. The breaking of the oxirane ring and bond formation with the main amine are the first steps in the epoxy crosslinking reaction followed by the secondary amine reconstructing the opening of another oxirane ring[207]. The polymerization reactions associated with BMI are known to be complicated[131]. Compared to other proposed reactions, ene reaction occurs quickly at lower temperatures and is projected to consume most of the maleimide and allyl groups in the equimolar case, which is the represented case[208]. The scope of this study is limited to the leading reaction in an equimolar

formulation as illustrated in figure 46. Ene adduct homopolymerization and etherification are among the processes that follow[209]. These processes are neglected to simplify the simulation and highlight the general influence of polymerization on the interaction energy[195].

The extent of monomer to polymer conversion for fluorinated cyanate ester, non-fluorinated cyanate ester, epoxy, and BMI was obtained as 91%, 95%, 82%, and 83%, respectively. In step 7, annealing was performed again at 700 K for 100 ps, followed by cooling to 300 K over 5 ns for a cooling rate of 80 K/ns. The simulation time for polymerization was 2 ns, with a 1 fs timestep. The ester, epoxy, and BMI monomers were polymerized using the same temperature and time parameters to keep the procedure consistent. The composites were further equilibrated after the polymerization and annealing steps (step 8) for 2 ns, as attested by figure 47, displaying a variation of the root-mean-square deviation (RMSD) with time. Note that RMSD represents the difference between a current position at a time and a reference position given by the center of mass. It is important to note that, until the monomer models were fully densified, a Lennard-Jones cutoff of 10.0 Å was used, and then the long-range interactions were taken into account for the polymer/BN composite system. For nonbonded Lennard-Jones and Coulombic interactions, the weighting coefficients were set at 0 for interactions involving 1–2, 0 for interactions involving 1–3, and 1 for interactions involving 1–4. As a result, atoms directly bonded or one bond away from each other experience no nonbonded interactions, but atoms two bonds apart fully experience nonbonded interactions.

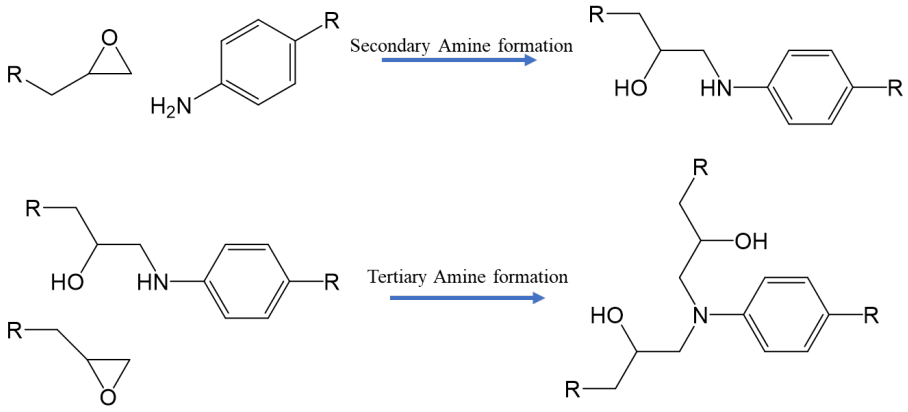

Figure 45: Epoxy monomers undergoing a two-step polymerization process. The rest of the monomer is represented by "R"

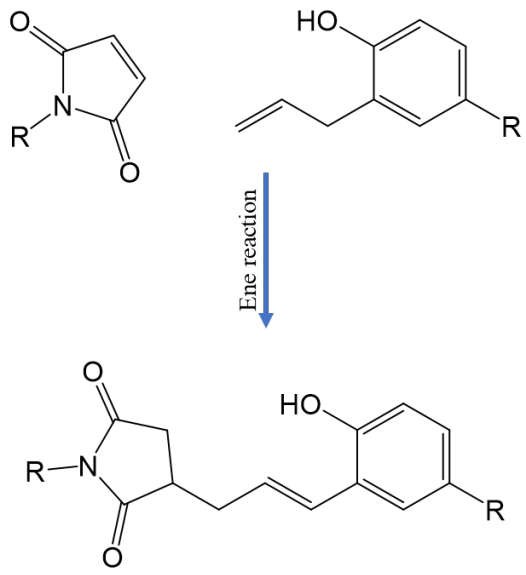

Figure 46: BMI monomers undergoing the ene reaction

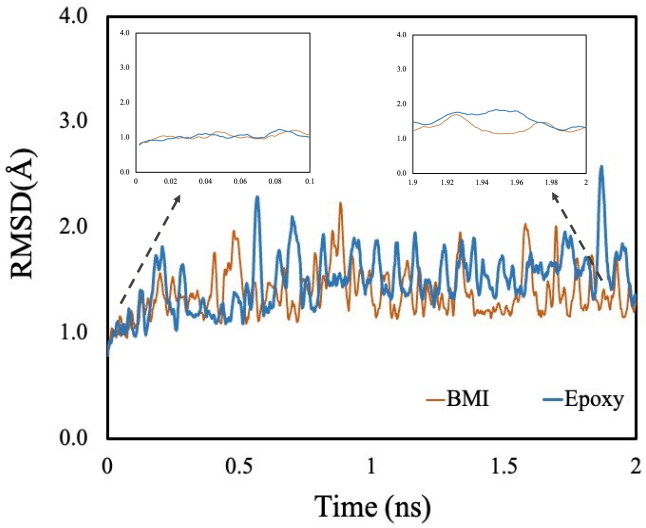

Figure 47: Calculated root-mean-square deviation (RMSD) variation with time for epoxy/BN and BMI/BN composites. Insets show the variation of RMSD from 0-0.1 and 1.9-2.0 ns

Finally, the mechanical response of the equilibrated composites was calculated, simulating the pull-apart experiments. A uniaxial strain was applied to the simulation box in a direction perpendicular to the BN plane until a maximum strain of 150% was reached, or complete separation occurred. Each composite system's stiffness, strength, and toughness were computed from the stress and strain recorded at each step.

6.3 Results and Discussions

6.3.1 Interaction Energy

The interaction energy (the nonbonded potential energy) between the polymer and the BN was extracted using the help of the "compute group/group" command in LAMMPS by averaging the values of 400 snapshots. A negative value of the interaction energy indicates attraction between the polymer and the bilayer. A more negative value than another indicates a greater attraction and thus a stronger interface. A stronger interface generally results in more load transfer from the polymer matrix to the BN reinforcement, thus allowing the composite to be used in more demanding applications.

Table 12: Calculated interaction energy of the polymer/BN composites.

Polymer/BN interface	**Polymer mass fraction (%)**	**Interaction energy (Kcal/mol)**	
		Un-polymerized	**Polymerized**
Fluorinated cyanate ester	40	-5372	-5065
Non-fluorinated cyanate ester	40	-6038	-5487
Epoxy	40	-5823	-5230
BMI	40	-6982	-6358

Table 12 lists the calculated interaction energy for cyanate esters, epoxy, and BMI polymers forming composites with a BN bilayer. The results suggest that BMI/BN has a stronger interface than the other polymer composites considered in this work. On the other hand, the non-fluorinated cyanate ester interface with BN interacts more strongly than the fluorinated cyanate ester interface with BN, possibly because the former contains an additional benzene ring and -OCN group. In a polymer composite consisting of graphitic materials, the van der Waals term dominates the interaction at the interface via the interaction of phenyl rings (of polymer) with the sp^2-bonded carbon rings (of a graphitic surface). Similarly, polymer-BN interfaces have cation- π and $\pi-\pi$ contributions from the phenyl rings that are present in polymers, which are illustrated in figure 48.

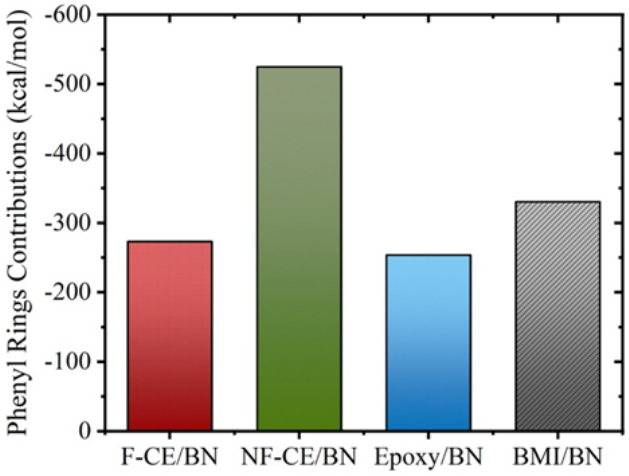

Figure 48: Interaction energy contribution per functional group for fluorinated (F), non-fluorinated (NF) cyanate esters (CE), epoxy, and BMI polymers forming the composite with a BN bilayer.

To evidence this response, we have provided an atom composition chart relating to all the models in Table 13, which shows that number of hydrogens is significantly higher than other atoms like oxygen and nitrogen. However, the number of carbon atoms which includes phenyl carbons as well as other carbons present in the polymers is also prominent and hence dictates the interaction energy contribution.

A higher degree of contributions from the phenyl groups for non-fluorinated ester relative to fluorinated ester or that for BMI relative to epoxy can be understood from the orientation of the phenyl groups in the equilibrated composite configurations. This is because the phenyl rings aligned to the sp^2-hybridized surface provide a significant contribution to the interaction energy. The orientation of a polymer relative to the surface was calculated by obtaining the dihedral angles of the phenyl rings on a plane relative to a plane of the bilayer. In this way, lower values of dihedral angles suggest a higher degree of alignment of phenyl rings with the BN surface. Similar findings are observed in MD based wetting study of epoxy on the BN surface [201].

Table 13: Atomic composition (in percentage) of fluorinated cyanate ester (F-CE), non-fluorinated cyanate ester (NF-CE), epoxy and BMI polymer models

	Atomic composition of polymer/BN models			
	F-CE	**NF-CE**	**Epoxy**	**BMI**
Total no. of atoms	39840	45040	47520	46608
H	9.6%	16.7%	24%	22%
C	20.5%	25.5%	21.2%	22.4%
O	2.4%	3.3%	3.4%	4.6%
N	2.4%	3.3%	2.3%	1.2%
F	7.2 %			
S			0.6%	
B (BN)	28.9%	25.6%	24.2%	24.5%
N (BN)	28.9%	25.6%	24.2%	24.5%

Figure 49 shows the distribution of the dihedral angles grouped into three categories, namely 0-10°, 11°-20°, and 21°-30° for both un-polymerized and polymerized cases. First, we notice that polymerization of the system results in fewer phenyl rings aligned parallel to the surface. This is obvious because the formation of networks during the polymerization process results in additional mobility constraints. Secondly, the BMI polymer shows a higher degree of alignment due to the planarization of the BMPM resin monomer (Figure 41D) relative to the case of epoxy/BN composite. As discussed previously, BMI polymer forms a more stable interface with the BN bilayers compared to the epoxy/BN composite. The fluorinated cyanate ester does not align well with the surface due to the trifluoromethyl groups causing greater steric hindrance in the polymer.

The non-fluorinated cyanate ester has more phenyl rings with dihedral angles in the range of 0-10° compared to the fluorinated cyanate ester, as also reported for cyanate esters forming composites with flCNTs[167].

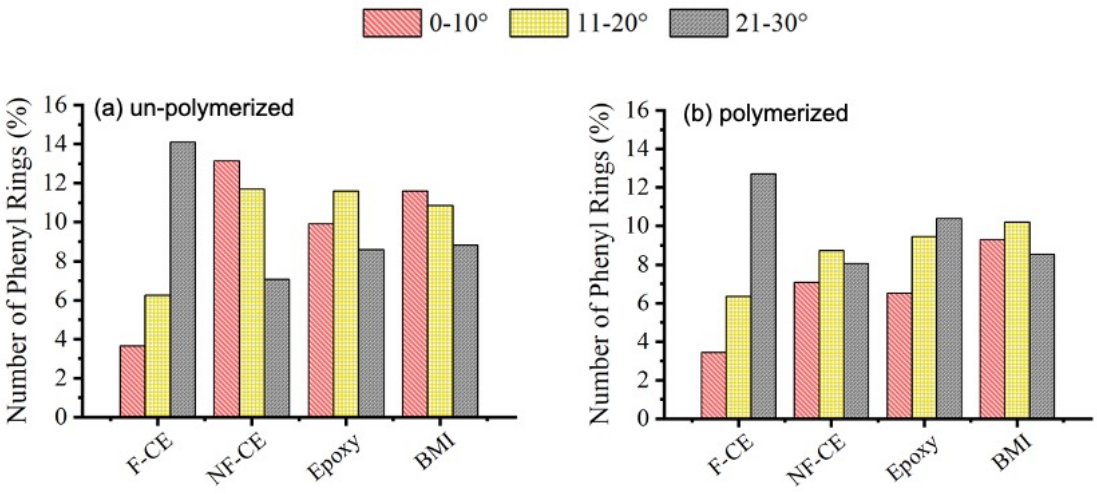

Figure 49: Percentage of phenyl rings less than the dihedral angle of 30 degrees near the BN compared to interaction energy for all four monomer/BN and polymer/BN systems

6.3.2 Mechanical Response

The mechanical response of the polymer/BN composites at 300 K and 1 atm was determined by applying a uniaxial tensile deformation to the composite systems normal to the BN bilayer. A strain of 150% of the equilibrated separation was applied (along the z-axis) for 7 ns with a timestep of 1 fs. Table 14 lists the mechanical response of the

polymer/BN composites in terms of peak strength, stiffness, and toughness. The peak strength in figure 50 is determined by the maximum stress in the simulation, stiffness is the ratio of stress versus strain in the linear portion of the stress-strain curve, and toughness is determined by the area under the stress-strain curve.

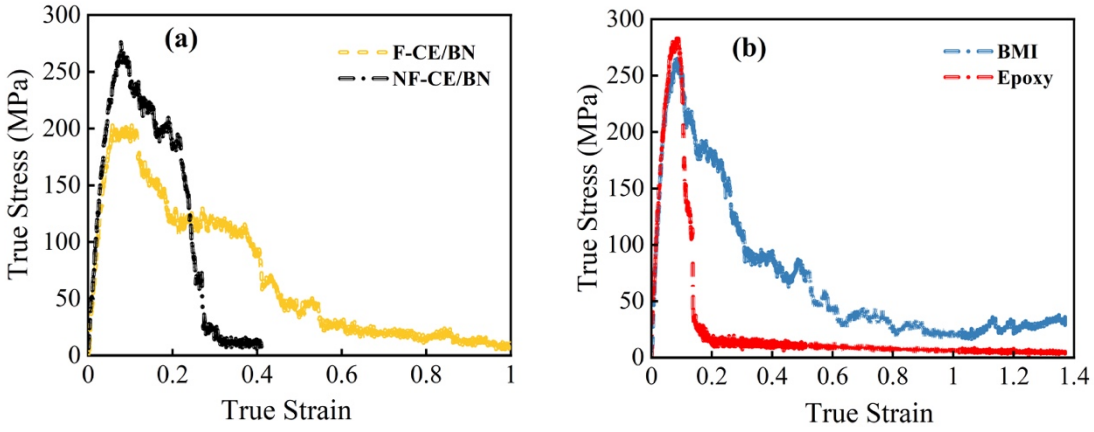

Figure 50: Calculated stress vs. strain curves for (a) fluorinated (F) and non-fluorinated (NF) cyanate esters and (b) epoxy and BMI forming complexes with a BN bilayer

Table 14: Mechanical response of polymer/BN composites

Polymer/BN composite	**Peak Strength (MPa)**	**Stiffness (GPa)**	**Toughness (MJ/m^3)**
Fluorinated ester	202.9	4.1	72.0
Non-fluorinated ester	276.1	4.8	51.5
Epoxy	283.0	4.9	37.0
BMI	265.4	5.2	98.0

The MD results for the cyanate ester/BN composites reveal that the non-fluorinated cyanate ester has a higher peak strength and stiffness than the fluorinated one, indicating that it is more resistant to (transverse tensile) delamination. On the other hand, fluorinated composites have significantly higher toughness than non-fluorinated ones, likely due to the steric hindrance of trifluoromethyl groups. Therefore, the fluorinated composites are more susceptible to fracture under the transverse tensile load. Snapshots of the atomistic configuration of fluorinated and non-fluorinated cyanate ester composites near the breaking point are shown in figure 51, displaying a sharper drop in the stress-strain curve as the interface breaks away quickly under transverse tensile load for non-fluorinated composite.

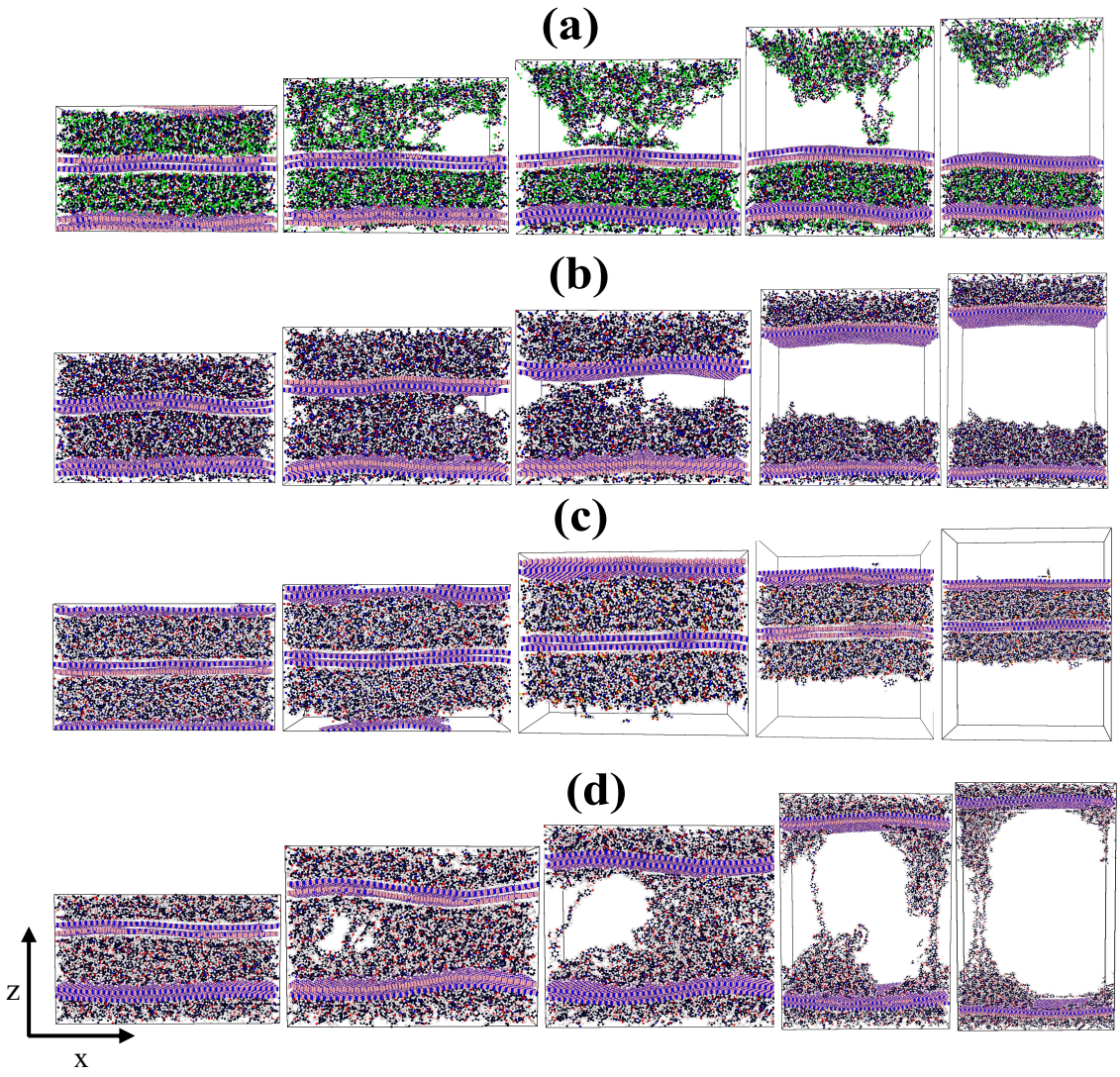

Figure 51: Snapshots for (a) fluorinated (F) cyanate ester (b) non-fluorinated (NF) cyanate ester (c) epoxy, and (d) BMI interfaces with BN Color codes: O- Red, H-White, B-pink, F- Green, N-Blue, C-Black, S- Yellow

Comparing the MD results obtained for the epoxy/BN and BMI/BN composites reveals that the former carries a lower toughness and stiffness, as attested by the stress-strain curves displayed in figure 50. It, therefore, appears to be a competition between the interlayer polymer-BN interaction at the interface and the intramolecular interaction within the polymer dictating the mechanical response of the composite under transverse tensile deformation. The epoxy/BN composite suddenly separates from the interface without breaking the polymer chains. In contrast, for the case of the BMI/BN composite, first, the polymer separates (cohesive failure) and then detaches from the interface (adhesive failure). Overall, the BMI/BN composite is predicted to have a higher (transverse tensile) fracture resistance despite stronger adhesion at the interface among the polymer composites considered. This may be due to the semi-ionic nature of the BN, together with the fact that the BMPM resin of BMI polymer exhibits a higher degree of planarization[210], yielding parallel orientation of the polymer with the surface.

Interestingly, the interface stability and the associated mechanical response of the polymer/BN composites obtained by the pull-apart simulations follow what was predicted for polymer/flCNT composites. For example, non-fluorinated ester forms a stronger interface with flCNT compared to that formed by fluorinated ester/flCNT composite. Non-fluorinated ester had higher transverse stiffness and peak strength but a lower toughness than fluorinated ester/flCNT composite[167].

Likewise, epoxy/flCNT composite forms a weaker interface relative to BMI/flCNT composite, with the interaction energy values being -5347 kcal/mol and -5987 kcal/mol, respectively[195] (Table 15). The BMI/flCNT is also predicted to have a significantly higher (transverse) stiffness and toughness than the epoxy/flCNT composite.

Table 15: Interaction energy of the polymer/flCNT composites[195]

	Interaction energy (kcal/mol)	
	un-polymerized	**polymerized**
F-CE/flCNT	-5816	-5283
NF-CE/ flCNT	-6374	-5626
Epoxy 977-3/ flCNT	-5901	-5346
BMI/ flCNT	-6040	-5987

6.4 Conclusion

The mechanical responses of fluorinated and non-fluorinated cyanate esters together with epoxy and BMI polymers forming interfaces with a BN bilayer representing a large diameter BNNT were investigated using the molecular dynamics method. Calculations find that the fluorine groups (-CF3) in the fluorinated ester cause steric hindrance, which decreases the polymer's flexibility and weakens the interface. The fluorinated cyanate ester interface is, therefore, predicted to have peak strength and (transverse) stiffness at the interface, which is smaller than the non-fluorinated interface. Epoxy/BN, on the other hand, have lower toughness and stiffness than BMI/BN, indicating a competition between the interlayer polymer-BN interaction at the interface and the intramolecular interaction within the polymer. In contrast, a higher degree of planarization of the BMI facilitates the strengthening of the interface, resulting in significantly higher toughness for the composite. It appears that BMI is the preferred polymer matrix when using BN nanomaterials as reinforcement compared to either cyanate ester or epoxy polymers. Based on the findings of the present study, it may be possible to guide the selection of resin systems in the development of new BN-based composites for structural applications, although none of the methodologies utilized in this study are immediately applicable when material selection is made. Therefore, a further experimental investigation is recommended to support the evidence before considering it for realization.

7 Summary and Future Perspectives

7.1 Summary

In the first part of this thesis, the optical absorption properties were investigated for multilayer 2D materials, namely antimonene, graphene, and borophene. The results based on first-principles calculations predict the absorbance in multilayer antimonene to be comparable to or higher than that calculated for multilayer graphene and borophene. We also find that multilayer borophene is nearly transparent with only a weak absorbance in the visible region, reflecting its anisotropic structural characteristics. Furthermore, a strong dependence of absorbance on topology is predicted for antimonene, graphene, and borophene, which results from the subtle variations in their stacking-dependent band structures. Multilayer antimonene is predicted to be a good candidate for optical power limiting applications in the IR region. In contrast, transparency in the visible region makes the multilayer borophene important for future photonics technologies.

In the second part of the thesis, molecular-level calculations were performed to relate the interfacial characteristics with the associated mechanical response in terms of stiffness using DFT and MD methods. Since the choice of the polymer matrix is an important factor in material design, the composite interface is formed by the resin (i.e., DGEBA and BMPM) or hardener (i.e., DETDA and DABPA) with graphene (or BN monolayer) was studied using DFT. The results show the nature of bonding at the interface governs the

interaction strength between resin (or hardener) and graphene. Subsequently, the mechanical response follows the hierarchical order of the interaction strength at the interface; the transverse stiffness of BMPM/graphene is higher than that of DGEBA/graphene. We also considered fluorinated and non-fluorinated cyanate ester monomers interacting with graphene (or BN) monolayer to understand how fluorine atoms influence the overall interfacial properties. We find that the fluorinated cyanate ester exhibits lower interaction energy and lower pull-apart force relative to the non-fluorinated cyanate ester, which is likely due to the steric hindrance of the fluorine atoms at the interface of the composite. Moreover, for all the monomers studied using DFT, the BN monolayer provides enhanced interfacial strength and, thereby, an improved transverse stiffness due to the semi-ionic nature of B–N bonds of the surface.

An MD study of the cyanate esters, BMI, and Epoxy 977-3 polymers with BN reinforcement was performed to analyze the effect of polymerization and the mechanical properties at the bulk level. Among the polymers considered, the planarity of BMI appears to play a major role in strengthening the interface between the polymers and the BN monolayer. Simulations of the pull-apart transverse tension experiment result in stiffer and tougher non-fluorinated ester interfaces than fluorinated ester interfaces. In contrast, epoxy/BN interfaces are predicted to have a much lower toughness (or resistance to fracture) than BMI/BN interfaces. Therefore, the BMI polymer matrix appears to be the preferred option for BN nanomaterials for structural applications compared to either

cyanate ester polymers or epoxy polymers. The results obtained at the molecular level are intended to help design the next-generation composites for structural applications.

7.2 Future Work

In this thesis, we have studied the optical properties of multilayered 2D materials like graphene, antimonene, and borophene using DFT. We have analyzed the structure-property relationships of polymers with graphene (or BN) interface. In terms of basic understanding, we have carried out a limited study on the optical properties of 2D materials and the mechanical properties of polymer composites. In the future, one needs to look into the heterostructures based on the elemental monolayers considered for optoelectronics applications.

For the polymer/BN composites, a detailed study of the various mass fractions of the composite will be valuable for comparing results with those previously obtained for polymer/flCNT composites. Also, while we used MD to study transverse tension for polymer/BN composites in this research, the influence of longitudinal tension on mechanical characteristics of identical composites could be interesting. Moreover, a similar methodology can be applied to examine other polymers' interactions with graphene or BN surfaces. It is expected that other high-performance polymer systems will need to be evaluated to determine which material is best suited for structural components in future aerospace vehicles.

8 Reference List

(1) Hanakata, P. Z. F. Studies of two-dimensional materials beyond graphene: from first-principles to machine learning approaches. Boston University, 2019.
(2) Tang, Y. *Two dimensional layered materials: First-principle investigation*; The Pennsylvania State University, 2016.
(3) Das, S.; Robinson, J. A.; Dubey, M.; Terrones, H.; Terrones, M. Beyond graphene: progress in novel two-dimensional materials and van der Waals solids. *Annual Review of Materials Research* 2015, *45*, 1-27.
(4) Xia, F.; Wang, H.; Xiao, D.; Dubey, M.; Ramasubramaniam, A. Two-dimensional material nanophotonics. *Nature Photonics* 2014, *8* (12), 899-907.
(5) Ponraj, J. S.; Xu, Z.-Q.; Dhanabalan, S. C.; Mu, H.; Wang, Y.; Yuan, J.; Li, P.; Thakur, S.; Ashrafi, M.; Mccoubrey, K. Photonics and optoelectronics of two-dimensional materials beyond graphene. *Nanotechnology* 2016, *27* (46), 462001.
(6) Zhang, T.; Lin, J. H.; Yu, Y. M.; Chen, X. R.; Liu, W. M. Stacked bilayer phosphorene: strain-induced quantum spin Hall state and optical measurement. *Sci Rep* 2015, *5*, 13927. DOI: 10.1038/srep13927.
(7) Wang, J. Two-dimensional semiconductors for ultrafast photonic applications. In *Optical Components and Materials XII*, 2015; International Society for Optics and Photonics: Vol. 9359, p 935902.
(8) Luo, A.-P.; Liu, M.; Wang, X.-D.; Ning, Q.-Y.; Xu, W.-C.; Luo, Z.-C. Few-layer MoS 2-deposited microfiber as highly nonlinear photonic device for pulse shaping in a fiber laser. *Photonics Research* 2015, *3* (2), A69-A78. Sobon, G. Mode-locking of fiber lasers using novel two-dimensional nanomaterials: graphene and topological insulators. *Photonics Research* 2015, *3* (2), A56-A63.
(9) Vela, A.; Moutinho, M.; Culchac, F.; Venezuela, P.; Capaz, R. B. Electronic structure and optical properties of twisted multilayer graphene. *Physical Review B* 2018, *98* (15), 155135.
(10) Hong, S.-Y.; Dadap, J. I.; Petrone, N.; Yeh, P.-C.; Hone, J.; Osgood Jr, R. M. Optical third-harmonic generation in graphene. *Physical Review X* 2013, *3* (2), 021014.
(11) Zhang, W.; Wang, Q.; Chen, Y.; Wang, Z.; Wee, A. T. Van der Waals stacked 2D layered materials for optoelectronics. *2D Materials* 2016, *3* (2), 022001.
(12) Butler, S. Z.; Hollen, S. M.; Cao, L.; Cui, Y.; Gupta, J. A.; Gutiérrez, H. R.; Heinz, T. F.; Hong, S. S.; Huang, J.; Ismach, A. F. Progress, challenges, and opportunities in two-dimensional materials beyond graphene. *ACS Nano* 2013, *7* (4), 2898-2926. Kiraly, B.; Liu, X.; Wang, L.; Zhang, Z.; Mannix, A. J.; Fisher, B. L.; Yakobson, B. I.; Hersam, M. C.; Guisinger, N. P. Borophene synthesis on Au (111). *ACS Nano* 2019, *13* (4), 3816-

3822. Wang, Z.-Q.; Lü, T.-Y.; Wang, H.-Q.; Feng, Y. P.; Zheng, J.-C. Review of borophene and its potential applications. *Frontiers of Physics* 2019, *14* (3), 1-20. Matthes, L.; Gori, P.; Pulci, O.; Bechstedt, F. Universal infrared absorbance of two-dimensional honeycomb group-IV crystals. *Physical Review B* 2013, *87* (3), 035438.
(13) Singh, D.; Gupta, S. K.; Sonvane, Y.; Lukačević, I. Antimonene: a monolayer material for ultraviolet optical nanodevices. *Journal of Materials Chemistry C* 2016, *4* (26), 6386-6390.
(14) Wang, Q. H.; Kalantar-Zadeh, K.; Kis, A.; Coleman, J. N.; Strano, M. S. Electronics and optoelectronics of two-dimensional transition metal dichalcogenides. *Nature Nanotechnology* 2012, *7* (11), 699-712.
(15) Massicotte, M. Ultrafast optoelectronics in 2D materials and their heterostructures. 2017.
(16) Hunt, W. H. Nanomaterials: Nomenclature, novelty, and necessity. *Jom* 2004, *56* (10), 13-18.
(17) Hafner, J. Ab-initio simulations of materials using VASP: Density-functional theory and beyond. *Journal of Computational Chemistry* 2008, *29* (13), 2044-2078.
(18) Cheng, J.; Wang, C.; Zou, X.; Liao, L. Recent advances in optoelectronic devices based on 2D materials and their heterostructures. *Advanced Optical Materials* 2019, *7* (1), 1800441.
(19) Neto, A. C.; Guinea, F.; Peres, N. M.; Novoselov, K. S.; Geim, A. K. The electronic properties of graphene. *Reviews of Modern Physics* 2009, *81* (1), 109.
(20) Geim, A. K.; Novoselov, K. S. The rise of graphene. In *Nanoscience and technology: a collection of reviews from nature journals*, World Scientific, 2010; pp 11-19.
(21) Huang, X.; Yin, Z.; Wu, S.; Qi, X.; He, Q.; Zhang, Q.; Yan, Q.; Boey, F.; Zhang, H. Graphene-based materials: synthesis, characterization, properties, and applications. *Small* 2011, *7* (14), 1876-1902. Wang, J.; Hernandez, Y.; Lotya, M.; Coleman, J. N.; Blau, W. J. Broadband nonlinear optical response of graphene dispersions. *Advanced Materials* 2009, *21* (23), 2430-2435.
(22) Yang, L.; Deslippe, J.; Park, C.-H.; Cohen, M. L.; Louie, S. G. Excitonic effects on the optical response of graphene and bilayer graphene. *Physical review letters* 2009, *103* (18), 186802.
(23) Ferrari, A. C.; Bonaccorso, F.; Fal'Ko, V.; Novoselov, K. S.; Roche, S.; Bøggild, P.; Borini, S.; Koppens, F. H.; Palermo, V.; Pugno, N. Science and technology roadmap for graphene, related two-dimensional crystals, and hybrid systems. *Nanoscale* 2015, *7* (11), 4598-4810.
(24) Wang, J.; Ma, F.; Sun, M. Graphene, hexagonal boron nitride, and their heterostructures: properties and applications. *RSC Advances* 2017, *7* (27), 16801-16822.

(25) Guo, Q.; Wang, G.; Batista, E. R.; Lau, K. C.; Yang, P. Two-Dimensional Nanomaterials as Anticorrosion Surface Coatings for Uranium Metal: Physical Insights from First-Principles Theory. *ACS Applied Nano Materials* 2021, *4* (5), 5038-5046.
(26) Bharech, S.; Kumar, R. A review on the properties and applications of graphene. *J Mater Sci Mech Eng* 2015, *2* (10), 70.
(27) Stankovich, S.; Dikin, D. A.; Dommett, G. H.; Kohlhaas, K. M.; Zimney, E. J.; Stach, E. A.; Piner, R. D.; Nguyen, S. T.; Ruoff, R. S. Graphene-based composite materials. *Nature* 2006, *442* (7100), 282-286.
(28) Papageorgiou, D. G.; Kinloch, I. A.; Young, R. J. Mechanical properties of graphene and graphene-based nanocomposites. *Progress in Materials Science* 2017, *90*, 75-127.
(29) Wei, J.; Atif, R.; Vo, T.; Inam, F. Graphene nanoplatelets in epoxy system: dispersion, reaggregation, and mechanical properties of nanocomposites. *Journal of Nanomaterials* 2015, *2015*.
(30) Nieto, A.; Bisht, A.; Lahiri, D.; Zhang, C.; Agarwal, A. Graphene reinforced metal and ceramic matrix composites: a review. *International Materials Reviews* 2017, *62* (5), 241-302. Young, R. J.; Kinloch, I. A.; Gong, L.; Novoselov, K. S. The mechanics of graphene nanocomposites: a review. *Composites Science and Technology* 2012, *72* (12), 1459-1476.
(31) Kondo, T. Recent progress in boron nanomaterials. *Science and Technology of Advanced Materials* 2017, *18* (1), 780-804.
(32) Mashhadzadeh, A. H.; Fereidoon, A.; Ahangari, M. G. Atomistic modeling of interfacial interaction between polyvinyl chloride and polypropylene with Boron-Nitride monolayer sheet: a density functional theory study. *Superlattices and Microstructures* 2017, *111*, 23-31. Falin, A.; Cai, Q.; Santos, E. J.; Scullion, D.; Qian, D.; Zhang, R.; Yang, Z.; Huang, S.; Watanabe, K.; Taniguchi, T. Mechanical properties of atomically thin boron nitride and the role of interlayer interactions. *Nature Communications* 2017, *8* (1), 1-9.
(33) Rasul, M. G.; Kiziltas, A.; Arfaei, B.; Shahbazian-Yassar, R. 2D boron nitride nanosheets for polymer composite materials. *NPJ 2D Materials and Applications* 2021, *5* (1), 1-18.
(34) Verma, A.; Parashar, A.; Packirisamy, M. Atomistic modeling of graphene/hexagonal boron nitride polymer nanocomposites: a review. *Wiley Interdisciplinary Reviews: Computational Molecular Science* 2018, *8* (3), e1346.
(35) Schakel, A. M. Time-dependent Ginzburg-Landau theory and duality. In *Topological Defects and the Non-Equilibrium Dynamics of Symmetry Breaking Phase Transitions*, Springer, 2000; pp 213-238.
(36) Born, M.; Oppenheimer, R. Zur quantentheorie der molekeln. *Annalen Der Physik* 1927, *389* (20), 457-484.

(37) Giustino, F. *Materials modelling using density functional theory: properties and predictions*; Oxford University Press, 2014.
(38) Sholl, D.; Steckel, J. A. *Density functional theory: a practical introduction*; John Wiley & Sons, 2011.
(39) Engel, E.; Dreizler, R. M. *Density functional theory*; Springer, 2013.
(40) Runge, E. "Density-functional theory for time-dependent systems.". *Physical Review Letters 52, no. 12 (1984): 997.*
(41) Martin, R. M. *Electronic structure: basic theory and practical methods*; Cambridge university press, 2020.
(42) Scholl, D.; Steckel, J. DFT calculations for surfaces of solids. *Density Functional Theory: A Practical Introduction, John Wiley & Sons, Inc* 2009. Gilbert, T. L. Hohenberg-Kohn Theorem for Nonlocal External Potentials. *Physical Review B* 1975, *12* (6), 2111-2120. DOI: DOI 10.1103/PhysRevB.12.2111.
(43) Dreizler, R. M.; Gross, E. K. *Density functional theory: an approach to the quantum many-body problem*; Springer Science & Business Media, 2012.
(44) Patterson, J. D. Density-functional theory of atoms and molecules: Robert G. Parr and Weitao Yang. Oxford University Press, New York, and Clarendon Press, Oxford (1989). US $55. 333 pages. Pergamon: 1989.
(45) Sprinborg. Methods of electronic structure calculations: from molecules to solid. 2000.
(46) Runge, E. "Density-functional theory for time-dependent systems.". *Physical Review Letters 52, no. 12 (1984): 997.*
(47) Hohenberg, P.; Kohn, W. Inhomogeneous electron gas. *Physical Review* 1964, *136* (3B), B864.
(48) Kohn, W.; Sham, L. J. Self-consistent equations including exchange and correlation effects. *Physical Review* 1965, *140* (4A), A1133.
(49) Staroverov, V. N. Density-functional approximations for exchange and correlation. *A Matter of Density* 2012, 125-156.
(50) Orio, M.; Pantazis, D. A.; Neese, F. Density functional theory. *Photosynthesis Research* 2009, *102* (2-3), 443-453.
(51) Cohen, A. J.; Mori-Sánchez, P.; Yang, W. Challenges for density functional theory. *Chemical Reviews* 2012, *112* (1), 289-320.
(52) Perdew, J. P.; Burke, K.; Wang, Y. Generalized gradient approximation for the exchange-correlation hole of a many-electron system (vol 54, pg 16 533, 1996). *Physical Review B* 1998, *57* (23), 14999-14999. DOI: DOI 10.1103/PhysRevB.57.14999.
(53) Garrity, K. F.; Bennett, J. W.; Rabe, K. M.; Vanderbilt, D. Pseudopotentials for high-throughput DFT calculations. *Computational Materials Science* 2014, *81*, 446-452.

(54) Hehre, W. J.; Stewart, R. F.; Pople, J. A. self-consistent molecular-orbital methods. i. use of gaussian expansions of Slater-type atomic orbitals. *Journal of Chemical Physics* 1969, *51* (6), 2657-2664.
(55) Slater, J. C.; Phillips, J. C. Quantum theory of molecules and solids Vol. 4: The self-consistent field for molecules and solids. *Physics Today* 1974, *27*, 49.
(56) Demkov, A. A.; Sharia, O.; Luo, X. H.; Lee, J. Density functional theory of high-k dielectric gate stacks. *Microelectron Reliab* 2007, *47* (4-5), 686-693. DOI: 10.1016/j.microrel.2007.02.009.
(57) Kitchin, J. Modeling materials using density functional theory. *Boston, Free Software Foundation* 2008.
(58) Marcelli, G.; Sadus, R. J. Molecular simulation of the phase behavior of noble gases using accurate two-body and three-body intermolecular potentials. *The Journal of Chemical Physics* 1999, *111* (4), 1533-1540.
(59) Allen, M.; Tildesley, D. Computer Simulation of Liquids (Clarendon Press, Oxford, 1987). Alder, B. J.; Wainwright, T. E. Studies in molecular dynamics. I. General method. *Journal of Chemical Physics* 1959, *31* (2), 459-466.
(60) Frenkel, D.; Smit, B. *Understanding molecular simulation: from algorithms to applications*; Elsevier, 2001.
(61) Verlet, L. Computer" experiments" on classical fluids. I. Thermodynamical properties of Lennard-Jones molecules. *Physical Review* 1967, *159* (1), 98.
(62) Swope, W. C.; Andersen, H. C.; Berens, P. H.; Wilson, K. R. A computer simulation method for the calculation of equilibrium constants for the formation of physical clusters of molecules: Application to small water clusters. *The Journal of Chemical Physics* 1982, *76* (1), 637-649.
(63) Van Gunsteren, W. F.; Berendsen, H. J. A leap-frog algorithm for stochastic dynamics. *Molecular Simulation* 1988, *1* (3), 173-185.
(64) Rapaport, D. C. *The art of molecular dynamics simulation*; Cambridge university press, 2004.
(65) Frenkel, D.; Smit, B.; Tobochnik, J.; McKay, S. R.; Christian, W. Understanding molecular simulation. *Computers in Physics* 1997, *11* (4), 351-354.
(66) Jorgensen, W. L.; Maxwell, D. S.; Tirado-Rives, J. Development and testing of the OPLS all-atom force field on conformational energetics and properties of organic liquids. *Journal of the American Chemical Society* 1996, *118* (45), 11225-11236.
(67) Van Duin, A. C.; Dasgupta, S.; Lorant, F.; Goddard, W. A. ReaxFF: a reactive force field for hydrocarbons. *Journal of Physical Chemistry A* 2001, *105* (41), 9396-9409.
(68) Ares, P.; Aguilar-Galindo, F.; Rodríguez-San-Miguel, D.; Aldave, D. A.; Díaz-Tendero, S.; Alcamí, M.; Martín, F.; Gómez-Herrero, J.; Zamora, F. Mechanical isolation

of highly stable antimonene under ambient conditions. *Advanced Materials* 2016, *28* (30), 6332-6336.
(69) Lei, T.; Liu, C.; Zhao, J.-L.; Li, J.-M.; Li, Y.-P.; Wang, J.-O.; Wu, R.; Qian, H.-J.; Wang, H.-Q.; Ibrahim, K. Electronic structure of antimonene grown on Sb2Te3 (111) and Bi2Te3 substrates. *Journal of Applied Physics* 2016, *119* (1), 015302.
(70) Pumera, M.; Sofer, Z. 2D monoelemental arsenene, antimonene, and bismuthene: beyond black phosphorus. *Advanced Materials* 2017, *29* (21), 1605299.
(71) Gibaja, C.; Rodriguez-San-Miguel, D.; Ares, P.; Gómez-Herrero, J.; Varela, M.; Gillen, R.; Maultzsch, J.; Hauke, F.; Hirsch, A.; Abellán, G. Few-layer antimonene by liquid-phase exfoliation. *Angewandte Chemie International Edition* 2016, *55* (46), 14345-14349.
(72) Kou, L.; Ma, Y.; Tan, X.; Frauenheim, T.; Du, A.; Smith, S. Structural and electronic properties of layered arsenic and antimony arsenide. *The Journal of Physical Chemistry C* 2015, *119* (12), 6918-6922.
(73) Wang, G.; Pandey, R.; Karna, S. P. Atomically thin group V elemental films: theoretical investigations of antimonene allotropes. *ACS applied materials & interfaces* 2015, *7* (21), 11490-11496.
(74) Ji, J.; Song, X.; Liu, J.; Yan, Z.; Huo, C.; Zhang, S.; Su, M.; Liao, L.; Wang, W.; Ni, Z. Two-dimensional antimonene single crystals grown by van der Waals epitaxy. *Nature Communications* 2016, *7*, 13352.
(75) Wu, X.; Shao, Y.; Liu, H.; Feng, Z.; Wang, Y. L.; Sun, J. T.; Liu, C.; Wang, J. O.; Liu, Z. L.; Zhu, S. Y. Epitaxial Growth and Air-Stability of Monolayer Antimonene on PdTe2. *Advanced Materials* 2017, *29* (11), 1605407.
(76) Shao, Y.; Liu, Z.-L.; Cheng, C.; Wu, X.; Liu, H.; Liu, C.; Wang, J.-O.; Zhu, S.-Y.; Wang, Y.-Q.; Shi, D.-X. Epitaxial growth of flat antimonene monolayer: A new honeycomb analogue of graphene. *Nano Letters* 2018, *18* (3), 2133-2139.
(77) Mannix, A. J.; Zhou, X.-F.; Kiraly, B.; Wood, J. D.; Alducin, D.; Myers, B. D.; Liu, X.; Fisher, B. L.; Santiago, U.; Guest, J. R. Synthesis of borophenes: Anisotropic, two-dimensional boron polymorphs. *Science* 2015, *350* (6267), 1513-1516.
(78) Feng, B.; Zhang, J.; Zhong, Q.; Li, W.; Li, S.; Li, H.; Cheng, P.; Meng, S.; Chen, L.; Wu, K. Experimental realization of two-dimensional boron sheets. *Nature Chemistry* 2016, *8* (6), 563-568.
(79) Liu, X.; Wang, L.; Li, S.; Rahn, M. S.; Yakobson, B. I.; Hersam, M. C. Geometric imaging of borophene polymorphs with functionalized probes. *Nat Commun* 2019, *10* (1), 1642. DOI: 10.1038/s41467-019-09686-w.
(80) Feng, B.; Sugino, O.; Liu, R.-Y.; Zhang, J.; Yukawa, R.; Kawamura, M.; Iimori, T.; Kim, H.; Hasegawa, Y.; Li, H. Dirac fermions in borophene. *Physical Review Letters* 2017, *118* (9), 096401.

(81) Boustani, I.; Quandt, A.; Hernández, E.; Rubio, A. New boron based nanostructured materials. *Journal of Chemical Physics* 1999, *110* (6), 3176-3185. Ozdogan, C.; Mukhopadhyay, S.; Hayami, W.; Guvenc, Z.; Pandey, R.; Boustani, I. The unusually stable B100 fullerene, structural transitions in boron nanostructures, and a comparative study of α-and γ-boron and sheets. *Journal of Physical Chemistry C* 2010, *114* (10), 4362-4375. Saxena, S.; Tyson, T. A. Insights on the atomic and electronic structure of boron nanoribbons. *Physical Review Letters* 2010, *104* (24), 245502. Penev, E. S.; Bhowmick, S.; Sadrzadeh, A.; Yakobson, B. I. Polymorphism of two-dimensional boron. *Nano Letters* 2012, *12* (5), 2441-2445. Zheng, B.; Yu, H.-t.; Lian, Y.-f.; Xie, Y. Novel α-and β-type boron sheets: Theoretical insight into their structures, thermodynamic stability, and work functions. *Chemical Physics Letters* 2016, *648*, 81-86. Ogitsu, T.; Schwegler, E.; Galli, G. β-Rhombohedral Boron: At the Crossroads of the Chemistry of Boron and the Physics of Frustration. *Chemical Reviews* 2013, *113* (5), 3425-3449. Lau, K. C.; Pandey, R. Thermodynamic stability of novel boron sheet configurations. *Journal of Physical Chemistry B* 2008, *112* (33), 10217-10220.

(82) Li, D.; Gao, J.; Cheng, P.; He, J.; Yin, Y.; Hu, Y.; Chen, L.; Cheng, Y.; Zhao, J. 2D boron sheets: structure, growth, and electronic and thermal transport properties. *Advanced Functional Materials* 2020, *30* (8), 1904349.

(83) Bezugly, V.; Kunstmann, J.; Grundkötter-Stock, B.; Frauenheim, T.; Niehaus, T.; Cuniberti, G. Highly conductive boron nanotubes: transport properties, work functions, and structural stabilities. *ACS Nano* 2011, *5* (6), 4997-5005. Saxena, S. *Handbook of boron nanostructures*; CRC Press, 2016. Lau, K. C.; Pandey, R.; Pati, R.; Karna, S. P. Theoretical study of electron transport in boron nanotubes. *Applied Physics Letters* 2006, *88* (21), 212111. Xie, Z.; Meng, X.; Li, X.; Liang, W.; Huang, W.; Chen, K.; Chen, J.; Xing, C.; Qiu, M.; Zhang, B. Two-dimensional borophene: Properties, fabrication, and promising applications. *Research* 2020, *2020*.

(84) Zhang, Z.; Yang, Y.; Penev, E. S.; Yakobson, B. I. Elasticity, Flexibility, and Ideal Strength of Borophenes. *Advanced Functional Materials* 2017, *27* (9). DOI: 10.1002/adfm.201605059.

(85) Peng, B.; Zhang, H.; Shao, H.; Ning, Z.; Xu, Y.; Ni, G.; Lu, H.; Zhang, D. W.; Zhu, H. Stability and strength of atomically thin borophene from first principles calculations. *Materials Research Letters* 2017, *5* (6), 399-407. DOI: 10.1080/21663831.2017.1298539.

(86) Wang, H.; Li, Q.; Gao, Y.; Miao, F.; Zhou, X.-F.; Wan, X. The ideal tensile strength and phonon instability of borophene. *arXiv preprint arXiv:1602.00456* 2016.

(87) Peng, B.; Zhang, H.; Shao, H.; Xu, Y.; Zhang, R.; Zhu, H. The electronic, optical, and thermodynamic properties of borophene from first-principles calculations. *Journal of Materials Chemistry C* 2016, *4* (16), 3592-3598.

(88) Li, L.; Yu, Y.; Ye, G. J.; Ge, Q.; Ou, X.; Wu, H.; Feng, D.; Chen, X. H.; Zhang, Y. Black phosphorus field-effect transistors. *Nature Nanotechnology* 2014, *9* (5), 372-377.
(89) Mak, K. F.; Lee, C.; Hone, J.; Shan, J.; Heinz, T. F. Atomically thin MoS 2: a new direct-gap semiconductor. *Physical Review Letters* 2010, *105* (13), 136805.
(90) Kumar, A.; Sachdeva, G.; Pandey, R.; Karna, S. P. Optical absorbance in multilayer two-dimensional materials: Graphene and antimonene. *Applied Physics Letters* 2020, *116* (26), 263102.
(91) Perdew, J. P.; Burke, K.; Ernzerhof, M. Generalized gradient approximation made simple. *Physical review letters* 1996, *77* (18), 3865.
(92) Grimme, S. Semiempirical GGA-type density functional constructed with a long-range dispersion correction. *Journal of computational chemistry* 2006, *27* (15), 1787-1799.
(93) Adamska, L.; Sadasivam, S.; Foley IV, J. J.; Darancet, P.; Sharifzadeh, S. First-principles investigation of borophene as a monolayer transparent conductor. *Journal of Physical Chemistry C* 2018, *122* (7), 4037-4045.
(94) Nair, R. R.; Blake, P.; Grigorenko, A. N.; Novoselov, K. S.; Booth, T. J.; Stauber, T.; Peres, N. M.; Geim, A. K. Fine structure constant defines visual transparency of graphene. *Science* 2008, *320* (5881), 1308-1308.
(95) Bao, Q.; Zhang, H.; Wang, Y.; Ni, Z.; Yan, Y.; Shen, Z. X.; Loh, K. P.; Tang, D. Y. Atomic-layer graphene as a saturable absorber for ultrafast pulsed lasers. *Advanced Functional Materials* 2009, *19* (19), 3077-3083. Ke, F.; Chen, Y.; Yin, K.; Yan, J.; Zhang, H.; Liu, Z.; John, S. T.; Wu, J.; Mao, H.-k.; Chen, B. Large bandgap of pressurized trilayer graphene. *Proceedings of the National Academy of Sciences* 2019, *116* (19), 9186-9190. Lui, C. H.; Li, Z.; Mak, K. F.; Cappelluti, E.; Heinz, T. F. Observation of an electrically tunable band gap in trilayer graphene. *Nature Physics* 2011, *7* (12), 944.
(96) Mak, K. F.; Sfeir, M. Y.; Misewich, J. A.; Heinz, T. F. The evolution of electronic structure in few-layer graphene revealed by optical spectroscopy. *Proceedings of the National Academy of Sciences* 2010, *107* (34), 14999-15004.
(97) Mak, K. F.; Sfeir, M. Y.; Wu, Y.; Lui, C. H.; Misewich, J. A.; Heinz, T. F. Measurement of the optical conductivity of graphene. *Physical review letters* 2008, *101* (19), 196405.
(98) Mak, K. F.; Shan, J.; Heinz, T. F. Electronic structure of few-layer graphene: experimental demonstration of strong dependence on stacking sequence. *Physical review letters* 2010, *104* (17), 176404.
(99) Mohan, B.; Kumar, A.; Ahluwalia, P. A first principle study of interband transitions and electron energy loss in mono and bilayer graphene: Effect of external electric field. *Physica E: Low-dimensional Systems and Nanostructures* 2012, *44* (7-8), 1670-1674. Yang, L. First-principles study of the optical absorption spectra of electrically gated

bilayer graphene. *Physical Review B* 2010, *81* (15), 155445. Farooq, M. U.; Hashmi, A.; Hong, J. Thickness dependent optical properties of multilayer BN/Graphene/BN. *Surface Science* 2015, *634*, 25-30.
(100) Gajdoš, M.; Hummer, K.; Kresse, G.; Furthmüller, J.; Bechstedt, F. Linear optical properties in the projector-augmented wave methodology. *Physical Review B* 2006, *73* (4), 045112.
(101) He, M.; Quan, C.; He, C.; Huang, Y.; Zhu, L.; Yao, Z.; Zhang, S.; Bai, J.; Xu, X. Enhanced nonlinear saturable absorption of MoS2/graphene nanocomposite films. *The Journal of Physical Chemistry C* 2017, *121* (48), 27147-27153.
(102) Yadav, P.; Srivastava, P. K.; Ray, N.; Ghosh, S. Robustness of the universal optical transmittance in monolayer and multilayer graphene flakes under Coulomb interactions. *Physical Review B* 2016, *94* (12), 121406.
(103) Koshino, M. Stacking-dependent optical absorption in multilayer graphene. *New Journal of Physics* 2013, *15* (1), 015010.
(104) Zhu, S.-E.; Yuan, S.; Janssen, G. Optical transmittance of multilayer graphene. *EPL (Europhysics Letters)* 2014, *108* (1), 17007.
(105) Lucarini, V.; Saarinen, J. J.; Peiponen, K.-E.; Vartiainen, E. M. *Kramers-Kronig relations in optical materials research*; Springer Science & Business Media, 2005.
(106) Bao, C.; Yao, W.; Wang, E.; Chen, C.; Avila, J.; Asensio, M. C.; Zhou, S. Stacking-dependent electronic structure of trilayer graphene resolved by nanospot angle-resolved photoemission spectroscopy. *Nano Letters* 2017, *17* (3), 1564-1568.
(107) Min, H.; MacDonald, A. H. Chiral decomposition in the electronic structure of graphene multilayers. *Physical Review B* 2008, *77* (15), 155416. Lobato, I.; Partoens, B. Multiple Dirac particles in AA-stacked graphite and multilayers of graphene. *Physical Review B* 2011, *83* (16), 165429.
(108) You, J.; Bongu, S.; Bao, Q.; Panoiu, N. Nonlinear optical properties and applications of 2D materials: theoretical and experimental aspects. *Nanophotonics* 2018, *8* (1), 63-97.
(109) Xu, Y.; Peng, B.; Zhang, H.; Shao, H.; Zhang, R.; Zhu, H. First-principle calculations of optical properties of monolayer arsenene and antimonene allotropes. *Annalen der Physik* 2017, *529* (4), 1600152.
(110) Mužević, M.; Pajtler, M. V.; Gupta, S. K.; Lukačević, I. Modulation Of Optical Properties With Multilayer Thickness In Antimonene And Indiene. *Advanced Materials Letters* 2019, *10* (4), 270-274.
(111) Aktürk, O. Ü.; Özçelik, V. O.; Ciraci, S. Single-layer crystalline phases of antimony: Antimonenes. *Physical review B* 2015, *91* (23), 235446.
(112) Sun, H.; Li, Q.; Wan, X. First-principles study of thermal properties of borophene. *Physical Chemistry Chemical Physics* 2016, *18* (22), 14927-14932.

(113) Zhong, H.; Huang, K.; Yu, G.; Yuan, S. Electronic and mechanical properties of few-layer borophene. *Physical Review B* 2018, *98* (5), 054104.
(114) Xu, J.; Zhang, J.; Zhang, W.; Lee, C.-S. Interlayer Nanoarchitectonics of Two-Dimensional Transition-Metal Dichalcogenides Nanosheets for Energy Storage and Conversion Applications. *Advanced Energy Materials* 2017, *7* (23). DOI: 10.1002/aenm.201700571.
(115) Ramasubramaniam, A.; Naveh, D.; Towe, E. Tunable band gaps in bilayer transition-metal dichalcogenides. *Physical Review B* 2011, *84* (20), 205325.
(116) Radue, M. Molecular Modeling of Aerospace Polymer Matrices Including Carbon Nanotube-Enhanced Epoxy. 2017.
(117) Melro, L.; Pyrz, R.; Jensen, L. R. A molecular dynamics study on the interaction between epoxy and functionalized graphene sheets. In *37th Risø International Symposium on Materials Science*, 2016; IOP Publishing: pp 363-372.
(118) Iijima, S. Helical microtubules of graphitic carbon. *Nature* 1991, *354* (6348), 56-58.
(119) Iijima, S.; Brabec, C.; Maiti, A.; Bernholc, J. Structural flexibility of carbon nanotubes. *The Journal of chemical physics* 1996, *104* (5), 2089-2092. Cornwell, C.; Wille, L. Elastic properties of single-walled carbon nanotubes in compression. *Solid state communications* 1997, *101* (8), 555-558.
(120) Popov, V. N. Carbon nanotubes: properties and application. *Materials Science and Engineering: R: Reports* 2004, *43* (3), 61-102. Thostenson, E. T.; Li, C.; Chou, T.-W. Nanocomposites in context. *Composites science and technology* 2005, *65* (3-4), 491-516. Treacy, M. J.; Ebbesen, T. W.; Gibson, J. M. Exceptionally high Young's modulus observed for individual carbon nanotubes. *nature* 1996, *381* (6584), 678-680.
(121) Chandra, Y.; Scarpa, F.; Adhikari, S.; Zhang, J.; Flores, E. S.; Peng, H.-X. Pullout strength of graphene and carbon nanotube/epoxy composites. *Composites Part B: Engineering* 2016, *102*, 1-8.
(122) Xiong, Q.; Meguid, S. Atomistic investigation of the interfacial mechanical characteristics of carbon nanotube reinforced epoxy composite. *European Polymer Journal* 2015, *69*, 1-15. Manoharan, M.; Sharma, A.; Desai, A.; Haque, M. A.; Bakis, C. E.; Wang, K. The interfacial strength of carbon nanofiber epoxy composite using single fiber pullout experiments. *Nanotechnology* 2009, *20* (29), 295701. Ganesan, Y.; Peng, C.; Lu, Y.; Loya, P. E.; Moloney, P.; Barrera, E.; Yakobson, B. I.; Tour, J. M.; Ballarini, R.; Lou, J. Interface toughness of carbon nanotube reinforced epoxy composites. *ACS applied materials & interfaces* 2011, *3* (2), 129-134.
(123) Li, Y.; Seidel, G. Multiscale modeling of the interface effects in CNT-epoxy nanocomposites. *Computational Materials Science* 2018, *153*, 363-381. Zhang, Y.; Zhuang, X.; Muthu, J.; Mabrouki, T.; Fontaine, M.; Gong, Y.; Rabczuk, T. Load transfer

of graphene/carbon nanotube/polyethylene hybrid nanocomposite by molecular dynamics simulation. *Composites Part B: Engineering* 2014, *63*, 27-33. Radue, M.; Odegard, G. M. Multiscale modeling of carbon fiber/carbon nanotube/epoxy hybrid composites: Comparison of epoxy matrices. *Composites Science and Technology* 2018, *166*, 20-26. Odegard, G. M.; Gates, T.; Wise, K.; Park, C.; Siochi, E. Constitutive modeling of nanotube–reinforced polymer composites. *Composites science and technology* 2003, *63* (11), 1671-1687.
(124) Zhang, X.; Li, Q.; Holesinger, T. G.; Arendt, P. N.; Huang, J.; Kirven, P. D.; Clapp, T. G.; DePaula, R. F.; Liao, X.; Zhao, Y. Ultrastrong, stiff, and lightweight carbon-nanotube fibers. *Advanced Materials* 2007, *19* (23), 4198-4201.
(125) Yu, M.-F.; Kowalewski, T.; Ruoff, R. S. Structural analysis of collapsed, and twisted and collapsed, multiwalled carbon nanotubes by atomic force microscopy. *Physical Review Letters* 2001, *86* (1), 87.
(126) Downes, R. D.; Hao, A.; Park, J. G.; Su, Y.-F.; Liang, R.; Jensen, B. D.; Siochi, E. J.; Wise, K. E. Geometrically constrained self-assembly and crystal packing of flattened and aligned carbon nanotubes. *Carbon* 2015, *93*, 953-966.
(127) Motta, M.; Moisala, A.; Kinloch, I. A.; Windle, A. H. High performance fibres from 'dog bone'carbon nanotubes. *Advanced Materials* 2007, *19* (21), 3721-3726.
(128) Choi, D.; Wang, Q.; Azuma, Y.; Majima, Y.; Warner, J.; Miyata, Y.; Shinohara, H.; Kitaura, R. Fabrication and characterization of fully flattened carbon nanotubes: a new graphene nanoribbon analogue. *Scientific Reports* 2013, *3* (1), 1-5.
(129) Miracle, D. Metal matrix composites–from science to technological significance. *Composites science and technology* 2005, *65* (15-16), 2526-2540.
(130) Atif, R.; Inam, F. Influence of macro-topography on damage tolerance and fracture toughness of monolithic epoxy for tribological applications. *World Journal of Engineering and Technology* 2016, *4* (02), 335.
(131) Morgan, R. J.; Shin, E. E.; Rosenberg, B.; Jurek, A. Characterization of the cure reactions of bismaleimide composite matrices. *Polymer* 1997, *38* (3), 639-646.
(132) Biron, M. *Thermoplastics and thermoplastic composites*; William Andrew, 2018. Agarwal, B. D.; Broutman, L. J.; Chandrashekhara, K. *Analysis and performance of fiber composites*; John Wiley & Sons, 2006.
(133) Eftekhari, M.; Fatemi, A. Tensile, creep and fatigue behaviours of short fibre reinforced polymer composites at elevated temperatures: a literature survey. *Fatigue & Fracture of Engineering Materials & Structures* 2015, *38* (12), 1395-1418. Aglan, H.; Qian, Z.; Mitra-Majumdar, D. The effect of temperature on the critical failure properties of advanced polymer composites. *Polymer testing* 1992, *11* (3), 169-184.
(134) Pilato, L. A.; Michno, M. J. *Advanced composite materials*; Springer Science & Business Media, 1994. Morgan, R. J.; Jurek, R. J.; Yen, A.; Donnellan, T. Toughening

procedures, processing and performance of bismaleimide-carbon fibre composites. *Polymer* 1993, *34* (4), 835-842.
(135) CHAHAL, R.; ADNAN, A.; ROY, A. Molecular Dynamics Study of Carbon Nanotube/Epoxy Interfaces Using ReaxFF. In *Proceedings of the American Society for Composites—Thirty-second Technical Conference*, 2017.
(136) Li, Y.; Liu, Y.; Peng, X.; Yan, C.; Liu, S.; Hu, N. Pull-out simulations on interfacial properties of carbon nanotube-reinforced polymer nanocomposites. *Computational Materials Science* 2011, *50* (6), 1854-1860. Stamboulis, A.; Baillie, C.; Schulz, E. Interfacial characterisation of flax fibre-thermoplastic polymer composites by the pull-out test. *Die Angewandte Makromolekulare Chemie* 1999, *272* (1), 117-120. Tsafack, T.; Alred, J. M.; Wise, K. E.; Jensen, B.; Siochi, E.; Yakobson, B. I. Exploring the interface between single-walled carbon nanotubes and epoxy resin. *Carbon* 2016, *105*, 600-606.
(137) Han, Y.; Elliott, J. Molecular dynamics simulations of the elastic properties of polymer/carbon nanotube composites. *Computational Materials Science* 2007, *39* (2), 315-323. Moniruzzaman, M.; Sahin, A.; Winey, K. I. Improved mechanical strength and electrical conductivity of organogels containing carbon nanotubes. *Carbon* 2009, *47* (3), 645-650.
(138) Zhong, X.; Yap, Y. K.; Pandey, R.; Karna, S. P. First-principles study of strain-induced modulation of energy gaps of graphene/BN and BN bilayers. *Physical review B* 2011, *83* (19), 193403.
(139) Kresse, G.; Joubert, D. From ultrasoft pseudopotentials to the projector augmented-wave method. *Physical Review B* 1999, *59* (3), 1758.
(140) Barber, A. H.; Cohen, S. R.; Wagner, H. D. Measurement of carbon nanotube–polymer interfacial strength. *Applied Physics Letters* 2003, *82* (23), 4140-4142. Cooper, C. A.; Cohen, S. R.; Barber, A. H.; Wagner, H. D. Detachment of nanotubes from a polymer matrix. *Applied Physics Letters* 2002, *81* (20), 3873-3875. DiFrancia, C.; Ward, T. C.; Claus, R. O. The single-fibre pull-out test. 1: Review and interpretation. *Composites Part A: Applied Science and Manufacturing* 1996, *27* (8), 597-612.
(141) Chorfi, H.; Lobato, Á.; Boudjada, F.; Salvadó, M. A.; Franco, R.; Baonza, V. G.; Recio, J. M. Computational Modeling of Tensile Stress Effects on the Structure and Stability of Prototypical Covalent and Layered Materials. *Nanomaterials* 2019, *9* (10), 1483.
(142) Tsai, M.-L.; Su, S.-H.; Chang, J.-K.; Tsai, D.-S.; Chen, C.-H.; Wu, C.-I.; Li, L.-J.; Chen, L.-J.; He, J.-H. Monolayer MoS2 heterojunction solar cells. *ACS nano* 2014, *8* (8), 8317-8322. Baonza, V. G.; Taravillo, M.; Cáceres, M.; Núñez, J. Universal features of the equation of state of solids from a pseudospinodal hypothesis. *Physical Review B* 1996, *53* (9), 5252.

(143) Giovannetti, G.; Khomyakov, P. A.; Brocks, G.; Kelly, P. J.; Van Den Brink, J. Substrate-induced band gap in graphene on hexagonal boron nitride: Ab initio density functional calculations. *Physical Review B* 2007, *76* (7), 073103.
(144) Tang, W.; Sanville, E.; Henkelman, G. A grid-based Bader analysis algorithm without lattice bias. *Journal of Physics: Condensed Matter* 2009, *21* (8), 084204.
(145) Gou, J.; Fan, B.; Song, G.; Khan, A. Study of affinities between single-walled nanotube and epoxy resin using molecular dynamics simulation. *International Journal of Nanoscience* 2006, *5* (01), 131-144.
(146) Ahangari, M. G.; Fereidoon, A.; Jahanshahi, M.; Ganji, M. Electronic and mechanical properties of single-walled carbon nanotubes interacting with epoxy: A DFT study. *Physica E: Low-dimensional Systems and Nanostructures* 2013, *48*, 148-156.
(147) Grabowski, S. J.; Sokalski, W. A.; Dyguda, E.; Leszczyński, J. Quantitative classification of covalent and noncovalent H-bonds. *The Journal of Physical Chemistry B* 2006, *110* (13), 6444-6446.
(148) Baonza, V. G.; Caceres, M.; Nunez, J. Universal compressibility behavior of dense phases. *Phys. Rev. B* 1995, *51* (1), 28-37. DOI: 10.1103/physrevb.51.28.
(149) Brosh, E.; Makov, G.; Shneck, R. Z. The spinodal constraint on the equation of state of expanded fluids. *Journal of Physics: Condensed Matter* 2003, *15* (19), 2991.
(150) Nayak, N. V. Composite materials in aerospace applications. *International Journal of Scientific and Research Publications* 2014, *4* (9), 1-10. Kesarwani, S. Polymer composites in aviation sector. *J. International Journal of Engineering Research & Technology* 2017, *6* (06), 518-525. Rana, S.; Fangueiro, R. Advanced composites in aerospace engineering. In *Advanced Composite Materials for Aerospace Engineering*, Elsevier, 2016; pp 1-15.
(151) https://www.nasa.gov/offices/oct/home/roadmaps/index.html.
(152) Kinloch, I. A.; Suhr, J.; Lou, J.; Young, R. J.; Ajayan, P. M. Composites with carbon nanotubes and graphene: An outlook. *Science* 2018, *362* (6414), 547-553.
(153) Sachdeva, G.; Lobato, A. l.; Pandey, R.; Odegard, G. M. Mechanical Response of Polymer Epoxy/BMI Composites with Graphene and a Boron Nitride Monolayer from First Principles. *ACS Applied Polymer Materials* 2021.
(154) Ottiger, P.; Pfaffen, C.; Leist, R.; Leutwyler, S.; Bachorz, R. A.; Klopper, W. Strong N− H··· π hydrogen bonding in amide− benzene interactions. *Journal of Physical Chemistry B* 2009, *113* (9), 2937-2943.
(155) Kandelbauer, A. Cyanate ester resins. In *Handbook of Thermoset Plastics*, Elsevier, 2022; pp 587-617.
(156) Wooster, T. J.; Abrol, S.; Hey, J. M.; MacFarlane, D. R. Thermal, mechanical, and conductivity properties of cyanate ester composites. *Composites Part A: Applied Science and Manufacturing* 2004, *35* (1), 75-82.

(157) Nair, C. R.; Mathew, D.; Ninan, K. Cyanate ester resins, recent developments. In *New Polymerization Techniques and Synthetic Methodologies*, Springer, 2001; pp 1-99. Hamerton, I.; Hay, J. N. Recent technological developments in cyanate ester resins. *High Performance Polymers* 1998, *10* (2), 163-174. Brand, R.; Harrison, E. *Development of Tough, Moisture Resistant Laminating Resins*; GENERAL DYNAMICS SAN DIEGO CA CONVAIR DIV, 1982.
(158) Fang, T.; Shimp, D. A. Polycyanate esters: science and applications. *Progress in Polymer Science* 1995, *20* (1), 61-118.
(159) Hamerton, I. *Chemistry and technology of cyanate ester resins*; Springer Science & Business Media, 2012.
(160) Henkelman, G.; Arnaldsson, A.; Jónsson, H. A fast and robust algorithm for Bader decomposition of charge density. *Computational Materials Science* 2006, *36* (3), 354-360.
(161) Hod, O. Graphite and hexagonal boron-nitride have the same interlayer distance. Why? *Journal of Chemical Theory and Computation* 2012, *8* (4), 1360-1369.
(162) Blöchl, P. E. Projector augmented-wave method. *Physical Review B* 1994, *50* (24), 17953.
(163) Cozzi, F.; Ponzini, F.; Annunziata, R.; Cinquini, M.; Siegel, J. S. Polar Interactions between Stacked π Systems in Fluorinated 1, 8-Diarylnaphthalenes: Importance of Quadrupole Moments in Molecular Recognition. *Angewandte Chemie International Edition in English* 1995, *34* (9), 1019-1020. Hunter, C. A.; Sanders, J. K. The nature of. pi.-. pi. interactions. *Journal of the American Chemical Society* 1990, *112* (14), 5525-5534. Anslyn, E. V.; Dougherty, D. A. *Modern physical organic chemistry*; University science books, 2006.
(164) Sinnokrot, M. O.; Valeev, E. F.; Sherrill, C. D. Estimates of the ab initio limit for π− π interactions: The benzene dimer. *Journal of the American Chemical Society* 2002, *124* (36), 10887-10893.
(165) Nasrabadi, A. T.; Foroutan, M. Interactions between polymers and single-walled boron nitride nanotubes: a molecular dynamics simulation approach. *Journal of Physical Chemistry B* 2010, *114* (47), 15429-15436.
(166) Lv, C.; Xue, Q.; Xia, D.; Ma, M.; Xie, J.; Chen, H. Effect of chemisorption on the interfacial bonding characteristics of graphene− polymer composites. *Journal of Physical Chemistry C* 2010, *114* (14), 6588-6594. Liang, Y.-Y.; Xu, J.-Z.; Liu, X.-Y.; Zhong, G.-J.; Li, Z.-M. Role of surface chemical groups on carbon nanotubes in nucleation for polymer crystallization: Interfacial interaction and steric effect. *Polymer* 2013, *54* (23), 6479-6488. Castner, D. G.; Grainger, D. W.; Pellerite, M.; Anton, D. *Fluorinated surfaces, coatings, and films*; ACS Publications, 2001.

(167) Pisani, W. A.; Radue, M. S.; Patil, S. U.; Odegard, G. M. Interfacial modeling of flattened CNT composites with cyanate ester and PEEK polymers. *Composites Part B: Engineering* 2021, *211*, 108672.
(168) Bellucci, S.; Balasubramanian, C.; Micciulla, F.; Rinaldi, G. CNT composites for aerospace applications. *Journal of Experimental Nanoscience* 2007, *2* (3), 193-206. Siochi, E. J.; Harrison, J. S. Structural nanocomposites for aerospace applications. *MRS Bulletin* 2015, *40* (10), 829-835.
(169) Harris, P. J. Carbon nanotube composites. *International Materials Reviews* 2004, *49* (1), 31-43.
(170) Gangineni, P. K.; Yandrapu, S.; Ghosh, S. K.; Anand, A.; Prusty, R. K.; Ray, B. C. Mechanical behavior of Graphene decorated carbon fiber reinforced polymer composites: An assessment of the influence of functional groups. *Composites Part A: Applied Science and Manufacturing* 2019, *122*, 36-44. Balakrishna, B.; Menon, A.; Cao, K.; Gsänger, S.; Beil, S. B.; Villalva, J.; Shyshov, O.; Martin, O.; Hirsch, A.; Meyer, B. Dynamic Covalent Formation of Concave Disulfide Macrocycles Mechanically Interlocked with Single-Walled Carbon Nanotubes. *Angewandte Chemie International Edition* 2020, *59* (42), 18774-18785. Star, A.; Stoddart, J. F.; Steuerman, D.; Diehl, M.; Boukai, A.; Wong, E. W.; Yang, X.; Chung, S. W.; Choi, H.; Heath, J. R. Preparation and properties of polymer-wrapped single-walled carbon nanotubes. *Angewandte Chemie* 2001, *113* (9), 1771-1775. Baskaran, D.; Mays, J. W.; Bratcher, M. S. Noncovalent and nonspecific molecular interactions of polymers with multiwalled carbon nanotubes. *Chemistry of Materials* 2005, *17* (13), 3389-3397.
(171) De, S.; Fulmali, A. O.; Shivangi, P.; Choudhury, S.; Prusty, R. K.; Ray, B. C. Interface modification of carbon fiber reinforced epoxy composite by hydroxyl/carboxyl functionalized carbon nanotube. *Materials Today: Proceedings* 2020, *27*, 1473-1478. Farooq, M. U.; Jan, R.; Azeem, M.; Umer, M. A.; Akram, M. A.; Khan, A. N.; Ahmad, I.; Khan, S. A.; Umar, Z. A.; Liaqat, U. Enhanced mechanical properties of functionalized BN nanosheets-polymer composites. *Journal of Polymer Research* 2020, *27* (10), 1-9.
(172) Chen, J.; Wang, K.; Zhao, Y. Enhanced interfacial interactions of carbon fiber reinforced PEEK composites by regulating PEI and graphene oxide complex sizing at the interface. *Composites Science and Technology* 2018, *154*, 175-186. Li, J. Interfacial studies on the O3 modified carbon fiber-reinforced polyamide 6 composites. *Applied Surface Science* 2008, *255* (5), 2822-2824.
(173) Zhang, H.; Li, W. Plasma-grafting polymerization on carbon fibers and its effect on their composite properties. *Applied Surface Science* 2015, *356*, 492-498.
(174) Liu, F.; Shi, Z.; Dong, Y. Improved wettability and interfacial adhesion in carbon fibre/epoxy composites via an aqueous epoxy sizing agent. *Composites Part A: Applied Science and Manufacturing* 2018, *112*, 337-345.

(175) Wang, Y.; Colas, G.; Filleter, T. Improvements in the mechanical properties of carbon nanotube fibers through graphene oxide interlocking. *Carbon* 2016, *98*, 291-299.
(176) Blase, X.; Rubio, A.; Louie, S. G.; Cohen, M. L. Stability and band gap constancy of boron nitride nanotubes. *EPL (Europhysics Letters)* 1994, *28* (5), 335.
(177) Chopra, N. G.; Luyken, R.; Cherrey, K.; Crespi, V. H.; Cohen, M. L.; Louie, S. G.; Zettl, A. Boron Nitride Nanotubes. *Science* 1995, *269* (5226), 966-967.
(178) Xiao, Y.; Yan, X.; Cao, J.; Ding, J.; Mao, Y.; Xiang, J. Specific heat and quantized thermal conductance of single-walled boron nitride nanotubes. *Physical Review B* 2004, *69* (20), 205415.
(179) Boldrin, L.; Scarpa, F.; Chowdhury, R.; Adhikari, S. Effective mechanical properties of hexagonal boron nitride nanosheets. *Nanotechnology* 2011, *22* (50), 505702.
(180) Li, L. H.; Cervenka, J.; Watanabe, K.; Taniguchi, T.; Chen, Y. Strong oxidation resistance of atomically thin boron nitride nanosheets. *ACS Nano* 2014, *8* (2), 1457-1462. Krishnan, A.; Dujardin, E.; Ebbesen, T.; Yianilos, P.; Treacy, M. Young's modulus of single-walled nanotubes. *Physical Review B* 1998, *58* (20), 14013.
(181) Naskar, A. K.; Keum, J. K.; Boeman, R. G. Polymer matrix nanocomposites for automotive structural components. *Nature Nanotechnology* 2016, *11* (12), 1026-1030.
(182) Hussain, F.; Hojjati, M.; Okamoto, M.; Gorga, R. E. Polymer-matrix nanocomposites, processing, manufacturing, and application: an overview. *Journal of Composite Materials* 2006, *40* (17), 1511-1575. Garces, J. M.; Moll, D. J.; Bicerano, J.; Fibiger, R.; McLeod, D. G. Polymeric nanocomposites for automotive applications. *Advanced Materials* 2000, *12* (23), 1835-1839.
(183) Ciofani, G.; Raffa, V.; Menciassi, A.; Cuschieri, A. Cytocompatibility, interactions, and uptake of polyethyleneimine-coated boron nitride nanotubes by living cells: Confirmation of their potential for biomedical applications. *Biotechnology and Bioengineering* 2008, *101* (4), 850-858. Horvath, L.; Magrez, A.; Golberg, D.; Zhi, C.; Bando, Y.; Smajda, R.; Horvath, E.; Forro, L.; Schwaller, B. In vitro investigation of the cellular toxicity of boron nitride nanotubes. *ACS Nano* 2011, *5* (5), 3800-3810.
(184) Lei, W.; Zhang, H.; Wu, Y.; Zhang, B.; Liu, D.; Qin, S.; Liu, Z.; Liu, L.; Ma, Y.; Chen, Y. Oxygen-doped boron nitride nanosheets with excellent performance in hydrogen storage. *Nano Energy* 2014, *6*, 219-224. Yu, Y.-X. A dispersion-corrected DFT study on adsorption of battery active materials anthraquinone and its derivatives on monolayer graphene and h-BN. *Journal of Materials Chemistry A* 2014, *2* (23), 8910-8917.
(185) Jang, S. K.; Youn, J.; Song, Y. J.; Lee, S. Synthesis and characterization of hexagonal boron nitride as a gate dielectric. *Scientific Reports* 2016, *6* (1), 1-9.
(186) Wang, D.; Zhou, K.; Yang, W.; Xing, W.; Hu, Y.; Gong, X. Surface modification of graphene with layered molybdenum disulfide and their synergistic reinforcement on

reducing fire hazards of epoxy resins. *Industrial & Engineering Chemistry Research* 2013, *52* (50), 17882-17890. Chandrasekaran, S.; Sato, N.; Tölle, F.; Mülhaupt, R.; Fiedler, B.; Schulte, K. Fracture toughness and failure mechanism of graphene based epoxy composites. *Composites Science and Technology* 2014, *97*, 90-99. King, J. A.; Klimek, D. R.; Miskioglu, I.; Odegard, G. M. Mechanical properties of graphene nanoplatelet/epoxy composites. *Journal of Applied Polymer Science* 2013, *128* (6), 4217-4223.

(187) Chen, X.; Zhang, L.; Park, C.; Fay, C. C.; Wang, X.; Ke, C. Mechanical strength of boron nitride nanotube-polymer interfaces. *Applied Physics Letters* 2015, *107* (25), 253105.

(188) Rouhi, S. Molecular dynamics simulation of the adsorption of polymer chains on CNTs, BNNTs and GaNNTs. *Fibers and Polymers* 2016, *17* (3), 333-342.

(189) Odegard, G.; Clancy, T.; Gates, T. Modeling of the mechanical properties of nanoparticle/polymer composites. *Polymer* 2005, *46* (2), 553-562. Odegard, G.; Frankland, S.; Gates, T. Effect of nanotube functionalization on the elastic properties of polyethylene nanotube composites. *Aiaa Journal* 2005, *43* (8), 1828-1835.

(190) Li, J.; Chen, J.; Zhu, M.; Song, H.; Zhang, H. Interfacial characteristics of boron nitride nanosheet/epoxy resin nanocomposites: a molecular dynamics simulation. *Applied Sciences* 2019, *9* (14), 2832.

(191) Nasrabadi, A. T.; Foroutan, M. Interactions between polymers and single-walled boron nitride nanotubes: a molecular dynamics simulation approach. *The Journal of Physical Chemistry B* 2010, *114* (47), 15429-15436.

(192) Rasul, M. G.; Kiziltas, A.; Malliakas, C. D.; Rojaee, R.; Sharifi-Asl, S.; Foroozan, T.; Shahbazian-Yassar, R.; Arfaei, B. Polyethylene-BN nanosheets nanocomposites with enhanced thermal and mechanical properties. *Composites Science and Technology* 2021, *204*, 108631.

(193) Meng, W.; Huang, Y.; Fu, Y.; Wang, Z.; Zhi, C. Polymer composites of boron nitride nanotubes and nanosheets. *Journal of Materials Chemistry C* 2014, *2* (47), 10049-10061. Jakubinek, M. B.; Ashrafi, B.; Martinez-Rubi, Y.; Guan, J.; Rahmat, M.; Kim, K. S.; Dénommée, S.; Kingston, C. T.; Simard, B. Boron nitride nanotube composites and applications. In *Nanotube Superfiber Materials*, Elsevier, 2019; pp 91-111.

(194) Goyal, S.; Cochran, E. W. Cyanate ester composites to improve thermal performance: A review. *Polymer International* 2022, *71* (5), 583-589.

(195) Deshpande, P. P.; Radue, M. S.; Gaikwad, P.; Bamane, S.; Patil, S. U.; Pisani, W. A.; Odegard, G. M. Prediction of the Interfacial Properties of High-Performance Polymers and Flattened CNT-Reinforced Composites Using Molecular Dynamics. *Langmuir* 2021, *37* (39), 11526-11534.

(196) Toldy, A.; Szolnoki, B.; Marosi, G. Flame retardancy of fiber-reinforced epoxy resin composites for aerospace applications. *Polymer Degradation and Stability* 2011, *96* (3), 371-376.
(197) May, C. *Epoxy resins: chemistry and technology*; Routledge, 2018.
(198) Iredale, R. J.; Ward, C.; Hamerton, I. Modern advances in bismaleimide resin technology: A 21st century perspective on the chemistry of addition polyimides. *Progress in Polymer Science* 2017, *69*, 1-21. Ning, Y.; Li, D. s.; Wang, M. c.; Jiang, L. Eugenol-derived bismaleimide high-performance resins and composites using diisocyanate as property modifier. *Macromolecular Materials and Engineering* 2019, *304* (4), 1800713. Zhao, Q.; Li, X.; Tian, Z.; Ma, H.; Hou, X.; Wang, Y.; Wang, Y. Controlling degradation and recycling of carbon fiber reinforced bismaleimide resin composites via selective cleavage of imide bonds. *Composites Part B: Engineering* 2022, *231*, 109595.
(199) Heinz, H.; Lin, T.-J.; Kishore Mishra, R.; Emami, F. S. Thermodynamically consistent force fields for the assembly of inorganic, organic, and biological nanostructures: the INTERFACE force field. *Langmuir* 2013, *29* (6), 1754-1765.
(200) Bamane, S. S.; Gaikwad, P. S.; Radue, M. S.; Gowtham, S.; Odegard, G. M. Wetting Simulations of High-Performance Polymer Resins on Carbon Surfaces as a Function of Temperature Using Molecular Dynamics. *Polymers* 2021, *13* (13), 2162.
(201) Bamane SS, K. K., Heinz H, Odegard G. Force field parameterization and molecular dynamics simulation of epoxy resin interaction with boron nitride nanotube surfaces. *ChemRxiv. Cambridge* 2022, *Cambridge Open Engage*.
(202) Patil, S. U.; Radue, M. S.; Pisani, W. A.; Deshpande, P.; Xu, H.; Al Mahmud, H.; Dumitrică, T.; Odegard, G. M. Interfacial characteristics between flattened CNT stacks and polyimides: A molecular dynamics study. *Computational Materials Science* 2020, *185*, 109970.
(203) Plimpton, S. Fast parallel algorithms for short-range molecular dynamics. *Journal of Computational Physics* 1995, *117* (1), 1-19.
(204) Stukowski, A. Visualization and analysis of atomistic simulation data with OVITO–the Open Visualization Tool. *Modeling and Simulation in Materials Science and Engineering* 2009, *18* (1), 015012.
(205) Genidy, M. S.; Madhukar, M. S.; Russell, J. D. A new method to reduce cure-induced stresses in thermoset polymer composites, Part II: Closed loop feedback control system. *Journal of Composite Materials* 2000, *34* (22), 1905-1925. Goertzen, W. K.; Kessler, M. Thermal and mechanical evaluation of cyanate ester composites with low-temperature processability. *Composites Part A: Applied Science and Manufacturing* 2007, *38* (3), 779-784.
(206) Gissinger, J. R.; Jensen, B. D.; Wise, K. E. Modeling chemical reactions in classical molecular dynamics simulations. *Polymer* 2017, *128*, 211-217.

(207) Bandyopadhyay, A.; Valavala, P. K.; Clancy, T. C.; Wise, K. E.; Odegard, G. M. Molecular modeling of crosslinked epoxy polymers: The effect of crosslink density on thermomechanical properties. *Polymer* 2011, *52* (11), 2445-2452. Radue, M. S.; Jensen, B. D.; Gowtham, S.; Klimek-McDonald, D. R.; King, J. A.; Odegard, G. M. Comparing the mechanical response of di-, tri-, and tetra-functional resin epoxies with reactive molecular dynamics. *Journal of Polymer Science Part B: Polymer Physics* 2018, *56* (3), 255-264.
(208) Rozenberg, B.; Bojko, G.; Morgan, R.; Shin, E. Cure mechanism of the 4, 4'-(n, n'-bismaleimide) diphenylmethane-2, 2'-diallylbisphenol a system. *Высокомолекулярные соединения. Серия А* 2001, *43* (4), 630-645.
(209) Radue, M. S.; Varshney, V.; Baur, J. W.; Roy, A. K.; Odegard, G. M. Molecular modeling of cross-linked polymers with complex cure pathways: a case study of bismaleimide resins. *Macromolecules* 2018, *51* (5), 1830-1840.
(210) Kirmani, M. H.; Sachdeva, G.; Pandey, R.; Odegard, G. M.; Liang, R.; Kumar, S. Cure Behavior Changes and Compression of Carbon Nanotubes in Aerospace Grade Bismaleimide-Carbon Nanotube Sheet Nanocomposites. *ACS Applied Nano Materials* 2021, *4* (3), 2476-2485. Sachdeva, G.; Lobato, A. l.; Pandey, R.; Odegard, G. M. Mechanical Response of Polymer Epoxy/BMI Composites with Graphene and a Boron Nitride Monolayer from First Principles. *ACS Applied Polymer Materials* 2021, *3* (2), 1052-1059.
(211) Van Duin, A. C.; Dasgupta, S.; Lorant, F.; Goddard, W. A. ReaxFF: a reactive force field for hydrocarbons. *The Journal of Physical Chemistry A* 2001, *105* (41), 9396-9409. Senftle, T. P.; Hong, S.; Islam, M. M.; Kylasa, S. B.; Zheng, Y.; Shin, Y. K.; Junkermeier, C.; Engel-Herbert, R.; Janik, M. J.; Aktulga, H. M. The ReaxFF reactive force-field: development, applications and future directions. *npj Computational Materials* 2016, *2* (1), 1-14. Liu, L.; Liu, Y.; Zybin, S. V.; Sun, H.; Goddard III, W. A. ReaxFF-lg: Correction of the ReaxFF reactive force field for London dispersion, with applications to the equations of state for energetic materials. *The Journal of Physical Chemistry A* 2011, *115* (40), 11016-11022.

A Appendix

A.1 Preferential Stacking of BMI over CNTs

We have performed a close examination of the preferential molecular stacking of BMI components on CNTs using atomistic simulations based on the molecular dynamics (MD) method. In a periodic model employing a supercell of 30 Å × 30 Å × 35 Å, a large diameter (~8 nm) CNT was simulated by a similar graphitic structure of graphene as shown in Figure 1. The structural configurations of BMI components were obtained using the state-of-the-art first-principles method as described in reference 191 [153] and are listed in Table 10. The reactive force field ReaxFF with the parameterizations of Liu et al. [211] as implemented in the Large-scale Atomic/Molecular Massively Parallel Simulator program (LAMMPS) [203] was used for the MD calculations. In graphene-supported calculations, a given stacking configuration was relaxed keeping graphene frozen until the maximum forces acting on the constituents became smaller than 10^{-7} kcal/mole-Å.

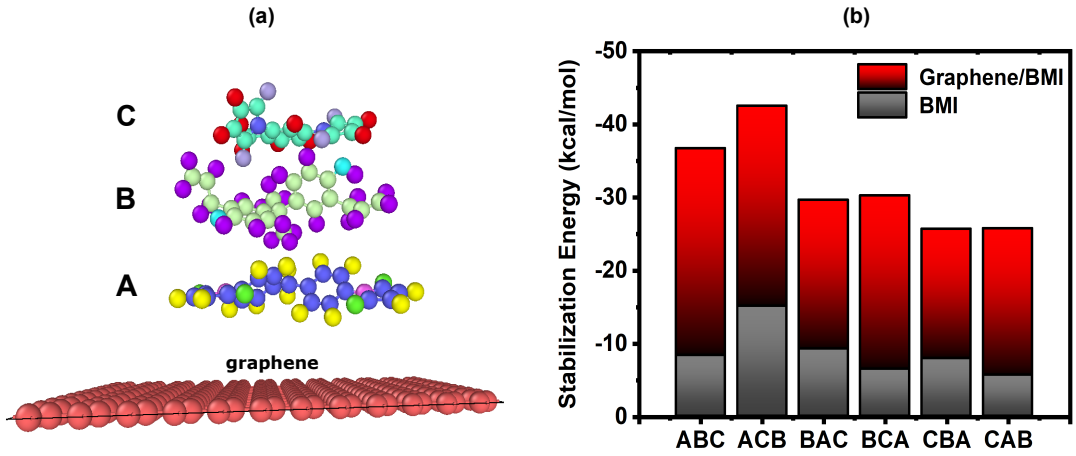

Figure A 1: (a) A ball and stick model of composite considered for MD calculations. The BMI components, 4,4 Bismaleimidodiphenylmethane, 0,0 Diallyl Bisphenol A, and BMI-1,3- tolyl are labeled as A, B, and C, respectively. A large diameter carbon nanotube is simulated by the graphitic structure of graphene. (b) Calculated stabilization energy of various stacking configurations of BMI components on graphene. Grey: binding energy, Red: interaction energy with graphene

Table A 1: The binding energies and interlayer distances for the various stacking of BMI with respect to its constituents and Interaction energy and interlayer distances for BMI on graphene. The BMI components, 4,4 Bismaleimidodiphenylmethane, 0,0 Diallyl Bisphenol A, and BMI- 1,3- tolyl are listed as A, B, and C, respectively

Stacking configurations	**Graphene-supported stacking configurations - Interlayer distance (Å)**	**Interlayer distance within the configuration (Å)**	**Binding energy (kcal/mol)**
ABC	-	1.8, 1.8	-8.4
ACB	-	1.6, 1.4	-15.1
BAC	-	1.7, 2.5	-9.3
BCA	-	1.4, 2.1	-6.5
CBA	-	1.2, 2.3	-7.9
CAB	-	2.0, 1.8	-5.7
Stacking configurations on graphene			**Interaction energy (kcal/mol)**
Graphene/ABC	2.8	1.9, 1.8	-28.3
Graphene /ACB	2.8	1.6, 1.2	-27.5
Graphene /BAC	2.1	1.5, 2.5	-20.4
Graphene /BCA	2.1	1.8, 2.1	-23.8
Graphene /CBA	2.7	1.2, 2.3	-17.7
Graphene /CAB	2.7	2.0, 1.8	-20.1

It is worth mentioning that the BMI components, namely 4,4 Bismaleimidodiphenylmethane, 0,0 Diallyl Bisphenol A, BMI-1,3- tolyl are represented as A, B, C components, respectively in Figure 1. Furthermore, we use the stabilization energy of a given stacked configuration on graphene to be a guiding factor to determine the preferential molecular stacking of BMI components. For a given stacking configuration, the stabilization energy is defined as the sum of its interaction energy with graphene and its binding energy with respect to its constituents.

The calculated stabilization energy of several stacking configurations is shown in Figure 1b. and the respective interaction energies and binding energies are listed in Table 9. We find that the ACB or ABC configurations interacting with graphene are energetically preferred with the stabilization energies of -42, and -39 kcal/mol, respectively. Note that a negative value of the energy suggests the stability of the stacking configuration on graphene. This is followed by the preference of the stacking configurations of BCA~BAC (-30 kcal/mol) >CAB~CBA (-25 kcal/mol) on graphene.

Table A 2: Some of the representative structural parameters and binding energy/atom of the BMI components, 4,4 Bismaleimidodiphenylmethane, 0,0 Diallyl Bisphenol A, and BMI- 1,3- tolyl labeled as A, B, C, respectively. The binding energy is calculated with respect to its constituents. The details of density functional theory calculations are given in reference 191.

BMI components	**A**	**B**	**C**
Binding energy/atom (eV)	- 4.14	- 3.19	- 4.21
Bond distance, C-C (Å)	1.50	1.40	1.41
C-H (Å)	1.08	1.09	1.08
C-O (Å)	1.22	1.37	1.22
C-N (Å)	1.41	-	1.41
Bond angle, C-C-C (°) (Benzene ring)	121.8	121.2	119.8

Overall, we find that the stacking configuration with the BMI component, A (i.e., 4,4 Bismaleimidodiphenylmethane) interacting with graphene facilitates the energetically preferred configuration. This preferential stacking of ACB (or ABC) on graphene can be understood in terms of the effective area of contact [153] at the interface. In the present work, the effective area of contact is calculated using the estimated length and width of the surface covered by a component using its distance of one end to the other in both x- and y-directions. The calculated areas of contact for A, B, and C components are 113, 94, and 53 $Å^2$, respectively reflecting the fact that the aromatic ring of monomer A is aligned parallel to graphene in the ACB (or ABC) stacked configurations. Thus, a larger degree of van der Waals interaction occurs between component A and graphene at the interface yielding ACB (or ABC) to be the preferred molecular stacking on graphene. The potential

for the preferential stacking of the different BMI components around the CNTs, can have important implications on the cure behavior of the BMI in the composite and consequently on the overall mechanical properties of the composite.

A.2 Computational Resources

All the simulations were run on Superior HPC, few of monomer's simulation were run on local workstation at MTU

Computing time

System	No- Of Atoms	Simulation Description	No. Of Processors	CPU Time (Hrs.)
DFT				
MONOMERS	10-25	Relaxation	8	<1
MULTILAYER GRAPHENE, ANTIMONENE AND BOROPHENE	2-40	Relaxation	16	<10
	2-40	Optical Properties	16	<24
GRAPHENE/BN MONOLAYER	300	Relaxation	32	120
		SCF	16	24
MONOMER/MONOLAYER	350	Relaxation	32	192
MONOMER/MONOLAYER	350	Pull-Apart (Multiple SCF)	16 Each	400
MD				
POLYMER/BN	~47000	Annealing	24	160
		Equilibration	16	36
		Polymerization	32	144
		Deformation	32	504

A.3 Modelling Potential Energy Surfaces to Develop Force Field Parameters

Methodology: Density functional theory - B3LYP exchange-correlation functional and a 6-31G (d, p) basis set. The maximum force convergence for geometry optimization = 10^{-4} eV/Å. The convergence criteria for RMS density matrix and total energy were 10^{-8} and 10^{-6} eV, respectively.

A.3.1 Melamine

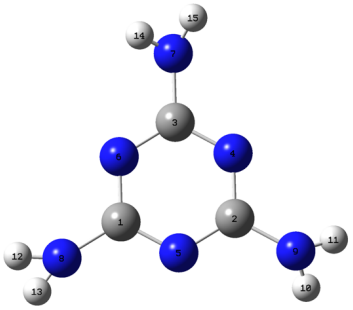

Figure A 2: The ball and stick model of Melamine molecule

Structural parameters for Melamine

Properties	B3LYP/6-31G (d, p)
Bond length (Å)	
R (NH)	1.0
R (CN)	1.36
Bond Angle (°)	
A(CNH)	117.5
A(HNH)	119.3
A(N7C3N4)	116.7
A(N4C2N5)	126.55

Energy Surface

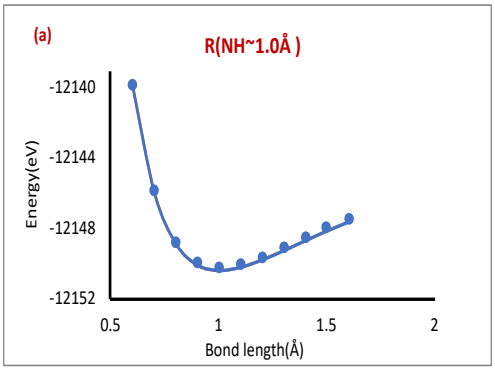

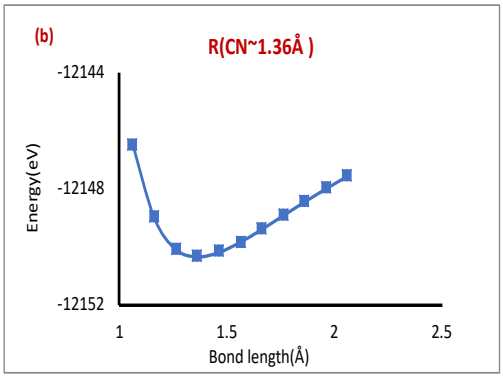

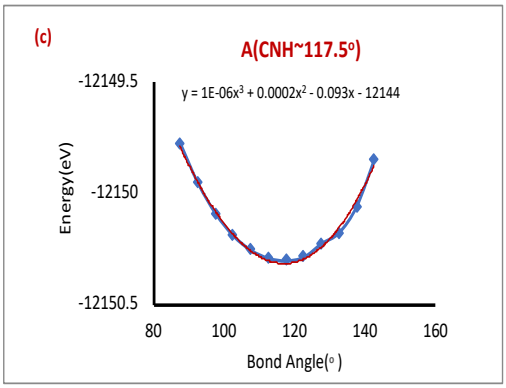

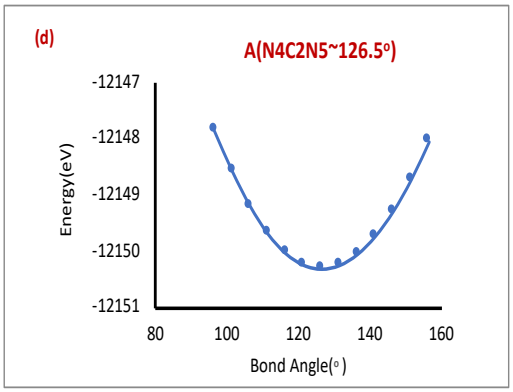

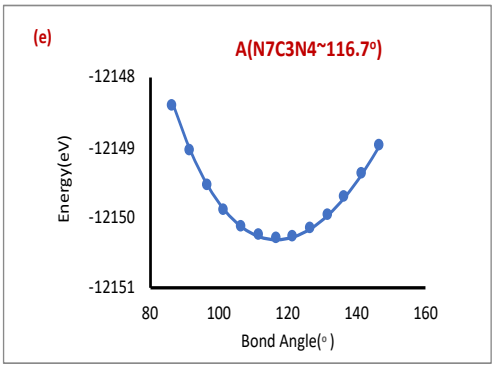

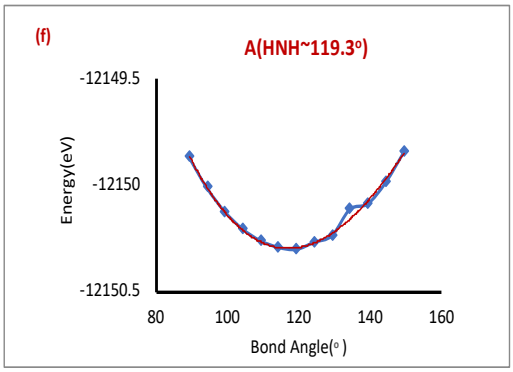

Bond length (Å)	Energy (eV)
Energy vs. Bond length (NH)	
0.61	-12139.95
0.71	-12145.94
0.81	-12148.82
0.91	-12150.02
1.01	-12150.31
1.11	-12150.12
1.21	-12149.70
1.31	-12149.17
1.41	-12148.61
1.51	-12148.05
1.61	-12147.53
Energy vs. Bond length (CN)	
1.06	-12146.48
1.16	-12148.98
1.26	-12150.05
1.36	-12150.30
1.46	-12150.15
1.56	-12149.81
1.66	-12149.37
1.76	-12148.90
1.86	-12148.44
1.96	-12147.98
2.06	-12147.56

Bond angle (^{0})	Energy (eV)
Energy vs. Angle (N4C2N5)	
96.56	-12147.84
101.56	-12148.56
106.56	-12149.18
111.56	-12149.68
116.56	-12150.03
121.56	-12150.23
126.56	-12150.30
131.56	-12150.24
136.56	-12150.04
141.56	-12149.72
146.56	-12149.28
151.56	-12148.72
156.56	-12148.05
Energy vs. Angle (N7C3N4)	
86.71	-12148.4
91.71	-12149.05
96.71	-12149.54
101.71	-12149.9
106.71	-12150.13
111.71	-12150.26
116.71	-12150.31
121.71	-12150.27
126.71	-12150.15
131.71	-12149.96
136.71	-12149.7
141.71	-12149.37
146.71	-12148.98

Bond angle (^{0})	Energy (eV)
Energy vs. Angle (HNH)	
89.31	-12149.87
94.31	-12150.01
99.31	-12150.13
104.31	-12150.21
109.31	-12150.27
114.31	-12150.3
119.31	-12150.31
124.31	-12150.27
129.31	-12150.24
134.31	-12150.12
139.31	-12150.09
144.31	-12149.99
149.31	-12149.85
Energy vs. Angle (CNH)	
87.50	-12149.78
92.50	-12149.96
97.50	-12150.09
102.50	-12150.2
107.50	-12150.26
112.50	-12150.3
117.50	-12150.31
122.50	-12150.3
127.50	-12150.23
132.50	-12150.18
137.50	-12150.1
142.50	-12149.85

A.3.2 Norbornane

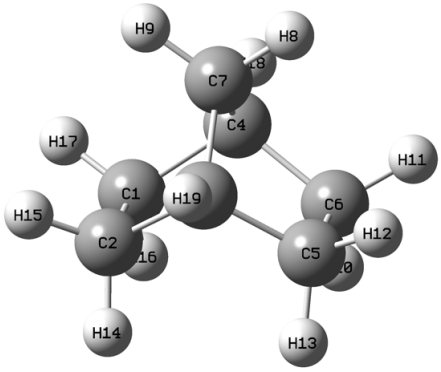

Figure A 3: The ball and stick model of Norbornane molecule

Calculated structural parameters of Norbornane

Properties	B3LYP/6-31G (d, p)
Bond length (Å)	
R(C-C)	1.52
R (C-H)	1.09
Bond Angle (°)	
A(C-C-H)	110.8
A(H-C-H)	108.7
A(C3-C7-C4)	94.3
A(C1-C4-C6)	108.5

Energy Surface

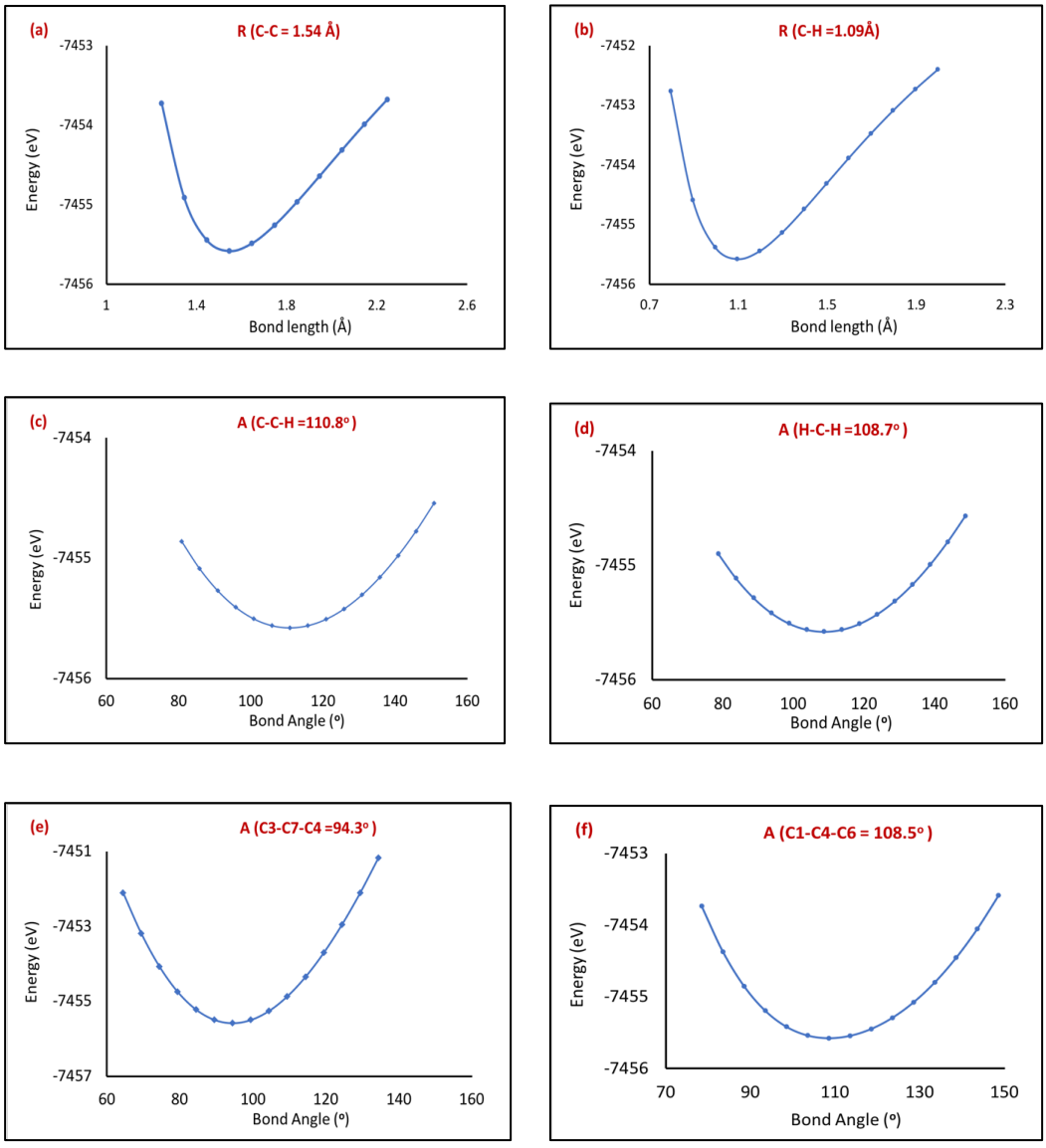

Bond length (Å)	Energy (eV)
Energy vs. Bond length (C-C)	
1.2	-7453.72
1.3	-7454.91
1.4	-7455.44
1.5	-7455.58
1.6	-7455.48
1.7	-7455.26
1.8	-7454.97
1.9	-7454.64
2.0	-7454.31
2.1	-7453.99
2.2	-7453.68
Energy vs. Bond length (C-H)	
0.8	-7452.77
0.9	-7454.59
1.0	-7455.38
1.1	-7455.58
1.2	-7455.45
1.3	-7455.14
1.4	-7454.75
1.5	-7454.32
1.6	-7453.89
1.7	-7453.48
1.8	-7453.09
1.9	-7452.73
2.0	-7452.41

Bond Angle (^{o})	Energy
Energy vs. Angle (H-C-H)	
78.7	-7454.90
83.7	-7455.11
88.7	-7455.28
93.7	-7455.42
98.7	-7455.51
103.7	-7455.57
108.7	-7455.58
113.7	-7455.56
118.7	-7455.51
123.7	-7455.43
128.7	-7455.31
133.7	-7455.17
138.7	-7454.99
143.7	-7454.79
148.7	-7454.57
Energy vs. Bond Angle (C3-C7-C4)	
64.4	-7452.10
69.4	-7453.19
74.4	-7454.07
79.4	-7454.75
84.4	-7455.22
89.4	-7455.49
94.4	-7455.58
99.4	-7455.49
104.4	-7455.25
109.4	-7454.86
114.4	-7454.34
119.4	-7453.70
124.4	-7452.95
129.4	-7452.10
134.4	-7451.17

Energy vs. Bond Angle (C-C-H)	
80.8	-7454.86
85.8	-7455.09
90.8	-7455.27
95.8	-7455.41
100.8	-7455.51
105.8	-7455.56
110.8	-7455.58
115.8	-7455.56
120.8	-7455.51
125.8	-7455.43
130.8	-7455.31
135.8	-7455.16
140.8	-7454.98
145.8	-7454.78
150.8	-7454.55
Energy vs. Bond Angle (C1-C4-C6)	
78.5	-7453.74
83.5	-7454.37
88.5	-7454.85
93.5	-7455.20
98.5	-7455.42
103.5	-7455.54
108.5	-7455.58
113.5	-7455.54
118.5	-7455.45
123.5	-7455.29
128.5	-7455.08
133.5	-7454.80
138.5	-7454.46
143.5	-7454.05
148.5	-7453.59

A.3.3 Diphenyl-Ether

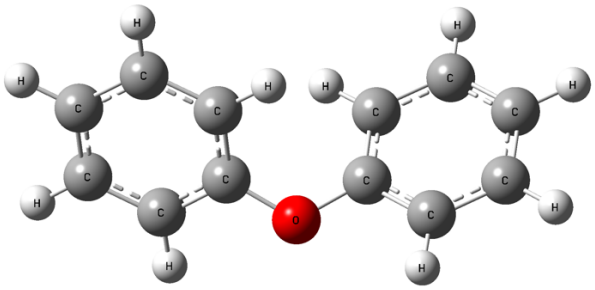

Figure A 4: The ball and stick model of Diphenyl ether molecule.

Energy Surface

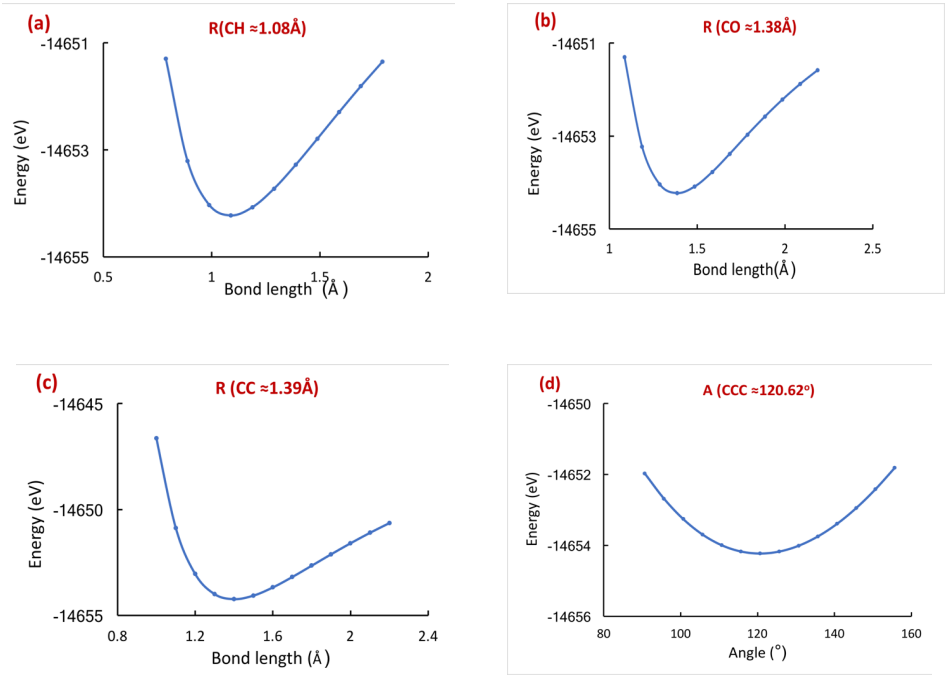

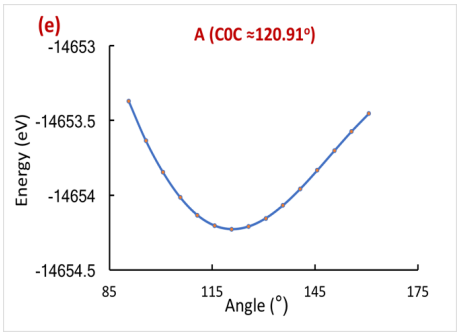
(e)
A (COC ≈120.91°)
-14653
-14653.5
-14654
-14654.5
Energy (eV)
85
115
145
175
Angle (°)

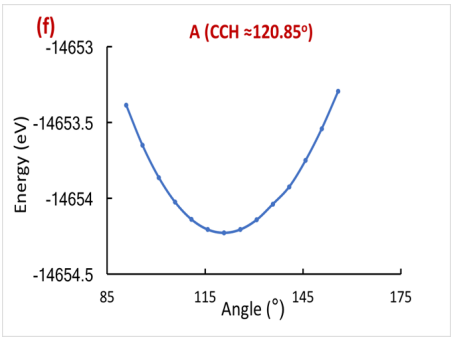
(f)
A (CCH ≈120.85°)
-14653
-14653.5
-14654
-14654.5
Energy (eV)
85
115
145
175
Angle (°)

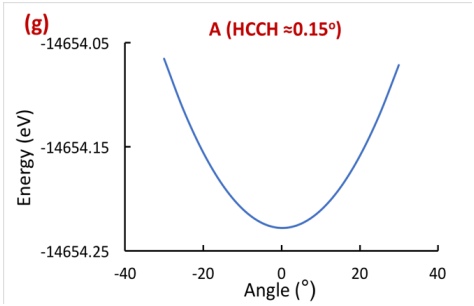
(g)
A (HCCH ≈0.15°)
-14654.05
-14654.15
-14654.25
Energy (eV)
-40
-20
0
20
40
Angle (°)

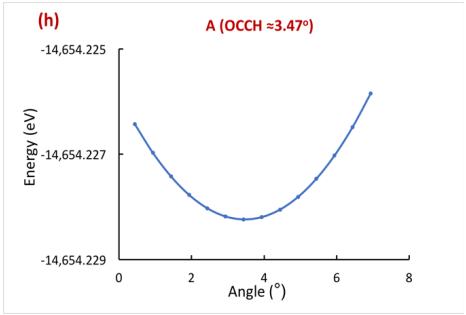
(h)
A (OCCH ≈3.47°)
-14,654.225
-14,654.227
-14,654.229
Energy (eV)
0
2
4
6
8
Angle (°)

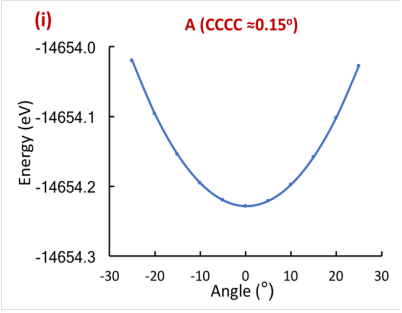
(i)
A (CCCC ≈0.15°)
-14654.0
-14654.1
-14654.2
-14654.3
Energy (eV)
-30
-20
-10
0
10
20
30
Angle (°)

Bond length (Å)	Energy (eV)
Energy vs. Bond length (CH)	
0.79	-14651.30
0.89	-14653.21
0.99	-14654.03
1.09	-14654.23
1.19	-14654.07
1.29	-14653.73
1.39	-14653.28
1.49	-14652.79
1.59	-14652.30
1.69	-14651.8
1.79	-14651.35
Energy vs. Bond length (CO)	
1.09	-14651.31
1.19	-14653.23
1.29	-14654.04
1.39	-14654.23
1.49	-14654.09
1.59	-14653.77
1.69	-14653.38
1.79	-14652.97
1.89	-14652.58
1.99	-14652.21
2.09	-14651.88
Energy vs. Bond length (CC)	
1.00	-14646.63
1.10	-14650.87
1.20	-14653.04
1.30	-14653.99
1.40	-14654.23
1.50	-14654.06
1.60	-14653.68
1.70	-14653.18
1.80	-14652.65
1.90	-14652.11
2.00	-14651.59
2.10	-14651.10
2.20	-14650.63

Bond angle (^{0})	Energy (eV)
Energy vs. Angle (CCC)	
90.64	-14651.97
95.64	-14652.69
100.64	-14653.26
105.64	-14653.69
110.64	-14653.99
115.64	-14654.17
120.64	-14654.23
125.64	-14654.17
130.64	-14654.01
135.64	-14653.75
140.64	-14653.39
145.64	-14652.94
150.64	-14652.42
155.64	-14651.81
Energy vs. Angle (COC)	
90.63	-14653.37
95.63	-14653.63
100.63	-14653.85
105.63	-14654.01
110.63	-14654.13
115.63	-14654.20
120.63	-14654.23
125.63	-14654.21
130.63	-14654.15
135.63	-14654.07
140.63	-14653.96
145.63	-14653.83
150.63	-14653.70
155.63	-14653.57
160.63	-14653.45
Energy vs. Angle (CCH)	
90.84	-14653.39
95.84	-14653.65
100.84	-14653.86
105.84	-14654.03
110.84	-14654.14
115.84	-14654.21
120.84	-14654.23
125.84	-14654.21
130.84	-14654.14
135.84	-14654.04

Energy vs. Dihedral angle (OCCH)	
0.44	-14654.22643
0.94	-14654.22697
1.44	-14654.22742
1.94	-14654.22777
2.44	-14654.22803
2.94	-14654.22818
3.44	-14654.22824
3.94	-14654.22819
4.44	-14654.22805
4.94	-14654.22781
5.44	-14654.22747
5.94	-14654.22703
6.44	-14654.22648
6.94	-14654.2258
Energy vs. Dihedral angle (HCCH)	
-30.07	-14654.07
-25.07	-14654.12
-20.07	-14654.16
-15.07	-14654.19
-10.07	-14654.21
-5.07	-14654.22
-0.07	-14654.23
4.92	-14654.22
9.92	-14654.21
14.92	-14654.19
19.92	-14654.16
24.92	-14654.12
29.92	-14654.07
Energy vs. Dihedral angle (CCCC)	
-25.07	-14654.02
-20.07	-14654.10
-15.07	-14654.15
-10.07	-14654.19
-5.07	-14654.22
-0.07	-14654.23
4.93	-14654.22
9.93	-14654.20
14.93	-14654.16
19.93	-14654.10

A.3.4 Dimethylamine

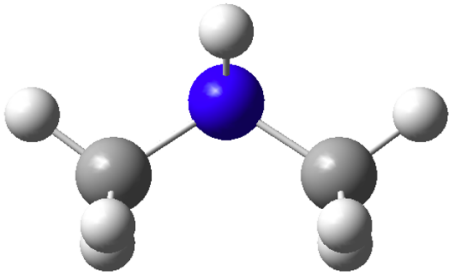

Figure A 5: The ball and stick model of Dimethylamine molecule.

Structural parameters of Dimethylamine

Properties	B3LYP/6-31G(d,p)
Bond length (Å)	
R(C-N)	1.46
R (C-H)	1.09
R (N-H)	1.01
Bond Angle (^{o})	
A(C-N-C)	112.8
A(H-C-H)	108.2
A(H-N-C)	109.2
A(H-C-N)	109.8

Energy Surface

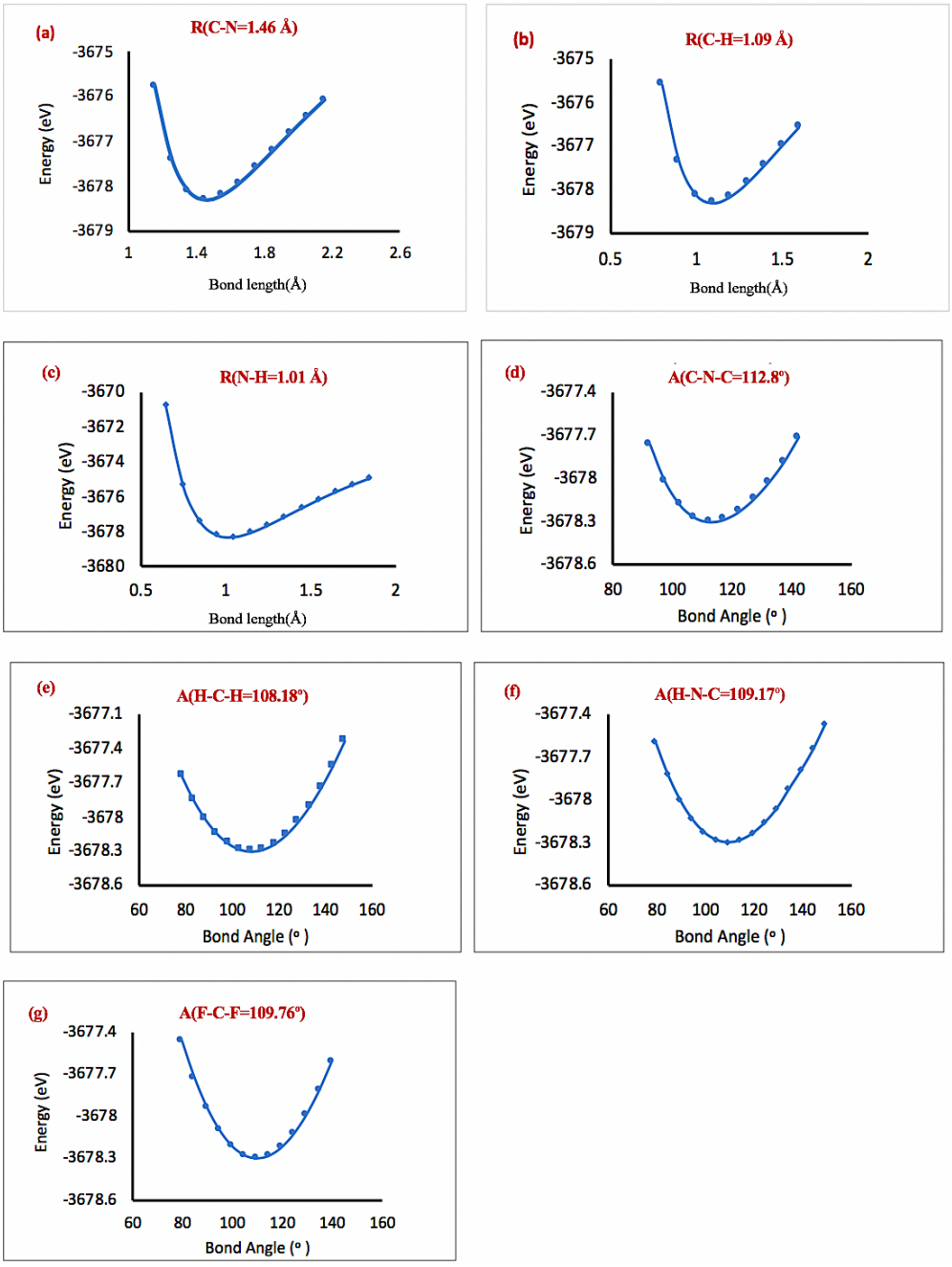

Bond length (Å)	Energy (eV)
Energy vs. Bond length (C-N)	
0.95	-3666.84
1.05	-3672.60
1.15	-3675.77
1.25	-3677.39
1.35	-3678.11
1.45	-3678.30
1.55	-3678.19
1.65	-3677.92
1.75	-3677.58
1.85	-3677.19
1.95	-3676.81
2.05	-3676.43
2.15	-3676.08
Energy vs. Bond length (C-H1)	
0.77	-3674.72
0.87	-3676.92
0.97	-3677.94
1.07	-3678.28
1.17	-3678.25
1.27	-3678.01
1.37	-3677.69
1.47	-3677.32
1.57	-3676.95
1.67	-3676.60
1.77	-3676.27
Energy vs. Bond length (C-H2)	
0.80	-3675.57
0.90	-3677.36
1.00	-3678.12
1.10	-3678.30
1.20	-3678.16
1.30	-3677.83
1.40	-3677.43
1.50	-3676.99
1.60	-3676.56

Energy vs. Bond length (N-H)	
0.65	-3670.76
0.75	-3675.28
0.85	-3677.38
0.95	-3678.18
1.05	-3678.28
1.15	-3678.03
1.25	-3677.61
1.35	-3677.12
1.45	-3676.62
1.55	-3676.14
1.65	-3675.69
Bond angle (^{0})	**Energy (eV)**
Energy vs. Angle (C-N-C)	
92.3	-3677.76
97.3	-3678.02
102.3	-3678.18
107.3	-3678.27
112.3	-3678.30
117.3	-3678.28
122.3	-3678.23
127.3	-3678.14
132.3	-3678.03
137.3	-3677.89
142.3	-3677.71
Energy vs. Angle (H-C-H)	
78.2	-3677.64
83.2	-3677.85
88.2	-3678.01
93.2	-3678.14
98.2	-3678.23
103.2	-3678.28
108.2	-3678.30
113.2	-3678.28
118.2	-3678.24
123.2	-3678.15
128.2	-3678.04
133.2	-3677.90
138.2	-3677.74

Energy vs. Angle (H-N-C)	
79.2	-3677.59
84.2	-3677.82
89.2	-3678.00
94.2	-3678.13
99.2	-3678.23
104.2	-3678.28
109.2	-3678.30
114.2	-3678.28
119.2	-3678.24
124.2	-3678.16
129.2	-3678.06
134.2	-3677.93
139.2	-3677.79
Energy vs. Angle (H-C-N)	
79.6	-3677.46
84.6	-3677.72
89.6	-3677.94
94.6	-3678.10
99.6	-3678.21
104.6	-3678.28
109.6	-3678.30
114.6	-3678.28
119.6	-3678.22
124.6	-3678.12
129.6	-3677.99
134.6	-3677.82
139.6	-3677.61

A.3.5 Phenyl-cyanate

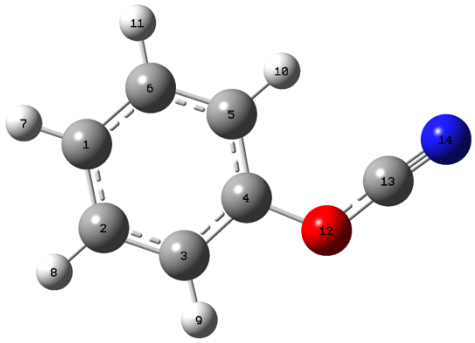

Figure A 6: The ball and stick model of Phenyl-cyanate molecule.

Structural parameters of Phenyl-cyanate

Properties	**B3LYP/6-31G(d,p)**
Bond length (Å)	
R(C4-O12)	1.42
R (C-C)	1.38
R (O12-C13)	1.29
R (C≡N)	1.16
Bond Angle (°)	
A(C-O-C)	119.0
A(C-C-H)	120.6
A(O-C-C)	122.3

Energy Surface

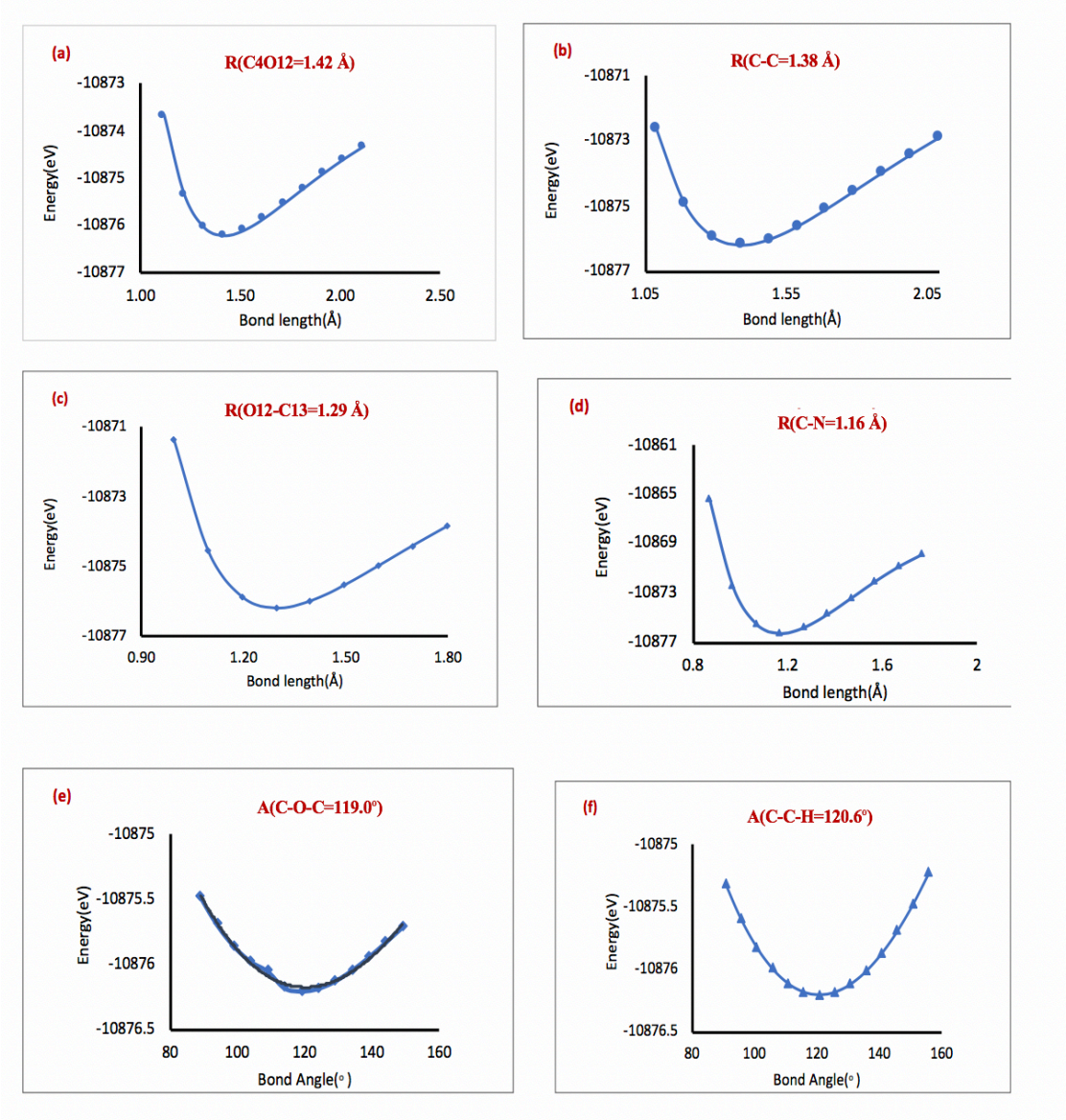

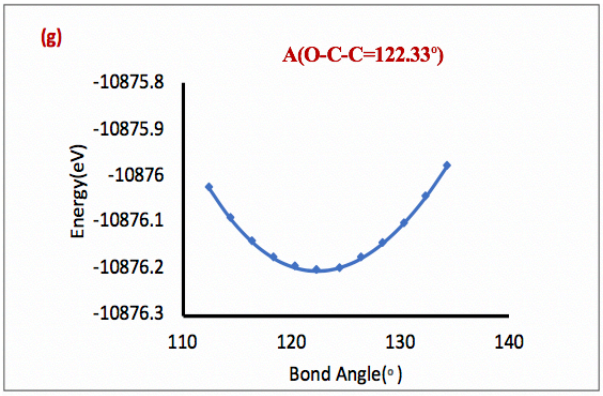
(g)
A(O-C-C=122.33°)
-10875.8
-10875.9
-10876
-10876.1
-10876.2
-10876.3
Energy(eV)
110
120
130
140
Bond Angle(°)

Bond length (Å)	Energy (eV)
Energy vs. Bond length (C4-O12)	
1.12	-10873.68
1.22	-10875.33
1.32	-10876.03
1.42	-10876.20
1.52	-10876.10
1.62	-10875.84
1.72	-10875.53
1.82	-10875.21
1.92	-10874.89
2.02	-10874.60
2.12	-10874.33
Energy vs. Bond length (C-C)	
1.08	-10872.65
1.18	-10874.95
1.28	-10875.95
1.38	-10876.20
1.48	-10876.03
1.58	-10875.63
1.68	-10875.12
1.78	-10874.55
1.88	-10873.99
1.98	-10873.44
2.08	-10872.92
Energy vs. Bond length (O12-C13)	
0.99	-10871.36
1.09	-10874.55
1.19	-10875.88
1.29	-10876.20
1.39	-10876.0
1.49	-10875.54
1.59	-10874.98
1.69	-10874.40
1.79	-10873.86

Energy vs. Bond length (C-N)	
0.86	-10865.39
0.96	-10872.47
1.06	-10875.47
1.16	-10876.20
1.26	-10875.73
1.36	-10874.67
1.46	-10873.38
1.56	-10872.07
1.66	-10870.87
1.76	-10869.89
Bond angle (^{0})	**Energy (eV)**
Energy vs. Angle (C-O-C)	
89.0	-10875.48
94.0	-10875.69
99.0	-10875.86
104.0	-10875.98
109.0	-10876.05
114.0	-10876.18
119.0	-10876.20
124.0	-10876.18
129.0	-10876.13
134.0	-10876.04
139.0	-10875.94
144.0	-10875.83
149.0	-10875.71
Energy vs. Angle (O-C-C)	
112.3	-10876.03
114.3	-10876.09
116.3	-10876.14
118.3	-10876.18
120.3	-10876.20
122.3	-10876.20
124.3	-10876.20
126.3	-10876.18
128.3	-10876.15
130.3	-10876.10
132.3	-10876.05
134.3	-10875.98

Bond angle (^{0})	Energy (eV)
Energy vs. Angle (C-O-C)	
89.0	-10875.48
94.0	-10875.69
99.0	-10875.86
104.0	-10875.98
109.0	-10876.05
114.0	-10876.18
119.0	-10876.20
124.0	-10876.18
129.0	-10876.13
134.0	-10876.04
139.0	-10875.94
144.0	-10875.83
149.0	-10875.71
Energy vs. Angle (C-C-H)	
90.6	-10875.32
95.6	-10875.60
100.6	-10875.82
105.6	-10875.99
110.6	-10876.11
115.6	-10876.18
120.6	-10876.20
125.6	-10876.18
130.6	-10876.12
135.6	-10876.01
140.6	-10875.80
145.6	-10875.69
150.6	-10875.48
155.6	-10875.23

A.3.6 Phenyl vinyl sulfone

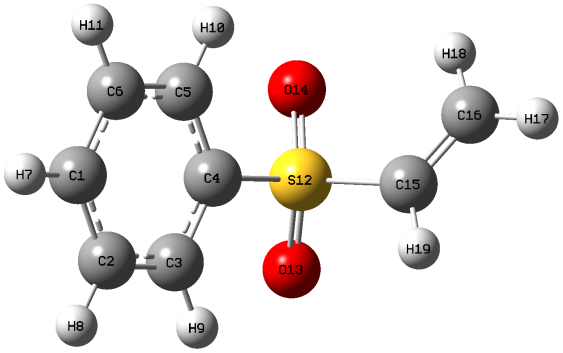

Figure A 7: The ball and stick model of Phenyl vinyl sulfone molecule.

Calculated structural parameters of Phenyl vinyl sulfone

Properties	B3LYP/6-31G(d,p)
Bond length (Å)	
R(C-C)	1.39
R(C=C)	1.32
R (C-H)	1.08
R(S=O)	1.47
R(S-C)	1.79
Bond Angle (°)	
A(C=C-H)	121.0
A(H-C-H)	118.3
A(S-C-H)	114.2
A(C-S-C)	103.6
A(O=S=O)	121.5
A(S-C=C)	120.4

Energy Surface

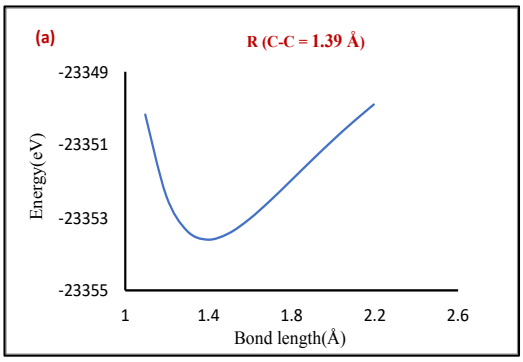

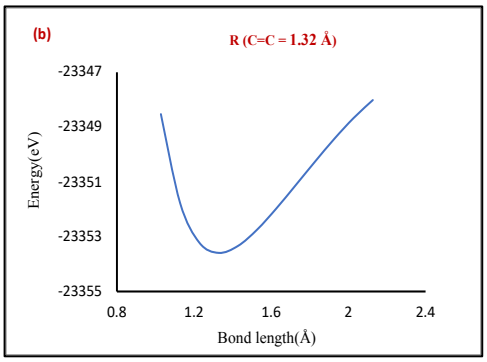

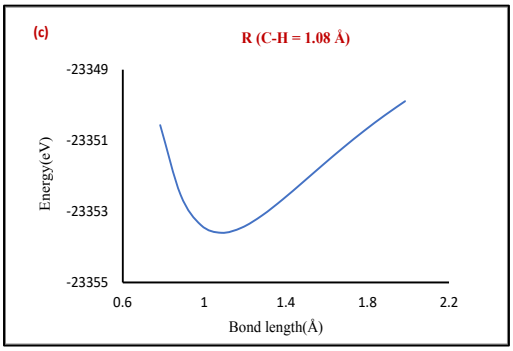

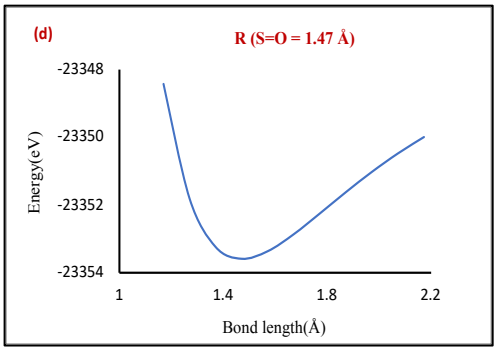

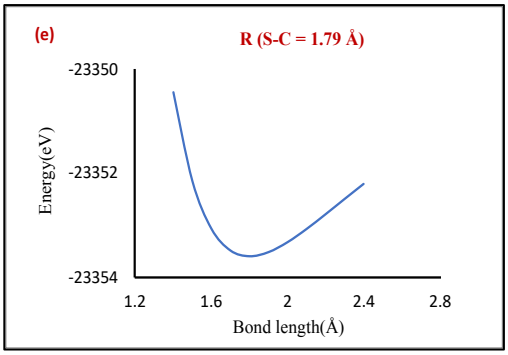

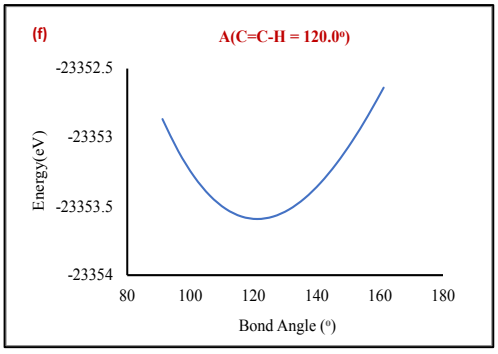

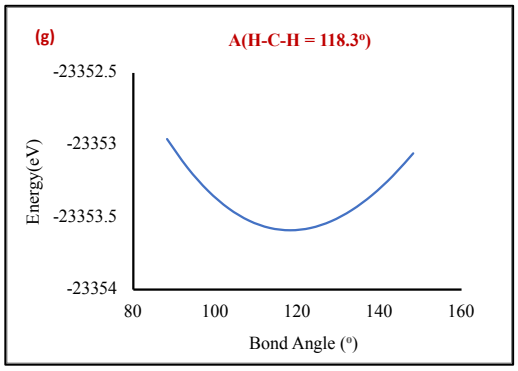
(g)
A(H-C-H = 118.3º)
-23352.5
-23353
-23353.5
-23354
Energy(eV)
80
100
120
140
160
Bond Angle (º)

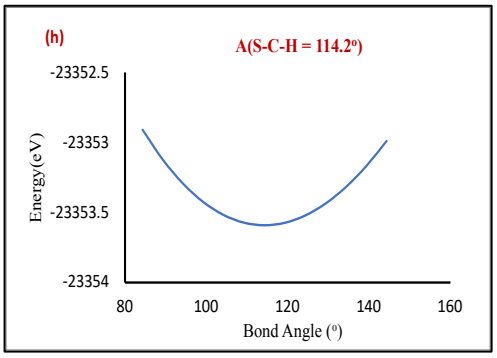
(h)
A(S-C-H = 114.2º)
-23352.5
-23353
-23353.5
-23354
Energy(eV)
80
100
120
140
160
Bond Angle (º)

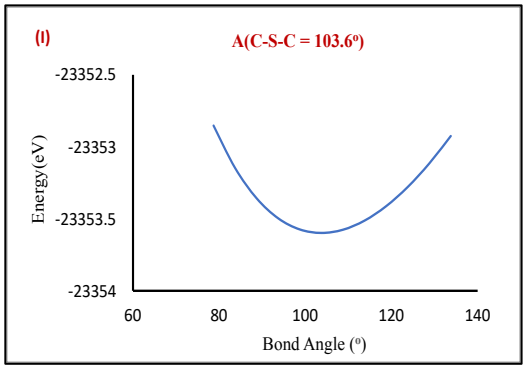
(I)
A(C-S-C = 103.6º)
-23352.5
-23353
-23353.5
-23354
Energy(eV)
60
80
100
120
140
Bond Angle (º)

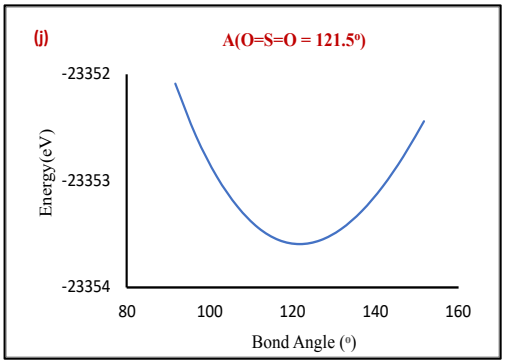
(j)
A(O=S=O = 121.5º)
-23352
-23353
-23354
Energy(eV)
80
100
120
140
160
Bond Angle (º)

Bond length (Å)	Energy (eV)
Energy vs. Bond length (C-C)	
1.09	-23350.17
1.19	-23352.38
1.29	-23353.35
1.39	-23353.59
1.49	-23353.43
1.59	-23353.04
1.69	-23352.53
1.79	-23351.98
1.89	-23351.43
1.99	-23350.89
2.09	-23350.37
2.19	-23349.89
Energy vs. Bond length (C=C)	
1.02	-23348.54
1.12	-23351.78
1.22	-23353.22
1.32	-23353.59
1.42	-23353.34
1.52	-23352.74
1.62	-23351.97
1.72	-23351.13
1.82	-23350.27
1.92	-23349.44
2.02	-23348.69
2.12	-23348.03
Energy vs. Bond length (S-C)	
1.39	-23350.45
1.49	-23352.15
1.59	-23353.07
1.69	-23353.48
1.79	-23353.59
1.89	-23353.51
1.99	-23353.32
2.09	-23353.07
2.19	-23352.79
2.29	-23352.50
2.39	-23352.21

Energy vs. Bond length (C-H)	
0.78	-23350.56
0.88	-23352.52
0.98	-23353.38
1.08	-23353.59
1.18	-23353.45
1.28	-23353.10
1.38	-23352.65
1.48	-23352.16
1.58	-23351.66
1.68	-23351.18
1.78	-23350.72
1.88	-23350.28
1.98	-23349.88
Energy vs. Bond length (S=O)	
1.17	-23348.43
1.27	-23351.81
1.37	-23353.24
1.47	-23353.59
1.57	-23353.37
1.67	-23352.87
1.77	-23352.26
1.87	-23351.63
1.97	-23351.03
2.07	-23350.48
2.17	-23350.00
Energy vs. Angle (S-C=C)	
95.47	-23352.76
100.47	-23353.07
105.47	-23353.31
110.47	-23353.48
115.47	-23353.57
120.47	-23353.59
125.47	-23353.57
130.47	-23353.51
135.47	-23353.41
140.47	-23353.29
145.47	-23353.14
150.47	-23352.96

Bond angle (^{0})	Energy (eV)
Energy vs. Bond Angle (C=C-H)	
91.06	-23352.87
96.06	-23353.10
101.06	-23353.28
106.06	-23353.42
111.06	-23353.52
116.06	-23353.57
121.06	-23353.59
126.06	-23353.58
131.06	-23353.52
136.06	-23353.44
141.06	-23353.33
146.06	-23353.19
151.06	-23353.03
156.06	-23352.84
161.06	-23352.64
Energy vs. Angle (C-S-C)	
78.63	-23352.85
83.63	-23353.15
88.63	-23353.35
93.63	-23353.49
98.63	-23353.57
103.63	-23353.59
108.63	-23353.57
113.63	-23353.51
118.63	-23353.41
123.63	-23353.28
128.63	-23353.11
133.63	-23352.92
78.63	-23352.85
83.63	-23353.15
88.63	-23353.35

Energy vs. Angle (H-C-H)	
88.30	-23352.96
93.30	-23353.16
98.30	-23353.32
103.30	-23353.44
108.30	-23353.53
113.30	-23353.58
118.30	-23353.59
123.30	-23353.58
128.30	-23353.53
133.30	-23353.45
138.30	-23353.35
143.30	-23353.22
148.30	-23353.06
Energy vs. Angle (S-C-H)	
84.28	-23352.91
89.28	-23353.12
94.28	-23353.30
99.28	-23353.43
104.28	-23353.52
109.28	-23353.57
114.28	-23353.59
119.28	-23353.58
124.28	-23353.52
129.28	-23353.44
134.28	-23353.32
139.28	-23353.17
144.28	-23352.99
Energy vs. Angle (O=S=O)	
91.56	-23352.09
96.56	-23352.58
101.56	-23352.96
106.56	-23353.24
111.56	-23353.44
116.56	-23353.56
121.56	-23353.59
126.56	-23353.56
131.56	-23353.45
136.56	-23353.28
141.56	-23353.06
146.56	-23352.77
151.56	-23352.44

A.3.7 Phthalic anhydride

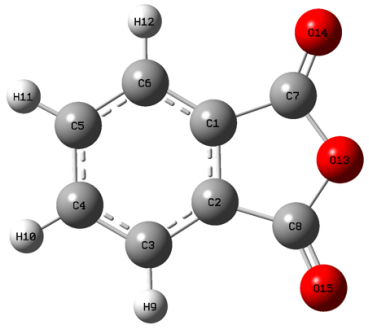

Figure A 8: The ball and stick model of phthalic anhydride.

Structural parameters of phthalic anhydride

Properties	**B3LYP/6-31G (d,p)**
Bond length (Å)	
R (C1-C7)	1.48
R(C1-C2)	1.39
R(C7=O14)	1.19
Bond Angle (^{o})	
A(C1-C7-O13)	107.1
A(C7-O13-C8)	110.2
A(C7-C1-C3)	121.7
A(C1-C7-O14)	130.6
A(O13-C7-O14)	122.2
A(C1-C3-C5)	117.0

Energy Surface

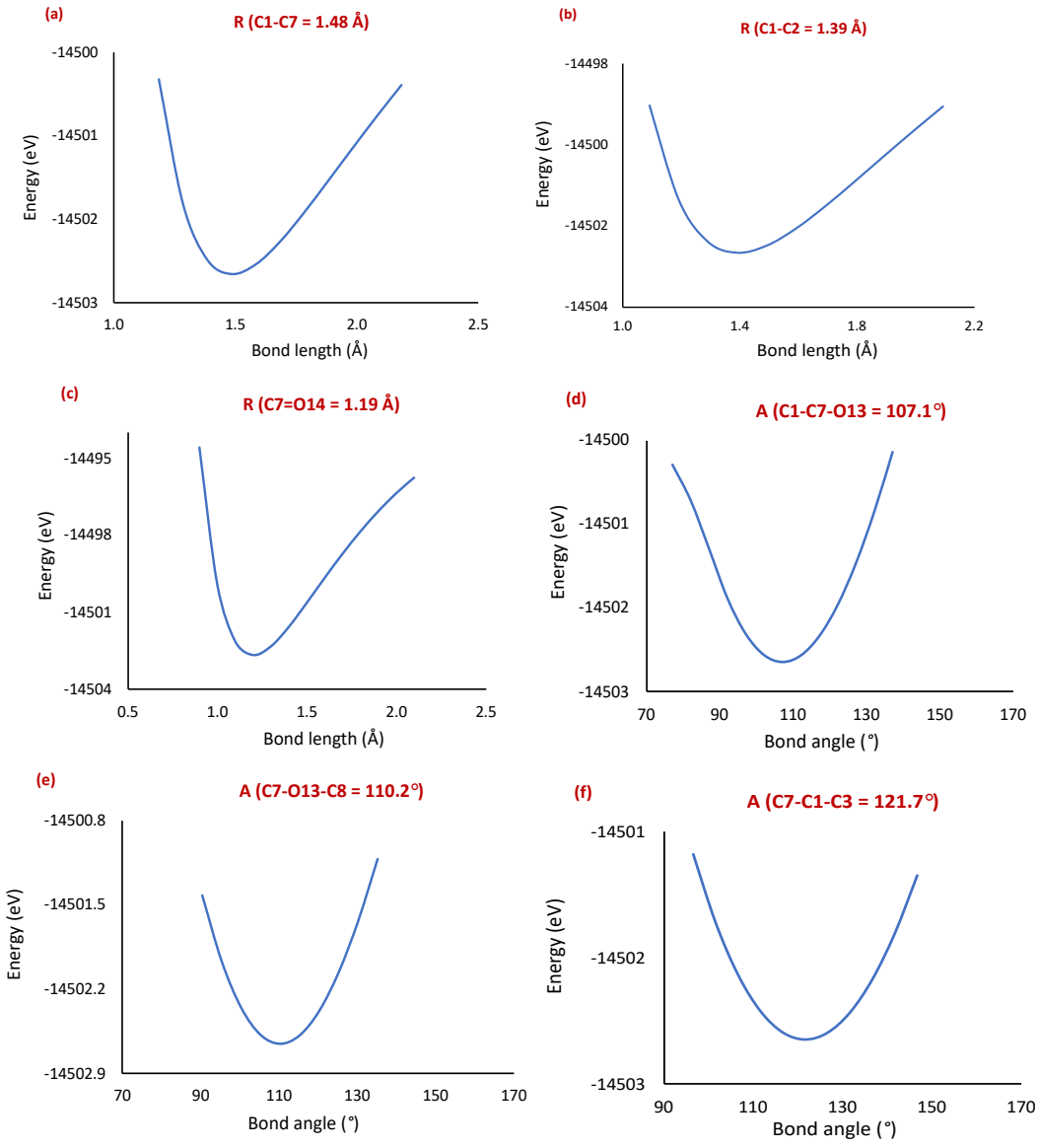

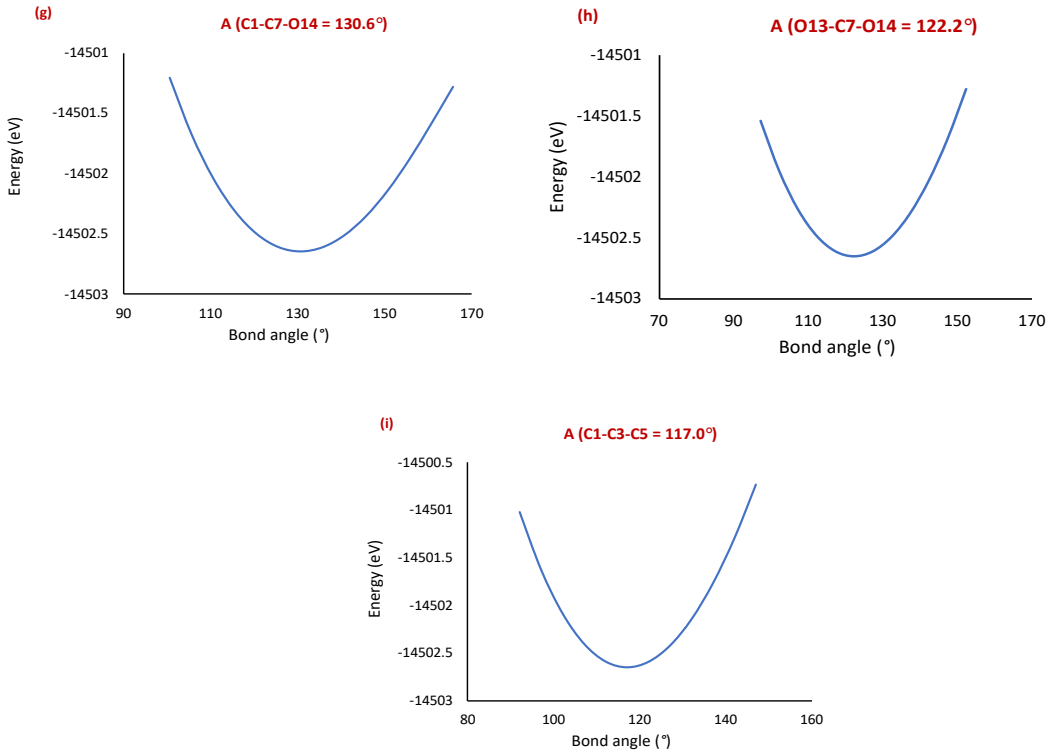
(g)
A (C1-C7-O14 = 130.6°)
-14501
-14501.5
-14502
-14502.5
-14503
Energy (eV)
90
110
130
150
170
Bond angle (°)
(h)
A (O13-C7-O14 = 122.2°)
-14501
-14501.5
-14502
-14502.5
-14503
Energy (eV)
70
90
110
130
150
170
Bond angle (°)
(i)
A (C1-C3-C5 = 117.0°)
-14500.5
-14501
-14501.5
-14502
-14502.5
-14503
Energy (eV)
80
100
120
140
160
Bond angle (°)

Bond length (Å)	Energy (eV)
Energy vs. length (C1-C7)	
0.88	-14483.76
0.98	-14492.28
1.08	-14497.44
1.18	-14500.32
1.28	-14501.81
1.38	-14502.48
1.48	-14502.65
1.58	-14502.53
1.68	-14502.26
1.78	-14501.91
1.88	-14501.52
1.98	-14501.13
2.08	-14500.75
2.18	-14500.39
Energy vs. length (C1-C2)	
1.09	-14499.03
1.19	-14501.36
1.29	-14502.39
1.39	-14502.65
1.49	-14502.47
1.59	-14502.05
1.69	-14501.50
1.79	-14500.89
1.89	-14500.27
1.99	-14499.65
2.09	-14499.06
Energy vs. length (C7-014)	
0.90	-14494.56
1.00	-14499.90
1.10	-14502.11
1.20	-14502.65
1.30	-14502.31
1.40	-14501.55
1.50	-14500.62
1.60	-14499.64
1.70	-14498.70
1.80	-14497.83
1.90	-14497.04
2.00	-14496.35

Bond angle (^{0})	Energy (eV)
E vs. Angle (C1-C7-O14)	
100.61	-14501.20
105.61	-14501.67
110.61	-14502.04
115.61	-14502.32
120.61	-14502.50
125.61	-14502.61
130.61	-14502.65
135.61	-14502.61
140.61	-14502.52
145.61	-14502.36
150.61	-14502.14
155.61	-14501.88
160.61	-14501.59
E vs. Angle (O13-C7-O14)	
92.28	-14501.04
97.28	-14501.54
102.28	-14501.95
107.28	-14502.26
112.28	-14502.48
117.28	-14502.61
122.28	-14502.65
127.28	-14502.61
132.28	-14502.49
137.28	-14502.30
142.28	-14502.03
147.28	-14501.69
152.28	-14501.28
E vs. Angle (C1-C3-C5)	
92.05	-14501.02
97.05	-14501.63
102.05	-14502.09
107.05	-14502.40
112.05	-14502.59
117.05	-14502.65
122.05	-14502.59
127.05	-14502.42
132.05	-14502.14
137.05	-14501.77
142.05	-14501.30
147.05	-14500.73

Bond Angle (^{0})	Energy (eV)
Energy vs. Bond Angle (C1-C7-O13)	
77.10	-14500.30
82.10	-14500.73
87.10	-14501.30
92.10	-14501.89
97.10	-14502.32
102.10	-14502.57
107.10	-14502.65
112.10	-14502.57
117.10	-14502.34
122.10	-14501.97
127.10	-14501.47
132.10	-14500.86
137.10	-14500.15
Energy vs. Bond Angle (C7-O13-C8)	
90.25	-14501.42
95.25	-14501.97
100.25	-14502.35
105.25	-14502.58
110.25	-14502.65
115.25	-14502.58
120.25	-14502.38
125.25	-14502.06
130.25	-14501.63
135.25	-14501.12
Energy vs. Angle (C7-C1-C13)	
96.72	-14501.18
101.72	-14501.72
106.72	-14502.13
111.72	-14502.42
116.72	-14502.59
121.72	-14502.65
126.72	-14502.59
131.72	-14502.43
136.72	-14502.17
141.72	-14501.81
146.72	-14501.34

A.3.8 2- propylphenol

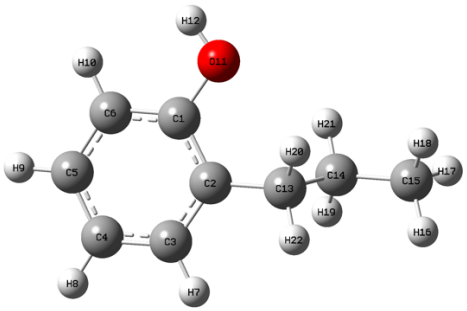

Figure A 9: The ball and stick model of 2-Propylphenol molecule.

Calculated structural parameters of 2-Propylphenol

Properties	B3LYP/6-31G (d,p)
Bond length (Å)	
R(C13-C14)	1.54
R(C=O)	1.37
R (C13-H20)	1.10
R(O-H)	0.96
Bond Angle (º)	
A(C-O-H)	108.9
A(C13-C14-C15)	112.6
A(C3-C2-C13)	121.8
A(C2-C13-H20)	109.5

Energy Surface

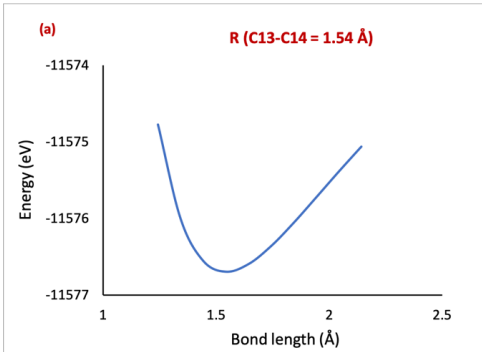

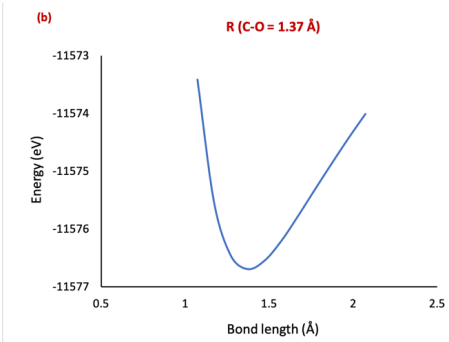

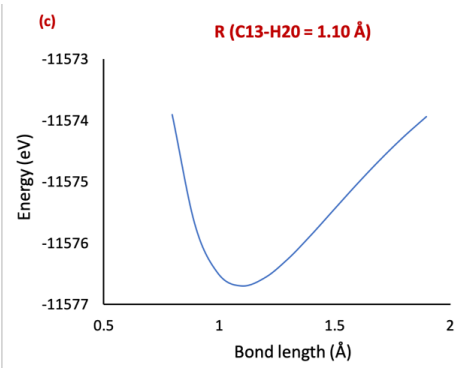

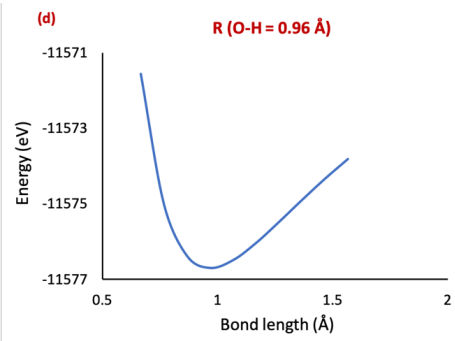

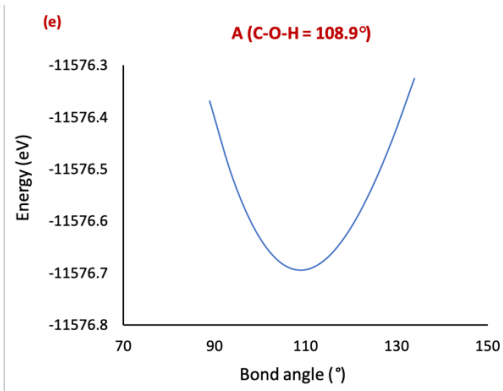

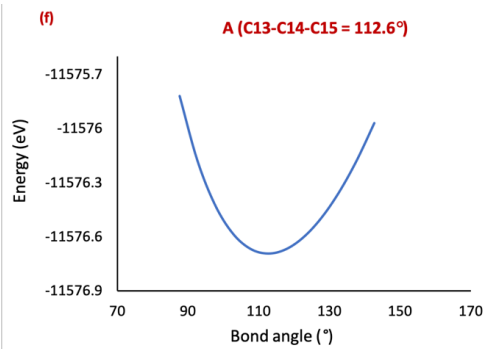

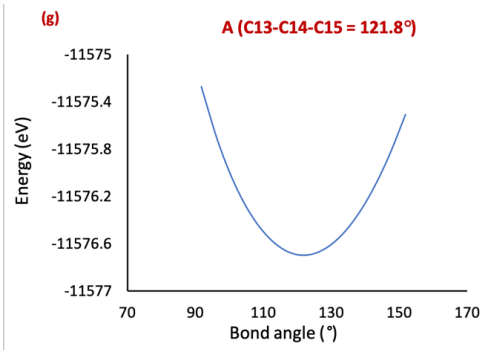
(g)
A (C13-C14-C15 = 121.8°)
-11575
-11575.4
-11575.8
-11576.2
-11576.6
-11577
Energy (eV)
70
90
110
130
150
170
Bond angle (°)

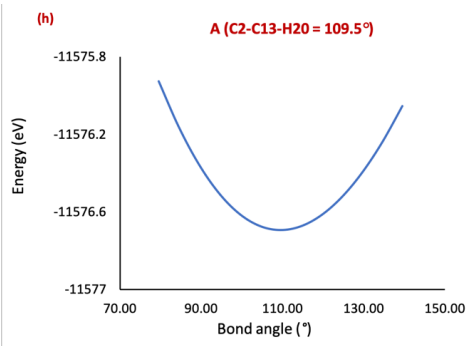
(h)
A (C2-C13-H20 = 109.5°)
-11575.8
-11576.2
-11576.6
-11577
Energy (eV)
70.00
90.00
110.00
130.00
150.00
Bond angle (°)

Bond length (Å)	Energy (eV)
Energy vs. Bond length (O-H)	
0.67	-11571.56
0.77	-11574.99
0.87	-11576.37
0.97	-11576.70
1.07	-11576.49
1.17	-11576.04
1.27	-11575.48
1.37	-11574.90
1.47	-11574.34
1.57	-11573.81
1.67	-11573.68
Bond angle (^{0})	**Energy (eV)**
Energy vs. Bond Angle (C-O-H)	
88.90	-11576.369
93.90	-11576.516
98.90	-11576.617
103.90	-11576.676
108.90	-11576.695
113.90	-11576.677
118.90	-11576.627
123.90	-11576.549
128.90	-11576.446
133.90	-11576.326
138.90	-11576.192
143.90	-11576.050
Energy vs. Angle (C13-C14-C15)	
87.65	-11575.82
92.65	-11576.18
97.65	-11576.42
102.65	-11576.58
107.65	-11576.67
112.65	-11576.70
117.65	-11576.67
122.65	-11576.60
127.65	-11576.50
132.65	-11576.36
137.65	-11576.18
142.65	-11575.97

Bond length (Å)	Energy (eV)
Energy vs. Bond length (C-C)	
1.24	-11574.78
1.34	-11576.00
1.44	-11576.55
1.54	-11576.70
1.64	-11576.60
1.74	-11576.36
1.84	-11576.06
1.94	-11575.73
2.04	-11575.39
2.14	-11575.06
Energy vs. Bond length (C-O)	
1.07	-11573.41
1.17	-11575.56
1.27	-11576.47
1.37	-11576.70
1.47	-11576.55
1.57	-11576.20
1.67	-11575.77
1.77	-11575.31
1.87	-11574.86
1.97	-11574.43
2.07	-11574.01
Energy vs. Bond length (C13-H20)	
0.80	-11573.91
0.90	-11575.72
1.00	-11576.50
1.10	-11576.70
1.20	-11576.56
1.30	-11576.26
1.40	-11575.87
1.50	-11575.45
1.60	-11575.04
1.70	-11574.64
1.80	-11574.27
1.90	-11573.94

Bond angle (^{0})	Energy (eV)
Energy vs. Angle (C3-C2-C13)	
91.82	-11575.27
96.82	-11575.74
101.82	-11576.11
106.82	-11576.37
111.82	-11576.55
116.82	-11576.66
121.82	-11576.70
126.82	-11576.66
131.82	-11576.56
136.82	-11576.39
141.82	-11576.16
146.82	-11575.87
151.82	-11575.51
Energy vs. Angle (C2-C13-H20)	
79.50	-11575.93
84.50	-11576.17
89.50	-11576.36
94.50	-11576.51
99.50	-11576.61
104.50	-11576.68
109.50	-11576.70
114.50	-11576.68
119.50	-11576.62
124.50	-11576.53
129.50	-11576.40
134.50	-11576.24
139.50	-11576.06

A.3.9 4-vinyl 1-cyclohexene 1, 2-epoxide

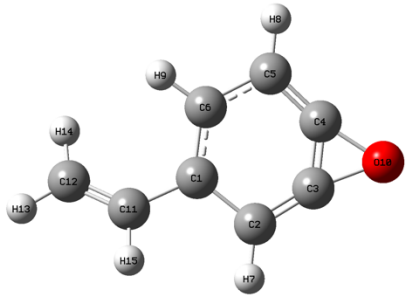

Figure A 10: The ball and stick model of 4-vinyl 1-cyclohexene 1, 2-epoxide

Structural parameters of 4-vinyl 1-cyclohexene 1, 2-epoxide

Properties	B3LYP/6-31G (d,p)
Bond length (Å)	
R(C11=C12)	1.33
R(C1-C11)	1.47
R (O10-C4)	1.46
R(C2-H7)	1.08
Bond Angle (°)	
A(C6-C1-C11)	121.7
A(C1-C11=C12)	127.2
A(C2-C1-C11)	116.9

Energy Surface

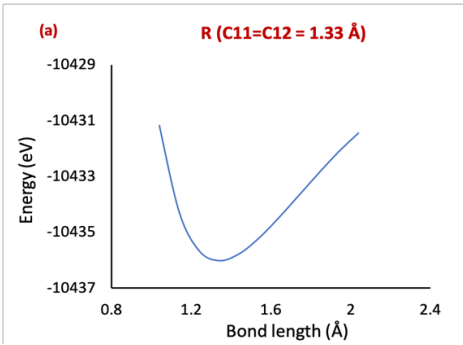

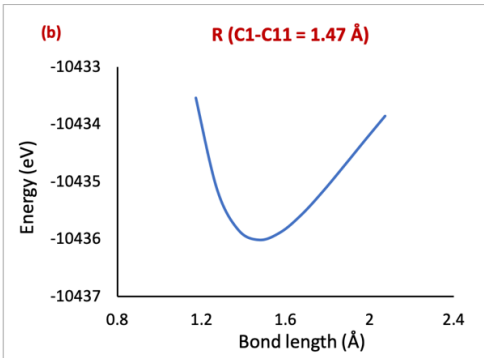

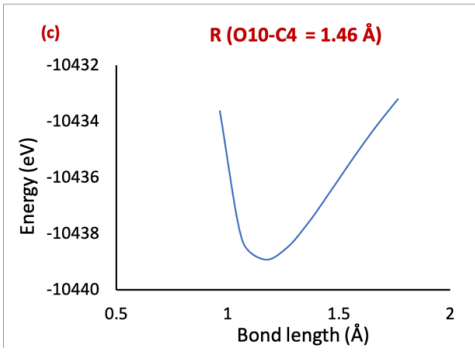

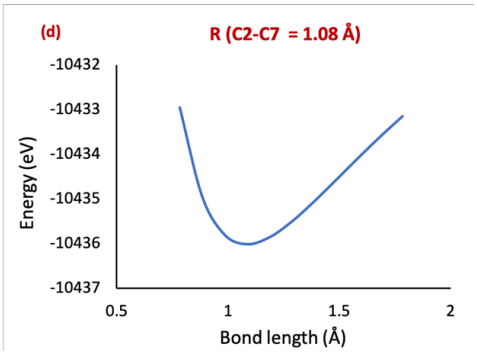

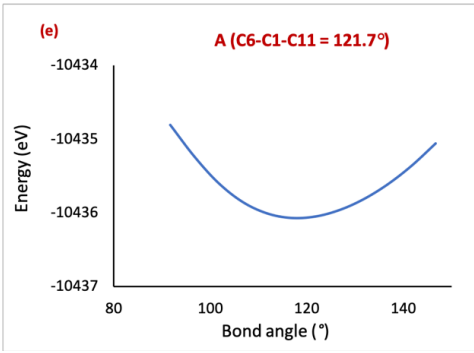

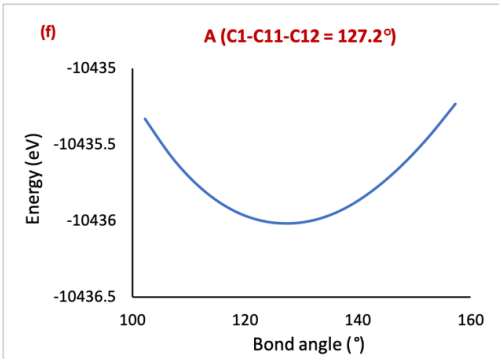

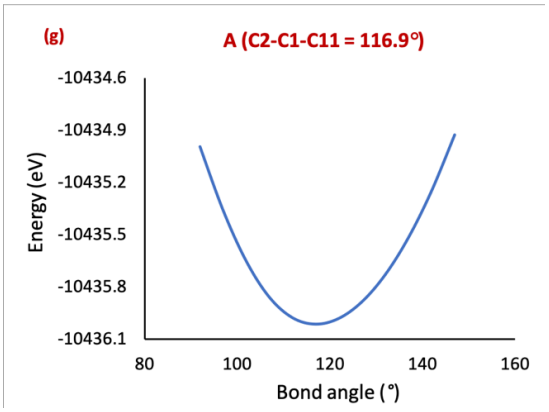
(g)
A (C2-C1-C11 = 116.9°)
-10434.6
-10434.9
-10435.2
-10435.5
-10435.8
-10436.1
Energy (eV)
80
100
120
140
160
Bond angle (°)

Bond length (Å)	Energy (eV)
Energy vs. Bond length (C11-C12)	
1.04	-10431.18
1.14	-10434.29
1.24	-10435.66
1.34	-10436.02
1.44	-10435.78
1.54	-10435.21
1.64	-10434.48
1.74	-10433.69
1.84	-10432.89
1.94	-10432.13
Energy vs. Bond length (C1-C11)	
1.17	-10433.54
1.27	-10435.13
1.37	-10435.83
1.47	-10436.02
1.57	-10435.89
1.67	-10435.59
1.77	-10435.19
1.87	-10434.75
1.97	-10434.30
2.07	-10433.86
Energy vs. Bond length (O10-C4)	
0.96	-10433.64
1.06	-10438.22
1.16	-10438.93
1.26	-10438.52
1.36	-10437.59
1.46	-10436.46
1.56	-10435.30
1.66	-10434.20
1.76	-10433.21

Energy vs. Bond length (C2-H7)	
0.78	-10432.95
0.88	-10434.94
0.98	-10435.80
1.08	-10436.02
1.18	-10435.87
1.28	-10435.52
1.38	-10435.08
1.48	-10434.59
1.58	-10434.09
1.68	-10433.61
1.78	-10433.15
Bond angle (^{0})	**Energy (eV)**
Energy vs. Bond Angle (C6-C1-C11)	
91.69	-10434.81
96.69	-10435.24
101.69	-10435.60
106.69	-10435.85
111.69	-10436.01
116.69	-10436.07
121.69	-10436.05
126.69	-10435.96
131.69	-10435.82
136.69	-10435.62
141.69	-10435.36
146.69	-10435.06
Energy vs. Angle (C1-C11-C12)	
102.24	-10435.33
107.24	-10435.59
112.24	-10435.79
117.24	-10435.92
122.24	-10435.99
127.24	-10436.02
132.24	-10435.99
137.24	-10435.93
142.24	-10435.81
147.24	-10435.65
152.24	-10435.46

Bond angle (^{0})	Energy (eV)
Energy vs. Angle (C2-C1-C11)	
91.92	-10434.99
96.92	-10435.36
101.92	-10435.65
106.92	-10435.86
111.92	-10435.98
116.92	-10436.02
121.92	-10435.98
126.92	-10435.89
131.92	-10435.73
136.92	-10435.52
141.92	-10435.25
146.92	-10434.93

A.3.10 Diphenyl-Ether

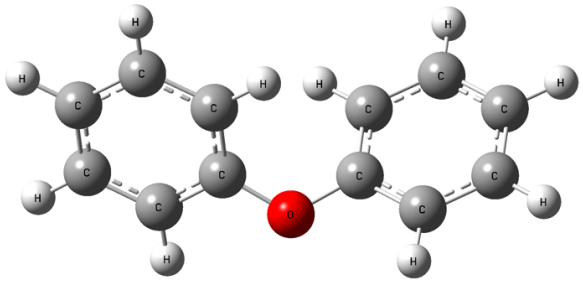

Figure A 11: The ball and stick model of Diphenyl-Ether molecule

Energy Surface

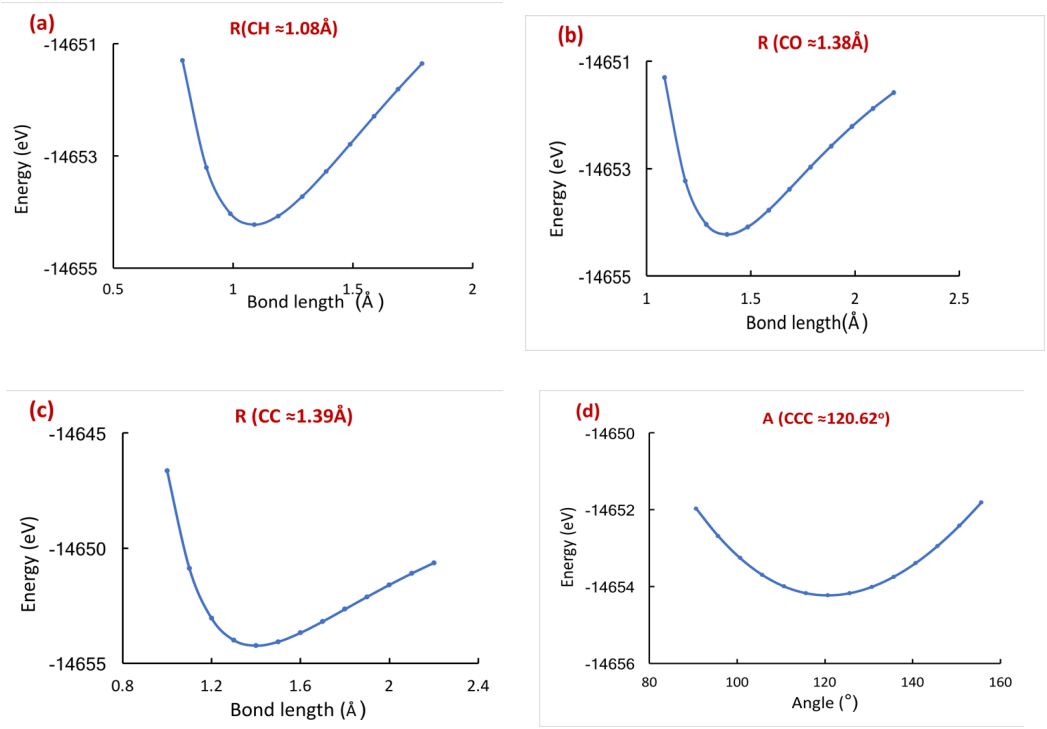

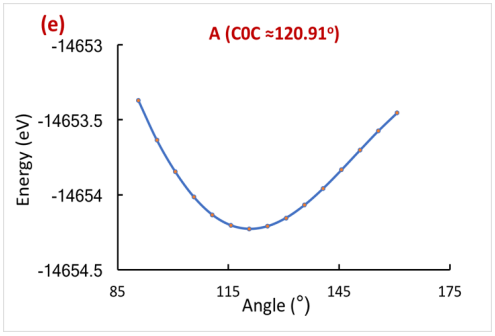
(e)
A (C0C ≈120.91°)
-14653
-14653.5
-14654
-14654.5
Energy (eV)
85
115
145
175
Angle (°)

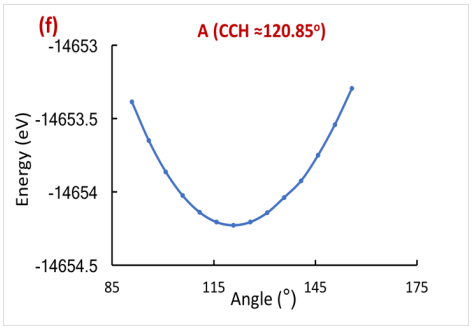
(f)
A (CCH ≈120.85°)
-14653
-14653.5
-14654
-14654.5
Energy (eV)
85
115
145
175
Angle (°)

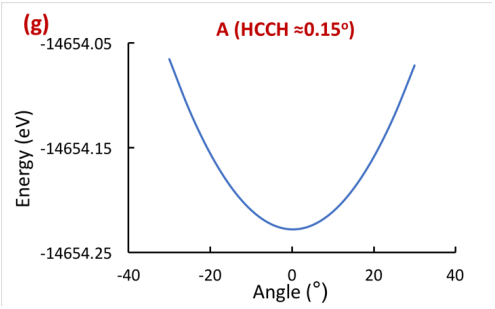
(g)
A (HCCH ≈0.15°)
-14654.05
-14654.15
-14654.25
Energy (eV)
-40
-20
0
20
40
Angle (°)

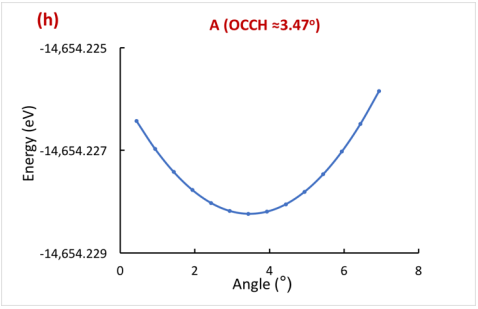
(h)
A (OCCH ≈3.47°)
-14,654.225
-14,654.227
-14,654.229
Energy (eV)
0
2
4
6
8
Angle (°)

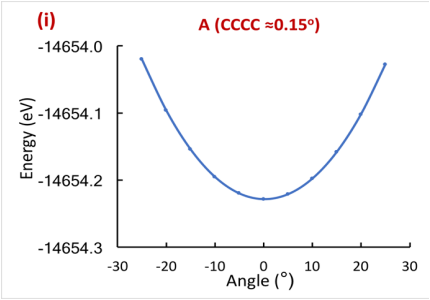
(i)
A (CCCC ≈0.15°)
-14654.0
-14654.1
-14654.2
-14654.3
Energy (eV)
-30
-20
-10
0
10
20
30
Angle (°)

Bond length (Å)	Energy (eV)
Energy vs. Bond length (CH)	
0.79	-14651.29
0.89	-14653.20
0.99	-14654.03
1.09	-14654.22
1.19	-14654.07
1.29	-14653.72
1.39	-14653.27
1.49	-14652.79
1.59	-14652.29
1.69	-14651.81
1.79	-14651.35
CO	
1.09	-14651.30
1.19	-14653.22
1.29	-14654.03
1.39	-14654.22
1.49	-14654.09
1.59	-14653.77
1.69	-14653.38
1.79	-14652.97
1.89	-14652.57
1.99	-14652.21
2.09	-14651.88
CC	
1.00	-14646.62
1.10	-14650.86
1.20	-14653.04
1.30	-14653.99
1.40	-14654.22
1.50	-14654.06
1.60	-14653.67
1.70	-14653.18
1.80	-14652.64
1.90	-14652.10
2.00	-14651.58
2.10	-14651.09
2.20	-14650.63

Bond angle (^{0})	Energy (eV)
Energy vs. Angle (CCC)	
90.64	-14651.97
95.64	-14652.68
100.64	-14653.25
105.64	-14653.69
110.64	-14653.99
115.64	-14654.170
120.64	-14654.23
125.64	-14654.17
130.64	-14654.01
135.64	-14653.74
140.64	-14653.39
145.64	-14652.94
150.64	-14652.41
155.64	-14651.81
COC	
90.63	-14653.37
95.63	-14653.63
100.63	-14653.84
105.63	-14654.01
110.63	-14654.13
115.63	-14654.20
120.63	-14654.22
125.63	-14654.21
130.63	-14654.15
135.63	-14654.10
140.63	-14653.96
145.63	-14653.83
150.63	-14653.70
155.63	-14653.57
160.63	-14653.45
CCH	
90.84	-14653.39
95.84	-14653.65
100.84	-14653.86
105.84	-14654.02
110.84	-14654.14
115.84	-14654.21
120.84	-14654.23
125.84	-14654.21
130.84	-14654.14
135.84	-14654.04
140.84	-14653.90
145.84	-14653.75
150.84	-14653.54

A.3.11 Glycidol

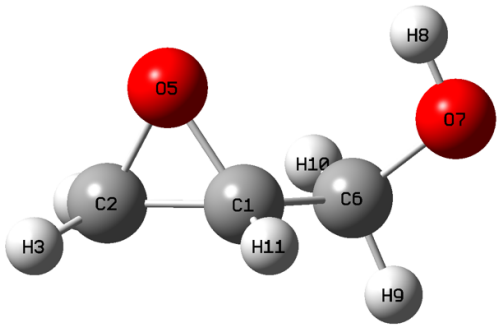

Figure A 12: The ball and stick model of Glycidol molecule

Calculated structural parameters of Glycidol

Properties	B3LYP/6-31G(d,p)
Bond length (Å)	
R(C-O)	1.4
R (C-H)	1.1
R(C-C)	1.5
Bond Angle (°)	
A(C-O-C)	61.4
A(C-C-C)	122.0
A(H4-C2-H3)	115.1
A(H9-C6-H10)	108.0
A(C-O-H)	106.4
A(C1-C2-H3)	119.6
A(C1-C6-H10)	109.1
A(C6-C1-H11)	115.4

Energy Surface

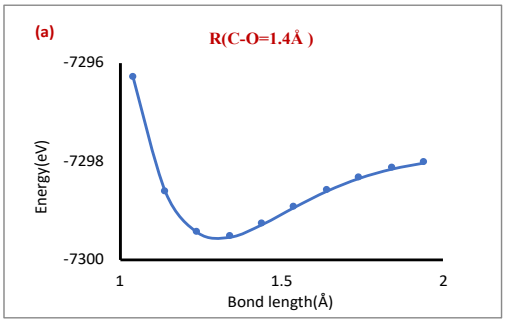

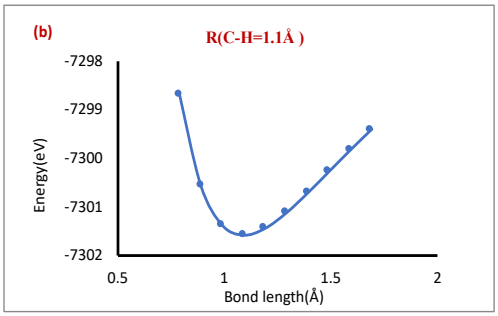

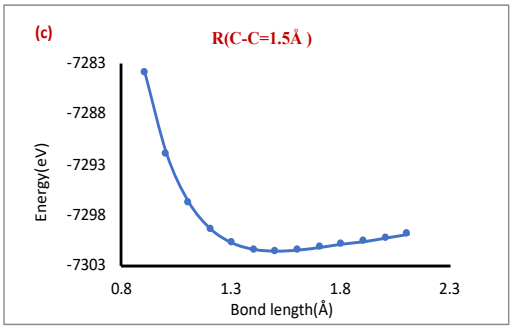

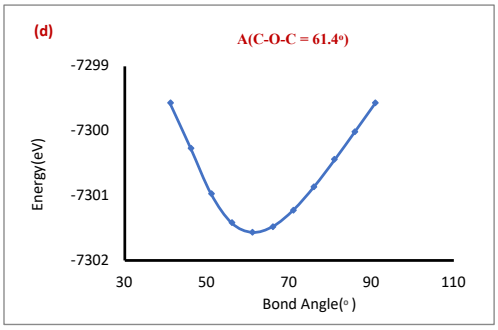

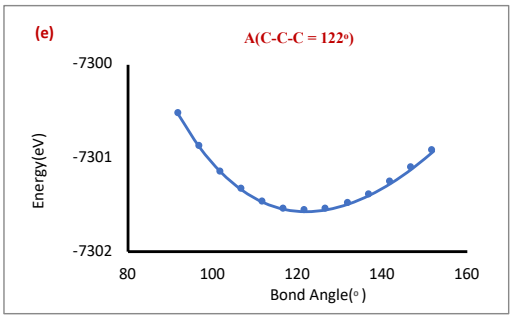

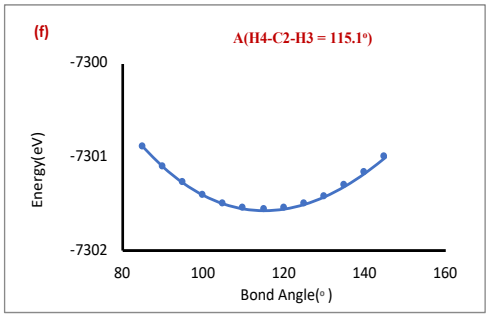

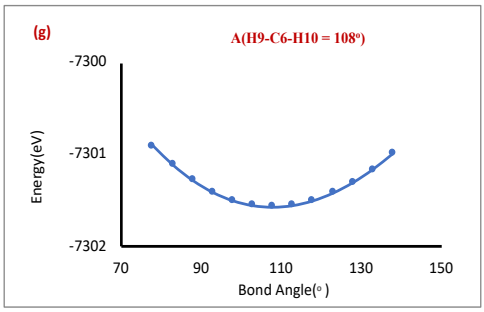
(g)
A(H9-C6-H10 = 108°)
-7300
-7301
-7302
Energy(eV)
70
90
110
130
150
Bond Angle(°)

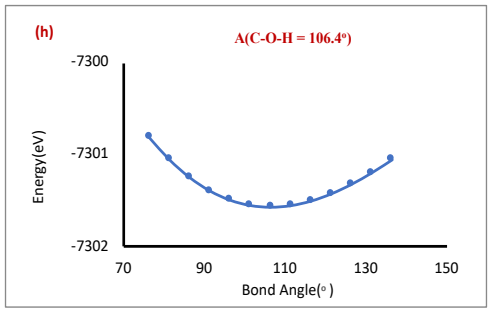
(h)
A(C-O-H = 106.4°)
-7300
-7301
-7302
Energy(eV)
70
90
110
130
150
Bond Angle(°)

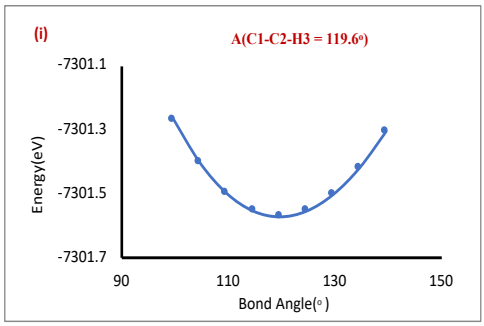
(i)
A(C1-C2-H3 = 119.6°)
-7301.1
-7301.3
-7301.5
-7301.7
Energy(eV)
90
110
130
150
Bond Angle(°)

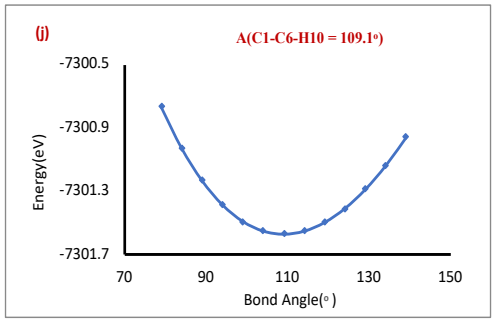
(j)
A(C1-C6-H10 = 109.1°)
-7300.5
-7300.9
-7301.3
-7301.7
Energy(eV)
70
90
110
130
150
Bond Angle(°)

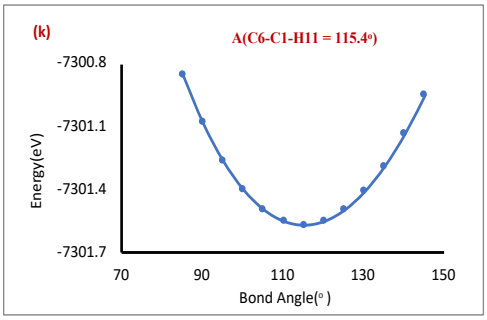
(k)
A(C6-C1-H11 = 115.4°)
-7300.8
-7301.1
-7301.4
-7301.7
Energy(eV)
70
90
110
130
150
Bond Angle(°)

Bond length (Å)	Energy (eV)
Energy vs. Bond length (C-O)	
1.0	-7296.30
1.1	-7298.62
1.2	-7299.44
1.3	-7299.53
1.4	-7299.27
1.5	-7298.92
1.6	-7298.59
1.7	-7298.33
1.8	-7298.15
1.9	-7298.02
Energy vs. Bond length (C-H)	
0.8	-7298.67
0.9	-7300.55
1.0	-7301.36
1.1	-7301.57
1.2	-7301.43
1.3	-7301.11
1.4	-7300.71
1.5	-7300.26
1.6	-7299.82
1.7	-7299.40
Energy vs. Bond length (C-O)	
0.9	-7283.89
1.0	-7291.98
1.1	-7296.72
1.2	-7299.38
1.3	-7300.78
1.4	-7301.41
1.5	-7301.57
1.6	-7301.46
1.7	-7301.20
1.8	-7300.87
1.9	-7300.63
2.0	-7300.27
2.1	-7299.91

Bond angle (^{0})	Energy (eV)
Energy vs. Angle (C-O-C)	
41.1	-7299.58
46.1	-7300.27
51.1	-7300.98
56.1	-7301.42
61.1	-7301.57
66.1	-7301.48
71.1	-7301.22
76.1	-7300.86
81.1	-7300.45
86.1	-7300.01
91.1	-7299.56
Energy vs. Angle (C-C-C)	
92.0	-7300.53
97.0	-7300.88
102.0	-7301.15
107.0	-7301.34
112.0	-7301.47
117.0	-7301.55
122.0	-7301.57
127.0	-7301.55
132.0	-7301.49
137.0	-7301.39
142.0	-7301.27
147.0	-7301.11
152.0	-7300.92
Energy vs. Angle (H4-C2-H3)	
85.1	-7300.89
90.1	-7301.11
95.1	-7301.28
100.1	-7301.41
105.1	-7301.50
110.1	-7301.55
115.1	-7301.57
120.1	-7301.55
125.1	-7301.50
130.1	-7301.42
135.1	-7301.31
140.1	-7301.17

Bond angle (^{0})	Energy (eV)
Energy vs. Angle (H9-C6-H10)	
78.0	-7300.91
83.0	-7301.11
88.0	-7301.28
93.0	-7301.41
98.0	-7301.50
103.0	-7301.55
108.0	-7301.57
113.0	-7301.55
118.0	-7301.50
123.0	-7301.42
128.0	-7301.30
133.0	-7301.16
138.0	-7300.99
Energy vs. Angle (C-O-H)	
76.5	-7300.81
81.5	-7301.05
86.5	-7301.24
91.5	-7301.39
96.5	-7301.49
101.5	-7301.55
106.5	-7301.57
111.5	-7301.55
116.5	-7301.50
121.5	-7301.42
126.5	-7301.32
131.5	-7301.19
Energy vs. Angle (C1-C2-H3)	
99.6	-7301.27
104.6	-7301.40
109.6	-7301.50
114.6	-7301.55
119.6	-7301.57
124.6	-7301.55
129.6	-7301.50
134.6	-7301.42
139.6	-7301.31

Bond angle (^{0})	Energy (eV)
Energy vs. Angle (C1-C6-H10)	
79.1	-7300.77
84.1	-7301.03
89.1	-7301.23
94.1	-7301.38
99.1	-7301.49
104.1	-7301.55
109.1	-7301.57
114.1	-7301.55
119.1	-7301.49
124.1	-7301.41
129.1	-7301.29
134.1	-7301.14
Energy vs. Angle (C6-C1-H11)	
85.4	-7300.85
90.4	-7301.08
95.4	-7301.26
100.4	-7301.40
105.4	-7301.49
110.4	-7301.55
115.4	-7301.57
120.4	-7301.55
125.4	-7301.50
130.4	-7301.41
135.4	-7301.29
140.4	-7301.13

A.3.12 Methylamine

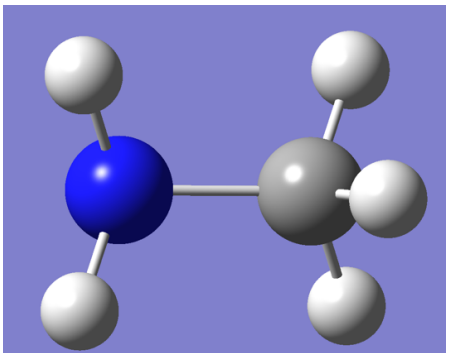

Figure A 13: The ball and stick model of methylamine molecule.

Structural parameters for methylamine

Properties	B3LYP/6-31G(d,p)
Bond length (Å)	
R (NH)	1.0
R (CN)	1.36
Bond Angle (°)	
A(CNH)	117.5
A(HNH)	119.3
A(N7C3N4)	116.7
A(N4C2N5)	126.55

Energy Surface

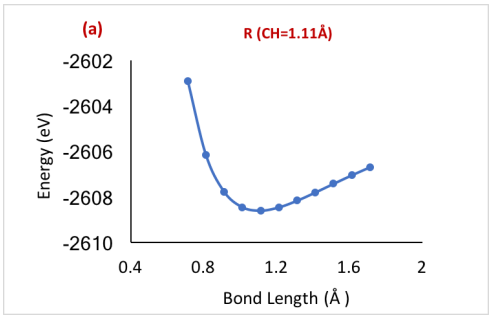

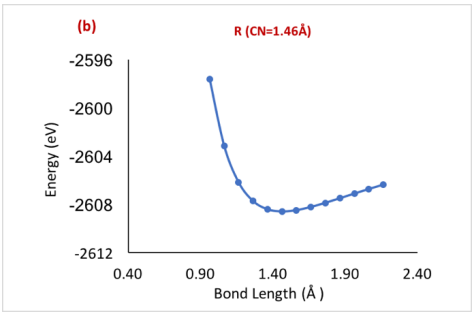

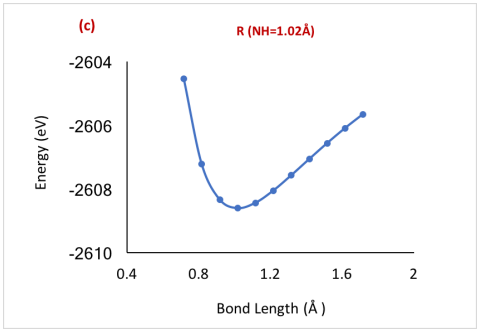

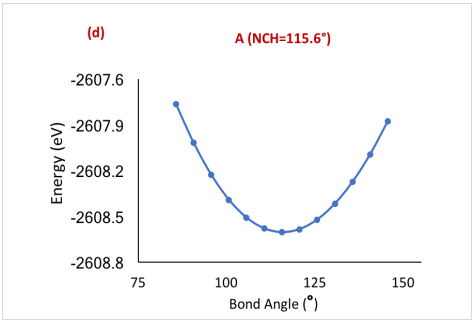

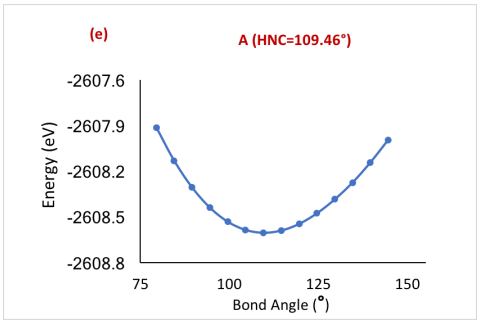

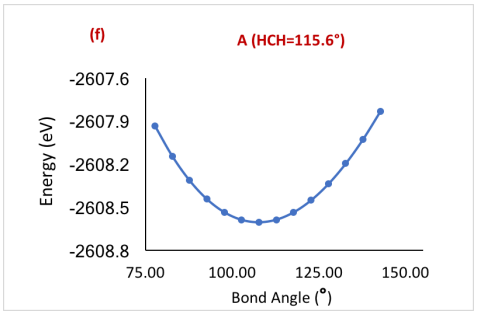

Bond length (Å)	Energy (eV)
Energy vs. Bond length (CH)	
0.71	-2602.91
0.81	-2606.17
0.91	-2607.78
1.01	-2608.46
1.11	-2608.60
1.21	-2608.46
1.31	-2608.17
1.41	-2607.81
1.51	-2607.43
1.61	-2607.05
Energy vs. Bond length (CN)	
0.96	-2597.64
1.06	-2603.17
1.16	-2606.19
1.26	-2607.74
1.36	-2608.43
1.46	-2608.60
1.56	-2608.50
1.66	-2608.23
1.76	-2607.89
1.86	-2607.51
1.96	-2607.12
2.06	-2606.75
2.16	-2606.38
Energy vs. Bond length (NH)	
0.72	-2604.54
0.82	-2607.22
0.92	-2608.33
1.02	-2608.60
1.12	-2608.44
1.22	-2608.05
1.32	-2607.57
1.42	-2607.06
1.52	-2606.56
1.62	-2606.09
1.72	-2605.65

Bond angle (^{0})	Energy (eV)
Energy vs. Angle (NCH)	
85.61	-2607.77
90.61	-2608.02
95.61	-2608.23
100.61	-2608.39
105.61	-2608.51
110.61	-2608.58
115.61	-2608.60
120.61	-2608.58
125.61	-2608.52
130.61	-2608.42
135.61	-2608.27
140.61	-2608.09
145.61	-2607.88
Energy vs. Angle (HNC)	
79.46	-2607.92
84.46	-2608.13
89.46	-2608.31
94.46	-2608.44
99.46	-2608.53
104.46	-2608.59
109.46	-2608.60
114.46	-2608.59
119.46	-2608.55
124.46	-2608.48
129.46	-2608.39
134.46	-2608.28
139.46	-2608.14
144.46	-2608.00

Bond angle (^{0})	Energy (eV)
Energy vs. Angle (HCH)	
77.71	-2607.93
82.71	-2608.14
87.71	-2608.31
92.71	-2608.44
97.71	-2608.53
102.71	-2608.59
107.71	-2608.60
112.71	-2608.59
117.71	-2608.53
122.71	-2608.45
127.71	-2608.34
132.71	-2608.20
137.71	-2608.03
142.71	-2607.83

A.4 Permissions for reuse of published paper in chapter 3

AIP PUBLISHING LICENSE
TERMS AND CONDITIONS

Apr 01, 2022

This Agreement between Ms. Geeta Sachdeva ("You") and AIP Publishing ("AIP Publishing") consists of your license details and the terms and conditions provided by AIP Publishing and Copyright Clearance Center.

License Number	5272080271009
License date	Mar 18, 2022
Licensed Content Publisher	AIP Publishing
Licensed Content Publication	Applied Physics Letters
Licensed Content Title	Optical absorbance in multilayer two-dimensional materials: Graphene and antimonene
Licensed Content Author	Ashok Kumar, Geeta Sachdeva, Ravindra Pandey, et al
Licensed Content Date	Jun 29, 2020
Licensed Content Volume	116
Licensed Content Issue	26
Type of Use	Thesis/Dissertation
Requestor type	Author (original article)

A.5 Permissions for reuse of published paper in chapter 4

3/18/22, 3:50 PM Rightslink® by Copyright Clearance Center

CCC RightsLink

Home | Help | Live Chat | Geeta Sachdeva

Mechanical Response of Polymer Epoxy/BMI Composites with Graphene and a Boron Nitride Monolayer from First Principles

ACS Publications

Author: Geeta Sachdeva, Álvaro Lobato, Ravindra Pandey, et al

Publication: ACS Applied Polymer Materials

Publisher: American Chemical Society

Date: Feb 1, 2021

Copyright © 2021, American Chemical Society

PERMISSION/LICENSE IS GRANTED FOR YOUR ORDER AT NO CHARGE

This type of permission/license, instead of the standard Terms and Conditions, is sent to you because no fee is being charged for your order. Please note the following:

- Permission is granted for your request in both print and electronic formats, and translations.
- If figures and/or tables were requested, they may be adapted or used in part.
- Please print this page for your records and send a copy of it to your publisher/graduate school.
- Appropriate credit for the requested material should be given as follows: "Reprinted (adapted) with permission from {COMPLETE REFERENCE CITATION}. Copyright {YEAR} American Chemical Society." Insert appropriate information in place of the capitalized words.
- One-time permission is granted only for the use specified in your RightsLink request. No additional uses are granted (such as derivative works or other editions). For any uses, please submit a new request.

If credit is given to another source for the material you requested from RightsLink, permission must be obtained from that source.

BACK CLOSE WINDOW

© 2022 Copyright - All Rights Reserved | Copyright Clearance Center, Inc. | Privacy statement | Terms and Conditions
Comments? We would like to hear from you. E-mail us at customercare@copyright.com

A.6 Permissions for use of Figure 1b

4/18/22, 9:32 AM Rightslink® by Copyright Clearance Center

CCC RightsLink

Home | Help | Live Chat | Sign in | Create Account

ACS Publications

Two-Dimensional Nanomaterials as Anticorrosion Surface Coatings for Uranium Metal: Physical Insights from First-Principles Theory

Author: Qing Guo, Gaoxue Wang, Enrique R. Batista, et al
Publication: ACS Applied Nano Materials
Publisher: American Chemical Society
Date: May 1, 2021

Copyright © 2021, American Chemical Society

PERMISSION/LICENSE IS GRANTED FOR YOUR ORDER AT NO CHARGE

This type of permission/license, instead of the standard Terms and Conditions, is sent to you because no fee is being charged for your order. Please note the following:

- Permission is granted for your request in both print and electronic formats, and translations.
- If figures and/or tables were requested, they may be adapted or used in part.
- Please print this page for your records and send a copy of it to your publisher/graduate school.
- Appropriate credit for the requested material should be given as follows: "Reprinted (adapted) with permission from {COMPLETE REFERENCE CITATION}. Copyright {YEAR} American Chemical Society." Insert appropriate information in place of the capitalized words.
- One-time permission is granted only for the use specified in your RightsLink request. No additional uses are granted (such as derivative works or other editions). For any uses, please submit a new request.

If credit is given to another source for the material you requested from RightsLink, permission must be obtained from that source.

BACK CLOSE WINDOW

A.7 Permissions for use of Appendix A.1

4/18/22, 11:45 AM Rightslink® by Copyright Clearance Center

CCC RightsLink

Home | Help | Live Chat | Sign in | Create Account

ACS Publications

Cure Behavior Changes and Compression of Carbon Nanotubes in Aerospace Grade Bismaleimide-Carbon Nanotube Sheet Nanocomposites

Author: Mohammad Hamza Kirmani, Geeta Sachdeva, Ravindra Pandey, et al
Publication: ACS Applied Nano Materials
Publisher: American Chemical Society
Date: Mar 1, 2021

Copyright © 2021, American Chemical Society

PERMISSION/LICENSE IS GRANTED FOR YOUR ORDER AT NO CHARGE

This type of permission/license, instead of the standard Terms and Conditions, is sent to you because no fee is being charged for your order. Please note the following:

- Permission is granted for your request in both print and electronic formats, and translations.
- If figures and/or tables were requested, they may be adapted or used in part.
- Please print this page for your records and send a copy of it to your publisher/graduate school.
- Appropriate credit for the requested material should be given as follows: "Reprinted (adapted) with permission from {COMPLETE REFERENCE CITATION}. Copyright {YEAR} American Chemical Society." Insert appropriate information in place of the capitalized words.
- One-time permission is granted only for the use specified in your RightsLink request. No additional uses are granted (such as derivative works or other editions). For any uses, please submit a new request.

If credit is given to another source for the material you requested from RightsLink, permission must be obtained from that source.

BACK CLOSE WINDOW